Electrocatalyst Advancements for Acidic Oxygen Evolution Reaction: From Synthesis to Reliable Performance Evaluation

Inaugural dissertation
of the Faculty of Science,
University of Bern

presented by

Aline Bornet

from Château d'Œx

Supervisor of the doctoral thesis:
Prof. Dr. Matthias Arenz

Department of Chemistry, Biochemistry and Pharmaceutical Sciences

COPYRIGHT NOTICE

You are free to:

Share – copy and redistribute the material in any medium or format

Under the following terms:

Attribution - You must give appropriate credit, provide a link to the license, and indicate if changes were made. You may do so in any reasonable manner, but not in any way that suggests the licensor endorses you or your use.

NonCommercial – You may not use the material for commercial purposes

NoDerivatives – if you remix, transform, or build upon the material,you may not distribute the modified material.

No additional restrictions – You may nt apply legal terms or technological measures that legally restrict others from doing anything the license permits

For any reuse or distribution, you must take clear to others the license terms of this work.

Any of these conditions can be waived if you get permission from the copyright holder.

Nothing in this impairs or restricts the author's moral rights according to international law.

The detailed license agreement can be found at
https://creativecommons.org/licenses/by-nc-nd/4.0/legalcode.en

This license does not apply to Figure 2.2. The corresponding copyright has been acquired. This license does not apply to Manuscript II and III. The corresponding license is indicated on p.76 and p.111, respectively.

Electrocatalyst Advancements for Acidic Oxygen Evolution Reaction: From Synthesis to Reliable Performance Evaluation

Inaugural dissertation
of the Faculty of Science,
University of Bern

presented by

Aline Bornet

from Château d'Œx

Supervisor of the doctoral thesis:
Prof. Dr. Matthias Arenz

Department of Chemistry, Biochemistry and Pharmaceutical Sciences

Accepted by the Faculty of Science

Bern, June 21st, 2024

The Dean
Prof. Dr. Herwegh

À ma maman, Hind,
Et ma grande sœur, Ornina.
Pour votre soutien indéfectible
durant toutes ces années.

ABSTRACT

Storage of renewable energy surplus is of paramount importance for tackling the ongoing climate change. Proton exchange membrane water electrolysers (PEMWEs), which split water into H_2, the energy carrier, and O_2 by electrical means, are valuable technologies for both storing renewable energy as well as providing an important base chemical. While the catalyst at the cathodic side, where H_2 evolves, is well-established, the materials that catalyse the anode reaction still require optimisation to overcome the sluggish kinetics of the oxygen evolution reaction (OER). Therefore, this thesis focuses on the acidic OER, investigating model and high-surface-area Ir-based catalysts using both fundamental and more applied approaches.

In the first part of the thesis, a commercially available IrO_2 catalyst served as a benchmark to deepen the fundamental understanding of the commonly used galvanostatic stability test in an aqueous model system (AMS). This constant current stability protocol was systematically investigated using three distinct backing electrode materials (glassy carbon (GC), Au and Ti), along with two different electrochemical testing platforms, namely a standard rotating disc electrode (RDE) and a 180° inverted RDE. In addition to buoyancy, periodic oxygen reduction reaction on top of galvanostatic screening was conducted to ensure the elimination of O_2 gas bubbles obstructing active sites. This way, it was demonstrated that in contrast to claims in literature, electrogenerated gas bubbles have a negligible effect on the observed abrupt potential rise. Combined characterisation methods such as identical location scanning electron microscopy and energy dispersive X-ray spectroscopy, Raman spectroscopy and gas detection, provided evidence that instead, the degradation of the backing electrode material is the main factor responsible for the discrepancies between AMS and membrane electrode assemblies observed in the literature. By utilising half-covered stationary GC electrodes in an H-type cell, the mechanism underlying the substrate passivation was elucidated, providing a conclusive description of the typically observed potential transient.

In the second part of the thesis, the focus was directed on developing nanoparticulate Ir-based catalysts to optimise the utilisation of iridium given its scarcity on Earth. Metallic Ir and $Ir_{0.4}Ru_{0.6}$ nanoparticles (NPs) were synthesised *via* a reproducible and straightforward colloidal route, avoiding the use of any surfactant. These NPs were subsequently immobilised onto commercially available carbon black and antimony-doped tin oxide (ATO) supports. The performance evaluation of these four catalysts was conducted using a gas diffusion electrode (GDE) setup at temperatures of 30, 40 and 60 °C. This test bed enables conducting experiments under conditions resembling those of a PEMWE, such as the usage of an electrolyte membrane, high loadings, and elevated temperatures. The catalysts were first activated (i.e., the NPs were oxidised) and subsequently tested and compared through 5-minute galvanostatic steps. Surprisingly, despite the tendency of carbon to corrode, carbon-immobilised NPs exhibited superior performance than ATO-immobilised counterparts. This

phenomenon was particularly pronounced at 60 °C. This unexpected trend was attributed to the instability of the ATO support caused by antimony leaching.

The GDE setup was further employed to investigate the influence of the substrate on the performance of $(Ir_{0.7}Ru_{0.3})_{0.96}Ni_{0.04}$ NPs immobilised onto a developed ATO support. The catalyst was synthesised in a solvothermal flow reactor, wherein the NPs are directly formed onto the support material. Two substrates were compared: one derived from fuel cell approaches, namely a carbon gas diffusion layer (GDL), and the one prevalent in PEMWE, namely a titanium porous transport layer (PTL). Our investigations revealed that while GDL is more appropriate than PTL for studying catalyst activity due to its simple and cost-effective electrode preparation, it is unsuitable for stability studies. Indeed, the GDL cannot withstand the harsh oxidative conditions and degrades rapidly. Conversely, despite requiring more elaborated electrode preparation methods, PTLs are more resistant and must therefore be the preferred choice for stability measurements.

List of Publications

Publications Included in the Thesis

The numbering follows the order of the publication presented in this thesis. "*" refers to equal contribution.

I. **A. Bornet***, P. Moreno-García*, A. Dutta, S. Vesztergom, M. Liechti, M. Arenz, and P. Broekmann. Disentangling the Limitations of RDE-based OER Stability Assessment: Bubble Retention or Interface Passivation? *In preparation.*

II. **A. Bornet**, R. Pittkowski, T. M. Nielsen, E. Berner, A. Maletzko, J. Schröder, J. Quinson, J. Melke, K. M. Ø. Jensen, and M. Arenz. Influence of Temperature on the Performance of Carbon- and ATO-Supported Oxygen Evolution Reaction Catalysts in a Gas Diffusion Electrode Setup. *ACS Catal.* **2023**, 13, 7568-7577. https://doi.org/10.1021/acscatal.3c01193.

III. **A. Bornet**, S. Pitscheider, A. Maletzko, N. Seselj, E. Bertheussen, C. M. Pedersen, G. K. H. Wiberg, J. Melke, C. Kallesøe, and M. Arenz. Beyond RDE Characterisation - Unveiling IrRu/ATO OER Catalyst Stability with GDE Setup. *Submitted to Electrochimica Acta.*

Publications Not Included in the Thesis

The numbering follows the order of appearance.

i. J. Schröder, V. A. Mints, **A. Bornet**, E. Berner, M. F. Tovini, J. Quinson, G. K. H. Wiberg, F. Bizzotto, H. A. El-Sayed, and M. Arenz. The Gas Diffusion Electrode Setup as Straightforward Testing Device for Proton Exchange Membrane Water Electrolyzer Catalysts. *JACS Au* ***2021****, 1, 247-251*. https://doi.org/10.1021/jacsau.1c00015.

ii. J. Melke, A. Maletzko, E. D. Gomez Villa, **A. Bornet**, G. K. H. Wiberg, M. Arenz, L. Sandig-Predzymirska, A. Thiere, A. Charitos, M. Stelter, Z. Wang, S. Pitscheider, E. Bertheussen, C. M. Pedersen, S. Finsdóttir, M. S. Kokborg, D. G. Berman, S. Dalvang, S. Müller, F. Seidel, N. Seselj, M. Höglinger, S. Kartusch, J. Eder, M. Macherhammer, A. Trattner, and C. Kallesøe. Recycalyse – New Sustainable and Recyclable Catalytic Materials for Proton Exchange Membrane Electrolysers. *Chem. Ing. Tech.* ***2024****, 96 (1-2), 126-142*. https://doi.org/10.1002/cite.202300143.

iii. R. Pittkowski, S. Punke, A. S. Anker, **A. Bornet**, N. Magnard, N. Schlegel, M. Mirolo, J. Drnec, J. J. K. Kirkensgaard, M. Arenz, and K. M. Ø. Jensen. Following Structural Changes in Iridium Nanoparticles during Oxygen Evolution Electrocatalysis with Operando X-Ray Total Scattering. *Submitted to JACS*, ChemRvix: https://doi.org/10.26434/chemrxiv-2023-zbtlg-v2.

iv. E. Bertheussen*, S. Pitscheider*, S. R. Susan*, R. Pittkowski, K. Svane, **A. Bornet**, H. E. M. Wisaeus, K. M. Ø. Jensen, J. Rossmeisl, M. Arenz, C. Kallesøe, and C. M. Pedersen. Impact of Nickel on Iridium-Ruthenium Structure and Activity for the Oxygen Evolution Reaction under Acidic Condition. *Submitted to ACS Material Au.*

v. A. Maletzko, E. D. Gomez Villa, B. Kintzel, H. Fietzek, G. Schmidt, J. Christen, P. Veit, P. Kühne, **A. Bornet**, M. Arenz, and J. Melke. Interaction of Catalysts for Unitized Regenerative Fuel Cells. *Submitted to Journal of Electrochemistry Society.*

ABBREVIATIONS

AEM	Adsorbate evolution mechanism
AMS	Aqueous model system
AST	Accelerated stress test
ATO	Antimony-doped tin oxide
a.u.	Arbitrary units
AWE	Alkaline water electrolyser
BoL	Beginning-of-life
BP	Bipolar plate
BSE	Backscattered electron
CCM	Catalyst-coated membrane
CE	Counter electrode
CL	Catalyst layer
CV	Cyclic voltammogram
DTI	Danish Technological Institute
EDX	Energy dispersive X-ray spectroscopy
EoL	End-of-life
EXAFS	Extended X-ray absorption fine structure
fcc	Face-centred cubic
FTO	Fluorine-doped tin oxide
GC	Glassy carbon
GDE	Gas diffusion electrode
GDL	Gas diffusion layer
hcp	Hexagonal close-packed
HEA	High entropy alloy
HER	Hydrogen evolution reaction
ICP-MS	Inductively coupled plasma-mass spectrometry
IL	Identical location
iRDE	Inverted rotating disc electrode
ITO	Indium-doped tin oxide
LOM	Lattice oxygen mechanism
MEA	Membrane electrode assembly
MPL	Microporous layer
NP	Nanoparticle
OER	Oxygen evolution reaction
ORR	Oxygen reduction reaction
PDF	Pair distribution function
PEMWE	Proton exchange membrane water electrolyser
PFSA	Perfluorosulfonic acid

PGM	Platinum group metal
ppm	Part per million
ppt	Part per trillion
PTL	Porous transport layer
RDE	Rotating disc electrode
RE	Reference electrode
RHE	Reversible hydrogen electrode
rpm	Rotation per minute
SAXS	Small-angle X-ray scattering
SE	Secondary electron
SEM	Scanning electron microscopy
SFS	Solvothermal flow synthesis
SOWE	Solid oxide water electrolyser
SR	Synchrotron radiation
TE	Transmitted electron
TEM	Transmission electron microscopy
TF	Thin film
TGA	Thermogravimetry analysis
WAXS	Wide-angle X-ray scattering
XANES	X-ray absorption near edge spectroscopy
XAS	X-ray absorption spectroscopy

TABLE OF CONTENTS

CHAPTER 1

INTRODUCTION

1.1 HYDROGEN AS A LONG-TERM ENERGY STORAGE SOLUTION

On December 12th, 2015, during the COP21, the Paris Climate Agreement was ratified by 196 parties. It aimed to combat the ongoing climate change by maintaining the global average temperature to less than 2 °C (ideally less than 1.5 °C) above the pre-industrial level.[1] The drastic and rapid reduction of anthropogenic emissions from fossil fuels along with the expansion of renewable energy technologies to the terawatt (TW) level can contribute to the realisation of this ambitious target. It has been shown that, in a best-case scenario, solar and wind power can be expanded up to 20 TW by 2050.[2] To allow such a scenario to happen and to encourage the dissemination of renewable technologies within our society and politics, it is of paramount importance to address two critical limitations: the intermittent energy output and the mismatch between energy production and demand. A clear answer to these drawbacks is an efficient and cost-effective energy storage solution.

Several mature storage technologies already exist, such as pumped-hydro, compressed air energy storage, and batteries. While the former two are constrained by their massive size and specific geographical dependencies, battery systems are often smaller and decentralised. However, due to their relatively low energy density and limited storage capability, batteries are not optimal candidates for seasonal storage. Energy storage into chemical bonds represents, on the other hand, an attractive and convenient alternative, offering high energy density, scalability, and the potential for a direct integration with other industrial sectors.[3] As a result, the "Hydrogen Economy" has gained considerable attention over the recent years as a promising transition towards a more sustainable and environmentally friendly society.[4]

But why hydrogen?

Hydrogen has a remarkably high gravimetric energy density compared to traditional carbon-based fuels (Figure 1.1A). This property positions hydrogen as a first-choice candidate for energy storage, despite its poor volumetric energy density at ambient pressure, see Figure 1.1B. Compressing H_2 to 700 bar or liquefying it improves its volumetric energy density by a factor of 100 or 1000, respectively.[5] Moreover, H_2 utilisation goes beyond being a carbon-free fuel; it can potentially be introduced into other industrial sectors, such as the production of renewable ammonia by the Haber-Bosch process.[6] This multifaceted function of hydrogen makes it a cornerstone in the transition to a greener future.

Green H_2 is defined as hydrogen generated through a clean method and a zero-emission energy source. Water electrolysers, powered by wind or solar energy, enable the production of such green H_2. Currently, as the cost of electricity dictates the extent of electrolytic H_2 production, only around 4% of worldwide H_2 is produced by water electrolysis.[3,7] However, the production of green H_2 is expected to soar considerably given the constant growth in renewable energy capacity and the recent advances in water electrolyser technologies.[7]

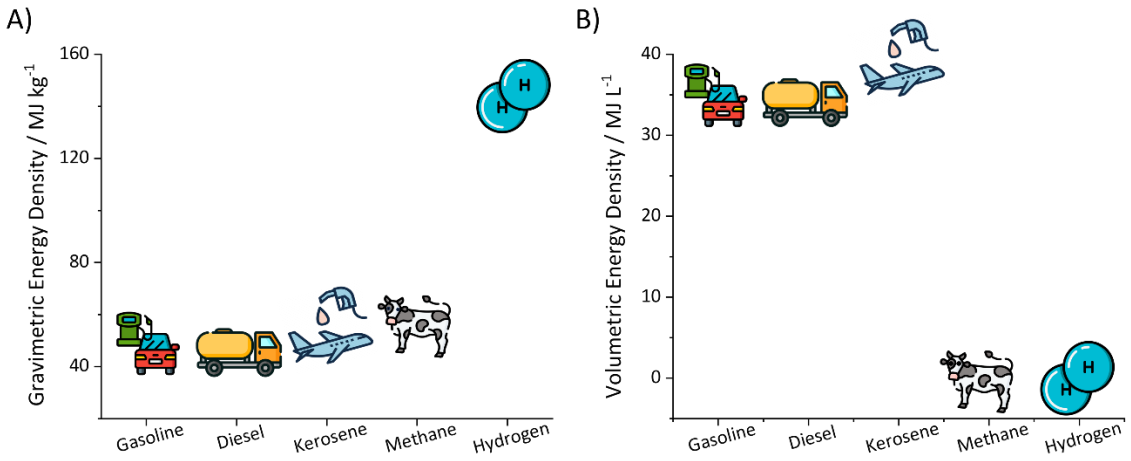

Figure 1.1. *(A) Gravimetric and (B) volumetric energy densities of most common fuels. Hydrogen herein refers to hydrogen at ambient pressure. Graph plotted with data from Tashie-Lewis et al.*[5]

1.2 WATER ELECTROLYSERS

Water electrolysers are technological devices used to split water (whether in liquid or vapour state) by electrical means into gaseous hydrogen and oxygen, as shown in Equation 1.1:

$$2H_2O \rightarrow 2H_2(g) + O_2(g) \qquad (1.1)$$

Based on the nature of their electrolyte media, water electrolysers are divided into three main categories: alkaline, acidic, or solid oxide. Although solid oxide water electrolysers (SOWEs) stand as the most efficient technology among the three, their development is still at laboratory stage.[8] Therefore, they are not addressed further in this thesis. On the other hand, traditional alkaline water electrolysers (AWEs) and proton exchange membrane water electrolysers (PEMWEs) are commercially available technologies. Both systems are described and compared in the following paragraphs. Table 1.1 summarises the main features of both types of electrolysers.

AWE is a well-established technology with principles introduced over a century ago. Industrial-scale installations for hydrogen production, reaching up to the megawatt scale, have been operational since the beginning of the 20th century. The electrolyser comprises two electrodes immersed in a liquid electrolyte, typically 30% aqueous KOH, and separated by a diaphragm (Figure 1.2A). The latter must be permeable to OH^- ions and H_2O molecules while impeding the crossover of the produced gases to ensure purity, efficiency, and safety. While the use of abundant and non-precious metals (e.g., Ni or Co) as electrocatalysts presents a significant

advantage, AWE suffers from several limitations originating from the utilisation of a liquid electrolyte and a diaphragm. In practice, the diaphragm does not completely fulfil its function, as gas cross-diffusion between compartments is evidenced under low load, posing not only purity but also safety issues due to the potential explosive recombination of H_2 and O_2 into water. Furthermore, large ohmic losses are observed due to the transportation of hydroxide ions through the electrolyte and the diaphragm, resulting in low current densities and a slow response to electrical power input. Finally, due to the utilisation of the liquid electrolyte, the installations are often large and bulky.[9,10]

It is noteworthy that recent progress has been made in developing an anion polymer electrolyte water electrolyser. This technology aims to combine the advantages of a traditional AWE such as non-noble electrocatalysts with those of PEMWE, for example, a membrane electrolyte – see more details below.[11] However, like SOWE, its development remains at a research stage and thus, is not discussed further in this thesis.

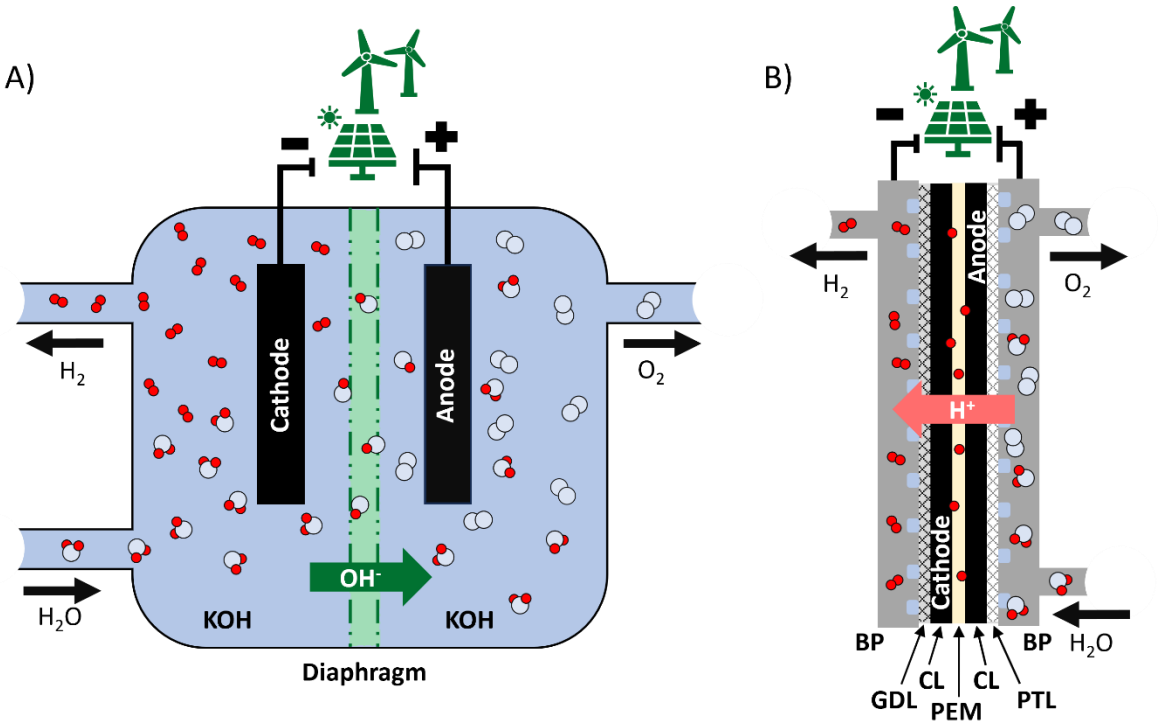

Figure 1.2. *Schematic illustrations of (A) AWE and (B) PEMWE. BP: bipolar plate; GDL: gas diffusion layer; CL: catalyst layer; PEM: proton exchange membrane; PTL: porous transport layer.*

The development of PEMWE traces back to the 1960s and 1970s with the elaboration of a thin (50-250 µm thick) perfluorosulfonic acid (PFSA) solid electrolyte by DuPont. Russell et al. have demonstrated that the integration of such a thin electrolyte membrane into a water electrolyser enables reaching current densities close to 2 A cm^{-2} at a cell voltage of 2 V with an operating temperature of 80 °C.[12] This acidic electrolyte membrane was the "game changer" that overcame the aforementioned limitations of the AWE. Notable achievements included higher hydrogen purity along with a higher level of safety. Enhanced mobility of the charge carrier (H^+ ions) enabled a fast response to (fluctuating) power input, while reduced ohmic losses facilitated reaching higher current densities. Moreover, given the dual role of the

membrane (as gas separator and electrolyte), only pure water was fed to the electrolyser. Hydrogen compression was reduced or avoided owing to the high-pressure operation possibilities.[9,10,13] Finally, a more compact design was implemented, as illustrated in Figure 1.2B.

Table 1.1 *Technical characteristic comparison between alkaline and PEM water electrolyser.*

	AWE	*PEMWE*
Electrolyte	30% aqueous KOH or 25% aqueous NaOH [8,14]	PFSA solid membrane (e.g., Nafion®, Aquivion®) [8]
Charge carrier	OH^- [8]	H^+ [8]
Anode catalyst	Ni, Co [8]	Ir, Ru [8]
Operating temperature	60-80 °C [9]	50-80 °C [14]
Output pressure	atmospheric-15 bar [15]	30-60 bar [15]
Current density	0.3-0.5 A cm^{-2} [16]	> 2 A cm^{-2} [16]
Voltage efficiency	76-82% [17]	70-90% [17]
Start-up time	1-10 min [15]	1 s to 5 min [15]
Hydrogen purity	99.9% [13]	>99.99% [13]
Lifetime stack	<90'000 h [9]	<20'000 h [9]
Lifetime system	30-40 years [17]	5-20 years [17]

Since then, PEMWE has been commercialised, but only for small niche applications. Its deployment into the large-scale market is prevented by its own set of challenges, particularly with respect to the material cost. Only a few expensive and rare materials can withstand the highly corrosive environment of PEMWE. The current collectors (bipolar plates) made from gold- or platinum-coated titanium constitute more than half of the entire PEMWE expenses, whereas the cost contribution of the electrocatalysts amounts only to less than 10%.[18] Besides the financial aspect, it is essential to stress that the catalysts are currently manufactured from scarce platinum group metals (PGMs) and thus, represent the bottleneck for scaling-up PEMWE systems. State-of-the-art catalysts are platinum at the cathode and iridium at the anode, with loadings ranging from 0.4 to 0.6 and 2.0 to 2.5 mg_{metal} cm^{-2}, respectively.[10] Considering the current state of PEMWE and the annual mining production, 1 TW energy storage would consume 30% and 400% of the yearly platinum and iridium production, respectively.[19] Thus, a reduction in noble metal loading of at least one order magnitude has to be implemented to facilitate the widespread adoption of PEMWE technology in the market. Furthermore, it is important to mention that a wide expansion of PEMWE in Europe is only feasible if good international diplomatic and economic relations are maintained. Indeed, PGMs are unevenly distributed on Earth, with concentrations in South Africa, Russia, the United States, Zimbabwe, and Canada.[20] Unfortunately, considering the current worldwide situation - i.e., wars, growing population, and significant emigration due to the climate crisis - this ideal scenario is fragile. Therefore, strategies to both mitigate the PGM content and

reduce Europe's reliance on imports from external nations are urgently required. In this regard, the Recycalyse project started 4.5 years ago.

1.3 RECYCALYSE PROJECT

The Recycalyse project, launched on April 1st, 2020, was funded by the European Union's Horizon 2020 Research and Innovation Programme. This project was rooted in a pressing need for effective and low-cost energy storage with a minimal environmental footprint. Focused on tackling the currently existing barrier of PEMWE for its commercial adoption along with reducing European dependence on PGM supplies, the Recycalyse project aimed to develop "new sustainable and **RECY**clable **CA**talytic materials for proton exchange membrane electro**LYSE**rs".[21]

The overall Recycalyse concept followed a circular economy, in which the entire chain of PEMWE was scrutinized by 11 collaborating partners coming from academic and industrial sectors (see Figure 1.3A). This circular economy included first the anodic catalyst development and production, then its integration into membrane electrode assemblies (MEAs), which were later used in a self-assembled electrolyser stack, and finally the recycling and regeneration of materials to enter once again the entire loop (Figure 1.3B).

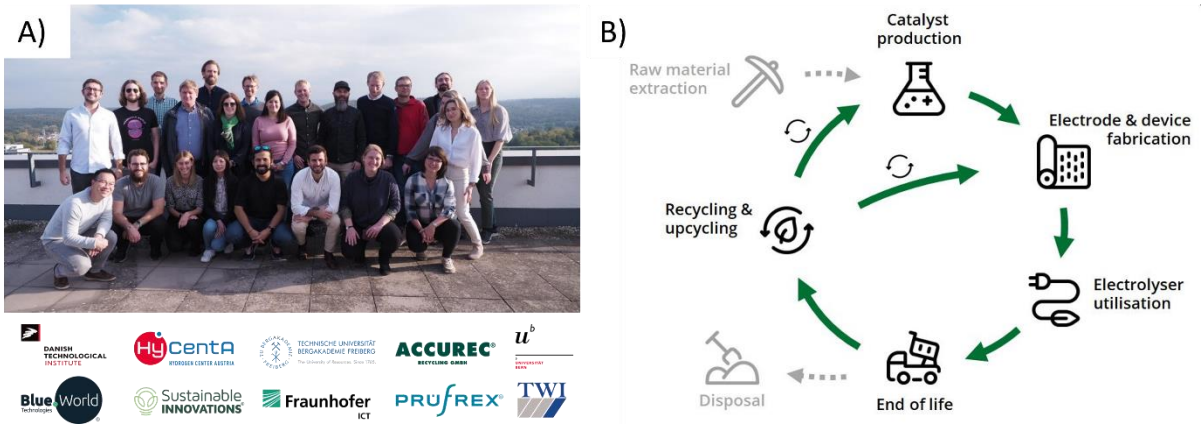

Figure 1.3. *(A) Picture of the Recycalyse consortium taken during the 5th general assembly meeting in Fraunhofer-Institute for Chemical Technology in Pfinztal, Germany and (B) the illustrative circular economy of the Recycalyse project. Picture and image taken from* [21,22].

The Recycalyse project had two main objectives:

1) The development and manufacture of a sustainable oxygen evolution reaction (OER) catalyst with improved activity and stability. This catalyst should have a reduced amount or ideally a complete elimination of PGMs.
2) The establishment of a recycling scheme for both the catalyst and the entire system.

After 3.5 years of collaborative efforts, Recycalyse successfully achieved its objectives.[21] Firstly, the utilisation of a support material for immobilising IrRuNi nanoparticles (NPs) enabled a reduction in PGM content while boosting the activity. MEAs were developed and optimised, and subsequently tested in a PEMWE stack built by a partner of the consortium (Figure 1.4). Finally, a recycling scheme was established to recover the structural components and MEAs,

with a special focus on the precious metal recovery. Thus, the achievements within the Recycalyse project marked significantly improved steps towards a more sustainable and circular approach to PEMWE systems.[23]

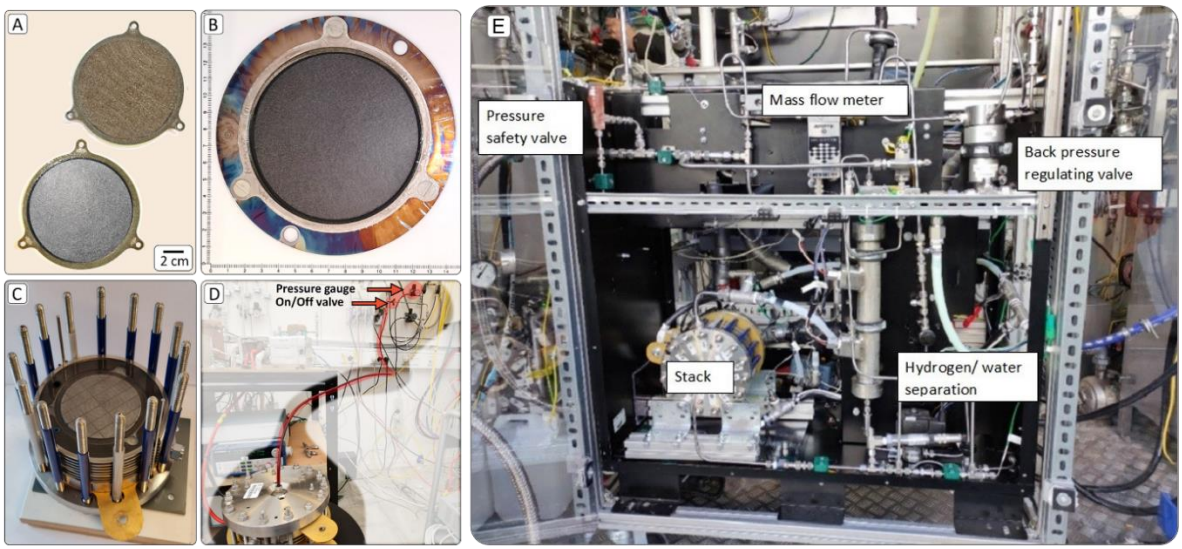

Figure 1.4. *Pictures of the Recycalyse (A) developed MEAs, (B) MEA immobilised on a titanium back plate, (C) PEMWE stack being assembled, (D) PEMWE stack being tested for gas leakage, and (E) overall test bed. Images taken from* [23].

1.4 Outline of the Thesis

As a member of the Recycalyse consortium, the focus of my doctoral research was on the oxygen evolution reaction of PEMWE. The University of Bern was the first link in the circular concept of the Recycalyse project. We devoted most of our efforts to the design of catalyst materials with reduced PGM content and their screening on a laboratory scale by means of the different setups. In this regard, during my thesis, supported catalysts were prepared *via* a colloidal synthetic route and three distinct test beds were used to evaluate the catalyst performance: the traditional rotating disc electrode (RDE), an inverted RDE (iRDE) and a gas diffusion electrode (GDE) setup. During the second year of my doctoral studies, I spent a one-month visit at the facilities of two consortium partners located in Copenhagen, Denmark, namely the Danish Technological Institute and Blue World Technologies. During this period, I acquired valuable insights into the process of synthesis scaling-up using a solvothermal flow reactor, as well as the preparation of electrodes using advanced and industrially relevant equipment.

In the following Chapter 2, the theory of the acidic oxygen evolution reaction is discussed along with insights into the currently reported studies and prevailing trends in the literature. Moreover, the methodologies employed during my doctoral studies are concisely described. The detailed experimental procedures for each performed experiment are documented in the publications in the Appendix.

In Chapters 3 to 5, the main findings of my work are described and discussed, preceded by a concise motivation section, and if available, the submitted/published abstract. Each Chapter

concludes with a description of my contributions to the corresponding work. The manuscripts of these Chapters are arranged based on a logical rather than chronological sequence.

Chapter 3, under manuscript preparation, focuses on the limitations of aqueous mode systems for stability evaluation. In this regard, an inverted RDE was employed to disentangle the two main drawbacks reported in the literature. To ensure a fair comparison without batch differences, a commercially available IrO_2 is used as a catalyst in these experiments.

In the next Chapter (published), a surfactant-free synthesis was employed to prepare different supported catalysts, subsequently characterised by several techniques. Their activity was compared in a GDE setup, i.e., under more practical and relevant conditions.

In Chapter 5 of this thesis (submitted), I focused on assessing the viability of using a GDE setup for stability tests. In this regard, using the optimised Recycalyse catalyst, two different substrates were compared through a stability protocol.

Finally, the conclusions and perspectives of the entire thesis are discussed in Chapter 6.

Important notes:

- Throughout my thesis, I will use the words “support” and “substrate”. Both have different meanings: “support” refers to the material used to immobilise the nanoparticles, e.g., high-surface-area carbon Ketjen Black, while “substrate” refers to the material of the electrode on which the catalyst is deposited, e.g., glassy carbon or gas diffusion layer. “Backing electrode material” is used as a synonym for “substrate”.
- The catalyst refers to the OER active sites, i.e., the nanoparticles, and the support material, if employed.
- Finally, when “gas diffusion layer” (GDL) is mentioned, it refers to a carbon-based material, while “porous transport layer” (PTL) refers to a titanium-based material.

CHAPTER 2

THE ACIDIC OXYGEN EVOLUTION REACTION: FROM THEORY TO EXPERIMENTAL METHODOLOGY

2.1 ACIDIC WATER ELECTROLYSIS – THERMODYNAMICS AND KINETICS

Water electrolysis corresponds to the reaction of splitting a stable water molecule to molecular hydrogen and oxygen by electrical means. Thus, the overall reaction (Equation 1.1) can be subdivided into two half-cell reactions, the hydrogen evolution reaction (HER) occurring at the cathode (Equation 2.1) and the oxygen evolution reaction (OER) at the anode (Equation 2.2). The Equations 2.1 and 2.2 are valid under acidic conditions.

$$2H^+ + 2e^- \rightarrow H_2 \tag{2.1}$$

$$H_2O \rightarrow \frac{1}{2}O_2 + 2H^+ + 2e^- \tag{2.2}$$

The reversible standard cell potential, E°_{cell}, of the overall reaction is calculated using Equation 2.3:

$$E^{\circ}_{cell} = -\frac{\Delta G^{\circ}}{z\,F} = 1.23\ V \tag{2.3}$$

where ΔG° represents the change in standard Gibbs free energy (237.2 kJ mol^{-1}), z the number of electrons transferred per H_2O molecule, and F the Faraday constant (96485 C mol^{-1}).[24]

When the standard cell potential varies from unit activity, the cell potential, E_{cell}, is described by the Nernst equation, which is commonly written in a base 10 log at 25 °C (Equation 2.4):

$$E_{cell} = E^{\circ}_{cell} - \frac{0.059}{z}\ log(Q) \tag{2.4}$$

where Q represents the reaction quotient, which corresponds to the ratio between the concentration of the products and the reactants.[25]

Under operational conditions, i.e., upon passage of faradaic current, the electrode potential deviates from the reversible E°_{cell} and the electrochemical process can be treated as irreversible. The excess of potential required is termed overpotential η and can be divided into activation, ohmic and mass transport components.[25]

The activation overpotential represents the energetic barrier that must be overcome to initiate any redox reaction. Figure 2.1A illustrates a typical activation energy scheme required to drive the reaction, along with the role of a catalyst in reducing this activation barrier.[25] The activation overpotential is further split into cathodic (here: η_{HER}) and anodic (η_{OER}) parts, as depicted in Figure 2.1B.

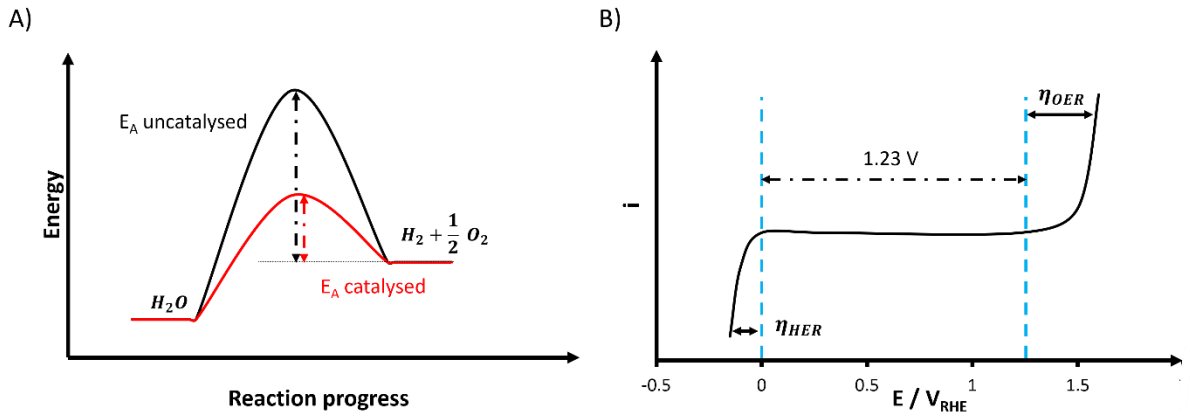

Figure 2.1. *(A) Representative activation energy scheme for an endothermic process, where E_A stands for activation energy and (B) schematic comparison of the HER and OER overpotentials assuming no η_{Ohmic} and no η_{Mass}. Images adapted from [26].*

Additionally to the activation overpotential, the ohmic overpotential (η_{Ohmic}) accounts for the losses inherent to the system, e.g., cell design, membrane, and electrolyte (i.e., the movement of ions), while the mass transport overpotential (η_{Mass}) accounts for the limitations given by the transport of species to and from the electrode surface.[25]

Hence, the cell potential under operational conditions is defined by Equation 2.5:

$$E_{cell} = E^{\circ}_{cell} + \eta_{HER} + \eta_{OER} + \eta_{Ohmic} + \eta_{Mass} \tag{2.5}$$

η_{Ohmic} and η_{Mass} are non-faradaic losses, implying the absence of electron transfer during these processes. These overpotentials are minimised through an optimisation of the experiment components (e.g., cell design and electrolyte). The activation overpotential is related to the electron transfer occurring at the electrode interface. The utilisation of Pt NPs immobilised onto high-surface-area carbon support (Pt/C) as a cathodic catalyst renders the contribution of η_{HER} marginal to the kinetic barriers. Consequently, the principal contributor to the significant energy losses during water electrolysis is η_{OER}. This is attributed to the sluggish kinetics of the oxygen evolution reaction, which necessitates a four-electron transfer.[10]

At thermodynamic equilibrium, the net current density, j, is equal to zero. At this point, the balanced faradaic activity is termed as the exchange current density, j_0. Under no mass transfer effects, the relationship between the net current density, the exchange current density and the activation overpotential is given by the Butler-Volmer equation (Equation 2.6),

$$j = j_0 \left\{ exp\left(\frac{(1-\alpha)zF\eta}{RT}\right) - exp\left(\frac{-\alpha zF\eta}{RT}\right) \right\} \tag{2.6}$$

where α represents the charge coefficient transfer, R the gas constant (8.314 J K^{-1} mol^{-1}), and T the temperature.[27]

The first exponential term is the contribution of the oxidation current, and the second one is the contribution of the reduction current. For large overpotentials, one of the exponential terms becomes negligible. For instance, at large positive overpotentials, i.e., during OER, the second exponential term is negligible. This approximation yields the Tafel equation, which represents a linear semi-logarithmic dependence between the overpotential of one half-reaction and the current density (Equation 2.7):[10,27]

$$\eta = a \ln(j) - b \tag{2.7}$$

where a describes the so-called Tafel slope and b the Tafel constant, which can be used to calculate the exchange current density.

The exchange current density and the Tafel slope are two important descriptors of the performance of a catalyst. In the literature, the Tafel slope is commonly used as a metric for evaluating the catalyst activity, with a smaller Tafel slope indicating a superior catalyst. Moreover, under certain conditions, the Tafel slope is also used to determine the rate-determining step of a reaction.[26,28,29]

2.2 The Acidic Oxygen Evolution Reaction – Mechanism

As aforementioned, OER is a complex multistep process involving four-electron transfer. In the most widely accepted mechanism known as the adsorbate evolution mechanism (AEM), each electron release is coupled with a proton. This mechanism assumes that oxygen atoms in molecular O_2 originate exclusively from water. The mechanism is described by Equations 2.8-2.11, where * denotes an active site of the catalyst.[30]

$$* + H_2O \rightarrow HO^* + H^+ + e^- \tag{2.8}$$

$$HO^* \rightarrow O^* + H^+ + e^- \tag{2.9}$$

$$O^* + H_2O \rightarrow HOO^* + H^+ + e^- \tag{2.10}$$

$$HOO^* \rightarrow * + O_2 + H^+ + e^- \tag{2.11}$$

In the two initial steps (Equations 2.8 and 2.9), a water molecule is adsorbed on an active site and then successively dissociated to adsorbed O (O*). Subsequently, another water molecule interacts with O* to form the adsorbed OOH (HOO*) (Equations 2.10 and 2.11). The latter is further oxidised to form molecular O_2. Using this mechanism and RuO_2 as a model system, Rossmeisl and co-workers found through density functional theory calculations that an overpotential η=0.37 V is necessary to initiate the OER, with the formation of HOO* identified as the rate-limiting step.[30] Extending their study to IrO_2, they calculated a slightly higher overpotential: η=0.56 V. Later, it was suggested that the difference in Gibbs free energy between O* and HO* ($\Delta G^0_{O^*} - \Delta G^0_{HO^*}$) serves as a unique descriptor for the OER activity, as the variation in the OER overpotential from one oxide surface to the next is determined by

the O* adsorption energy.[31] This descriptor was used to draw a so-called Volcano plot, which is a graphical representation of the Sabatier principle. The latter stipulates that in order to be optimal, the interaction between the catalyst surface and a reaction intermediate should neither be too strong nor too weak.[32] If an intermediate interacts too strongly with the catalyst surface, it will not desorb and thus, poison the surface. On the contrary, if the interaction is too weak, the bond will fail to form so that no reaction will take place. In Figure 2.2, where the OER overpotential is plotted against $\Delta G^0_{O^*} - \Delta G^0_{HO^*}$, catalysts located on the left of the optimum bind the intermediate too strongly, whereas those on the right too weakly. Notably, RuO_2 emerges as the optimal catalyst according to Volcano plot.

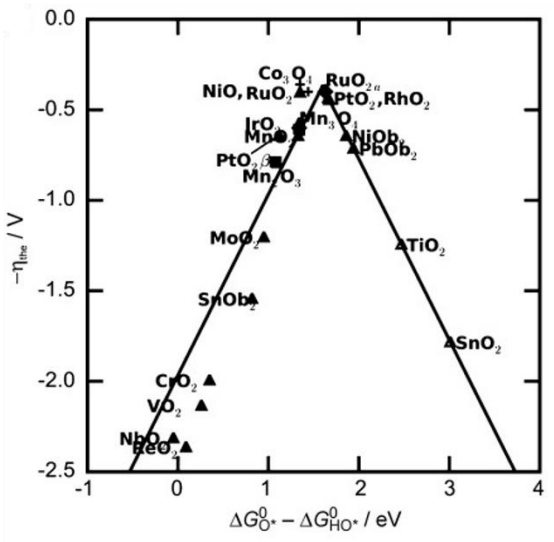

Figure 2.2. *Volcano plot representing the theoretical OER overpotential as function of* $\Delta G^0_{O^*} - \Delta G^0_{HO^*}$. *Figure reprinted with permission from* [31].

Although AEM is widely considered as the conventional OER mechanism, alternative mechanisms have been proposed. For instance, using ^{18}O-isotope combined with differential electrochemical mass spectrometry, both Comninellis and co-workers, as well as Krtil and co-workers demonstrated that a lattice oxygen from the oxide catalyst surface was also taking part in the mechanism.[33,34] This led to the proposition of the lattice oxygen mechanism (LOM), in which molecular O_2 is formed by oxygen atoms originating from both the water and the oxide catalyst. Contrary to AEM, LOM assumes a direct O-O coupling on the oxide surface, thus avoiding the formation of HOO*.[35,36]

Regardless of whether the catalytic process undergoes the AEM or LOM, optimising the catalyst is essential to achieve enhanced OER catalytic activity. Section 2.3 outlines various approaches employed to attain this objective.

2.3 THE OER CATALYST

As shown in Figure 2.1A, a catalyst enables the lowering of the activation energy, thereby enhancing the reaction rate. Consequently, a catalyst changes the kinetics of a reaction without affecting its thermodynamics.[37]

During OER, given the high applied potential, all electrocatalysts exist in an oxide form. The following subsections provide a summary of the state-of-the-art electrocatalysts for OER, the advancements beyond them along with various synthesis methods.

2.3.1 The State-of-the-Art Catalyst

Since the first demonstration of PEMWE in 1973, unsupported rutile IrO_2 is considered the state-of-the-art electrocatalyst for the OER, owing to its favourable equilibrium among activity, stability, and conductivity. Although RuO_2 was found to be more active (as indicated by the optimum of the Volcano plot, see Figure 2.2), its practical use is limited due to its instability, i.e., dissolution, under acidic OER conditions.[38] As iridium supply is considered the bottleneck for the large-scale implementation of PEMWE into our society,[39] efforts to reduce its utilisation have been intensively pursued in recent years.

One of the first strategies to enhance the catalytic performance involves the adoption of IrO_x nanoparticles to maximise their surface-to-mass ratio as compared to their bulk equivalents.[40] Unlike oxygen reduction reaction (ORR), there have been relatively few systematic studies on the effect of particle size on catalytic performance.[41] On the other hand, various approaches have actively been undertaken to tailor the morphology of the nanoparticles. Besides the traditional nanospheres,[38,42–44] 2D structures such as iridium nanosheets have been proposed as a suitable substitute.[45–47] Furthermore, 3D nanostructures, including nanowires[48,49] or hollow structures such as nanoframes,[50,51] have garnered attention as potential candidates to enhance OER performance.

Tuning the crystal structure of iridium has also been proposed to enhance its catalytic properties. It was found that amorphous IrO_x exhibits higher activity than rutile IrO_2 but lower stability.[52,53]

Nevertheless, apart from tailoring morphological and crystallinity aspects, research on improving iridium monoxide is limited, and alternative strategies need to be explored to further tune it. In the following subsections, two such strategies, namely the modification of the composition and the incorporation of support material, are briefly discussed.

2.3.2 Beyond State-of-the-Art – Multi-Elemental Composition

A multi-elemental composition, where one or more heteroatoms are incorporated into iridium particle, represents the first intuitive strategy to enhance its intrinsic activity by fine-tuning its electronic structure. This approach was initially explored in the early study by Kötz and Stucki, who, in an effort to improve the stability of RuO_2, alloyed it with IrO_2.[54] Their investigation revealed that the addition of 20% IrO_2 to RuO_2 not only significantly reduced the corrosion rate of RuO_2 but also outperformed the activity of pure IrO_2.

The approach of diluting the content of iridium with a diverse range of elements has been widely adopted by research groups. For instance, in their series of Ir-Ni composite oxides, Xu et al. observed that $Ir_{0.7}Ni_{0.3}O_2$ composite exhibited the highest OER activity among the tested compositions.[55] This enhancement was attributed to an improved conductivity resulting from the addition of nickel in the IrO_2 host lattice.

Alloying iridium with other non-precious elements has also garnered significant attention in the scientific community. For instance, $Ir_{0.6}Cu_{0.4}$ alloyed microspheres prepared by Zhou et al. exhibited an enhanced activity compared to pure iridium, reducing the overpotential at a current density of 10 mA cm^{-2} by ca. 80 mV.[56] Moreover, the emergence of another class of alloy, namely the high entropy alloy (HEA), offers new possibilities for optimising OER catalysts. HEAs, composed of five or more elements in near-equiatomic percentage, are seen as a novel platform for a wide range of applications.[57–60] In the field of OER electrocatalysts, Maulana et al. introduced IrFeCoNiCu-HEA NPs prepared on a carbon paper substrate *via* a microwave-assisted shock synthesis.[60] This HEA demonstrated enhanced mass and specific activity compared to a monometallic iridium counterpart.

Finally, Ir-free (or Ru-free) catalysts have also been reported.[61–63] Although this signifies a drastic reduction in PEMWE cost, it is at the expense of activity and stability. Therefore, such catalysts are unlikely to replace precious metal-based catalysts in the near future, given that a PEMWE is expected to last more than 10 years.[10]

2.3.3 Beyond State-of-the-Art – Supported Catalyst

An alternative approach to spare expensive precious metals in PEMWE involves using an inexpensive support material onto which the active sites, i.e., the NPs, are dispersed. A uniform dispersion of the NPs on a support material prevents their agglomeration, thereby increasing the number of exposed active sites and maximising their utilisation.[40] The requirements for a suitable support material are porosity, large surface area, high electrical conductivity, and high corrosion resistance.[36]

Carbon black (e.g., Vulcan and Ketjen Black) is widely employed as a support material, particularly in PEM fuel cells,[64–67] and has also been proposed as a potential support for OER catalysts. However, despite its high electrical conductivity and large surface area, carbon black is an inappropriate support for OER catalysts due to its tendency to undergo corrosion.[68,69] This corrosion leads to severe consequences, such as a reduction in active surface area, alterations in pore structure, and an acceleration of particle agglomeration and detachment.[68]

As a result, considerable efforts have been devoted to identifying alternative support materials. Mesoporous metal oxides, such as TiO_2[70–73] and SnO_2[74] have attracted attention due to their high corrosion resistance property. However, these candidates exhibit poor electrical conductivity, thereby necessitating the addition of dopants.[43,75–86] In particular, antimony-, fluorine-, and indium-doped tin oxides (ATO, FTO, and ITO, respectively) have emerged as promising support candidates. Nonetheless, ongoing debates persist regarding their stability under operational conditions.

For instance, Strasser and co-workers did not report any instability of their developed ATO, FTO and ITO based on capacitance data obtained during potential cycling between 1.0 and 1.8 V vs the reversible hydrogen electrode (RHE) at scan rate of 500 mV s^{-1} for 10'000 cycles.[78] A year later, the same group demonstrated the superior stability of their developed ATO compared to a commercial ATO and carbon black using a galvanostatic protocol (1 mA cm^{-2} for 15 h), during which the potential jump was attributed to the degradation of the catalyst.[87]

However, as discussed in Section 2.5.1 and Chapter 3, caution must be observed when interpreting the potential cut-off during galvanostatic experiments.

Contradictory findings were reported by Cherevko et al.[79,80] and Maillard et al.,[81,88] with both independent research groups observing a preferential antimony leaching followed by a tin dissolution, when using ATO as a support material. In addition, the dissolution of antimony and tin was also recorded during ORR, supporting the instability of ATO support material.[89] These observations are in line with the data obtained in Chapter 4.

In the context of finding improved support materials, several candidates were synthesised and characterised during the Recycalyse project. Among them, mesoporous ATO with an Sb-doping level of 7.5 mol% emerged as the most promising candidate in terms of conductivity (5.3 S cm^{-1}) and surface area (76.14 m^2 g^{-1}).[23]

During my thesis, I initially used a commercially available ATO sample, which was compared to a commercially available carbon black support (Chapter 4). Subsequently, the optimised Recycalyse support material was employed and briefly compared to the commercial ATO in Chapter 5.

2.3.4 Catalyst Synthesis

There exist several synthetic methods for preparing electrocatalysts. Adams fusion and ethylene glycol colloidal synthesis are among the most widely used ones,[9] while other techniques like incipient wetness impregnation[38,90] or magnetron sputtering[91] are also found in the literature.

In my thesis, two different methods were used to prepare the supported electrocatalysts. In Chapter 5, a surfactant-free colloidal approach using a low boiling-point solvent (ethanol) was employed to prepare four distinct supported catalysts. This synthetic route offers the advantage of not using any capping agents or additives that could potentially block the catalytic active sites. Thus, the additional step of cleaning the NPs from these organic components was (partially) avoided.[92,93] Moreover, this method follows a procedure in which the NPs are first synthesised and then immobilised onto a support material. As a result, a higher degree of flexibility can be achieved compared to the direct formation of NPs onto a support material, allowing independent control and tuning of several parameters such as composition, support material, and loading. In this way, several small batches of catalyst can be synthesised and systematically compared. Finally, the simplicity and the low cost of this approach make it appealing and relevant for both academic and industrial applications.[42,94–96]

The steps of this colloidal synthesis are illustrated in Figure 2.3 and consist of *1)* the reduction of the precious metal precursor salts in alkaline ethanol under reflux, namely the formation of the NPs, *2)* the mixing of the as-synthesised NPs with the pre-dispersed support material in ethanol, *3)* the deposition of the NPs onto the support and the evaporation of the solvent, and *4)* the evaporation of volatile side products. The resulting black powder was subsequently used for physical catalyst characterisation and preparation of inks. The latter correspond to the dispersion of the catalyst in a solvent mixture and are used to prepare the electrodes (see Section 2.5.3).

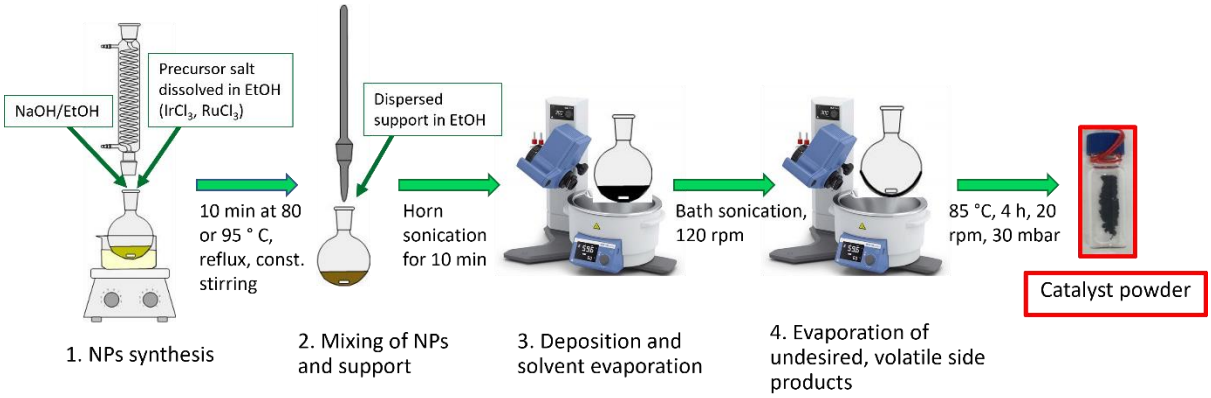

***Figure 2.3**. Synthesis steps used to produce the supported electrocatalysts of Chapter 5.*

A solvothermal flow synthesis (SFS) approach, which also avoids the use of surfactants, is used in Chapter 6 to prepare the optimised Recycalyse catalyst. Unlike the colloidal method described above, this approach involves the direct formation of NPs onto the support material ("one-pot" synthesis). By using near-supercritical fluids at elevated temperatures and high pressure (see Figure 2.4A), the SFS enables the synthesis of supported NPs with precise control of their composition and particle size distribution.[97,98] The optimised Recycalyse catalyst, synthesised by the Danish Technological Institute (DTI) partners (picture in Figure 2.4B), is of particular interest from an industrial standpoint due to the utilisation of water as the only solvent. Moreover, the catalyst can be produced continuously and in large quantities.[23]

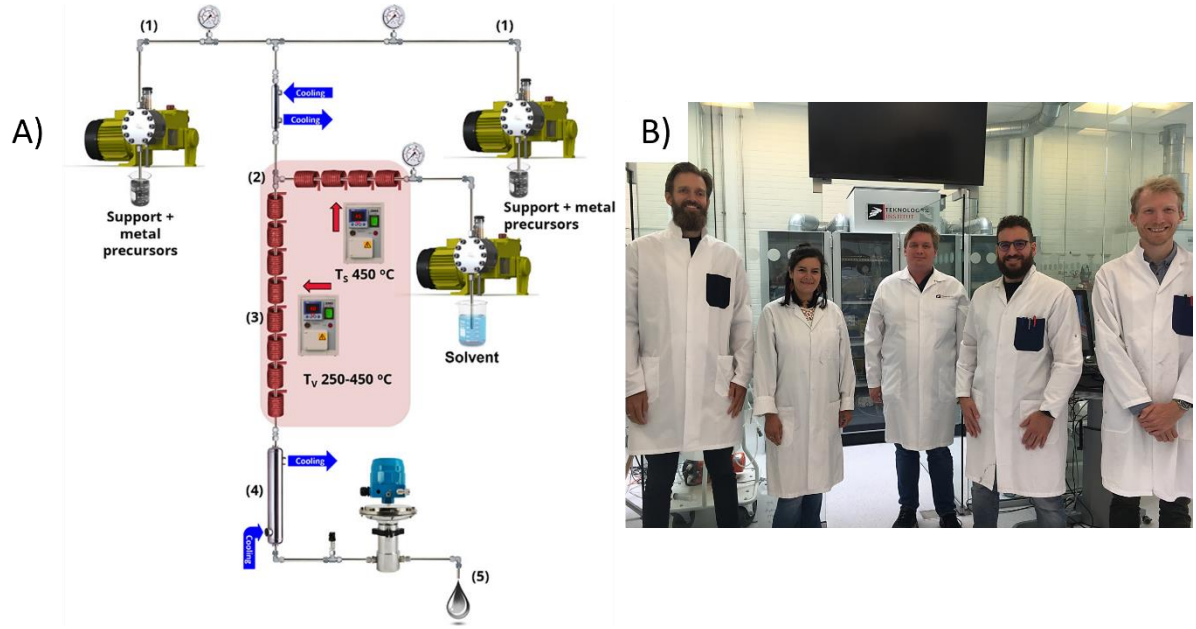

***Figure 2.4.** (A) Schematic of the SFS process and (B) a picture of DTI partners and myself in front of the SFS reactor during my one-month visit in Copenhagen. The SFS process consists of (1) pressurising the cold metal precursors and support material mixture to 300 bar at a fixed flow, (2) heating the mixture with the 450 °C hot solvent (H_2O), (3) passing the warm mixture (250-300 °C) through a 250-450 °C heated section, (4) cooling the dispersion to room temperature, and (5) collecting the solution through a pressure relieve valve. The scheme is taken from [23].*

2.4 CATALYST CHARACTERISATION METHODOLOGY

Typically, the catalyst is investigated before, during (*in-situ*/*operando*) or after (*post-mortem*) exposure to electrochemical conditions. In this section, a concise overview of all methods used to characterise the catalysts and the electrodes during my PhD thesis is provided. The detailed experimental procedure for each characterisation technique is given in the appended manuscripts.

2.4.1 Microscopy

Microscopic techniques are used to obtain visual information about the catalyst or the electrode, focusing on aspects such as morphology, size, or dispersion of the catalyst onto a support material. Microscopy is a local technique, meaning that the selected images are chosen by the user and may not be fully representative of the entire sample.

While a light microscope uses visible light as a probe to interact with the exposed matter, scanning and transmission electron microscopes (SEM and TEM, respectively) use electrons as another form of radiation.[99,100] Due to the small wavelength of electrons, SEM and TEM offer much higher resolution compared to traditional visible-light microscopes. Moreover, electrons are ionising radiation, producing a wide range of secondary signals from the targeted sample, such as secondary electron (SE), backscattered electron (BSE), transmitted electron (TE) and characteristic X-rays (see Figure 2.5).

During SEM measurements, the electrons detected are reflected from the specimen, while during TEM measurements, the recorded electrons are transmitted through the specimen. Therefore, a thin sample is required to perform TEM experiments.[99]

The reflected electrons in SEM are the SE and the BSE. While a SE stems from an atom of the specimen and results from inelastic interaction between the primary electrons (i.e., electron beam) and the matter (panel i) in Figure 2.5A), a BSE is reflected after elastic interactions between the electron beam and the specimen, see panel ii) in Figure 2.5A. Different types of information are collected depending on the electrons detected, as these originate from different regions in the sample (Figure 2.5B). While SE provides more details about the surface of the sample, BSE, which originates from deeper regions in the sample, provides topographic and compositional information (the higher the atomic number, the brighter the material).[100]

Both SEM and TEM techniques are complementary, having each their own set of advantages and disadvantages. For instance, SEM can provide insights of the 3D structure, whereas TEM is limited to 2D information. On the other hand, TEM allows for much higher resolution, reaching atomic scales, which SEM cannot.

Additionally, identical location (IL) microscopy allows for obtaining information on the exact same location before and after treatment.[101,102] This method is commonly used to study catalyst degradation as it is neither intrusive nor contaminating. Nevertheless, caution must be observed when using organic solvents, such as surfactants during catalyst synthesis, due to the formation of a passive layer on top of the catalyst.[103]

Throughout the thesis, a light microscope was used to assess the quality of the electrodes, while SEM and TEM images were recorded to obtain information about the possible detachment of material (Chapter 3), the substrate degradation (Chapter 3), the thickness of the catalyst layer (Chapter 4), the nanoparticle size (Chapter 4), and their dispersion onto a support material (Chapters 4 and 5).

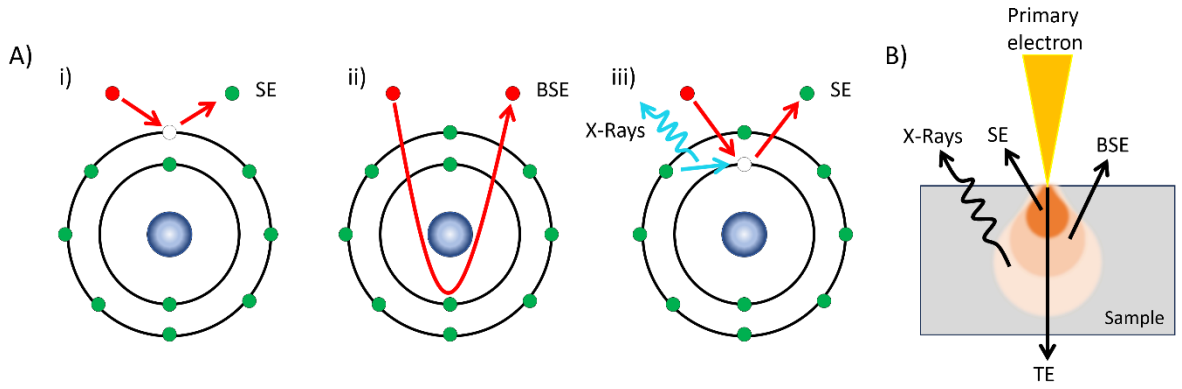

Figure 2.5. *(A) Different types of emitted electrons and radiation in an SEM with i) SE, ii) BSE, and iii) SE and characteristic X-rays and (B) depth profile with the different signals generated by the interaction between the primary electron beam and the sample.*

2.4.2 Energy Dispersive X-Ray Spectroscopy (EDX)

EDX is commonly used in combination with TEM or SEM. Similar to the latter two techniques, it uses an electron beam to interact with the sample, which in return emits specific X-rays as illustrated in Figure 2.5. Given that each element has a unique X-ray emission spectrum, this technique is used to extract information about the elemental composition of a sample.[104] For instance, it can determine the ratio between elements in a multi-elemental sample or the loading of NPs on a support material. When a mapping scanning procedure is employed, insights into the homogeneity of the sample can be assessed. Moreover, the loss of catalyst during degradation studies can be determined when the technique is used in an IL mode.

In this thesis, SEM/EDX was used to determine the degradation of the catalyst and the substrate (Chapters 3 and 4), the homogeneity of the NPs on the substrate (Chapters 3 and 4), the elemental composition of the NPs (Chapters 4 and 5), and their loading on the support (Chapter 5).

2.4.3 Thermogravimetry Analysis (TGA)

TGA investigates the changes in weight as a function of time or temperature. During TGA measurements, the sample is subjected to controlled heating or cooling using a specified temperature ramp in a defined atmosphere.[105]

As carbon burns at elevated temperatures, TGA was used in Chapter 4 to validate the assumed catalyst loading on the gas diffusion layer, with the remaining weight detected corresponding to the oxidised catalyst.

2.4.4 Synchrotron X-Ray-based Techniques

Synchrotron radiation (SR) refers to electromagnetic radiation produced by accelerating electrons close to the speed of light. This results in high-energy electrons of the order of a few GeV, while conventional X-ray laboratory sources typically operate with lower-energy electrons in the KeV range. The radiations produced by sealed X-ray tubes is limited to the fluorescence lines of the anode material, usually copper, molybdenum, or tungsten, i.e., a fixed energy. In contrast, SR is characterised as "white light" encompassing a wide range of energies. This light beam can be scanned through a range of specific wavelengths by passing through a monochromator, offering a large versatility in terms of experimental techniques. Furthermore, the brilliance of SR, i.e., the flux that is focused onto the sample (flux per unit area per solid angle), is in the order of 10^8 times higher than that of X-ray laboratory sources, thereby enabling the exploration of the atomic properties of materials.[106–108]

In addition to standard *ex-situ* experiments, SR facilitates the performance of *in-situ* and *operando* experiments, during which structural changes in materials are observed under (quasi)operational conditions. This capability is particularly valuable for investigating real-time dynamic processes, such as the oxidation of metallic OER catalysts under reaction conditions.[106]

During my PhD research, I visited multiple times SR facilities to investigate Ir and IrRu NPs. Various techniques were employed, including small-angle X-ray scattering (SAXS), X-ray total scattering combined with pair distribution function (PDF) analysis, and X-ray absorption spectroscopy (XAS). My research primarily focused on *ex-situ* experiments providing valuable insights into the structural properties of the materials under investigation, such as particle size and structural changes. A brief description of these three techniques is found below.

2.4.4.1 SAXS

When recording SAXS data, the scattering angles of interest are small ($2\theta < 5°$), resulting in a relatively long path for the scattered X-ray beam to the detector (2-3 m). This characteristic, depicted in Figure 2.6, distinguishes SAXS from wide-angle X-ray scattering (WAXS) or total scattering techniques, which typically involve shorter paths (in the order of hundreds of centimetres). The SAXS technique typically covers the region of reciprocal space corresponding to materials in the size range of 1 to 100 nm, making this technique appropriate for assessing particle size and shape. Unlike microscopy, which is a local technique, SAXS enables to probe a larger region, thereby providing a more representative picture of the entire sample.[107,109]

During my thesis, SAXS measurements were conducted to compare particle growth before and after activation (Chapter 4). A critical but essential step in the data analysis was the background subtraction, given the presence of the support and the substrate during the measurements. Therefore, additional background measurements were performed to facilitate this subtraction.

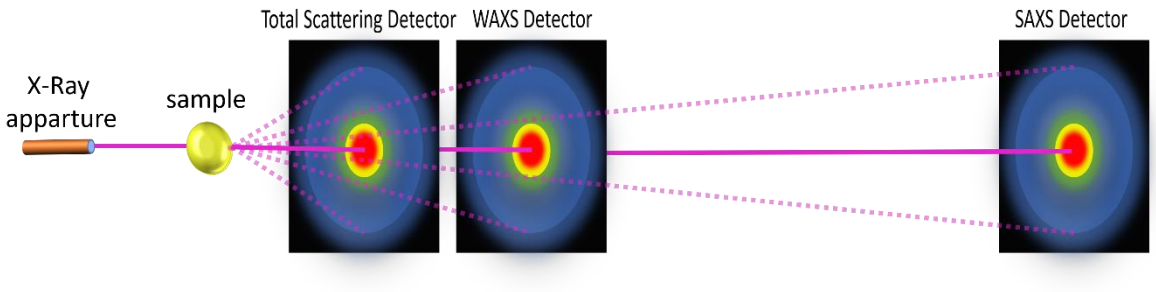

***Figure 2.6**. Schematic comparison of the corresponding sample-to-detector distances for total scattering (PDF), WAXS and SAXS measurements. Image adapted from* [106].

2.4.4.2 PDF

PDF analysis of total scattering patterns is a relatively new technique that provides a large set of nanoscale structural information using both Bragg peaks and diffuse scattering. As depicted in Figure 2.6, the total scattering detector is positioned close to the sample to enable the detection of the low intensity diffuse scattering. PDF data are obtained by Fourier transforming the total scattering pattern, thereby providing the probability of finding an atom at a specific distance from another atom, even beyond the unit cell size. Contrary to a conventional powder X-ray diffraction, PDF analysis offers the capability to identify amorphous structure, rendering it of particular interest for studying OER IrO_x catalyst.[107,110]

In Chapter 4 of my thesis, PDF analysis was employed to determine the crystallinity of the synthesised Ir and IrRu NPs and to assess the remaining metallic content after activation. Similar to SAXS, background subtraction plays a crucial role in PDF analysis to ensure an accurate description of the sample.

2.4.4.3 XAS

A full XAS spectrum, which is obtained from the relaxation of excited electrons, consists of two parts: the X-ray absorption near edge structure (XANES) and the extended X-ray absorption fine structure (EXAFS). The XANES region, spanning from 30 to ca. 40 eV, reveals information on the electronic and the local geometric structure surrounding the central absorbing atom. The absorption edge position often serves as a fingerprint for the oxidation state of the absorbing element, while the shape of the XANES spectrum depicts its local geometric structure.[111] The EXAFS region, spanning from ca. 40 to ca. 1000 eV, provides insights into the local structure around the central absorbing atom, such as near-neighbour distance distributions and coordination numbers.[112]

Throughout my thesis, this technique was applied to confirm the versatility of the synthesis, i.e., ensuring that the support does not influence the active catalytic sites. Additionally, it was employed to determine the alloy nature of the IrRu NPs and to monitor the ageing process of the NPs (Chapter 4).

2.4.5 Inductively Coupled Plasma-Mass Spectrometry (ICP-MS)

In electrocatalysis, ICP-MS is a technique used to detect and quantify trace amounts of multi-elements dissolved in the electrolyte, achieving sensitivity down to the part per trillion (ppt, ng L^{-1}) range. The procedure involves the initial steps of drying, vaporising, and atomising the electrolyte sample, followed by its ionisation in an Ar plasma reaching up to 7000 °C. Finally, the resulting atomic ions are sorted by their mass-to-charge ratio in the mass spectrometer.[113]

Recently, two descriptors using ICP-MS data have been introduced as a metric for benchmarking the intrinsic stability of electrocatalysts. The first descriptor, the activity-stability factor, was proposed by Kim et al.[114] in 2017 and the second one, the S-number, was introduced by Geiger et al.[115] a year later. Although described by slightly different equations, both descriptors normalise the OER performance to the noble metal dissolution. For instance, the unitless S-number calculates the ratio between the amount of generated O_2, derived from the total charge transfer, and the amount of dissolved metal. In both cases, a higher number signifies a more stable catalyst.

In Chapter 3 of my thesis, ICP-MS results were used to calculate the S-numbers of IrO_2 deposited on three different backing electrode materials.

2.4.6 Raman Spectroscopy

Raman spectroscopy is a powerful analytical technique that measures the vibrational modes of matter. The Raman effect is based on the inelastic light-scattering events (Stokes and Antistokes) between the irradiating monochromatic light and the sample, in opposition to Rayleigh scattering, which corresponds to elastic events (Figure 2.7). As the vibrational energy levels are unique to each molecule, the Raman spectrum provides a fingerprint of each of them, allowing their identification and characterisation. Raman active vibration is in general symmetric modes of non-polar groups, which implies that metals are indistinguishable in a Raman spectrum.[116]

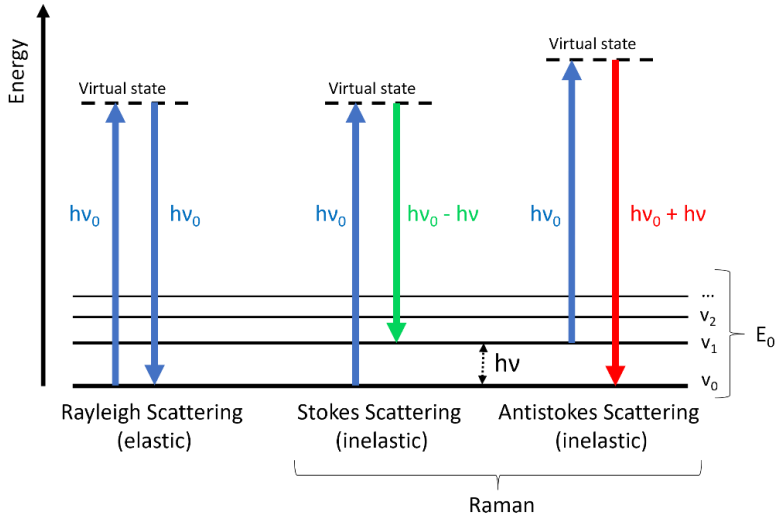

Figure 2.7. *Jablonski diagram of Rayleigh and Raman scattering.*

In Chapter 3, Raman spectroscopy was used to confirm the presence of IrO_2 after the abrupt potential jump during the galvanostatic protocol, as well as to identify the substrate degradation. These measurements were performed on three backing electrode materials.

2.4.7 Gas Chromatography

Chromatography is a process employed to separate individual components within a mixture. The separation of the components present in a mobile phase is based on their affinity to adsorb on a stationary phase. Consequently, the components elute from the chromatographic column and reach the detector at distinct times (retention time). In gas chromatography, the mobile phase is gaseous, while the stationary phase can be either solid or liquid (in my case, solid).[117] This method is primarily used to identify, quantify, and purify products of a reaction rather than to characterise a catalyst per se.

In Chapter 3, gas chromatography was used to characterise the catalyst and the substrate passivation by detecting and quantifying the presence of O_2, CO and CO_2 during the electrolysis.

2.5 Electrochemical Performance Screening Methods

2.5.1 The State-of-the-Art Setup – The Rotating Disc Electrode (RDE)

Screening the electrochemical performance of an OER catalyst directly in a "real" electrolyser is desirable; however, it is often hindered by high costs and time-consuming procedures and is therefore seldom pursued.[118] Consequently, simpler testing platforms are typically used to evaluate the performance of electrocatalysts, going from fundamental to applied systems. The two commonly used setups for evaluating OER performance are the rotating disc electrode and the single-cell membrane electrode assembly (MEA). The latter closely resembles an electrolyser stack, which consists of several MEAs, see Figure 1.4C. Nevertheless, the complex deconvolution of individual components and the necessity of advanced and costly laboratory installations make MEA testing unsuitable for fast and straightforward catalyst screening.[119]

On the other hand, the RDE setup, with its three-electrodes configuration (Figure 2.8), facilitates the investigation of an individual electrode in a rapid, cost-effective, and straightforward manner. Inspired by fuel cell ORR studies, thin-film-(TF-) RDE tests, during which a thin catalyst film is deposited on the electrode tip, are typically performed to determine the activity and stability of OER catalysts.[38,118,120,121]

Recently, catalyst stability has become a hot topic in the OER electrocatalysis community. Several research groups have focused on establishing a standardised protocol to evaluate OER stability.[122–126] For instance, a decade ago, McCrory et al. proposed a galvanostatic step of 10 mA cm^{-2} for 2 h as a stability descriptor.[122] Since then, galvanostatic steps of varying current density values have been performed to compare the stability of catalysts. During these experiments, the sudden jump in potential was attributed to catalyst degradation, see Figure 2.9.[53,87,127,128] Currently, ongoing discussions aim to better understand and describe the abrupt increase in potential. In fact, it is worth noting that the potential increase cannot be entirely attributed to the catalyst degradation, as the results obtained through aqueous model system

(AMS), such as the RDE setup, are inconsistent with the MEA tests (during which the same catalyst does not exhibit severe degradation).[129] This inconsistency underscores the limitations of AMS for OER stability evaluation, which have been intensively addressed in the recent literature.[118,120,121,125,130–140]

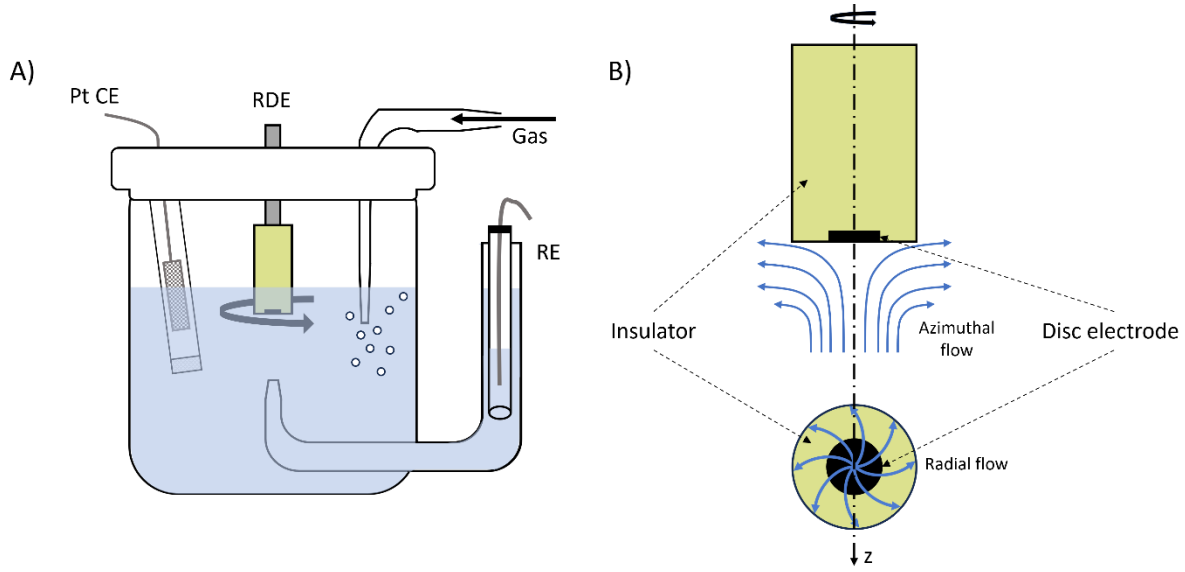

Figure 2.8. *(A) Schematic representation of an RDE setup and (B) the resultant flows (radial and azimuthal). RE: reference electrode, CE: counter electrode.*

When conducting TF-RDE investigations, two main challenges arise. First, the material of the backing electrode on which the catalyst ink is drop-casted needs to feature the following three key properties: *i)* high conductivity, *ii)* high stability, and *iii)* inertness. While the widely used glassy carbon (GC) substrate exhibits high conductivity, it is prone to passivation under acidic and oxidative OER conditions. This passivation weakens the electrical contact between the substrate and the catalyst and thereby increases the overall resistance (resulting in higher ohmic losses).[125,132,141] For instance, Edgington et al. found, through spectroscopic analysis, that GC forms an insulating oxide layer at the GC|catalyst interface.[125] Increasing the catalyst loading on GC delayed the formation of the passivated layer. The authors attributed this phenomenon to a higher coverage of the GC, which limits the penetration of the electrolyte to the GC surface, thereby hindering its passivation. Another microscopic and spectroscopic study by Yi et al. revealed the structural changes on the GC surface under acidic and alkaline OER conditions, confirming the non-electrochemical inertness of this substrate.[141]

Alternative materials, such as Au, have been utilised as substrates for OER degradation tests as well. Despite improved stability compared to GC, Au eventually undergoes dissolution and passivation under the harsh OER conditions.[118,132,142–144] As no ideal backing electrode materials that are truly inert and stable under the OER conditions exist, it is of major importance to consider this limitation when evaluating catalyst stability in AMS.

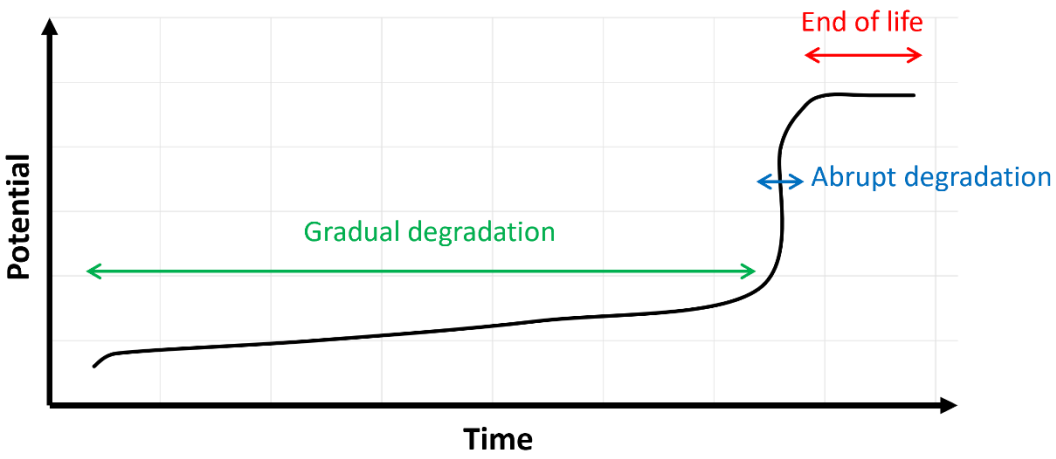

Figure 2.9. *Graphical illustration of constant current-based stability test proposed by McCrory et al.*[122] *and its common interpretation.*

The second major drawback of AMS is a direct consequence of the evolution of O_2 bubbles. The accumulation of macroscopic bubbles on the catalyst surface is a well-known limitation of the RDE setup during gas-evolving processes, due to its downward-facing configuration.[145] Recently, micro and nanobubbles trapped within the pores of the catalyst have also been identified as crucial. For instance, El-Sayed and co-workers attributed the gradual increase in potential, followed by a cascading effect and a final plateau (see Figure 2.9), during galvanostatic degradation tests, to the shielding of catalytic active sites by the electrogenerated micro and nanobubbles.[138] This process was accelerated by applying a higher current. To overcome this limitation, the authors proposed to hold the catalyst at open circuit potential in an Ar-saturated electrolyte for 30 min after reaching the potential plateau. Through comparison of the first and 30th cycling voltammogram (CV) with the one after Ar purging, they observed a slight recovery of catalyst activity. Therefore, they attributed the jump to high overpotential not to the catalyst degradation but rather to the blinding of the catalyst by trapped gas bubbles. To further support the hypothesis of bubble accumulation, Hartig-Weiss et al. subjected the electrochemical cell and/or the electrolyte to ultrasonication while conducting CVs or constant current measurements.[146] In doing so, they provided evidence that the accumulation of bubbles is a significant drawback of AMS. Nevertheless, it must be highlighted that in their study, the authors used an iridium disc, which does not represent adequately the typically performed TF-RDE experiments. Moreover, the utilisation of an ultrasonic horn during TF-RDE testing can lead to erroneous conclusions on catalyst stability due to possible mechanical detachment of the catalyst from the substrate, which would be hardly distinguishable from intrinsic degradation. Finally, Tovini et al., in a study comparing the discrepancies between RDE and MEA to assess OER stability, concluded that the decrease in activity was ***exclusively*** due to the microscopic O_2 bubbles trapped inside the catalytic porous structure.[136]

Recognising the limitations of galvanostatic measurements as a stability metric for OER catalysts in AMS, researchers have devoted their efforts to the development of alternative catalyst-specific metrics.[114,115,147] Recently, the S-number, introduced by Geiger et al.,[115] has gained increasing attention within the electrocatalysis community.[88,125,130,148] This stability

metric calculates the ratio between the produced O_2 and the metal dissolution (see Section 2.4.5). The standardisation of this metric and a meaningful accelerating stress test (AST) should enable a fairer comparison among electrocatalysts.

2.5.2 Beyond State-of-the-Art – the Inverted RDE (iRDE)

Tovini et al., in their concluding remarks on the comparison between RDE and MEA, wrote: "If it would be possible to prevent the accumulation of the microscopic oxygen bubbles within the catalyst layer during the measurement, it might be possible to design a proper stability protocol for testing OER catalysts using RDE measurements."[136]

In a typical gas-evolving RDE experiment, the generated gas bubbles adhere to the electrode surface and are only eliminated with sufficient force convection. A simple yet sophisticated approach to circumvent this limitation is achieved by inverting the RDE by 180°, as proposed by Zdunek and Selman in 1992.[149] Their innovative design, known as the iRDE, was validated with the ferro/ferricyanide redox couple, thus confirming that the iRDE complies with the same hydrodynamic and convective equations as the standard RDE.

Upward-facing electrodes allowing the removal of gas bubbles from the catalyst surface solely due to buoyancy (i.e., no electrode rotation) are found in the literature.[121,125] Vertical electrodes have also been proposed to overcome bubble retention.[121] However, this 90° configuration does not entirely eliminate the gas bubbles making precise electrochemical measurement challenging.[149] Figure 2.10 illustrates the three discussed electrode orientations (downward-facing, upward-facing, and vertical electrodes).

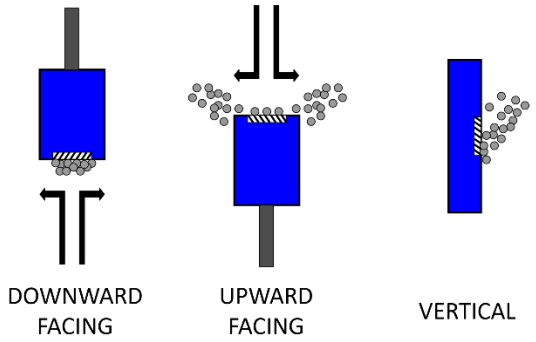

Figure 2.10. *Sketch of the three electrode orientations encountered in the literature. Image adapted from* [149].

Coupling the inversion of the electrode with the rotation raises its own set of challenges, as adequate design and sealing are necessary to prevent electrolyte leakage. Therefore, only a few research groups have implemented the iRDE in their experimental investigations.[150–155] Among them, Moreno-García and co-workers have designed a hermetically sealed iRDE permitting the online analysis of gaseous products *via* a gas chromatographic detection system.[153,156,157] Their custom-made setup was successfully applied for relevant gas-evolving processes such as CO_2 reduction reaction, metal deposition, and HER.

Despite the potential of the upward-facing RDE to address the challenges of catalyst shielding by electrogenerated gas bubbles, such a setup has not yet been implemented to study water

oxidation. Therefore, during my thesis, in a collaborative project with the group of Prof. Broekmann, the iRDE setup was used to bypass the gas bubble limitation.

2.5.3 Beyond State-of-the-Art – the Gas Diffusion Electrode (GDE) Setup

Although iRDE presents a promising solution to address the bubbles-related issues (see Chapter 3), certain fundamental disparities between AMS and MEA cannot be fully resolved by this screening platform. Awareness of the intrinsic limitations of AMS originated from the fuel cell scientific community, which proposed the design of a GDE setup to mitigate these challenges and benchmark the ORR catalyst.[158] This GDE setup, seen as a bridging screening platform between AMS and MEA, can more closely mimic conditions of an applied device (fuel cell or electrolyser), while still studying individual half-cell reactions. For instance, higher catalyst loadings up to 1 mg cm^{-2} are used, a membrane is introduced, and the operating conditions (temperature and pressure) are easily adjustable.[159–161] The integration of a membrane in the three-electrodes configured GDE setup allows for the physical separation of the catalyst from the electrolyte so that the catalyst is fed from the backside. This reduces the mass transport limitations, enabling higher current densities to be reached, which represents a major advantage of the GDE setup over AMS.[162,163]

Since the introduction of the GDE as an intermediary test bed, it has primarily been used to investigate the ORR[65,164,165] and CO_2 reduction reaction.[166–168] Initially tested with concentrated phosphoric acid at elevated temperature for fuel cells research by Wiberg et al. in the group of Prof. Arenz,[159] the custom-made GDE setup has since been stepwise adapted to broaden its utilisation to OER. Recently, the adapted GDE setup was benchmarked for OER for the first time using a commercial IrO_2.[160] In this study, we compared the GDE to an RDE setup and assessed the influence of different parameters on the catalyst performance, such as reactant flow rate and temperature, using a gas diffusion layer (GDL) as a substrate. Additionally, we performed a short-term stability test (1 h at 10 mA mg_{Ir}^{-1}) using a porous transport layer (PTL) as a substrate, what is typically used in PEMWE. Later, the GDE setup was used by Collantes-Jiménez et al. employing liquid water as a reactant and a PTL substrate in a modified GDE setup to evaluate the activity of self-supported IrO_x.[169] With these improved conditions, the authors demonstrated the feasibility of achieving current densities above 2 A cm^{-2}, i.e., conditions even closer to PEMWE. Furthermore, in a proof-of-concept study where different Ir oxides were screened in an RDE, GDE and MEA setups, Geuss et al. observed a good agreement in activity obtained between RDE and GDE, while results obtained in MEA diverged from those in the GDE setup.[163] These observed disparities were attributed to differences in the catalyst layer|membrane interface. The authors concluded that despite these discrepancies, the GDE setup is an adequate half-cell setup to bridge the gap between AMS and MEA.

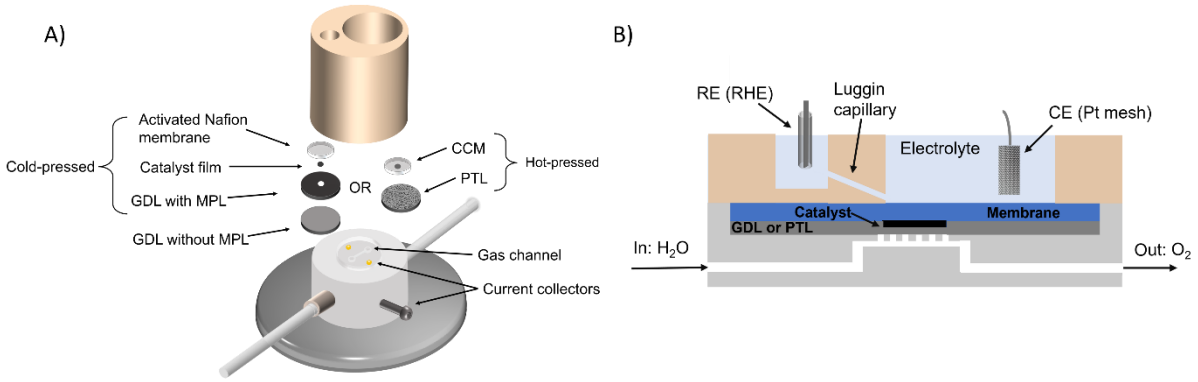

Figure 2.11. *Schematic of (A) the GDE setup and (B) its cross-section.*

The schematic of the GDE setup used throughout my PhD thesis is depicted in Figure 2.11. In comparison with the initial GDE setup used by Schröder et al.[160], a Luggin capillary was added, thereby reducing the solution resistance (smaller iR drop). Using humidified water as a reactant, I first utilised the setup to compare the activity of four synthesised catalysts, which were deposited on a GDL (Chapter 4). Later, using the optimised Recycalyse catalyst, I underscored the importance of selecting the appropriate substrate during stability measurements, see Chapter 5.

When a GDL was selected as substrate, the electrodes were prepared *via* vacuum filtration, following the methodology proposed by Yarlagadda et al.[170] This straightforward and cost-effective method enables reproducible and uniform catalyst films with loadings approaching those used in PEMWE. Nonetheless, as demonstrated in Chapter 5, GDLs are unsuitable for stability measurement due to carbon corrosion[171] so that PTLs were used instead. The preparation of PTL-electrode differs from the simple vacuum filtration approach and typically occurs in two steps. Firstly, catalyst-coated membranes (CCMs) are prepared by directly spraying the catalyst onto the membrane or *via* a decal method. The decal method consists of transferring the catalyst, typically deposited on a Teflon sheet, onto an activated membrane.[9] In the second step, the CCM is hot-pressed onto the PTL. Although the PTL-electrode preparation approach requires more advanced laboratory equipment, it is unavoidable for reliable stability assessment. In Chapter 5, I prepared the PTL-electrodes by directly spaying the catalyst onto the membrane and hot-pressing the latter onto PTLs at the facilities of a Recycalyse partner, Blue World Technologies in Denmark.

CHAPTER 3

DISENTANGLING THE LIMITATIONS OF RDE-BASED OER STABILITY ASSESSMENT: BUBBLE RETENTION OR INTERFACE PASSIVATION?

3.1 MOTIVATION

Recently, the determination of the stability of OER catalysts has garnered significant attention. However, straightforward and cost-effective methodologies to reliably assess this performance feature are still missing. Indeed, large disparities exist between the results of the commonly used galvanostatic AST conducted in AMS (RDE measurements), and MEAs. In AMS, the catalyst survives only a few hours (under typically applied current densities) before undergoing a performance loss that is typically linked to degradation. In contrast, in MEAs, the performance can be maintained for extended periods ranging from several days to even months.[129,136]

Currently, these substantial discrepancies are attributed to two limitations of AMS rather than to intrinsic catalyst degradation. The first one is due to the substrate onto which the catalyst is drop-casted. It has been proposed that the backing electrode material undergoes passivation, leading to the electrical isolation of the catalyst.[125,132,141] The second limitation consists of the accumulation of gas bubbles isolating the catalyst from the electrolyte. This latter limitation is currently proposed as the major factor contributing to the observed discrepancies between AMS and MEA measurements. Thorough investigations have described the trapping of O_2 gas bubbles within the porous structure of the catalyst as the main reason for the potential jump during galvanostatic stability protocols.[136,138,139,146] Nevertheless, both drawbacks have yet to be independently studied owing to the absence of appropriate instruments for their deconvoluted analysis.

To fill this experimental gap, we employed an inverted RDE as a testing platform capable of unravelling both limitations during a constant current AST. As outlined in Section 2.5.2, this novel test bed exploits the buoyancy of the gas bubbles to efficiently remove them from the catalyst surface. This way, the observed discrepancies between AMS and MEAs can be conclusively isolated and ascribed to one of the aforementioned limitations or their combined effect. Furthermore, the utilisation of stationary vertical electrodes half-covered by catalyst material enabled the elucidation of the mechanism underlying the abrupt potential rise.

3.2 MOST SIGNIFICANT FINDINGS

In this study, a commercial IrO_2 was employed as a benchmark OER catalyst to deepen the understanding of galvanostatic stability measurements in AMS. The catalyst was drop-casted onto three distinct backing electrode materials: glassy carbon (GC), gold (Au), and titanium (Ti). While the former two are widely used in RDE-based AMS measurements, the latter, although less conventional, was selected to resemble the MEA substrate.

The catalyst stability was first evaluated in a conventional RDE setup (Figure 2.8) *via* the standard constant current AST protocol. These experiments served as a baseline for the following investigation. A constant current density of 30 mA cm^{-2} was applied, corresponding to mass current densities of 3.0 A mg_{IrO2}^{-1} and 0.6 A mg_{IrO2}^{-1} for electrode loadings of 10 μg_{IrO2} cm^{-2} and 50 μg_{IrO2} cm^{-2}, respectively. The resulting potential transients are depicted in Figure 3.1. Regardless of the substrate material and the loading, the expected pattern described in Figure 2.9 was observed, characterised by the gradual potential increase followed by its abrupt rise, and finally, the potential plateau.

Several discrepancies were observed across the different backing electrode materials and loadings. First, regardless of the backing electrode material, increase of catalyst loading prolonged the time required to reach the final potential plateau, aligning with findings reported by Edgington et al.[125] According to the interpretation proposed by McCrory and co-workers,[122] the observed potential cut-off indicates total catalyst degradation. Following this interpretation, our results indicate that the stability of the catalyst was substantially influenced by the backing electrode material. Interestingly, despite its prevalence in PEMWE applications as substrate material, the Ti-electrode exhibited the fastest degradation. At low catalyst loading (Figure 3.1A), the GC-electrode required a slightly longer duration to reach the degradation plateau than the Ti-electrode. The Au-electrode exhibited, on the other hand, the highest stability, in line with prior studies indicating superior stability of catalysts deposited on gold compared to GC substrate.[132,172] At higher loading (Figure 3.1D), the difference between GC- and Au-electrodes diminished, with both demonstrating equal stability duration. Therefore, based on the results obtained by RDE and the interpretation of McCrory, this catalyst would not sustain MEA testing. However, IrO_2 is the prevailing catalyst in the current PEMWE. The stronger influence of the substrate material on the catalyst stability at low loadings compared to higher ones suggests that the galvanostatic tests provide operational degradation of the electrode assembly rather than intrinsic degradation of the catalyst.

To better understand the disparities between RDE and MEA results, we employed a recently introduced direct intrinsic stability descriptor, namely the S-number, (see Section 2.4.5). The S-numbers corresponding to the experiments in Figures 3.1A and D were calculated by *post-mortem* ICP-MS measurements and compared with pseudo-S-numbers calculated based on McCrory's interpretation, i.e., a total catalyst degradation. Their ratios are displayed in Figure 3.1C and F. The substantially larger $S_{ICP\text{-}MS}$-numbers indicate minimal iridium dissolution. Therefore, the catalyst should sustain several hours or even days of testing, similar to MEA experiments.

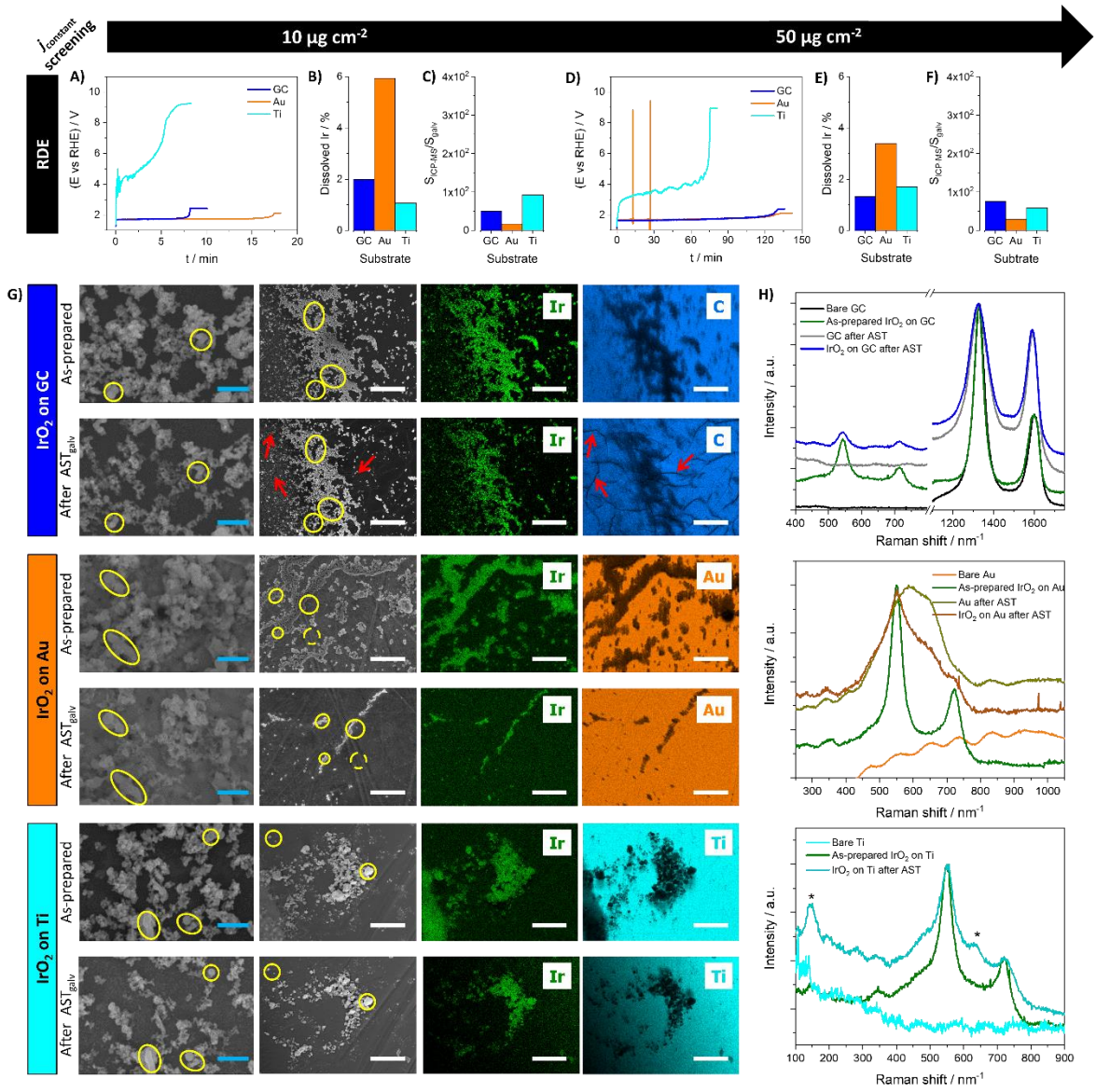

Figure 3.1. *(A) Electrocatalytic OER potential transients of IrO_2 measured at 30 mA cm^{-2} with a loading of 10 μg_{IrO2} cm^{-2} in an RDE setup, (B) corresponding Ir dissolution measured via ICP-MS and (C) ratio between the S-numbers calculated based on the ICP-MS and the electrochemical data. (D)-(F) Corresponding results with a loading of 50 μg_{IrO2} cm^{-2}. (G) IL-SEM images and IL-SEM/EDX mapping of the three distinct backing electrode materials loaded with 50 μg_{IrO2} cm^{-2}. The yellow circles highlight specific catalyst clusters recognisable before and after OER. The red arrows underscore the alteration of the GC backing electrode material. The blue scale bars correspond to 200 nm and the white ones to 25 µm. (H) Raman spectra of the bare backing electrode materials, the backing electrode materials with IrO_2, the bare backing electrode materials after AST, and the backing electrode materials with IrO_2 after AST. The stars highlight characteristic TiO_x peaks. Electrolyte: O_2-saturated 0.1 M H_2SO_4. Rotation rate: 1000 rpm.*

To shine light on these contradictory findings, the electrodes were further investigated by means of IL-SEM/EDX and Raman spectroscopy before and after electrochemical treatment. The IL-SEM/EDX analysis revealed the presence of large amounts of catalyst after the potential jump. While some detachment of the catalyst was noticed, intrinsic degradation, i.e., dissolution, was minimal. This was supported by an unchanged morphology of the

agglomerated NPs in the high-magnification SEM images, thereby corroborating the ICP-MS data in Figure 3.1B and E. Furthermore, the appearance of characteristic IrO_2 peaks[173] at 560 and 720 nm^{-1} in the *post-mortem* Raman spectra confirmed our IL-SEM/EDX observations (Figure 3.1H). These findings were consistently observed across the three backing electrode materials and in duplicate measurements.

Interestingly, these two analytical techniques also evidenced modifications in the substrates. In particular, *post-mortem* IL-SEM/EDX images displayed cracks on the GC substrate surface (indicated by the red arrows in Figure 3.1G). Moreover, the Raman intensity ratio of the D to G bands of the used GC-electrodes decreased in comparison to the as-prepared electrode (Figure 3.1H, upper panel). This change in the Raman signal indicates oxidation of the GC substrate.[118] Analogously, characteristic oxidation peaks appeared for Au- and Ti-electrodes as results of the applied electrolysis (Figure 3.1H, middle and bottom panel, respectively).[174,175] These observations corroborate previous studies documenting substrate modifications after electrochemical treatment.[125,132,141] Therefore, the potential jump does not reflect intrinsic catalyst degradation and might be related to operational failure (e.g., substrate degradation).

Indeed, in the recent and extensive studies by El-Sayed and co-workers,[136–139,146] the potential cut-off observed during galvanostatic AST experiments was attributed to system artifacts rather than intrinsic catalyst degradation. The authors proposed that electrogenerated gas bubbles are trapped within the porous catalytic structure, thereby obstructing active sites. Moreover, they suggested that the retention of gas bubbles on the electrode surface was the key challenge in achieving reliable stability assessment in AMS. They proposed that if a method capable of removing the gas bubbles blocking the active sites existed, it would enable accurate stability measurements, see quotation in Section 2.5.2.

Therefore, to address the detrimental influence of O_2 gas bubbles during stability experiments, we proposed the utilisation of a 180° inverted RDE, which employs buoyancy in addition to force convection to eliminate bubbles. Previous studies[153,156,157] have shown that this approach is an effective technique to overcome the challenge imposed by gas bubble retention. iRDE experiments were conducted under the same applied conditions as for experiments shown in Figures 3.1A and D (30 mA cm^{-2} galvanostatic step with two different loadings on three distinct backing electrode materials). Surprisingly, the potential transients and $S_{ICP\text{-}MS}$-numbers obtained with the iRDE setup closely resembled those obtained with the conventional RDE setup, see Figures 3.2A and B. These findings suggest that gas bubbles blinding the catalyst do not account for the sudden potential rise and do not represent the main reason for the disparities between AMS and MEAs studies.

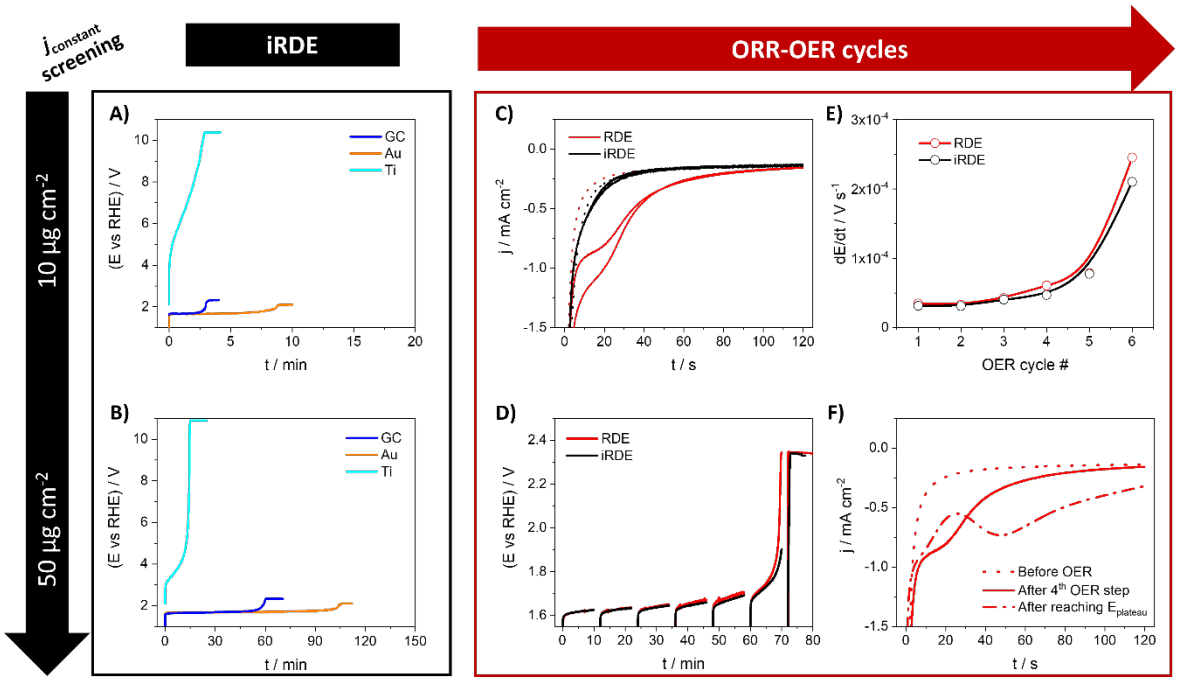

Figure 3.1. *Electrocatalytic OER potential transients of IrO_2 measured at 30 mA cm^{-2} with a loading of (A) 10 μg_{IrO2} cm^{-2} and (B) 50 μg_{IrO2} cm^{-2} in an iRDE setup. (C) Selected ORR steps at 0.2 V vs RHE followed by (D) alternating 10-minute OER steps at 10 mA cm^{-2} in an RDE (red) and iRDE (black) setup. The dotted curves in panel (C) correspond to ORR steps prior any OER step. (E) Time evolution of the potential slope for each OER cycle. (F) ORR steps prior any OER step (dotted line), after the 4th OER step (full line), and after reaching the potential plateau (dash-dotted line) performed in an RDE setup. The catalyst loading of panels (C) to (F) was 50 μg_{IrO2} cm^{-2}. Electrolyte: O_2-saturated 0.1 M H_2SO_4.Rotation rate: 150 rpm.*

To effectively validate this hypothesis, the catalyst was subjected to alternating 2-minute potentiostatic ORR and 10-minute galvanostatic OER cycles (0.2 V vs RHE, respectively 10 mA cm^{-2}).[120] This way, if O_2 gas bubbles were retained within the catalyst pores in the course of the OER, an ORR cycle would reduce them and the subsequent galvanostatic OER would start with a bubble-free catalyst layer. The results of these experiments are displayed in Figures 3.2C and D for both the conventional RDE (red curves) and iRDE setups (black curves). The first ORR potentiostatic step (i.e., prior any OER, dashed lines) in Figure 3.2C showed a reductive current with both setups. This reductive current, reaching rapidly a mass transport-limited value, corresponds to the reduction of O_2 from the electrolyte (experiments performed in O_2-saturated 0.1 M H_2SO_4 electrolyte). The subsequent ORR steps during normal RDE experiments (full red curves) exhibited an additional current that we attributed to the reduction of trapped O_2 gas bubbles. Remarkably, no additional reductive current was recorded for any ORR steps during iRDE measurements (full black curves). And yet, despite the fact that we prevent the retention of O_2 bubbles inside the porous IrO_2 catalyst by two independent approaches (i.e., iRDE and alternating ORR-OER cycling), the galvanostatic OER screening does not showcase the prolonged catalyst lifetimes expected by El-Sayed's hypothesis. Thus, although the gas bubbles had a certain influence during RDE experiments, the sharp potential jump observed in RDE and iRDE measurements could not be solely ascribed to them. The weak impact of trapped gas bubbles using the classical RDE was

translated into a higher resistance, indicated by a higher slope during the gradual potential increase, see Figures 3.2D and E. Another impact of gas bubbles in RDE is the possible full screening of the surface by them when conducting OER at high current densities. One such event is presented in Figure 3.1D (orange curve) where compliance voltage was attained as result of full catalyst blockage by macroscopic bubbles. Nevertheless, such a macroscopic bubble was not detrimental as once mechanically removed, the potential transient recovered until it rose to the plateau.

Interestingly, when an ORR step was performed immediately after facing the degradation plateau, an additional reduction process occurred (dash-dotted curve, Figure 3.2F). This suggests that other reducible species were formed only upon reaching the plateau. A similar feature was observed with the iRDE, however without the contribution of oxygen reduction current (i.e., the large reductive current within the first 20 s).

Thus, the abrupt potential rise previously erroneously attributed to catalyst degradation and more recently to bubble retention results from another phenomenon. To investigate the nature of the products formed after the potential jump, galvanostatic experiments at a current density of 10 mA cm^{-2} were performed using GC-electrodes loaded with 50 μg_{IrO2} cm^{-2} and coupled to online gas chromatography. Figure 3.3 depicts the resulting potential transients along with the online gas detection. O_2 production was the only faradaic process observed before the appearance of the potential plateau. As soon as the latter occurred, the production of O_2 abruptly decreased (Figure 3.3A). This would suggest, at first glance, that the catalyst becomes inactive. On the other hand, CO and CO_2 were detected from the moment the potential jump appeared (Figures 3.3B and C). Given the design of the experiment, the two carbonaceous products could only originate from the GC backing electrode. Moreover, the production of CO and CO_2 was significantly lower compared to O_2, which was also confirmed by decreased amount of bubble evolution from the catalyst layer (Figure 3.3D).

In conclusion, our results conclusively demonstrate that the observed potential cut-off during galvanostatic measurements originates neither from the degradation of the catalyst nor the blinding of gas bubbles, but ***exclusively*** from the degradation of the backing electrode material. Note that minimisation of the gas bubble effect on other relevant electrochemical processes has led to major technical advances.[176] A prime example of this is the acceleration of gas bubble detachment by means of dimensionally stable anodes that reduce the voltage in an electrochemical reactor by more than 1 V. This has enabled massive electricity savings worldwide.[177] However, we prove that the bubble retention in RDE-based OER stability studies is minor.

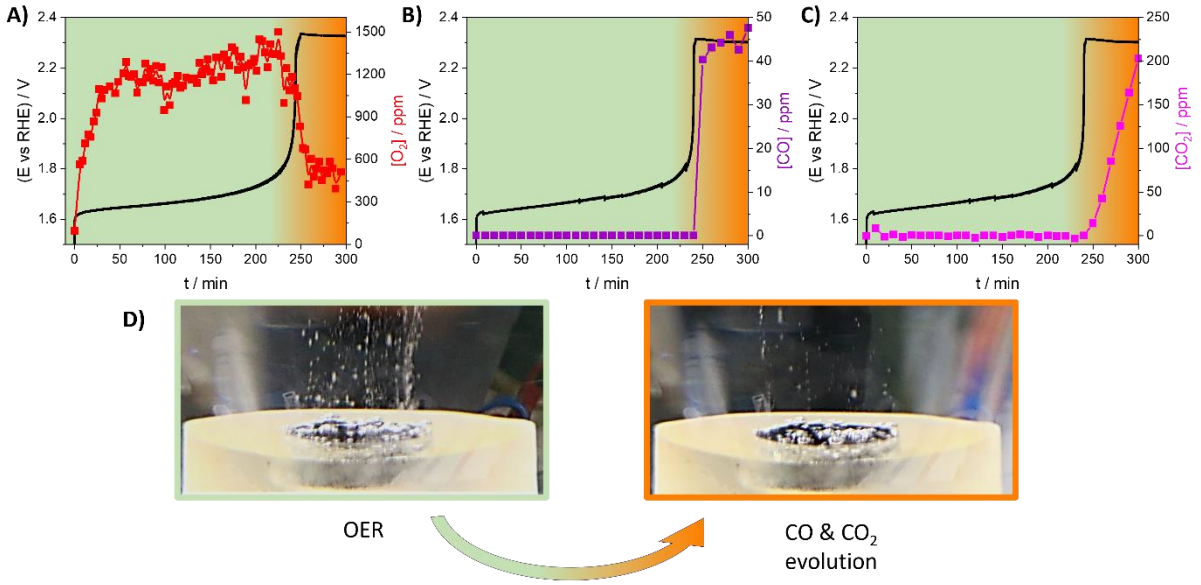

Figure 3.3. *Electrocatalytic OER potential transients of IrO_2 drop-casted on GC measured at 10 mA cm^{-2} with a loading of 50 μg_{IrO2} cm^{-2} in iRDE setup and online gas chromatography detection of (A) O_2, (B) CO, and (C) CO_2. (D) Pictures of the electrode before (green frame) and after (orange frame) reaching the potential plateau. Electrolyte: Ar-saturated 0.1 M H_2SO_4. The pictures were taken at 0 rpm.*

Although the potential jump can now be conclusively attributed to a single phenomenon, namely the degradation of the substrate, the sudden and sharp potential rise and corresponding production of GC oxidation products appear counterintuitive. Indeed, one would expect a progressive increase in CO and CO_2 production as the potential gradually mounts.

To elucidate the mechanism behind this abrupt rise, complementary experiments were designed using stationary GC-electrodes in an H-type electrochemical cell. The catalyst was drop-casted only on one-half of the exposed GC substrate. A current density of 10 mA cm^{-2} (relative to the total exposed area) was applied and the gas-evolving process was recorded with a conventional camera. Additionally, the side products were analysed by online gas chromatography. Although the catalyst-free GC surface was in direct contact with the electrolyte, no products of its oxidation were detected before the potential rise appeared (contrary to control experiments performed with bare GC electrode). Again, CO and CO_2 were detected only after the potential jump, similar to our previous experiment with a completely covered RDE tip. Correspondingly, gas bubbles evolved only from the catalyst-covered surface as long as the potential plateau did not appear and started emerging from the catalyst-free GC upon its manifestation (see Figure 3.4A and B). This suggests that the OER on the surface of the IrO_2 catalyst is the only active faradaic process as long as the apparent degradation is absent. Only in the subsequent stage, the kinetically unfavoured substrate oxidation takes over.

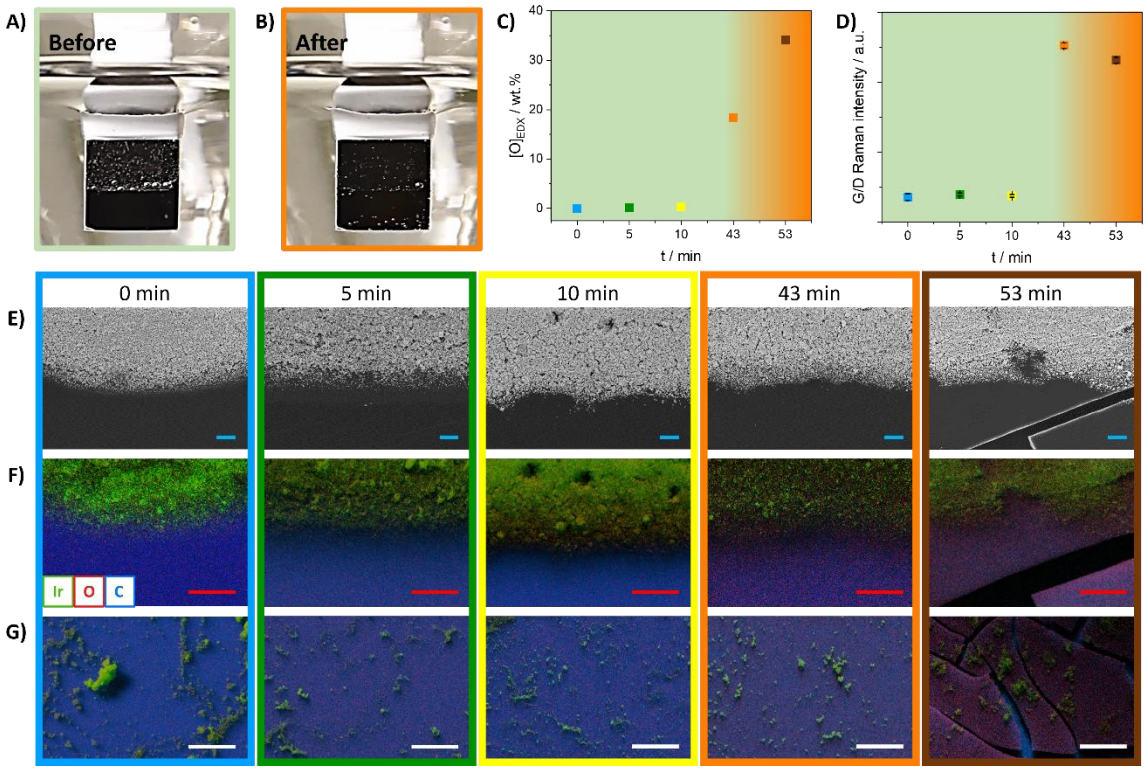

Figure 3.4. *Pictures of the stationary GC electrode (A) before and (B) after the potential jump. The electrode was divided in two, where only the upper half was covered by the catalyst with a loading of 50 μg_{IrO2} cm^{-2} and tested at 10 mA cm^{-2} (relative to the total exposed area). (C) O concentration detected by EDX and (D) the ratio between the G and D band calculated from Raman spectra as function of the different electrolysis durations. The error bars in panel (D) correspond to the standard deviation of three independent measurements on the same sample. (E) Low-magnification SEM images and SEM/EDX mappings at (F) low- and (G) high-magnifications of the GC electrodes at different electrolysis durations. The blue scale bars correspond to 2 µm, the red ones to 5 µm and the white ones to 25 µm. Electrolyte: Ar-saturated 0.1 M H_2SO_4.*

To track the evolution of the substrate degradation under galvanostatic OER conditions, similar experiments with variable durations were conducted. Two electrolyses were stopped at 5 and 10 minutes where only the gradually increasing potential was observed. Two more samples were prepared, one by stopping the electrolysis precisely at the moment when the potential reached the plateau and another one 10 minutes afterwards. These surfaces were examined through SEM/EDX as shown in Figures 3.4E to G. As depicted in Figure 3.4C, the oxygen concentration on the bare GC within the IrO_2-covered area (i.e., between catalyst islands) was negligible after 5 and 10 min electrolysis similarly to a sample non-subjected to electrolysis (0 min). In contrast, oxygen uptake by the substrate was clear for the sample that was electrochemically stressed until the potential transient showed the abrupt jump (at 43 min). For the sample whose electrolysis was sustained 10 min beyond the potential jump, an even higher oxygen concentration was detected. It is noteworthy that severe degradation of the substrate, characterised by cracks, was observed in the SEM/EDX images only after reaching the plateau (last column to the right in Figures 3.4E-G).

The samples were also analysed by a more surface-sensitive technique, namely Raman spectroscopy. The evolution of the relative signal intensities of the G and D bands also showed

that the bare substrate adjacent to the catalyst clusters oxidises only if the potentials reach the sharp increase (Figure3.4D). This also holds for the GC that was not coated with catalyst.

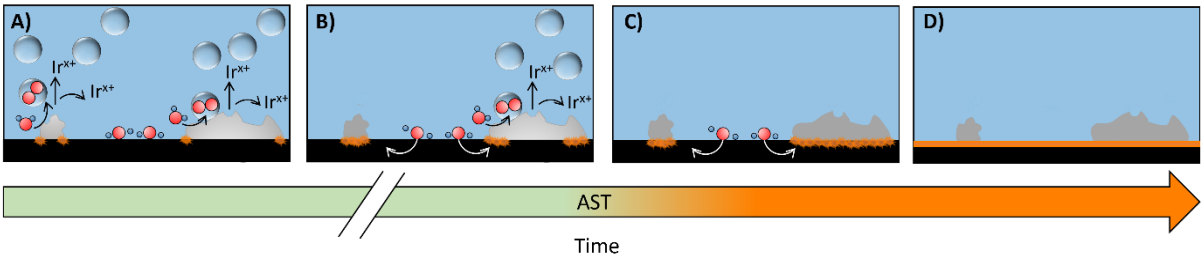

Figure 3.5. *Schematic illustration of the substrate degradation during galvanostatic experiments.*

Contrary to published studies that investigated the substrate degradation without catalyst,[118,125] our current work monitored the substrate degradation in presence of the catalyst. Based on the presented results, Figure 3.5 displays a degradation mechanism that explains the time evolution of the potential observed in galvanostatic OER screening. Initially, the kinetically favoured reaction, namely the OER, takes place on the catalyst surface. This induces large local current densities on all catalyst sites exposed to the electrolyte. This phenomenon also occurs at the three-phase interfaces where substrate, catalyst and electrolyte meet. Consequently, the substrate at these catalyst edges is subjected to much harsher oxidising conditions that induce a local substrate passivation (Figure 3.5A). As the galvanostatic experiment proceeds, the substrate passivation process gradually isolates the catalyst islands. Smaller catalyst clusters become fully electrically isolated at shorter time than the larger ones, resulting in increasingly harsher oxidising conditions for the still electrically attached larger clusters (Figure 3.5B). Eventually, all catalyst clusters become completely electrically isolated by the passivated substrate (Figure 3.5C). At this point, the until then kinetically unfavoured GC passivation sets in and the enforced constant current starts flowing through the unoxidised GC causing its complete passivation (Figure 3.5D). This process occurs in a very short time window which explains the abruptness of the potential jump. Finally, the potential stabilises as the thickness of the passivating layer gradually increases.

This proposed mechanism was developed based on rigorous study on the GC-electrode, as its degradation products are detectable *in-situ*. Nevertheless, it remains valid for the Au and Ti backing electrodes. In the case of the Au substrate, the kinetically unfavoured reaction taking over is gold dissolution (plateau at 2.1 V vs RHE). For Ti, it is known that under acidic conditions and highly anodic potentials, the surface of Ti easily passivates and forms a highly isolating layer. Accordingly, the corresponding potential transient exhibited the shortest duration and reached compliance voltage.

Finally, based on this mechanism, we could elucidate the reason why potential transients measured with the RDE setup lasted longer than those with iRDE setup (Figures 3.1A and D vs 3.2A and B). The accumulation of gas bubbles during the RDE measurements protected some of the three-phase interfaces, delaying the passivation of the substrate. Consequently, galvanostatic RDE measurements lasted longer than iRDE measurements since the latter lacked this “protection”. Furthermore, this also explained why El-Sayed and co-workers observed a recovery of activity in their standard RDE experiments after purging their

electrolyte with Ar.[138] In fact, some of their catalyst clusters were protected by the gas bubbles and thereby still electrically attached to the substrate. Therefore, after the diffusion of O_2 gas bubbles into the Ar-saturated electrolyte, the still electrically attached clusters remained active.

In conclusion, the large disparities between RDE and MEA during stability measurements arise from the use of non-inert backing electrode materials in AMS studies. On the other hand, gas bubbles blinding the active surfaces only have a minor influence on these measurements performed in AMS. This interfacial degradation might be of relevance for MEA operation as the interfacing between PTL and CCM is also known to suffer from corrosion phenomena.[178] Nevertheless, thorough MEA investigations are necessary to confirm this hypothesis.

3.3 Contribution to the Work

This study represents a collaborative effort between the research groups of Prof. Peter Broekmann and Prof. Matthias Arenz. Pavel Moreno-García and I contributed equally to this Chapter. We conceived the project, set up the experimental platforms and methodology, performed the electrochemical, Raman and gas chromatography experiments, and analysed the data. The corresponding manuscript, that will be written by Pavel Moreno-García and me, is not provided in the Appendix, as it is still at a preliminary stage. Abhijit Dutta provided technical support to carry out the Raman and gas chromatography experiments. Beatrice Frey and Mike Liechti helped carry out the SEM/EDX and ICP-MS characterisations. Soma Vesztergom, Abhijit Dutta, Matthias Arenz and Peter Broekmann contributed with discussions.

CHAPTER 4

INFLUENCE OF TEMPERATURE ON THE PERFORMANCE OF CARBON- AND ATO-SUPPORTED OER CATALYSTS IN A GDE SETUP

4.1 MOTIVATION

In response to the pressing need to reduce the precious metal content in OER catalysts, Ir and $Ir_{0.4}Ru_{0.6}$ were synthesised as ultrasmall NPs and subsequently immobilised on two distinct commercially available support materials: high-surface-area carbon flakes and mesoporous ATO. The utilisation of the particles was enhanced by the nanoscale dimensions, and by their dispersion on the support material, resulting in an increased surface-to-mass ratio. Thus, two methods presented in Section 2.3 were employed to lower the precious metal content. While carbon was chosen as a reference, ATO was selected for its promising characteristics (porosity, large surface area and high conductivity) as a potential support candidate.

Furthermore, a GDE setup was chosen as a screening platform to investigate the catalyst under loading and temperature conditions mimicking those found in PEMWEs. In previous work by group members and myself, this setup was benchmarked for the first time for the OER using a commercially available IrO_2.[160] In this work, I extended its usage to evaluate and compare systematically the four developed OER supported catalysts. In addition, I examined the viability of the two support materials as appropriate candidates for OER.

4.2 ABSTRACT OF THE PUBLICATION

State-of-the-art industrial electrocatalysts for the oxygen evolution reaction under acidic conditions are Ir-based. Considering the scarce supply of Ir, it is imperative to use the precious metal as efficiently as possible. In this work, we immobilised ultrasmall Ir and $Ir_{0.4}Ru_{0.6}$ nanoparticles on two different supports to maximise their dispersion. One high-surface-area carbon support serves as a reference but has limited technological relevance due to its lack of stability. The other support, ATO, has been proposed in the literature as a possible better support for OER catalysts. Temperature-dependent measurements performed in a recently developed GDE setup reveal that surprisingly the catalysts immobilised on commercial ATO performed worse than their carbon-immobilised counterparts. The measurements suggest that the ATO support deteriorates particularly fast at elevated temperatures.

4.3 MOST SIGNIFICANT FINDINGS

Ir and $Ir_{0.4}Ru_{0.6}$ NPs were synthesised through a colloidal surfactant-free synthesis, resulting in spherical particles with a diameter of approximately 1.5 nm. In a subsequent step, the NPs were immobilised on two different commercially available support materials: high-surface-area carbon Ketjen Black and mesoporous ATO, at a nominal metal loading of 50 wt.%. The resulting catalysts were Ir/C, $Ir_{0.4}Ru_{0.6}$/C, Ir/ATO, and $Ir_{0.4}Ru_{0.6}$/ATO. As discussed in Section 2.3.4, in addition to diminishing the contribution of the support material on the NP formation, this two-step approach offers considerable flexibility in varying independent synthesis parameters such as composition, support material, and metal loading. This represents an advantage over the formation of NPs in direct presence of a support material.[42,94–96]

The catalysts were characterised *ex-situ* at synchrotron facilities using XAS, PDF and SAXS techniques. The matching XAS spectra of Ir/C and Ir/ATO indicated metallic pristine catalysts independently of the support material. As expected from the versatility of the multi-step colloidal synthetic approach, the support material does not significantly influence the properties of the NPs.[179] Interestingly, upon deposition onto a GDL (i.e., the electrode) and storage in the air for months, the catalysts began to exhibit an oxide nature, which increased with prolonged storage duration. This oxidation process can be reversed through electrochemical treatment.[42] Furthermore, PDF analysis revealed a highly ordered structure of the pristine samples with Ir exhibiting a pure face-centred cubic (*fcc*) phase, while $Ir_{0.4}Ru_{0.6}$ was fitted with either a pure *fcc* phase or a mixed *fcc*: hexagonal close-packed (*hcp*) phase. According to these PDF results, a conclusive statement on the nature of the bimetallic catalyst was not feasible. Consequently, EXAFS investigations were conducted to ascertain the potential formation of an alloy. The EXAFS analysis showed coordination between the two elements, thereby confirming the alloyed nature of the $Ir_{0.4}Ru_{0.6}$ NPs.

Since the active phase under OER conditions is an oxide,[42] the catalysts were activated (i.e., oxidised) by maintaining a constant potential at 1.6 V vs RHE for 5 min prior to activity measurement. *Ex-situ* SAXS was used to track the expected increase in particle size as a result of its oxidation. The observed particle growth indicated that the applied potential, despite being relatively high, was not sufficient to fully oxidise the particles. These observations were supported by PDF and EXAFS analysis, which showed small contributions from metallic phase and metal-metal coordination, respectively.

The electrochemical performance of the four catalysts was then tested for the OER using a GDE setup (Figure 2.11). The electrodes were prepared by vacuum filtration, during which the catalyst was deposited on a GDL. The latter is composed of fibres and a microporous layer (MPL). The fibres form a macroporous network, allowing the reactant to reach the catalyst surface, while the MPL prevents the catalyst from penetrating the fibres. Thus, a localised, homogeneous, and ca. 12 µm thick catalyst film was deposited on the GDL surface, as illustrated in the cross-sectional SEM/EDX mapping of pristine $Ir_{0.4}Ru_{0.6}$/C in Figure 4.1.

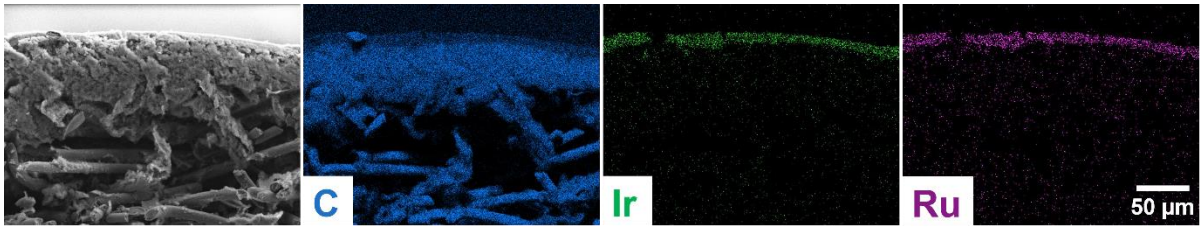

Figure 4.1. Cross-sectional SEM/EDX mapping of a GDL functionalised with pristine $Ir_{0.4}Ru_{0.6}$/C.

The protocol employed to test the OER catalyst activity consisted in 5-minute steady-state galvanostatic steps at three distinct temperatures: 30, 40, and 60 °C, using fresh electrodes for each temperature. Each catalyst was measured in triplicate to ensure robust reproducibility. The iR-corrected potential transients of $Ir_{0.4}Ru_{0.6}O_x$/C are displayed in Figure 4.2A as a representative example. A good reproducibility was observed among the samples and as expected from kinetics, higher temperatures improved the catalytic activity. Interestingly, the first galvanostatic steps unveiled a non-steady-state behaviour. The latter was ascribed to the continuing activation/oxidation of the NPs given the SAXS, PDF and EXAFS findings. It is noteworthy that although such behaviour is readily discernible during steady-state measurements, it is difficult to distinguish it in commonly applied potentiodynamic measurements (i.e., CVs). Therefore, steady-state activity measurements offer a more accurate evaluation of catalyst performance than potentiodynamic measurements, thereby avoiding its overestimation.

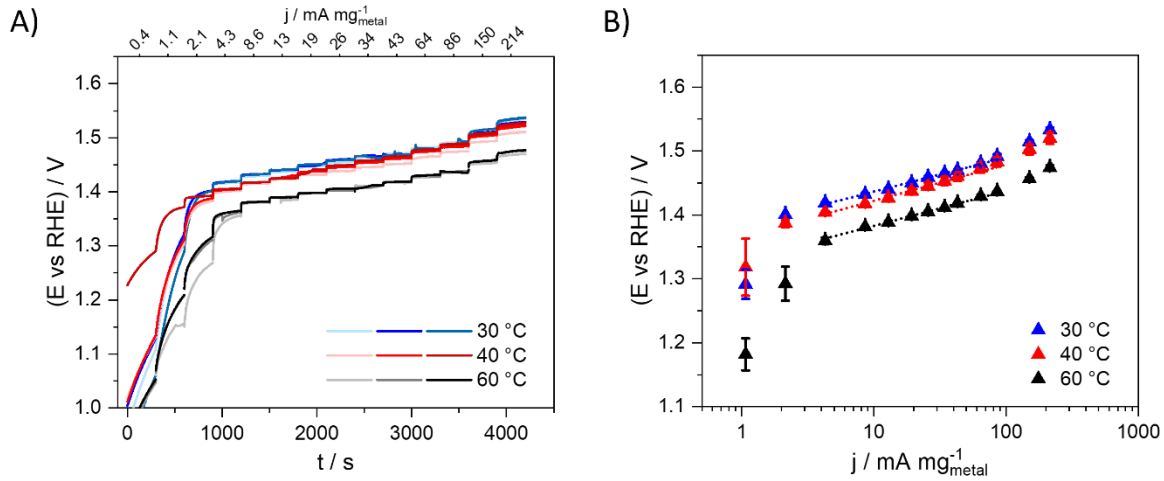

Figure 4.2. *(A) Electrocatalytic OER iR-corrected potential transients and (B) the corresponding Tafel plots (average of the last 100 s of each iR-corrected current step) of $Ir_{0.4}Ru_{0.6}O_x$/C at 30 (blue), 40 (red), and 60 °C (black). The error bars show the standard deviation of the three independent measurements, which were all performed in the GDE setup using 4 M $HClO_4$ as an electrolyte. Nominal loading: 654 μg_{metal} cm^{-2}.*

The Tafel slope (see Equation 2.7) was determined in the kinetically limited region spanning from 4 to 85 mA mg_{metal}^{-1}, i.e., where the entire enforced current is used to evolve O_2 (Figure 4.2B). At higher current densities (>100 mA mg_{metal}^{-1}), a slight deviation in the linear behaviour was observed, presumably related to mass transport limitation.[169] The Tafel slopes at 30 °C for all four catalysts, ranging from 53 to 62 mV dec^{-1}, were consistent with findings reported in the literature for Ir-based catalysts.[38,43,180,181]

The comparison among the four catalysts was conducted at a temperature-corrected overpotential of η=0.23 V.[182] This overpotential was chosen as it fell within the linear Tafel region of the individual catalyst at most temperatures. For IrO_x/C at 30 °C and IrO_x/ATO at 30 and 40 °C, the data were obtained via extrapolation.

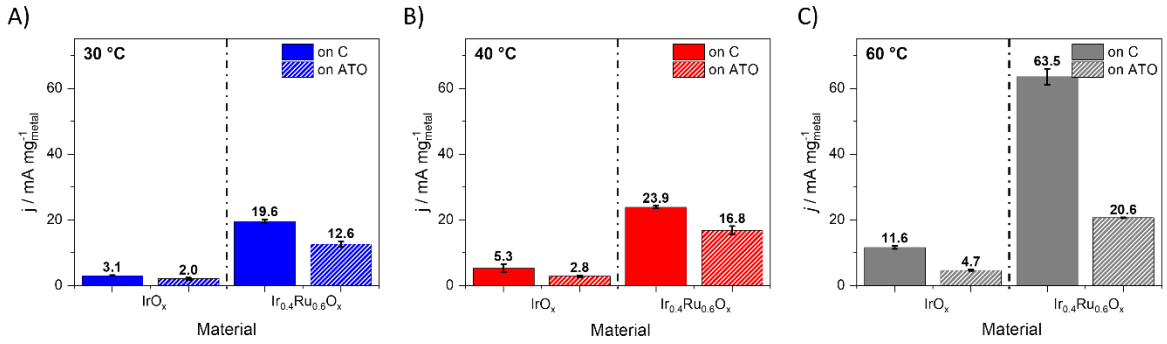

Figure 4.3. *Comparison of the OER activities reached at a temperature-corrected overpotential η=0.23 V for IrO_x (left-hand side of the graphs) and $Ir_{0.4}Ru_{0.6}O_x$ (right-hand side of the graphs) deposited on C (solid bars) or ATO (dashed bars) at (A) 30, (B) 40, and (C) 60 °C. The values were interpolated or extrapolated based on the Tafel slopes.*

The comparative bar diagrams presented in Figure 4.3 yielded two key findings. First, regardless of the support material, catalysts containing Ru exhibited higher mass activity than pure IrO_x. Despite a Ru-leaching during the activation step evidenced by EDX, $Ir_{0.4}Ru_{0.6}O_x$ catalysts demonstrated between 4.5 and 6.3-fold higher activity compared to their Ru-free counterparts, corroborating the early observations by Kötz and Stucki.[54] Second, comparing the influence of the support on the catalytic activity, it turned out that NPs immobilised on carbon were more active than those immobilised on ATO. Nevertheless, according to the characterisation, NPs on both support materials exhibited similar morphology, size distribution, crystalline structure, and ratio. It even appeared that the dispersion of the NPs on ATO was better than on carbon. Therefore, similar activities were expected independently of the support material, if not a better one for the ATO-immobilised NPs given the tendency of carbon to oxidise.[171] Interestingly, the opposite was observed and enhanced at elevated temperatures. Although carbon corrosion cannot be completely excluded, major contributions to the current seem unlikely. Indeed, they would have led to a time-dependent behaviour similar to what was observed during the first galvanostatic steps. Therefore, the superior activity of carbon-immobilised NPs was attributed to the higher conductivity of carbon over ATO (9.85 S cm^{-1} vs 0.0009 S cm^{-1}, respectively). Moreover, as discussed in Section 2.3.3, the latter tends to be even less conductive in the course of the reaction due to its instability (Sb leaching) under the harsh OER conditions. Comparing the average Sn:Sb ratio of pristine and *post-mortem* samples by EDX, such antimony leaching was also identified in our experiments.

Finally, the apparent OER activation energy ($E_{A,app}$) at η=0.23 V was estimated using the linearisation of the Arrhenius equation (Equation 4.1),

$$j = zF a_{app} \exp\left(\frac{-E_{A,app}}{RT}\right) \quad (4.1)$$

where a_{app} stands for the apparent preexponential factor which includes all entropic terms.

An OER $E_{A,app}$ of approximately 35 kJ mol^{-1} was calculated for the two carbon-supported NPs, aligning with findings of Hartig-Weiss et al.[43] Much lower $E_{A,app}$ values were obtained for IrO_x and $Ir_{0.4}Ru_{0.6}O_x$ immobilised on ATO (23 kJ mol^{-1} and 13 kJ mol^{-1}, respectively). With lower apparent activation energy, one would expect higher activities. However, our electrochemical data demonstrated the opposite. These discrepancies were attributed to the instability of the ATO under operational OER conditions.

In conclusion, the main challenge for efficient OER catalysts lies in finding appropriate OER support materials. Indeed, carbon material is not a viable alternative for long-term industrial applications owing to its tendency to corrode at high temperatures and oxidative OER conditions. In addition, NPs immobilised on commercially available ATO suffer from diminishing performance, promoted at elevated temperatures, rendering them even inferior to carbon. Thus, further efforts need to be devoted to designing improved support materials, which, subsequently, need to be tested under conditions closer to PEMWE.

4.4 Contribution to the Work

My contributions to this study were the synthesis of the four supported catalysts, the electrode preparation and the complete electrochemical characterisation in the GDE setup. Additionally, I recorded the TEM micrographs of the catalysts (NPs and support), while Jonathan Quinson recorded those of the pure NPs using a high-resolution TEM. The analysis of all micrographs was performed by me. EDX cross-sectional mappings were performed by Etienne Berner, which were then analysed by me. Synchrotron measurements were performed and analysed by Rebecca Pittkowski, Johanna Schröder, Tobias M. Nielsen, Kirsten M. Ø. Jensen, and me. Annabelle Maletzko and Julia Melke contributed to the work by carrying out the conductivity measurements. Matthias Arenz supervised the project and reviewed the manuscript and figures, I wrote, respectively made.

CHAPTER 5

BEYOND RDE CHARACTERISATION - UNVEILING IrRu/ATO OER CATALYST STABILITY WITH A GDE SETUP

5.1 MOTIVATION

Based on the findings in Chapter 4, the GDE setup is an appropriate approach to compare the activity of different catalysts. It was found that NPs immobilised onto commercial ATO were unexpectedly less performant than those supported on commercial carbon flakes. These counterintuitive results were attributed to the instability of the commercial ATO. Therefore, hereafter, a developed ATO support by Recycalyse partners with improved properties compared to its commercial counterpart was used instead.[23] The chosen catalyst for this study was the optimised Recycalyse catalyst, which has been already integrated into MEAs and the first-generation electrolyser stack (see Figure 1.4) without facing substantial degradation.[23] Therefore, these MEA results served as a reference for the here presented investigation.

Given the limitations of AMS to provide reliable catalyst stability insights, and thereby, the lack of straightforward stability experimental approaches, we resorted to GDE-based investigations as a viable strategy for stability testing at laboratory scale. The GDE setup has already proven appropriate to conduct degradation studies, but only under mild conditions and during short-term experiments.[160] Therefore, in the present study, stability measurements were extended to harsher conditions, thereby emphasising the necessity of selecting adequate substrates.

5.2 ABSTRACT OF THE PUBLICATION

In this study, we have investigated the stability of ATO supported IrRu nanoparticles, as catalyst for OER. Conventional stability tests using an RDE are demonstrated to lead to distorted results, a fact typically addressed to the massive formation of O_2 gas bubbles which block the catalytic active sites. In agreement with previous results, our investigations suggest that the observed decay in current density is not to be confused with catalyst degradation. To mitigate the limitations of the RDE approach, a GDE setup was used instead for the stability measurements. Using a carbon GDL as substrate for the catalyst film, similar beginning-of-life (BoL) and end-of-life (EoL) activities were observed in the low current density region; however, large disparities were found at larger current densities. For meaningful degradation studies, the carbon GDL had to be replaced by a titanium-based substrate. This way a more accurate assessment of the catalyst stability is demonstrated. Although at steady-state conditions the

tested IrRu/ATO catalyst exhibited a slight decrease in current densities with time, the BoL and EoL activities are nearly identical.

5.3 MOST SIGNIFICANT FINDINGS

In this study, the optimised Recycalyse catalyst consisting of $(Ir_{0.7}Ru_{0.3}O_x)_{0.96}Ni_{0.04}$ immobilised on a developed ATO support material with a total metal loading of 42 wt.%, was utilised to conduct stability tests. For simplicity, the catalyst is abbreviated as IrRu/ATO in the following discussion.

As presented in Section 2.5.1 and in Chapter 3, the traditional RDE setup proves inadequate for assessing stability of OER catalyst. Furthermore, despite circumventing the bubbles-related challenges by employing an inverted RDE setup, substrate passivation remained the major obstacle, hindering reliable stability measurements in AMS. In this context, the GDE setup plays an important role as an intermediate test bed between AMS and MEA for stability assessment. Additionally, this setup offers the advantage of applying conditions closer to PEMWE, as detailed in Section 2.5.3. Consequently, the identical GDE setup used in Chapter 4 was employed to investigate IrRu/ATO catalyst at 60 °C, following the protocol presented in Figure 5.1. First, galvanostatic steps similar to those in Chapter 4 were performed to determine the BoL activity. Then, the catalyst stability was recorded *via* an adaptatively compensated potentiostatic step. Finally, EoL activity was measured using the identical steps as during BoL activity.

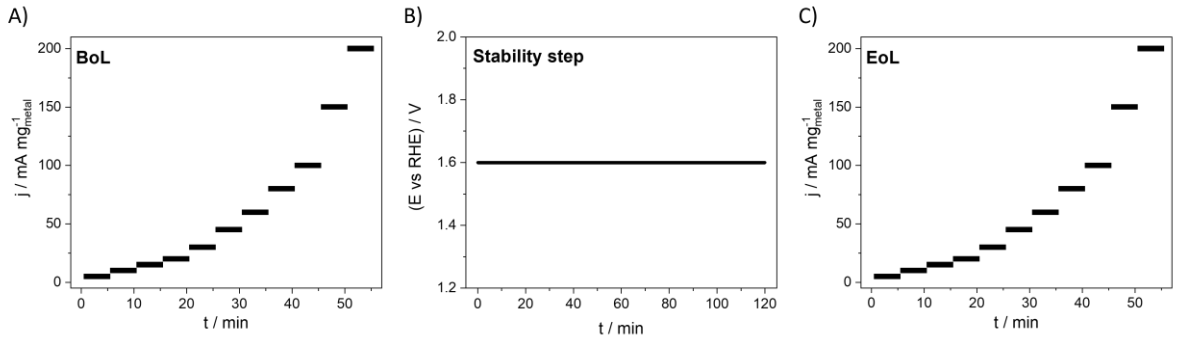

Figure 5.1. *Protocol used to assess the stability of the catalyst, with (A) BoL activity performed through constant current steps, (B) stability through a constant potential at 1.6 V vs RHE with an adaptative compensation, and (C) EoL activity through constant current steps.*

Similarly to Chapter 4, the electrodes with three different loadings (0.292, 0.500 and 1.000 mg_{metal} cm^{-2}) were prepared by deposition of the catalyst onto MPL-coated GDL *via* vacuum filtration. Figure 5.2A illustrates the loading dependence of the BoL activity for IrRu/ATO, which followed an inverse relationship. Higher loading correlates with lower mass activity, which was attributed to a lower catalyst utilisation. Moreover, the 5-minute galvanostatic steps demonstrated a relatively stable behaviour in the low current density region (up to 100 mA mg_{metal}^{-1}). However, deviations from the quasi-steady-state behaviour were observed at higher current densities, which were ascribed to mass transport limitation, in line with the observations by Collantes-Jiménez et al.[169] Furthermore, when looking at the highest loading

potential transients, i.e., 1.000 mg_{metal} cm^{-2}, strong oscillations were observed due to the massive formation and subsequent release of O_2 gas bubbles.

The Tafel slopes of IrRu/ATO of this current Chapter (developed ATO, pink) and of the preceding Chapter (commercial ATO, green) are compared in Figure 5.2B. At high current densities (> 80 mA mg_{metal}^{-1}), which are of interest for real application, the catalyst of the current study (i.e., with the developed ATO) demonstrated a slightly better performance (lower overpotential). It is noteworthy that the developed mesoporous ATO exhibits larger surface area and higher conductivity than its commercial counterpart,[23] thereby rendering it a better candidate as an OER support material. Thus, the slight improvement observed in Tafel slope was attributed to the improved properties of the developed ATO.

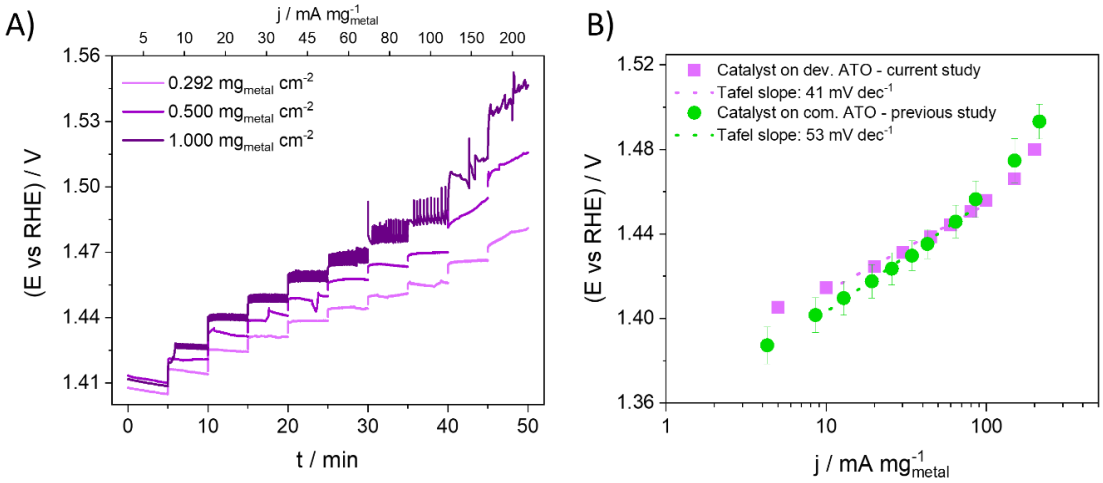

Figure 5.2. *(A) Loading dependence of OER iR-corrected potential transients for IrRu/ATO on a GDL. The measurements were performed in the GDE setup in an O_2 atmosphere at 60 °C using 4 M $HClO_4$ as an electrolyte. (B) Comparison of the Tafel slopes (average of the last 100 s of each iR-corrected current step) of the 0.292 mg_{metal} cm^{-2} IrRu/ATO of this current study and the one presented in Chapter 4 (similar loading – commercial (com.) ATO). The error bars for the green dots show the standard deviation of three independent measurements.*

Subsequently, we determined the stability of the catalyst by applying a constant potential of 1.6 V vs RHE for 2 h at 60 °C. Figure 5.3A illustrates a notable decline in current density of the 1.000 mg_{metal} cm^{-2} (violet curve) sample, demonstrating an overall activity loss of 77%. This trend was likewise observed for the two lower catalyst loadings.

Finally, BoL and EoL activities of IrRu/ATO catalyst deposited on a GDL were compared in Figure 5.3B. At low current density (up to 10 mA mg_{metal}^{-1}), similar BoL and EoL potential transients were observed. Nevertheless, upon extending the comparison to higher current densities, a substantial discrepancy emerged. The tremendous degradation was evidenced by the necessity of a potential exceeding 2 V vs RHE to sustain a current density of 150 mA mg_{metal}^{-1}. This underscored the importance of selecting appropriate experimental conditions. For example, in the work of Schröder et al.,[160] no drastic performance loss was observed during stability test, which may be explained by the milder conditions chosen (10 mA mg_{Ir}^{-1} for 1 h).

Nevertheless, as the optimised Recycalyse catalyst sustained MEA tests without severe degradation,[23] the performance decay could not be solely attributed to the catalyst. Thus, we

believe that rather than documenting the catalyst degradation, we witnessed the degradation of the GDL substrate. Given its composition of carbon-based fibres and MPL, the GDL substrate is prone to corrosion under the harsh OER conditions.[171] This hypothesis was supported by *post-mortem* images of burnt GDLs (coated and non-coated), as depicted in the inset of Figure 5.3B (light violet frame). In this respect, a more resistant substrate, namely PTL, was selected to pursue the investigation. Since PTLs are typically used in electrolyser stacks, the GDE experimental conditions are further aligning with PEMWE.

As mentioned in Section 2.5.3, the preparation methodology of PTL-electrodes differs from the GDL-electrodes due to the absence of MPL, preventing the catalyst from penetrating the substrate fibres. In real application, the prevalent approach involves the fabrication of CCMs, which are subsequently sandwiched between a GDL (cathode) and a PTL (anode).[9] In this this three-electrodes configured GDE study, the anodes were prepared by spraying the electrolyte membrane with the catalyst ink, resulting in one-sided CCMs, and subsequently hot-pressing the latter face down onto the PTLs.

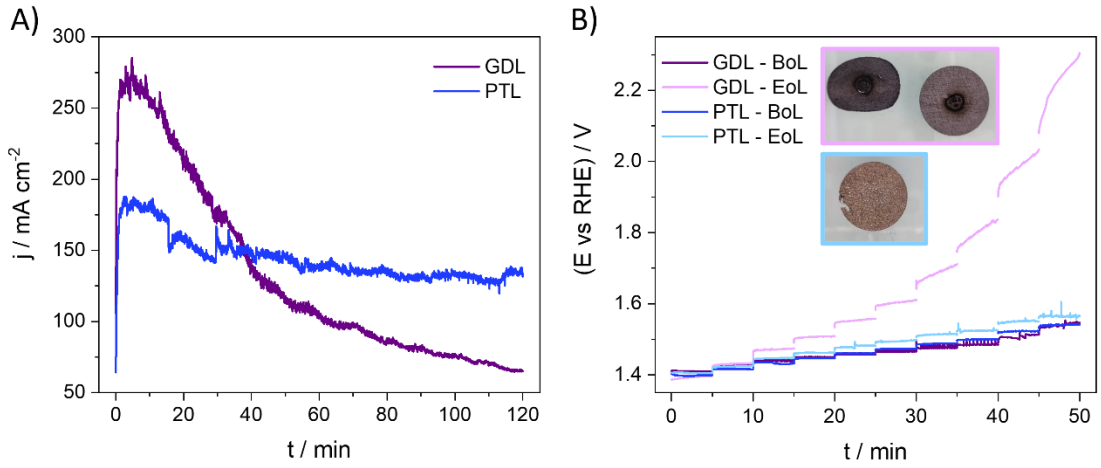

Figure 5.3. *(A) OER current density transients for IrRu/ATO on a GDL (violet curve) and on a PTL (blue curve) and (B) iR-corrected potential transients before (dark colour) and after (light tone) the potentiostatic step at 1.6 V vs RHE. The inset images in (B) represents the backside of the post-mortem GDLs (coated and non-coated, light violet frame) and PTL (light blue frame) electrodes. The nominal loading for the GDL-catalyst is 1.0 mg_{metal} cm^{-2} and the targeted one for the PTL-catalyst is 0.5 mg_{metal} cm^{-2}. The measurements were performed in the GDE setup in an O_2 atmosphere at 60 °C using 4 M $HClO_4$ as an electrolyte.*

A prepared PTL-electrode was tested following the same protocol as the GDL-electrode (Figure 5.1), and both substrates were compared in Figure 5.3. As depicted in Figure 5.3B, BoL activities of both electrode types were similar, indicating that both substrates are suitable for catalyst activity investigations. This finding is in line with our previous observations.[160] However, during the stability step, the PTL-electrode (blue curve) behaved considerably differently compared to its carbon-based electrode counterpart (violet curve) (Figure 5.3A). No substantial loss in activity was recorded over the two-hour experiment (loss: 28%). Moreover, comparing the BoL and EoL activity of the PTL system, it was observed that the potential transients of both were almost identical, resulting in only a slight deviation (17 mV dec^{-1}) in Tafel slope.

Three interpretations could account for the change in the Tafel slope. The first one entails a change in reaction mechanism. However, we refrained from this explanation, as a degraded sample is not expected to change its electron transfer mechanism. A second interpretation could arise from mass transport limitations, as humidified gas was used as a reactant instead of deionised liquid water.[163,169] However, as the determination of the Tafel slope was performed within the kinetic region (limited solely by the electron transfer), we believe this second interpretation does not correctly account for the deviation in Tafel slope. The final explanation is related to a change in resistance. Since neither burning of the PTL (see inset in Figure 5.3B (light blue frame)) nor a gap between the CCM and the PTL were witnessed, the observed increase in resistance between BoL and EoL steps could not refer to the degradation of PTL during this relatively short stability experiment. On the other hand, considering the tendency of antimony to leach out,[79–81,88] we believe this scenario more adequately addresses the change in the Tafel slope. This was further supported by the exponential function obtained from plotting the differences in potentials versus the current densities (i.e., $\Delta(E_{EoL}, E_{BoL})$ vs j). In the literature, exponential functions describing a resistance are attributed to a diode,[183] whereas a normal resistor would yield a linear behaviour (Ohm's law).[184] Given that ATO is a semiconductor, it should follow the exponential behaviour of a diode. Consequently, the observed rise in Tafel slope was most likely due to the degradation of ATO.

In conclusion, the GDE setup was employed to conduct catalyst stability experiments under experimental conditions close to those of PEMWE. While GDL substrates served as adequate candidates for initial catalyst activity screening, they were not recommended for conducting reliable stability tests given their susceptibility to corrosion. Conversely, PTL substrates offer higher corrosion resistance. Therefore, we advocate their usage for conducting reliable and accurate stability measurements, despite their higher cost and more elaborate electrode preparation. Furthermore, degradation protocols need to be carefully designed, for example, by applying high current density, to accurately assess the catalyst stability.

5.4 Contribution to the Work

In this study, I investigated the optimised Recycalyse catalyst, which was synthesised at the Danish Technological Institute by Simon Pitscheider, Erlend Bertheussen, Christoffer M. Pedersen and Christian Kallesøe. The support material was prepared by Annabelle Maletzko and Julia Melke at the Fraunhofer Institute for Chemical Technology. Nedjelko Seselj and I prepared the PTL-electrodes at Blue World Technologies during my one-month visit in Copenhagen, while the GDL-electrodes were prepared only by myself in Bern. I performed all the electrochemical characterisations. Additionally, I recorded and analysed the TEM micrographs. EDX and ICP-MS measurements were performed by technicians from the chemistry department in Bern and analysed by me. Gustav K. H. Wiberg developed the adaptative compensation. Matthias Arenz supervised the project and reviewed the manuscript and figures, I wrote, respectively made.

CHAPTER 6

CONCLUSIONS AND PERSPECTIVES

6.1 CONCLUSIONS

The assessment of reliable OER catalyst performance constituted the core of my thesis. To this end, I investigated the reaction on both commercially available and developed supported Ir-based catalysts using three different testing platforms: the conventional RDE, the inverted RDE, and the GDE setups.

In Chapter 3, the two distinct RDE setups were employed with the commonly used constant current stability protocol. First, it was demonstrated through IL-SEM/EDX and Raman spectroscopy that large amounts of catalyst were still present on the electrode surface after the potential cut-off. Then, using the inverted setup, we effectively debunked the prevailing misconception that the generation of O_2 gas bubbles is the sole limitation of AMS, as frequently stated in the literature. Although the gas bubbles present a limitation in the conventional RDE setup, our experiments with the inverted RDE demonstrated that they do not cause the sudden potential rise during galvanostatic measurements. Instead, we conclusively established that this potential increase stems from the electrical isolation of the iridium particles from the substrates. Thus, using the inverted RDE setup and applying alternating ORR-OER cycles enabled us to conclusively deconvolute the two major drawbacks observed in the traditional RDE configuration. Moreover, through SEM/EDX and Raman measurements, we thoroughly demonstrated that the substrate passivation initiates at the three-phase interfaces between the particle, the substrate, and the electrolyte, leading to a progressive isolation of the particles. Ultimately, the complete substrate passivation culminates in the abrupt potential rise. As a result, this complete electrical isolation of the OER catalyst particles triggers sequential, before kinetically unfavoured reactions, such as carbon oxidation to CO and CO_2 or gold dissolution. The relevance of this degradation channel could be applied beyond AMS, namely to MEA since the latter comprises a catalyst|PTL substrate interface as well.

These findings underscore the critical importance of selecting appropriate techniques for pursuing reliable stability tests. While insights garnered from fuel cell studies provide a valuable starting point, it is imperative to tailor OER methodologies to accurately reflect its unique environment. Therefore, relying solely on the TF-RDE technique for stability evaluations has resulted in misleading conclusions. Thus, it is essential to redesign and reevaluate the experimental methodology employed in OER investigations to allow precise degradation studies in AMS.

In the context of reducing the amount of PGMs in OER electrocatalysts, four supported catalysts were prepared in Chapter 4 *via* a surfactant-free colloidal synthetic route. The catalysts consisted of either metallic Ir or alloyed metallic $Ir_{0.4}Ru_{0.6}$ NPs deposited on either commercial carbon or commercial ATO supports. Their activity was evaluated in a GDE setup, designed to resemble PEMWE conditions, i.e., higher loading (ca. 0.3 mg_{metal} cm^{-2}) and elevated temperatures (30, 40, 60 °C). The study revealed that the NPs were not fully oxidised even after subjecting them to a constant potential of 1.6 V vs RHE for 5 min. The oxidation process was completed during the subsequent activity measurement, which involved a galvanostatic protocol with 5-minute steps. This steady-state protocol enabled us to carefully select the kinetic-limited region, where only the relevant reaction occurs, to extract the Tafel slopes without overestimation. The reported Tafel slope values were consistent with those in the literature. Furthermore, at high current densities (>100 mA mg_{metal}^{-1}), a deviation in the Tafel slope was observed, which was attributed to mass transport limitations. The four catalysts were compared at an overpotential lying within the Tafel slope at most of the temperatures. Two key points emerged:

1) Ru-containing catalysts consistently exhibited superior activity than their Ru-free counterparts, regardless of the support, and

2) Independently of the composition of the NPs, those immobilised on ATO support were less active than those supported on carbon. This disparity was enhanced at elevated temperatures.

While key point 1) was expected, key point 2) was rather surprising given the tendency of carbon to corrode under the harsh OER conditions. This phenomenon was ascribed to antimony leaching, which was promoted at 60 °C. This observation underscores the importance of identifying novel, more resistant support materials for OER and testing the catalyst under conditions that mimic those of an electrolyser stack.

In the last appended manuscript (Chapter 5), the optimised catalyst developed within Recycalyse was investigated. This catalyst consisted of $(Ir_{0.7}Ru_{0.3})_{0.96}Ni_{0.04}$ NPs immobilised on a developed ATO support. The ATO support demonstrated higher surface area and conductivity compared to its commercial counterpart used in Chapter 4. The catalyst was tested in the GDE setup at 60 °C with a protocol consisting of *i)* BoL activity *via* galvanostatic steps, *ii)* stability through constant potential, and *iii)* EoL activity identical to the BoL activity. In comparing a GDL and a PTL substrate, both were found to be adequate substrates for assessing BoL activity. In fact, for initial catalyst screening, we recommend using a GDL due to its economical aspect and simpler preparation. However, when seeking to determine the stability of a catalyst, we strongly advocate departing from carbon substrates. PTL substrates, typically used in PEMWE, are, on the other hand, suitable candidates despite its higher cost and the need for sophisticated devices to prepare the electrodes. During the stability step involving holding the potential at 1.6 V vs RHE for 5 min, the GDL-catalyst system exhibited a drastic loss of activity, whereas the activity of the PTL-catalyst system remained more or less stable. The substantial disparity was attributed to the degradation of the carbon material of the GDL. Furthermore, upon comparing BoL and EoL current steps, those of the GDL-catalyst system demonstrated large discrepancies at current densities higher than 10 mA mg_{metal}^{-1},

while those of the PTL-catalyst system nearly overlapped, resulting only in a slight difference in Tafel slopes. The latter was attributed to the leaching of antimony. Therefore, we assert the exclusive use of PTLs when assessing catalyst stability.

Last but not least, referring to the preceding discussion, it is essential to apply conditions that enable conclusive statements about the catalyst degradation. While low current density is typically used to estimate the stability of a catalyst, we demonstrated that these conditions do not adequately represent those in PEMWE. Indeed, a catalyst reported as stable under mild conditions, may not cope under those resembling PEMWE.

6.2 PERSPECTIVES

6.2.1 Overcoming Substrate Passivation

In the context of Chapter 3, where the lack of an inert substrate for galvanostatic AST measurements in AMS was revealed, the subsequent evident step is to mitigate the reported passivation of the backing electrode materials. In fact, despite its inherent limitations in evaluating the catalyst stability, AMS remains a convenient, affordable, and widely used approach at laboratory scale. Consequently, to pursue AMS experiments, an approach to diminish the three-phase interfaces where substrate, catalyst and electrolyte meet, i.e., where the passivation is initiated, is required.

This objective may be achieved through a substantial increase in electrode loading. As demonstrated in our study, a 5-fold loading increase prolonged the experimental duration of the GC-electrode by ca. 20-fold. However, such a strategy may deviate from the well-defined conditions governing the RDE technique.

An alternative approach involves the fabrication of a non-particulate, compact, and impermeable thin film onto the substrate. Such a film would protect the substrate from the electrolyte, similarly as the gas bubbles do, yet without any additional drawback. This thin film could serve either as a catalyst (i.e., an OER active oxide) or as a “second” impermeable and inert substrate onto which the catalyst NPs are drop-casted.

6.2.2 Lowering PGM Content in the Catalyst Layer

In this thesis, although the utilisation of support materials and nanoscale particles reduced the PGM content, Ir-based catalysts were still employed. As introduced in the first Chapter, iridium is among the rarest elements on Earth, necessitating an optimised utilisation. While a complete elimination of precious metal oxides seems an attractive strategy, it would compromise the long-term electrode durability due to the low stability of those elements in acidic media. Therefore, as outlined in Section 2.3.2, the design of multi-elemental catalysts, composed of a low amount of iridium and one or more non-precious metal oxides, appears as a promising approach.

Moreover, lowering metal loading on the support would contribute to a reduction in the use of iridium. Finally, to date, the electrode loadings correspond to 2.0-2.5 mg_{Ir} cm^{-2}. Decreasing this state-of-the-art electrode loading would facilitate the preservation of precious metals.

6.2.3 Designing Adequate Testing Methodology and Protocols

In this doctoral research, methodologies derived from fuel cell studies, such as TF-RDE, were employed to conduct stability tests. It was demonstrated that, while these methods are straightforward, they cannot be applied without any further considerations to OER investigations. Therefore, it is imperative to develop new testing methodologies that reflect the inherent conditions of OER to effectively compare novel catalysts. In this regard, considering the current limitations of the iRDE and RDE setups, the GDE setup stands as a promising testing platform for investigating catalysts. Nevertheless, attention must be paid to the selection of appropriate substrates based on the desired information (activity vs stability).

Moreover, the design of coherent protocols is of paramount importance to adequately assess the catalyst performance. For instance, galvanostatic steps prove to be a suitable approach for investigating catalyst activity. Unlike the common dynamic scans (CVs), this steady-state approach allows for the differentiation of various current contributions, thereby preventing overestimation of the catalyst performance. Regarding AST for evaluating intrinsic catalyst stability, relatively high potentiostatic (≥1.6 V vs RHE) or galvanostatic steps (greater than 10 mA cm^{-2} or 10 mA mg_{metal}^{-1}) are required for a prolonged duration (≥ one hour) to effectively stress the catalyst. Additionally, combining this steady-state mode with a dynamic operational mode can fully address the catalyst stability, as dynamic modes are believed to best mimic the fluctuations in the power output when PEMWEs are directly coupled to renewable energies.[185]

Furthermore, these improved protocols should be implemented under conditions close to PEMWE. In this regard, the utilisation of liquid water instead of humidified gas would align the conditions of the GDE setup more closely with those of MEAs. Finally, in addition to testing the catalyst at elevated temperatures, evaluating its performance in the recently introduced pressurised GDE setup, which enables conducting experiments at high pressure, would be beneficial.[161]

ACKNOWLEDGEMENT

Completing this doctoral thesis marks a significant achievement in my academic journey, and I still find it hard to believe that I have reached this milestone. I wish to express my heartfelt thanks to all who have contributed to this incredible odyssey.

First and foremost, my sincere gratitude goes to Prof. Dr. Matthias Arenz for giving me the opportunity to conduct my PhD project in his research group. I highly appreciated his valuable guidance and the freedom he gave me to develop my own ideas. Moreover, I am thankful for the numerous opportunities to participate in conferences and summer schools across various countries, and this despite starting this exciting PhD experience under Covid restrictions. I am also very grateful for the enriching experience of spending one month abroad, from which I benefited in many ways.

I extend my gratitude to Prof. Dr. Atsushi Urakawa for his acceptance of the evaluation of my doctoral research and for the time he dedicated to it.

For his kind recommendation following the completion my master thesis in his group, I kindly thank Prof. Dr. Peter Broekmann, who gave me the taste of research and the desire to pursue my studies for four more years.

I would like to thank also the entire Recycalyse consortium. Working within such a committed and collaborative group has been a great opportunity. I have always enjoyed gathering with all of you in person during our biannual meetings held at various facilities and found these experiences very enriching. In particular, I warmly thank Christian, Simon, Erlend, Christoffer, and Nedo for having hosted me in their Danish labs for one month. I also thank Joseph, who was both a good friend and guide during this month in Copenhagen.

My sincere thanks go to Gustav for the numerous discussions we had about science and everyday life. I deeply valued the time he always took to explain everything to me without hesitation, often multiple times, in a simple and non-judgmental way.

For their assistance in proof-reading parts of this thesis, I am thankful to Pavel, Gustav, Nicolas and Menglong.

Furthermore, I thank Beatrice for her countless hours spent on the SEM, thereby enabling me also to improve my German skills. I would also like to extend my thanks the workshop, the Ausgabe, the IT team as well as the Hausdienst team for their kind help and their warm “good morning”.

I am also grateful to the PhD Coalition, created in 2022, for fostering a pleasant and friendly atmosphere within the DCBP. Special thanks to Sophia, who very spontaneously agreed to the co-presidency of the association with me during our final year of PhD studies. It was nice to collaborate with someone as enterprising and committed as you.

A big thank you goes to my present and former friends and colleagues from the 6th floor. It was great to still feel very welcome and part of your big family. I will cherish all the happy memories from our time together in the labs and after work, such as the skiing, the numerous

memories from our time together in the labs and after work, such as the skiing, the numerous aperos and dinner, the hikes, the BBQs and the crazy game evenings. So, thank you to Pavel, Yuhui, Maria, Ivan, Alain, Ying, Nicola, Liliana, Abhi, Mike, Nandu, Kiran, Sasha, Soma, Huifang, Dennis, Mario, Julia, Yuzhen, Xin W., Xin Y., Yaqiang, Valery, Lorine, Noémi, Vilo and Vitali.

I am also grateful to the members of my current research group for the great working atmosphere, the enjoyable discussions during lunch and the fun times during our group activities and after work. I am happy to count some of you among my closest friends! My heartfelt thanks go to Renan, Nicolas, Menglong, Divyansh, Etienne, Gustav, Tim, Sven, Ahmad, Jonas, Ilya, Pascal, Naomi, Tobias, Joel, Leo, Johanne, Shima, Jia, Johanna, Jan, Rahel, Damin, Reshma, Rebecca, Stefanie, Jens, and Pablo.

I would like to also thank my friends in other research groups at the DCBP for the nice conversations in the staircase, the breaks between experiments, and the gathering after work. Thanks to Alicia, Yaser, Kaila, Isabelle, Priscilla, Rahul, Subrata, Viki, Gaetano, and Etienne. Additionally, I extend my appreciation to my friends, Lara, Cressida and Roxanne, outside the university for their constant encouragement and our long friendship.

Pavel, I am wholeheartedly grateful to have you as a partner, friend, and colleague for over five years. Throughout my doctoral journey, you have been there for me through the exciting highs and difficult lows. Your constant belief in me, even during moments of self-doubt, has been a source of strength. You tirelessly supported and encouraged me both at home and in the labs, providing assistance whenever I needed it. I cannot thank you enough for your steadfast love, support, and invaluable advice. Te amo.

Last but certainly not least, I am grateful beyond words to my mother, Hind, and my sister, Ornina, for their unwavering love, encouragement and emotional support throughout my entire academic journey which began many years ago. Your unconditional belief in me and my abilities, coupled with your cheerful attitude served as a constant source of motivation during the challenging periods and fuelled my determination to pursue my dreams. You have shaped me into the person I am today, and for that I am eternally thankful to have you as my family. Je vous aime.

To all of you, you have been an integral part of my journey, and I am truly fortunate to have you by my side!

DISCLOSURE OF USE OF AI-ASSISTED TECHNOLOGIES

☐ During the preparation of this work, I have NOT used any AI-assisted technologies.

☒ During the preparation of this work, I used the following tool:

ChatGPT 3.5 to improve the readability and the language of my thesis.

After using these tools/services, I reviewed and edited the content as needed and take full responsibility for the content of the publication. I am aware that in case of dis-compliance, the generated text is considered plagiarism with its legal consequences.

REFERENCES

(1) The United Nations Framework Convention on Climate Change (UNFCCC). *Key aspects of the Paris Agreement*. https://unfccc.int/most-requested/key-aspects-of-the-paris-agreement (accessed 2024-03-26).

(2) BP. *Bp Energy Outlook 2023*; 2023. https://www.bp.com/content/dam/bp/business-sites/en/global/corporate/pdfs/energy-economics/energy-outlook/bp-energy-outlook-2023.pdf (accessed 2024-03-13).

(3) Gür, T. M. Review of Electrical Energy Storage Technologies, Materials and Systems: Challenges and Prospects for Large-Scale Grid Storage. *Energy Environ Sci* **2018**, *11* (10), 2696–2767. https://doi.org/10.1039/C8EE01419A.

(4) Abe, J. O.; Popoola, A. P. I.; Ajenifuja, E.; Popoola, O. M. Hydrogen Energy, Economy and Storage: Review and Recommendation. *Int J Hydrogen Energy* **2019**, *44* (29), 15072–15086. https://doi.org/10.1016/j.ijhydene.2019.04.068.

(5) Tashie-Lewis, B. C.; Nnabuife, S. G. Hydrogen Production, Distribution, Storage and Power Conversion in a Hydrogen Economy-A Technology Review. *Chemical Engineering Journal Advances* **2021**, *8*, 100172. https://doi.org/10.1016/j.ceja.2021.100172.

(6) Rouwenhorst, K. H. R.; Travis, A. S.; Lefferts, L. 1921–2021: A Century of Renewable Ammonia Synthesis. *Sustainable Chemistry* **2022**, *3* (2), 149–171. https://doi.org/10.3390/suschem3020011.

(7) IRENA. *Global Renewables Outlook: Energy Transformation 2050*; Abu Dhabi, 2020. https://www.irena.org/publications/2020/Apr/Global-Renewables-Outlook-2020 (accessed 2024-04-20).

(8) Grigoriev, S. A.; Fateev, V. N.; Bessarabov, D. G.; Millet, P. Current Status, Research Trends, and Challenges in Water Electrolysis Science and Technology. *Int J Hydrogen Energy* **2020**, *45* (49), 26036–26058. https://doi.org/10.1016/j.ijhydene.2020.03.109.

(9) Carmo, M.; Fritz, D. L.; Mergel, J.; Stolten, D. A Comprehensive Review on PEM Water Electrolysis. *Int J Hydrogen Energy* **2013**, *38* (12), 4901–4934. https://doi.org/10.1016/j.ijhydene.2013.01.151.

(10) Zhang, K.; Liang, X.; Wang, L.; Sun, K.; Wang, Y.; Xie, Z.; Wu, Q.; Bai, X.; Hamdy, M. S.; Chen, H.; Zou, X. Status and Perspectives of Key Materials for PEM Electrolyzer. *Nano Research Energy* **2022**, *1* (3), e9120032. https://doi.org/10.26599/NRE.2022.9120032.

(11) Miller, H. A.; Bouzek, K.; Hnat, J.; Loos, S.; Bernäcker, C. I.; Weißgärber, T.; Röntzsch, L.; Meier-Haack, J. Green Hydrogen from Anion Exchange Membrane Water Electrolysis: A Review of Recent Developments in Critical Materials and Operating Conditions. *Sustain Energy Fuels* **2020**, *4* (5), 2114–2133. https://doi.org/10.1039/C9SE01240K.

(12) Russell J. H.; Nuttall L. J.; Fickett A. P. Hydrogen Generation by Solid Polymer Electrolyte Water Electrolysis. *Am. Chem. Sco. Div. Fuel Chem. Prepr* **1973**, *18*, 24–40.

(13) Buttler, A.; Spliethoff, H. Current Status of Water Electrolysis for Energy Storage, Grid Balancing and Sector Coupling via Power-to-Gas and Power-to-Liquids: A Review. *Renewable and Sustainable Energy Reviews* **2018**, *82*, 2440–2454. https://doi.org/10.1016/j.rser.2017.09.003.

(14) Guo, Y.; Li, G.; Zhou, J.; Liu, Y. Comparison between Hydrogen Production by Alkaline Water Electrolysis and Hydrogen Production by PEM Electrolysis. *IOP Conf Ser Earth Environ Sci* **2019**, *371* (4), 042022. https://doi.org/10.1088/1755-1315/371/4/042022.

(15) IRENA. *Hydrogen from Renewable Power: Technology Outlook for the Energy Transition*; Abu Dhabi, 2018. https://www.irena.org/publications/2018/Sep/Hydrogen-from-renewable-power (accessed 2024-05-05).

(16) Ayers, K. E.; Anderson, E. B.; Capuano, C.; Carter, B.; Dalton, L.; Hanlon, G.; Manco, J.; Niedzwiecki, M. Research Advances towards Low Cost, High Efficiency PEM Electrolysis. *ECS Trans* **2010**, *33* (1), 3–15. https://doi.org/10.1149/1.3484496.

(17) Abbasi, R.; Setzler, B. P.; Lin, S.; Wang, J.; Zhao, Y.; Xu, H.; Pivovar, B.; Tian, B.; Chen, X.; Wu, G.; Yan, Y. A Roadmap to Low-Cost Hydrogen with Hydroxide Exchange Membrane Electrolyzers. *Advanced Materials* **2019**, *31* (31). https://doi.org/10.1002/adma.201805876.

(18) IRENA. *GREEN HYDROGEN COST REDUCTION SCALING UP ELECTROLYSERS TO MEET THE 1.5°C CLIMATE GOAL*; Abu Dhabi., 2020. https://www.irena.org/publications/2020/Dec/Green-hydrogen-cost-reduction (accessed 2024-02-26).

(19) Kibsgaard, J.; Chorkendorff, I. Considerations for the Scaling-up of Water Splitting Catalysts. *Nat Energy* **2019**, *4* (6), 430–433. https://doi.org/10.1038/s41560-019-0407-1.

(20) Minke, C.; Suermann, M.; Bensmann, B.; Hanke-Rauschenbach, R. Is Iridium Demand a Potential Bottleneck in the Realization of Large-Scale PEM Water Electrolysis? *Int J Hydrogen Energy* **2021**, *46* (46), 23581–23590. https://doi.org/10.1016/j.ijhydene.2021.04.174.

(21) *CORDIS EU research results*. New sustainable and recyclable catalytic materials for proton exchange membrane electrolysers. https://cordis.europa.eu/project/id/861960/reporting (accessed 2024-04-17).

(22) *Recycalyse*. https://recycalyse.eu/ (accessed 2024-04-17).

(23) Melke, J.; Maletzko, A.; Gomez Villa, E. D.; Bornet, A.; Wiberg, G. K. H.; Arenz, M.; Sandig-Predzymirska, L.; Thiere, A.; Charitos, A.; Stelter, M.; Wang, Z.; Pitscheider, S.; Bertheussen, E.; Pedersen, C. M.; Finsdóttir, S.; Kokborg, M. S.; Berman, D. G.; Dalvang, S.; Müller, S. S.; Seidel, F.; Seselj, N.; Höglinger, M.; Kartusch, S.; Eder, J.; Macherhammer, M.; Trattner, A.; Kallesøe, C. Recycalyse – New Sustainable and Recyclable Catalytic Materials for Proton Exchange Membrane Electrolysers. *Chemie Ingenieur Technik* **2024**, *96* (1–2), 126–142. https://doi.org/10.1002/cite.202300143.

(24) Ursua, A.; Gandia, L. M.; Sanchis, P. Hydrogen Production From Water Electrolysis: Current Status and Future Trends. *Proceedings of the IEEE* **2012**, *100* (2), 410–426. https://doi.org/10.1109/JPROC.2011.2156750.

(25) Carmo, M.; Stolten, D. Energy Storage Using Hydrogen Produced From Excess Renewable Electricity. In *Science and Engineering of Hydrogen-Based Energy Technologies*; Elsevier, 2019; pp 165–199. https://doi.org/10.1016/B978-0-12-814251-6.00004-6.

(26) Wang, S.; Lu, A.; Zhong, C.-J. Hydrogen Production from Water Electrolysis: Role of Catalysts. *Nano Converg* **2021**, *8* (1), 4. https://doi.org/10.1186/s40580-021-00254-x.

(27) Bard, A. J.; Faulkner, L. R. *Electrochemical Methods: Fundamentals and Applications*, 2nd ed.; John Wiley & Sons, 2000.
(28) Anantharaj, S.; Noda, S. How Properly Are We Interpreting the Tafel Lines in Energy Conversion Electrocatalysis? *Mater Today Energy* **2022**, *29*, 101123. https://doi.org/10.1016/j.mtener.2022.101123.
(29) van der Heijden, O.; Park, S.; Vos, R. E.; Eggebeen, J. J. J.; Koper, M. T. M. Tafel Slope Plot as a Tool to Analyze Electrocatalytic Reactions. *ACS Energy Lett* **2024**, *9* (4), 1871–1879. https://doi.org/10.1021/acsenergylett.4c00266.
(30) Rossmeisl, J.; Qu, Z.-W.; Zhu, H.; Kroes, G.-J.; Nørskov, J. K. Electrolysis of Water on Oxide Surfaces. *Journal of Electroanalytical Chemistry* **2007**, *607* (1–2), 83–89. https://doi.org/10.1016/j.jelechem.2006.11.008.
(31) Man, I. C.; Su, H.; Calle-Vallejo, F.; Hansen, H. A.; Martínez, J. I.; Inoglu, N. G.; Kitchin, J.; Jaramillo, T. F.; Nørskov, J. K.; Rossmeisl, J. Universality in Oxygen Evolution Electrocatalysis on Oxide Surfaces. *ChemCatChem* **2011**, *3* (7), 1159–1165. https://doi.org/10.1002/cctc.201000397.
(32) Ooka, H.; Huang, J.; Exner, K. S. The Sabatier Principle in Electrocatalysis: Basics, Limitations, and Extensions. *Front Energy Res* **2021**, *9*. https://doi.org/10.3389/fenrg.2021.654460.
(33) Macounova, K.; Makarova, M.; Krtil, P. Oxygen Evolution on Nanocrystalline RuO_2 and $Ru_{0.9}Ni_{0.1}O_2$−δ Electrodes – DEMS Approach to Reaction Mechanism Determination. *Electrochem commun* **2009**, *11* (10), 1865–1868. https://doi.org/10.1016/j.elecom.2009.08.004.
(34) Fierro, S.; Nagel, T.; Baltruschat, H.; Comninellis, C. Investigation of the Oxygen Evolution Reaction on Ti/IrO_2 Electrodes Using Isotope Labelling and on-Line Mass Spectrometry. *Electrochem commun* **2007**, *9* (8), 1969–1974. https://doi.org/10.1016/j.elecom.2007.05.008.
(35) Wang, C.; Schechter, A.; Feng, L. Iridium-Based Catalysts for Oxygen Evolution Reaction in Acidic Media: Mechanism, Catalytic Promotion Effects and Recent Progress. *Nano Research Energy* **2023**, *2*, e9120056. https://doi.org/10.26599/NRE.2023.9120056.
(36) Yoon, H.; Ju, B.; Kim, D. Perspectives on the Development of Highly Active, Stable, and Cost-effective OER Electrocatalysts in Acid. *Battery Energy* **2023**, *2* (5). https://doi.org/10.1002/bte2.20230017.
(37) Chorkendorff, I.; Niemantsverdriet, J. W. Introduction to Catalysis. In *Concepts of Modern Catalysis and Kinetics*; Wiley, 2003; pp 1–21. https://doi.org/10.1002/3527602658.ch1.
(38) Reier, T.; Oezaslan, M.; Strasser, P. Electrocatalytic Oxygen Evolution Reaction (OER) on Ru, Ir, and Pt Catalysts: A Comparative Study of Nanoparticles and Bulk Materials. *ACS Catal* **2012**, *2* (8), 1765–1772. https://doi.org/10.1021/cs3003098.
(39) European Commission, Joint Research Centre, Bolard J.; Dolci F.; Gryc K.; Eynard U.; Georgakaki A.; Letout S.; Kuokkanen A.; Mountraki A; Ince E.; Shtjefni D. *Clean Energy Technology Observatory: Water Electrolysis and Hydrogen in the European Union - 2023 Status Report on Technology Development, Trends, Value Chains and Markets*; Publications Office of the European Union, Luxembourg, 2023. https://doi.org/10.2760/133010.

(40) Campelo, J. M.; Luna, D.; Luque, R.; Marinas, J. M.; Romero, A. A. Sustainable Preparation of Supported Metal Nanoparticles and Their Applications in Catalysis. *ChemSusChem* **2009**, *2* (1), 18–45. https://doi.org/10.1002/cssc.200800227.

(41) Katsounaros, I.; Cherevko, S.; Zeradjanin, A. R.; Mayrhofer, K. J. J. Oxygen Electrochemistry as a Cornerstone for Sustainable Energy Conversion. *Angewandte Chemie International Edition* **2014**, *53* (1), 102–121. https://doi.org/10.1002/ANIE.201306588.

(42) Bizzotto, F.; Quinson, J.; Zana, A.; Kirkensgaard, J. J. K.; Dworzak, A.; Oezaslan, M.; Arenz, M. Ir Nanoparticles with Ultrahigh Dispersion as Oxygen Evolution Reaction (OER) Catalysts: Synthesis and Activity Benchmarking. *Catal Sci Technol* **2019**, *9* (22), 6345–6356. https://doi.org/10.1039/C9CY01728C.

(43) Hartig-Weiss, A.; Miller, M.; Beyer, H.; Schmitt, A.; Siebel, A.; Freiberg, A. T. S.; Gasteiger, H. A.; El-Sayed, H. A. Iridium Oxide Catalyst Supported on Antimony-Doped Tin Oxide for High Oxygen Evolution Reaction Activity in Acidic Media. *ACS Appl Nano Mater* **2020**, *3* (3), 2185–2196. https://doi.org/10.1021/acsanm.9b02230.

(44) Lee, Y.; Suntivich, J.; May, K. J.; Perry, E. E.; Shao-Horn, Y. Synthesis and Activities of Rutile IrO_2 and RuO_2 Nanoparticles for Oxygen Evolution in Acid and Alkaline Solutions. *J Phys Chem Lett* **2012**, *3* (3), 399–404. https://doi.org/10.1021/jz2016507.

(45) Zu, L.; Qian, X.; Zhao, S.; Liang, Q.; Chen, Y. E.; Liu, M.; Su, B.-J.; Wu, K.-H.; Qu, L.; Duan, L.; Zhan, H.; Zhang, J.-Y.; Li, C.; Li, W.; Juang, J. Y.; Zhu, J.; Li, D.; Yu, A.; Zhao, D. Self-Assembly of Ir-Based Nanosheets with Ordered Interlayer Space for Enhanced Electrocatalytic Water Oxidation. *J Am Chem Soc* **2022**, *144* (5), 2208–2217. https://doi.org/10.1021/jacs.1c11241.

(46) Laha, S.; Lee, Y.; Podjaski, F.; Weber, D.; Duppel, V.; Schoop, L. M.; Pielnhofer, F.; Scheurer, C.; Müller, K.; Starke, U.; Reuter, K.; Lotsch, B. V. Ruthenium Oxide Nanosheets for Enhanced Oxygen Evolution Catalysis in Acidic Medium. *Adv Energy Mater* **2019**, *9* (15). https://doi.org/10.1002/aenm.201803795.

(47) Jiang, B.; Guo, Y.; Kim, J.; Whitten, A. E.; Wood, K.; Kani, K.; Rowan, A. E.; Henzie, J.; Yamauchi, Y. Mesoporous Metallic Iridium Nanosheets. *J Am Chem Soc* **2018**, *140* (39), 12434–12441. https://doi.org/10.1021/jacs.8b05206.

(48) Alia, S. M.; Shulda, S.; Ngo, C.; Pylypenko, S.; Pivovar, B. S. Iridium-Based Nanowires as Highly Active, Oxygen Evolution Reaction Electrocatalysts. *ACS Catal* **2018**, *8* (3), 2111–2120. https://doi.org/10.1021/acscatal.7b03787.

(49) Fu, L.; Yang, F.; Cheng, G.; Luo, W. Ultrathin Ir Nanowires as High-Performance Electrocatalysts for Efficient Water Splitting in Acidic Media. *Nanoscale* **2018**, *10* (4), 1892–1897. https://doi.org/10.1039/C7NR09377B.

(50) Park, J.; Young, ¶; Sa, J.; Baik, H.; Kwon, T.; Joo, S. H.; Lee, K. Iridium-Based Multimetallic Nanoframe@Nanoframe Structure: An Efficient and Robust Electrocatalyst toward Oxygen Evolution Reaction. **2017**. https://doi.org/10.1021/acsnano.7b00233.

(51) Jin, H.; Hong, Y.; Yoon, J.; Oh, A.; Chaudhari, N. K.; Baik, H.; Joo, S. H.; Lee, K. Lanthanide Metal-Assisted Synthesis of Rhombic Dodecahedral MNi (M = Ir and Pt) Nanoframes toward Efficient Oxygen Evolution Catalysis. *Nano Energy* **2017**, *42*, 17–25. https://doi.org/10.1016/J.NANOEN.2017.10.033.

(52) Reier, T.; Teschner, D.; Lunkenbein, T.; Bergmann, A.; Selve, S.; Kraehnert, R.; Schlögl, R.; Strasser, P. Electrocatalytic Oxygen Evolution on Iridium Oxide: Uncovering Catalyst-Substrate Interactions and Active Iridium Oxide Species. *J Electrochem Soc* **2014**, *161* (9), F876–F882. https://doi.org/10.1149/2.0411409jes.

(53) Massué, C.; Pfeifer, V.; Huang, X.; Noack, J.; Tarasov, A.; Cap, S.; Schlögl, R. High-Performance Supported Iridium Oxohydroxide Water Oxidation Electrocatalysts. *ChemSusChem* **2017**, *10* (9), 1943–1957. https://doi.org/10.1002/cssc.201601817.

(54) Kötz, R.; Stucki, S. Stabilization of RuO_2 by IrO_2 for Anodic Oxygen Evolution in Acid Media. *Electrochim Acta* **1986**, *31* (10), 1311–1316. https://doi.org/10.1016/0013-4686(86)80153-0.

(55) Xu, S.; Liu, Y.; Tong, J.; Hu, W.; Xia, Q. Iridium–Nickel Composite Oxide Catalysts for Oxygen Evolution Reaction in Acidic Water Electrolysis. *Russian Journal of Electrochemistry* **2016**, *52* (11), 1021–1031. https://doi.org/10.1134/S1023193516110124.

(56) Zhou, L.; Liu, X.; Wang, K.; Zhao, X.; Pu, H.; Zhang, T.; Jia, J.; Dong, K.; Deng, Y. One-Pot Synthesis of Alloy Ir–Cu Microspheres with Excellent Electro-Catalytic Activity Toward Oxygen Evolution Reaction under Acidic Conditions. *Energy & Fuels* **2020**, *34* (8), 9956–9962. https://doi.org/10.1021/acs.energyfuels.0c01581.

(57) Li, K.; Chen, W. Recent Progress in High-Entropy Alloys for Catalysts: Synthesis, Applications, and Prospects. *Mater Today Energy* **2021**, *20*, 100638. https://doi.org/10.1016/j.mtener.2021.100638.

(58) Jin, Z.; Lv, J.; Jia, H.; Liu, W.; Li, H.; Chen, Z.; Lin, X.; Xie, G.; Liu, X.; Sun, S.; Qiu, H. Nanoporous Al-Ni-Co-Ir-Mo High-Entropy Alloy for Record-High Water Splitting Activity in Acidic Environments. *Small* **2019**, *15* (47). https://doi.org/10.1002/smll.201904180.

(59) Zhu, H.; Zhu, Z.; Hao, J.; Sun, S.; Lu, S.; Wang, C.; Ma, P.; Dong, W.; Du, M. High-Entropy Alloy Stabilized Active Ir for Highly Efficient Acidic Oxygen Evolution. *Chemical Engineering Journal* **2022**, *431*, 133251. https://doi.org/10.1016/j.cej.2021.133251.

(60) Maulana, A. L.; Chen, P.-C.; Shi, Z.; Yang, Y.; Lizandara-Pueyo, C.; Seeler, F.; Abruña, H. D.; Muller, D.; Schierle-Arndt, K.; Yang, P. Understanding the Structural Evolution of IrFeCoNiCu High-Entropy Alloy Nanoparticles under the Acidic Oxygen Evolution Reaction. *Nano Lett* **2023**, *23* (14), 6637–6644. https://doi.org/10.1021/acs.nanolett.3c01831.

(61) Huynh, M.; Bediako, D. K.; Nocera, D. G. A Functionally Stable Manganese Oxide Oxygen Evolution Catalyst in Acid. *J Am Chem Soc* **2014**, *136* (16), 6002–6010. https://doi.org/10.1021/ja413147e.

(62) Zhao, L.; Cao, Q.; Wang, A.; Duan, J.; Zhou, W.; Sang, Y.; Liu, H. Iron Oxide Embedded Titania Nanowires – An Active and Stable Electrocatalyst for Oxygen Evolution in Acidic Media. *Nano Energy* **2018**, *45*, 118–126. https://doi.org/10.1016/j.nanoen.2017.12.029.

(63) Lai, Q.; Vediyappan, V.; Aguey-Zinsou, K.-F.; Matsumoto, H. One-Step Synthesis of Carbon-Protected Co_3O_4 Nanoparticles toward Long-Term Water Oxidation in Acidic Media. *Advanced Energy and Sustainability Research* **2021**, *2* (11). https://doi.org/10.1002/aesr.202100086.

(64) Mayrhofer, K. J. J.; Strmcnik, D.; Blizanac, B. B.; Stamenkovic, V.; Arenz, M.; Markovic, N. M. Measurement of Oxygen Reduction Activities via the Rotating Disc Electrode Method: From Pt Model Surfaces to Carbon-Supported High Surface Area Catalysts. *Electrochim Acta* **2008**, *53* (7), 3181–3188. https://doi.org/10.1016/j.electacta.2007.11.057.

(65) Pozio, A.; De Francesco, M.; Cemmi, A.; Cardellini, F.; Giorgi, L. Comparison of High Surface Pt/C Catalysts by Cyclic Voltammetry. *J Power Sources* **2002**, *105* (1), 13–19. https://doi.org/10.1016/S0378-7753(01)00921-1.

(66) Senthil Kumar, S. M.; Soler Herrero, J.; Irusta, S.; Scott, K. The Effect of Pretreatment of Vulcan XC-72R Carbon on Morphology and Electrochemical Oxygen Reduction Kinetics of Supported Pd Nano-Particle in Acidic Electrolyte. *Journal of Electroanalytical Chemistry* **2010**, *647* (2), 211–221. https://doi.org/10.1016/j.jelechem.2010.05.021.

(67) Sakthivel, M.; Drillet, J.-F. An Extensive Study about Influence of the Carbon Support Morphology on Pt Activity and Stability for Oxygen Reduction Reaction. *Appl Catal B* **2018**, *231*, 62–72. https://doi.org/10.1016/j.apcatb.2018.02.050.

(68) Maass, S.; Finsterwalder, F.; Frank, G.; Hartmann, R.; Merten, C. Carbon Support Oxidation in PEM Fuel Cell Cathodes. *J Power Sources* **2008**, *176* (2), 444–451. https://doi.org/10.1016/J.JPOWSOUR.2007.08.053.

(69) Kangasniemi, K. H.; Condit, D. A.; Jarvi, T. D. Characterization of Vulcan Electrochemically Oxidized under Simulated PEM Fuel Cell Conditions. *J Electrochem Soc* **2004**, *151* (4), E125. https://doi.org/10.1149/1.1649756.

(70) Mazúr, P.; Polonský, J.; Paidar, M.; Bouzek, K. Non-Conductive TiO_2 as the Anode Catalyst Support for PEM Water Electrolysis. *Int J Hydrogen Energy* **2012**, *37* (17), 12081–12088. https://doi.org/10.1016/j.ijhydene.2012.05.129.

(71) Bernt, M.; Gasteiger, H. A. Influence of Ionomer Content in IrO_2/TiO_2 Electrodes on PEM Water Electrolyzer Performance. *J Electrochem Soc* **2016**, *163* (11), F3179–F3189. https://doi.org/10.1149/2.0231611jes.

(72) Fuentes, R. E.; Farell, J.; Weidner, J. W. Multimetallic Electrocatalysts of Pt, Ru, and Ir Supported on Anatase and Rutile TiO_2 for Oxygen Evolution in an Acid Environment. *Electrochemical and Solid-State Letters* **2011**, *14* (3), E5. https://doi.org/10.1149/1.3528163.

(73) Oakton, E.; Lebedev, D.; Povia, M.; Abbott, D. F.; Fabbri, E.; Fedorov, A.; Nachtegaal, M.; Copéret, C.; Schmidt, T. J. IrO_2 -TiO_2 : A High-Surface-Area, Active, and Stable Electrocatalyst for the Oxygen Evolution Reaction. *ACS Catal* **2017**, *7* (4), 2346–2352. https://doi.org/10.1021/acscatal.6b03246.

(74) Xu, J.; Liu, G.; Li, J.; Wang, X. The Electrocatalytic Properties of an IrO_2/SnO_2 Catalyst Using SnO_2 as a Support and an Assisting Reagent for the Oxygen Evolution Reaction. *Electrochim Acta* **2012**, *59*, 105–112. https://doi.org/10.1016/j.electacta.2011.10.044.

(75) Fang, Z.; Tang, Z.; Lin, S.; Li, R.; Chen, X.; Tian, J.; Liu, L.; Peng, J.; Liu, S.; Fu, B.; Deng, T.; Wu, J. Doped TiO_2 -Supported IrO_2 Electrocatalysts with High Activity and Durability toward the Acidic Oxygen Evolution Reaction. *CrystEngComm* **2024**, *26* (4), 475–483. https://doi.org/10.1039/D3CE01036H.

(76) Hao, C.; Lv, H.; Zhao, Q.; Li, B.; Zhang, C.; Mi, C.; Song, Y.; Ma, J. Investigation of V-Doped TiO^2 as an Anodic Catalyst Support for SPE Water Electrolysis. *Int J Hydrogen Energy* **2017**, *42* (15), 9384–9395. https://doi.org/10.1016/j.ijhydene.2017.02.131.

(77) Hu, W.; Chen, S.; Xia, Q. IrO_2/Nb–TiO_2 Electrocatalyst for Oxygen Evolution Reaction in Acidic Medium. *Int J Hydrogen Energy* **2014**, *39* (13), 6967–6976. https://doi.org/10.1016/j.ijhydene.2014.02.114.

(78) Oh, H.; Nong, H. N.; Strasser, P. Preparation of Mesoporous Sb-, F-, and In-Doped SnO_2 Bulk Powder with High Surface Area for Use as Catalyst Supports in Electrolytic Cells. *Adv Funct Mater* **2015**, *25* (7), 1074–1081. https://doi.org/10.1002/adfm.201401919.

(79) Geiger, S.; Kasian, O.; Mingers, A. M.; Mayrhofer, K. J. J.; Cherevko, S. Stability Limits of Tin-Based Electrocatalyst Supports. *Scientific Reports 2017 7:1* **2017**, *7* (1), 1–7. https://doi.org/10.1038/s41598-017-04079-9.

(80) da Silva, G. C.; Venturini, S. I.; Zhang, S.; Löffler, M.; Scheu, C.; Mayrhofer, K. J. J.; Ticianelli, E. A.; Cherevko, S. Oxygen Evolution Reaction on Tin Oxides Supported Iridium Catalysts: Do We Need Dopants? *ChemElectroChem* **2020**, *7* (10), 2330–2339. https://doi.org/10.1002/CELC.202000391.

(81) Abbou, S.; Martin, V.; Claudel, F.; Sola, L.; Beauger, C.; Dubau, L.; Maillard, ric. Manipulating the Corrosion Resistance of SnO_2 Aerogels through Doping for Efficient and Durable Oxygen Evolution Reaction Electrocatalysis in Acidic Media. **2024**. https://doi.org/10.1021/acscatal.0c01084.

(82) Rajan, Z. S. H. S.; Binninger, T.; Kooyman, P. J.; Susac, D.; Mohamed, R. Organometallic Chemical Deposition of Crystalline Iridium Oxide Nanoparticles on Antimony-Doped Tin Oxide Support with High-Performance for the Oxygen Evolution Reaction. *Catal Sci Technol* **2020**, *10* (12), 3938–3948. https://doi.org/10.1039/D0CY00470G.

(83) Böhm, D.; Beetz, M.; Schuster, M.; Peters, K.; Hufnagel, A. G.; Döblinger, M.; Böller, B.; Bein, T.; Fattakhova-Rohlfing, D. Efficient OER Catalyst with Low Ir Volume Density Obtained by Homogeneous Deposition of Iridium Oxide Nanoparticles on Macroporous Antimony-Doped Tin Oxide Support. *Adv Funct Mater* **2020**, *30* (1). https://doi.org/10.1002/ADFM.201906670.

(84) Khan, I. A.; Morgen, P.; Gyergyek, S.; Sharma, R.; Andersen, S. M. Selection on Antimony-Doped Tin Oxide (ATO) as an Efficient Support for Iridium-Based Oxygen Evolution Reaction (OER) Catalyst in Acidic Media. *Mater Chem Phys* **2023**, *308*, 128192. https://doi.org/10.1016/j.matchemphys.2023.128192.

(85) Puthiyapura, V. K.; Mamlouk, M.; Pasupathi, S.; Pollet, B. G.; Scott, K. Physical and Electrochemical Evaluation of ATO Supported IrO_2 Catalyst for Proton Exchange Membrane Water Electrolyser. *J Power Sources* **2014**, *269*, 451–460. https://doi.org/10.1016/j.jpowsour.2014.06.078.

(86) Han, B.; Risch, M.; Belden, S.; Lee, S.; Bayer, D.; Mutoro, E.; Shao-Horn, Y. Screening Oxide Support Materials for OER Catalysts in Acid. *J Electrochem Soc* **2018**, *165* (10), F813–F820. https://doi.org/10.1149/2.0921810jes.

(87) Oh, H.-S.; Nong, H. N.; Reier, T.; Bergmann, A.; Gliech, M.; Ferreira de Araújo, J.; Willinger, E.; Schlögl, R.; Teschner, D.; Strasser, P. Electrochemical Catalyst–Support Effects and Their Stabilizing Role for IrO_x Nanoparticle Catalysts during the Oxygen

Evolution Reaction. *J Am Chem Soc* **2016**, *138* (38), 12552–12563. https://doi.org/10.1021/jacs.6b07199.

(88) Ferreira da Silva, C. D.; Claudel, F.; Martin, V.; Chattot, R.; Abbou, S.; Kumar, K.; Jiménez-Morales, I.; Cavaliere, S.; Jones, D.; Rozière, J.; Solà-Hernandez, L.; Beauger, C.; Faustini, M.; Peron, J.; Gilles, B.; Encinas, T.; Piccolo, L.; Barros de Lima, F. H.; Dubau, L.; Maillard, F. Oxygen Evolution Reaction Activity and Stability Benchmarks for Supported and Unsupported IrO_x Electrocatalysts. *ACS Catal* **2021**, *11* (7), 4107–4116. https://doi.org/10.1021/acscatal.0c04613.

(89) Cognard, G.; Ozouf, G.; Beauger, C.; Dubau, L.; López-Haro, M.; Chatenet, M.; Maillard, F. Insights into the Stability of Pt Nanoparticles Supported on Antimony-Doped Tin Oxide in Different Potential Ranges. *Electrochim Acta* **2017**, *245*, 993–1004. https://doi.org/10.1016/J.ELECTACTA.2017.05.178.

(90) Deutschmann, O.; Knözinger, H.; Kochloefl, K.; Turek, T. Heterogeneous Catalysis and Solid Catalysts. In *Ullmann's Encyclopedia of Industrial Chemistry*; Wiley-VCH Verlag GmbH & Co. KGaA: Weinheim, Germany, 2009. https://doi.org/10.1002/14356007.a05_313.pub2.

(91) Collantes Jiménez, P.; Sievers, G.; Quade, A.; Brüser, V.; Pittkowski, R. K.; Arenz, M. Gas Diffusion Electrode Activity Measurements of Iridium-Based Self-Supported Catalysts Produced by Alternated Physical Vapour Deposition. *J Power Sources* **2023**, *569*, 232990. https://doi.org/10.1016/j.jpowsour.2023.232990.

(92) Hou, Y.; Bolat, S.; Bornet, A.; Romanyuk, Y. E.; Guo, H.; Moreno-García, P.; Zelocualtecatl Montiel, I.; Lai, Z.; Müller, U.; Grozovski, V.; Broekmann, P. Photonic Curing: Activation and Stabilization of Metal Membrane Catalysts (MMCs) for the Electrochemical Reduction of CO_2. *ACS Catal* **2019**, *9* (10), 9518–9529. https://doi.org/10.1021/acscatal.9b03664.

(93) Gálvez-Vázquez, M. de J.; Xu, H. B.; Moreno-García, P. A.; Hou, Y. A.; Hu, H. A.; Wiley, B. J.; Vesztergom, S.; Broekmann, P. Unwrap Them First: Operando Potential- Induced Activation Is Required When Using PVP-Capped Ag Nanocubes as Catalysts of CO_2 Electroreduction. *Chimia (Aarau)* **2021**, *75* (3), 163. https://doi.org/10.2533/chimia.2021.163.

(94) Quinson, J.; Neumann, S.; Wannmacher, T.; Kacenauskaite, L.; Inaba, M.; Bucher, J.; Bizzotto, F.; Simonsen, S. B.; Theil Kuhn, L.; Bujak, D.; Zana, A.; Arenz, M.; Kunz, S. Colloids for Catalysts: A Concept for the Preparation of Superior Catalysts of Industrial Relevance. *Angewandte Chemie International Edition* **2018**, *57* (38), 12338–12341. https://doi.org/10.1002/anie.201807450.

(95) Quinson, J. Colloidal Surfactant-Free Syntheses of Precious Metal Nanoparticles for Electrocatalysis. *Curr Opin Electrochem* **2022**, *34*, 100977. https://doi.org/10.1016/j.coelec.2022.100977.

(96) Bizzotto, F.; Arenz, M.; Quinson, J. Surfactant-Free Ir Nanoparticles Synthesized in Ethanol: Catalysts for the Oxygen Evolution Reaction. *Mater Lett* **2022**, *308*, 131209. https://doi.org/10.1016/J.MATLET.2021.131209.

(97) Silva, H.; Hernandez-Fernandez, P.; Baden, A. K.; Hellstern, H. L.; Kovyakh, A.; Wisaeus, E.; Smitshuysen, T.; Chorkendorff, I.; Christensen, L. H.; Chakraborty, D.; Kallesøe, C. Supercritical Flow Synthesis of PtPdFe Alloyed Nanoparticles with Enhanced Low-

Temperature Activity and Thermal Stability for Propene Oxidation under Lean Exhaust Gas Conditions. *Catal Sci Technol* **2019**, *9* (23), 6691–6699. https://doi.org/10.1039/C9CY00634F.

(98) Kallesøe, C.; Clausen, H. F.; Christensen, L. H. METHOD OF PREPARING A CATALYST STRUCTURE. Patent WO 2015/104025 A1. July 26, 2015.

(99) Williams, D. B.; Carter, C. B. *Transmission Electron Microscopy*; Springer US: Boston, MA, 2009. https://doi.org/10.1007/978-0-387-76501-3.

(100) Zhou, W.; Apkarian, R.; Wang, Z. L.; Joy, D. Fundamentals of Scanning Electron Microscopy (SEM). In *Scanning Microscopy for Nanotechnology*; Zhou, W., Wang, Z. L., Eds.; Springer New York: New York, NY, 2006; pp 1–40. https://doi.org/10.1007/978-0-387-39620-0_1.

(101) Rahaman, M.; Dutta, A.; Zanetti, A.; Broekmann, P. Electrochemical Reduction of CO_2 into Multicarbon Alcohols on Activated Cu Mesh Catalysts: An Identical Location (IL) Study. *ACS Catal* **2017**, *7* (11), 7946–7956. https://doi.org/10.1021/acscatal.7b02234.

(102) Schlögl, K.; Mayrhofer, K. J. J.; Hanzlik, M.; Arenz, M. Identical-Location TEM Investigations of Pt/C Electrocatalyst Degradation at Elevated Temperatures. *Journal of Electroanalytical Chemistry* **2011**, *662* (2), 355–360. https://doi.org/10.1016/j.jelechem.2011.09.003.

(103) Hou, Y.; Kovács, N.; Xu, H.; Sun, C.; Erni, R.; Gálvez-Vázquez, M. de J.; Rieder, A.; Hu, H.; Kong, Y.; Liu, M.; Wiley, B. J.; Vesztergom, S.; Broekmann, P. Limitations of Identical Location SEM as a Method of Degradation Studies on Surfactant Capped Nanoparticle Electrocatalysts. *J Catal* **2021**, *394*, 58–66. https://doi.org/10.1016/j.jcat.2020.12.006.

(104) Abd Mutalib, M.; Rahman, M. A.; Othman, M. H. D.; Ismail, A. F.; Jaafar, J. Scanning Electron Microscopy (SEM) and Energy-Dispersive X-Ray (EDX) Spectroscopy. In *Membrane Characterization*; Elsevier, 2017; pp 161–179. https://doi.org/10.1016/B978-0-444-63776-5.00009-7.

(105) Loganathan, S.; Valapa, R. B.; Mishra, R. K.; Pugazhenthi, G.; Thomas, S. Thermogravimetric Analysis for Characterization of Nanomaterials. In *Thermal and Rheological Measurement Techniques for Nanomaterials Characterization*; Elsevier, 2017; Vol. 3, pp 67–108. https://doi.org/10.1016/B978-0-323-46139-9.00004-9.

(106) Sedigh Rahimabadi, P.; Khodaei, M.; Koswattage, K. R. Review on Applications of Synchrotron-based X-ray Techniques in Materials Characterization. *X-Ray Spectrometry* **2020**, *49* (3), 348–373. https://doi.org/10.1002/xrs.3141.

(107) Ingham, B. X-Ray Scattering Characterisation of Nanoparticles. *Crystallogr Rev* **2015**, *21* (4), 229–303. https://doi.org/10.1080/0889311X.2015.1024114.

(108) Bharti, A.; Goyal, N. Fundamental of Synchrotron Radiations. In *Synchrotron Radiation - Useful and Interesting Applications*; Joseph, D., Ed.; IntechOpen: Rijeka, 2019. https://doi.org/10.5772/intechopen.82202.

(109) Binninger, T.; Garganourakis, M.; Han, J.; Patru, A.; Fabbri, E.; Sereda, O.; Kötz, R.; Menzel, A.; Schmidt, T. J. Particle-Support Interferences in Small-Angle X-Ray Scattering from Supported-Catalyst Materials. *Phys Rev Appl* **2015**, *3* (2), 024012. https://doi.org/10.1103/PhysRevApplied.3.024012.

(110) Proffen, Th.; Billinge, S. J. L.; Egami, T.; Louca, D. Structural Analysis of Complex Materials Using the Atomic Pair Distribution Function — a Practical Guide. *Z Kristallogr Cryst Mater* **2003**, *218* (2), 132–143. https://doi.org/10.1524/zkri.218.2.132.20664.
(111) Gu, L.; Zhang, Y.; Kong, Q.; Yang, C. Synchrotron X-ray Characterization Techniques for the Development of Aqueous Zinc Ion Batteries. *ChemElectroChem* **2024**. https://doi.org/10.1002/celc.202300602.
(112) Billinge, S. J. L.; Levin, I. The Problem with Determining Atomic Structure at the Nanoscale. *Science (1979)* **2007**, *316* (5824), 561–565. https://doi.org/10.1126/science.1135080.
(113) Thomas, R. A Beginner's Guide to ICP-MS, Part I. *Spectroscopy* **2001**, *16* (4), 38–42.
(114) Kim, Y.-T.; Lopes, P. P.; Park, S.-A.; Lee, A.-Y.; Lim, J.; Lee, H.; Back, S.; Jung, Y.; Danilovic, N.; Stamenkovic, V.; Erlebacher, J.; Snyder, J.; Markovic, N. M. Balancing Activity, Stability and Conductivity of Nanoporous Core-Shell Iridium/Iridium Oxide Oxygen Evolution Catalysts. *Nat Commun* **2017**, *8* (1), 1449. https://doi.org/10.1038/s41467-017-01734-7.
(115) Geiger, S.; Kasian, O.; Ledendecker, M.; Pizzutilo, E.; Mingers, A. M.; Fu, W. T.; Diaz-Morales, O.; Li, Z.; Oellers, T.; Fruchter, L.; Ludwig, A.; Mayrhofer, K. J. J.; Koper, M. T. M.; Cherevko, S. The Stability Number as a Metric for Electrocatalyst Stability Benchmarking. *Nat Catal* **2018**, *1* (7), 508–515. https://doi.org/10.1038/s41929-018-0085-6.
(116) Campanella, B.; Palleschi, V.; Legnaioli, S. Introduction to Vibrational Spectroscopies. *ChemTexts* **2021**, *7* (1), 5. https://doi.org/10.1007/s40828-020-00129-4.
(117) Akash, M. S. H.; Rehman, K. Introduction to Chromatographic Techniques. In *Essentials of Pharmaceutical Analysis*; Akash, M. S. H., Rehman, K., Eds.; Springer Nature Singapore: Singapore, 2020; pp 147–156. https://doi.org/10.1007/978-981-15-1547-7_11.
(118) Zlatar, M.; Escalera-López, D.; Rodríguez, M. G.; Hrbek, T.; Götz, C.; Mary Joy, R.; Savan, A.; Tran, H. P.; Nong, H. N.; Pobedinskas, P.; Briega-Martos, V.; Hutzler, A.; Böhm, T.; Haenen, K.; Ludwig, A.; Khalakhan, I.; Strasser, P.; Cherevko, S. Standardizing OER Electrocatalyst Benchmarking in Aqueous Electrolytes: Comprehensive Guidelines for Accelerated Stress Tests and Backing Electrodes. *ACS Catal* **2023**, *13* (23), 15375–15392. https://doi.org/10.1021/acscatal.3c03880.
(119) Ehelebe, K.; Schmitt, N.; Sievers, G.; Jensen, A. W.; Hrnjić, A.; Collantes Jiménez, P.; Kaiser, P.; Geuß, M.; Ku, Y.-P.; Jovanovič, P.; Mayrhofer, K. J. J.; Etzold, B.; Hodnik, N.; Escudero-Escribano, M.; Arenz, M.; Cherevko, S. Benchmarking Fuel Cell Electrocatalysts Using Gas Diffusion Electrodes: Inter-Lab Comparison and Best Practices. *ACS Energy Lett* **2022**, *7* (2), 816–826. https://doi.org/10.1021/acsenergylett.1c02659.
(120) Wang, R.; Jiang, W.; Xia, D.; Liu, T.; Gan, L. Improving the Wettability of Thin-Film Rotating Disk Electrodes for Reliable Activity Evaluation of Oxygen Electrocatalysts by Triggering Oxygen Reduction at the Catalyst-Electrolyte-Bubble Triple Phase Boundaries. *J Electrochem Soc* **2018**, *165* (7), F436–F440. https://doi.org/10.1149/2.0371807jes.

(121) Karimi, V.; Sharma, R.; Morgen, P.; Andersen, S. M. Multiple Bubble Removal Strategies to Promote Oxygen Evolution Reaction: Mechanistic Understandings from Orientation, Rotation, and Sonication Perspectives. *ACS Appl Mater Interfaces* **2023**, *15* (42), 49233–49245. https://doi.org/10.1021/acsami.3c11290.

(122) McCrory, C. C. L.; Jung, S.; Peters, J. C.; Jaramillo, T. F. Benchmarking Heterogeneous Electrocatalysts for the Oxygen Evolution Reaction. *J Am Chem Soc* **2013**, *135* (45), 16977–16987. https://doi.org/10.1021/ja407115p.

(123) Spöri, C.; Kwan, J. T. H.; Bonakdarpour, A.; Wilkinson, D. P.; Strasser, P. The Stability Challenges of Oxygen Evolving Catalysts: Towards a Common Fundamental Understanding and Mitigation of Catalyst Degradation. *Angewandte Chemie International Edition* **2017**, *56* (22), 5994–6021. https://doi.org/10.1002/anie.201608601.

(124) Alia, S. M.; Danilovic, N. Rotating Disk Electrode Standardization and Best Practices in Acidic Oxygen Evolution for Low-Temperature Electrolysis. *Front Energy Res* **2022**, *10*. https://doi.org/10.3389/fenrg.2022.857663.

(125) Edgington, J.; Deberghes, A.; C. Seitz, L. Glassy Carbon Substrate Oxidation Effects on Electrode Stability for Oxygen Evolution Reaction Catalysis Stability Benchmarking. *ACS Appl Energy Mater* **2022**, *5* (10), 12206–12218. https://doi.org/10.1021/acsaem.2c01690.

(126) Spöri, C.; Brand, C.; Kroschel, M.; Strasser, P. Accelerated Degradation Protocols for Iridium-Based Oxygen Evolving Catalysts in Water Splitting Devices. *J Electrochem Soc* **2021**, *168* (3), 034508. https://doi.org/10.1149/1945-7111/abeb61.

(127) Arminio-Ravelo, J. A.; Quinson, J.; Pedersen, M. A.; Kirkensgaard, J. J. K.; Arenz, M.; Escudero-Escribano, M. Synthesis of Iridium Nanocatalysts for Water Oxidation in Acid: Effect of the Surfactant. *ChemCatChem* **2020**, *12* (5), 1282–1287. https://doi.org/10.1002/cctc.201902190.

(128) Arminio-Ravelo, J. A.; Jensen, A. W.; Jensen, K. D.; Quinson, J.; Escudero-Escribano, M. Electrolyte Effects on the Electrocatalytic Performance of Iridium-Based Nanoparticles for Oxygen Evolution in Rotating Disc Electrodes. *ChemPhysChem* **2019**, *20* (22), 2956–2963. https://doi.org/10.1002/cphc.201900902.

(129) Bernt, M.; Hartig-Weiß, A.; Tovini, M. F.; El-Sayed, H. A.; Schramm, C.; Schröter, J.; Gebauer, C.; Gasteiger, H. A. Current Challenges in Catalyst Development for PEM Water Electrolyzers. *Chem Ing Tech* **2020**, *92* (1–2), 31–39. https://doi.org/10.1002/CITE.201900101.

(130) Knöppel, J.; Möckl, M.; Escalera-López, D.; Stojanovski, K.; Bierling, M.; Böhm, T.; Thiele, S.; Rzepka, M.; Cherevko, S. On the Limitations in Assessing Stability of Oxygen Evolution Catalysts Using Aqueous Model Electrochemical Cells. *Nature Communications 2021 12:1* **2021**, *12* (1), 1–9. https://doi.org/10.1038/s41467-021-22296-9.

(131) Cherevko, S.; Katsounaros, I. And yet It Rotates! *Nat Catal* **2024**, *7* (1), 10–11. https://doi.org/10.1038/s41929-023-01100-5.

(132) Geiger, S.; Kasian, O.; Mingers, A. M.; Nicley, S. S.; Haenen, K.; Mayrhofer, K. J. J.; Cherevko, S. Catalyst Stability Benchmarking for the Oxygen Evolution Reaction: The Importance of Backing Electrode Material and Dissolution in Accelerated Aging Studies. *ChemSusChem* **2017**, *10* (21), 4140–4143. https://doi.org/10.1002/cssc.201701523.

(133) Petzoldt, P. J.; Kwan, J. T. H.; Bonakdarpour, A.; Wilkinson, D. P. Deconvoluting Reversible and Irreversible Degradation Phenomena in OER Catalyst Coated Membranes Using a Modified RDE Technique. *J Electrochem Soc* **2021**, *168* (2), 026507. https://doi.org/10.1149/1945-7111/abde7d.

(134) Murawski, J.; Scott, S. B.; Rao, R.; Rigg, K.; Zalitis, C.; Stevens, J.; Sharman, J.; Hinds, G.; Stephens, I. E. L. Benchmarking Stability of Iridium Oxide in Acidic Media under Oxygen Evolution Conditions: A Review: Part I. *Johnson Matthey Technology Review* **2024**, *68* (1), 121–146. https://doi.org/10.1595/205651323X16848455435118.

(135) Murawski, J.; Scott, S. B.; Rao, R.; Rigg, K.; Zalitis, C.; Stevens, J.; Sharman, J.; Hinds, G.; Stephens, I. E. L. Benchmarking Stability of Iridium Oxide in Acidic Media under Oxygen Evolution Conditions: A Review: Part II. *Johnson Matthey Technology Review* **2024**, *68* (1), 147–160. https://doi.org/10.1595/205651324X17055018154113.

(136) Tovini, M. F.; Hartig-Weiß, A.; Gasteiger, H. A.; El-Sayed, H. A. The Discrepancy in Oxygen Evolution Reaction Catalyst Lifetime Explained: RDE vs MEA - Dynamicity within the Catalyst Layer Matters. *J Electrochem Soc* **2021**, *168* (1), 014512. https://doi.org/10.1149/1945-7111/ABDCC9.

(137) Lazaridis, T.; Stühmeier, B. M.; Gasteiger, H. A.; El-Sayed, H. A. Capabilities and Limitations of Rotating Disk Electrodes versus Membrane Electrode Assemblies in the Investigation of Electrocatalysts. *Nature Catalysis 2022 5:5* **2022**, *5* (5), 363–373. https://doi.org/10.1038/s41929-022-00776-5.

(138) El-Sayed, H. A.; Weiß, A.; Olbrich, L. F.; Putro, G. P.; Gasteiger, H. A. OER Catalyst Stability Investigation Using RDE Technique: A Stability Measure or an Artifact? *J Electrochem Soc* **2019**, *166* (8), F458–F464. https://doi.org/10.1149/2.0301908jes.

(139) Trogisch, N.; Koch, M.; El Sawy, E. N.; El-Sayed, H. A. Microscopic Bubble Accumulation: The Missing Factor in Evaluating Oxygen Evolution Catalyst Stability during Accelerated Stress Tests. *ACS Catal* **2022**, *12* (21), 13715–13724. https://doi.org/10.1021/acscatal.2c03881.

(140) Edgington, J.; Seitz, L. C. Advancing the Rigor and Reproducibility of Electrocatalyst Stability Benchmarking and Intrinsic Material Degradation Analysis for Water Oxidation. *ACS Catal* **2023**, *13* (5), 3379–3394. https://doi.org/10.1021/acscatal.2c06282.

(141) Yi, Y.; Weinberg, G.; Prenzel, M.; Greiner, M.; Heumann, S.; Becker, S.; Schlögl, R. Electrochemical Corrosion of a Glassy Carbon Electrode. **2017**. https://doi.org/10.1016/j.cattod.2017.07.013.

(142) Cherevko, S.; Zeradjanin, A. R.; Topalov, A. A.; Kulyk, N.; Katsounaros, I.; Mayrhofer, K. J. J. Dissolution of Noble Metals during Oxygen Evolution in Acidic Media. *ChemCatChem* **2014**, *6* (8), 2219–2223. https://doi.org/10.1002/cctc.201402194.

(143) Zheng, Y.-R.; Vernieres, J.; Wang, Z.; Zhang, K.; Hochfilzer, D.; Krempl, K.; Liao, T.-W.; Presel, F.; Altantzis, T.; Fatermans, J.; Scott, S. B.; Secher, N. M.; Moon, C.; Liu, P.; Bals, S.; Van Aert, S.; Cao, A.; Anand, M.; Nørskov, J. K.; Kibsgaard, J.; Chorkendorff, I. Monitoring Oxygen Production on Mass-Selected Iridium–Tantalum Oxide Electrocatalysts. *Nat Energy* **2021**, *7* (1), 55–64. https://doi.org/10.1038/s41560-021-00948-w.

(144) Benck, J. D.; Pinaud, B. A.; Gorlin, Y.; Jaramillo, T. F. Substrate Selection for Fundamental Studies of Electrocatalysts and Photoelectrodes: Inert Potential Windows in Acidic,

Neutral, and Basic Electrolyte. *PLoS One* **2014**, *9* (10), e107942. https://doi.org/10.1371/journal.pone.0107942.

(145) Fabbri, E.; Habereder, A.; Waltar, K.; Kötz, R.; Schmidt, T. J. Developments and Perspectives of Oxide-Based Catalysts for the Oxygen Evolution Reaction. *Catal. Sci. Technol.* **2014**, *4* (11), 3800–3821. https://doi.org/10.1039/C4CY00669K.

(146) Hartig-Weiss, A.; Tovini, M. F.; Gasteiger, H. A.; El-Sayed, H. A. OER Catalyst Durability Tests Using the Rotating Disk Electrode Technique: The Reason Why This Leads to Erroneous Conclusions. *ACS Appl Energy Mater* **2020**, *3* (11), 10323–10327. https://doi.org/10.1021/acsaem.0c01944.

(147) Scott, S. B.; Sørensen, J. E.; Rao, R. R.; Moon, C.; Kibsgaard, J.; Shao-Horn, Y.; Chorkendorff, I. The Low Overpotential Regime of Acidic Water Oxidation Part II: Trends in Metal and Oxygen Stability Numbers. *Energy Environ Sci* **2022**, *15* (5), 1988–2001. https://doi.org/10.1039/D1EE03915F.

(148) Chen, Y.; Li, H.; Wang, J.; Du, Y.; Xi, S.; Sun, Y.; Sherburne, M.; Ager, J. W.; Fisher, A. C.; Xu, Z. J. Exceptionally Active Iridium Evolved from a Pseudo-Cubic Perovskite for Oxygen Evolution in Acid. *Nat Commun* **2019**, *10* (1), 572. https://doi.org/10.1038/s41467-019-08532-3.

(149) Zdunek, A. D.; Selman, J. R. A Novel Rotating Disk Electrode Cell Design: The Inverted Rotating Disk Electrode. *J Electrochem Soc* **1992**, *139* (9), 2549–2551. https://doi.org/10.1149/1.2221261.

(150) Bressers, P. M. M. C.; Kelly, J. J. A New Cell Design for the Inverted Rotating Disk Electrode. *J Electrochem Soc* **1995**, *142* (7), L114–L115. https://doi.org/10.1149/1.2044331.

(151) Bradley, P. E.; Landolt, D. New Cell Design for Inverted Rotating Disk Electrode. *J Electrochem Soc* **1997**, *144* (6), L145–L148. https://doi.org/10.1149/1.1837705.

(152) Parys, H. Van; Tourwé, E.; Breugelmans, T.; Depauw, M.; Deconinck, J.; Hubin, A. Modeling of Mass and Charge Transfer in an Inverted Rotating Disk Electrode (IRDE) Reactor. *Journal of Electroanalytical Chemistry* **2008**, *622* (1), 44–50. https://doi.org/10.1016/j.jelechem.2008.05.004.

(153) Moreno-García, P.; Kovács, N.; Grozovski, V.; Gálvez-Vázquez, M. de J.; Vesztergom, S.; Broekmann, P. Toward CO_2 Electroreduction under Controlled Mass Flow Conditions: A Combined Inverted RDE and Gas Chromatography Approach. *Anal Chem* **2020**, *92* (6), 4301–4308. https://doi.org/10.1021/acs.analchem.9b04999.

(154) Saibi, R.; Punathil Meethal, R.; Srinivasan, R. Mechanistic Analysis of Hydrogen Evolution Reaction on Pt in $HClO_4$ Using Inverted Rotating Disc Electrode. *Electroanalysis* **2020**, *32* (11), 2545–2554. https://doi.org/10.1002/elan.202060032.

(155) Mairhofer, K.; Rosenauer, P.; Nelhiebel, M.; Radl, S.; Larisegger, S.; Fafilek, G. An Inherently Leakage-Free Inverted Rotating Disk Electrode (IRDE) Design. *Journal of Electroanalytical Chemistry* **2022**, *917*, 116392. https://doi.org/10.1016/j.jelechem.2022.116392.

(156) Moreno-García, P.; Grozovski, V.; Vázquez, M. de J. G.; Mysuru, N.; Kiran, K.; Kovács, N.; Hou, Y.; Vesztergom, S.; Broekmann, P. Inverted RDE (IRDE) as Novel Test Bed for Studies on Additive-Assisted Metal Deposition under Gas-Evolution Conditions. *J Electrochem Soc* **2020**, *167* (4), 042503. https://doi.org/10.1149/1945-7111/ab7984.

(157) Liu, Y.; Webb, S.; Moreno-García, P.; Kulkarni, A.; Maroni, P.; Broekmann, P.; Milton, R. D. Facile Functionalization of Carbon Electrodes for Efficient Electroenzymatic Hydrogen Production. *JACS Au* **2023**, *3* (1), 124–130. https://doi.org/10.1021/jacsau.2c00551.

(158) Riasse, R.; Lafforgue, C.; Vandenberghe, F.; Micoud, F.; Morin, A.; Arenz, M.; Durst, J.; Chatenet, M. Benchmarking Proton Exchange Membrane Fuel Cell Cathode Catalyst at High Current Density: A Comparison between the Rotating Disk Electrode, the Gas Diffusion Electrode and Differential Cell. *J Power Sources* **2023**, *556*, 232491. https://doi.org/10.1016/j.jpowsour.2022.232491.

(159) Wiberg, G. K. H.; Fleige, M.; Arenz, M. Gas Diffusion Electrode Setup for Catalyst Testing in Concentrated Phosphoric Acid at Elevated Temperatures. *Review of Scientific Instruments* **2015**, *86* (2), 024102. https://doi.org/10.1063/1.4908169.

(160) Schröder, J.; Mints, V. A.; Bornet, A.; Berner, E.; Fathi Tovini, M.; Quinson, J.; Wiberg, G. K. H.; Bizzotto, F.; El-Sayed, H. A.; Arenz, M. The Gas Diffusion Electrode Setup as Straightforward Testing Device for Proton Exchange Membrane Water Electrolyzer Catalysts. *JACS Au* **2021**, *1* (3), 247–251. https://doi.org/10.1021/jacsau.1c00015.

(161) Wiberg, G. K. H.; Nösberger, S.; Arenz, M. Evolution of a GDE Setup: Beyond Ambient Conditions. *Curr Opin Electrochem* **2022**, *36*, 101129. https://doi.org/10.1016/j.coelec.2022.101129.

(162) Ehelebe, K.; Knöppel, J.; Bierling, M.; Mayerhöfer, B.; Böhm, T.; Kulyk, N.; Thiele, S.; Mayrhofer, K. J. J.; Cherevko, S. Platinum Dissolution in Realistic Fuel Cell Catalyst Layers. *Angewandte Chemie International Edition* **2021**, *60* (16), 8882–8888. https://doi.org/10.1002/anie.202014711.

(163) Geuß, M.; Milosevic, M.; Bierling, M.; Löttert, L.; Abbas, D.; Escalera-López, D.; Lloret, V.; Ehelebe, K.; Mayrhofer, K. J. J.; Thiele, S.; Cherevko, S. Investigation of Iridium-Based OER Catalyst Layers in a GDE Half-Cell Setup: Opportunities and Challenges. *J Electrochem Soc* **2023**, *170* (11), 114510. https://doi.org/10.1149/1945-7111/ad07ac.

(164) Ehelebe, K.; Seeberger, D.; Paul, M. T. Y.; Thiele, S.; Mayrhofer, K. J. J.; Cherevko, S. Evaluating Electrocatalysts at Relevant Currents in a Half-Cell: The Impact of Pt Loading on Oxygen Reduction Reaction. *J Electrochem Soc* **2019**, *166* (16), F1259–F1268. https://doi.org/10.1149/2.0911915jes.

(165) Loukrakpam, R.; Gomes, B. F.; Prokop, M.; Bauer, C.; Kutter, M.; Baier, F.; Kempe, R.; Roth, C. Challenges and Limitations of Accelerated Stress Testing in GDE Half-Cell Set-Ups. *J Power Sources* **2023**, *569*, 232905. https://doi.org/10.1016/j.jpowsour.2023.232905.

(166) Junge Puring, K.; Siegmund, D.; Timm, J.; Möllenbruck, F.; Schemme, S.; Marschall, R.; Apfel, U. Electrochemical CO_2 Reduction: Tailoring Catalyst Layers in Gas Diffusion Electrodes. *Adv Sustain Syst* **2021**, *5* (1). https://doi.org/10.1002/adsu.202000088.

(167) Xing, Z.; Hu, X.; Feng, X. Tuning the Microenvironment in Gas-Diffusion Electrodes Enables High-Rate CO_2 Electrolysis to Formate. *ACS Energy Lett* **2021**, *6* (5), 1694–1702. https://doi.org/10.1021/acsenergylett.1c00612.

(168) Kong, Y.; Hu, H.; Liu, M.; Hou, Y.; Kolivoška, V.; Vesztergom, S.; Broekmann, P. Visualisation and Quantification of Flooding Phenomena in Gas Diffusion Electrodes Used for Electrochemical CO_2 Reduction: A Combined EDX/ICP–MS Approach. *J Catal* **2022**, *408*, 1–8. https://doi.org/10.1016/j.jcat.2022.02.014.

(169) Collantes Jiménez, P.; Wiberg, G. K. H.; Sievers, G. W.; Brüser, V.; Arenz, M. Bridging the Gap between Basic Research and Application: A Half-Cell Setup for High Current Density Measurements of Ir-Based Oxygen Evolution Reaction Catalysts on Porous Transport Electrodes. *J Mater Chem A Mater* **2023**, *11* (37), 20129–20138. https://doi.org/10.1039/D3TA04136K.

(170) Yarlagadda, V.; McKinney, S. E.; Keary, C. L.; Thompson, L.; Zulevi, B.; Kongkanand, A. Preparation of PEMFC Electrodes from Milligram-Amounts of Catalyst Powder. *J Electrochem Soc* **2017**, *164* (7), F845–F849. https://doi.org/10.1149/2.1461707jes.

(171) Eastwood, B. J.; Christensen, P. A.; Armstrong, R. D.; Bates, N. R. Electrochemical Oxidation of a Carbon Black Loaded Polymer Electrode in Aqueous Electrolytes. *Journal of Solid State Electrochemistry* **1999**, *3* (4), 179–186. https://doi.org/10.1007/s100080050145.

(172) Alia, S. M.; Anderson, G. C. Iridium Oxygen Evolution Activity and Durability Baselines in Rotating Disk Electrode Half-Cells. *J Electrochem Soc* **2019**, *166* (4), F282–F294. https://doi.org/10.1149/2.0731904jes.

(173) Huang, Y. S.; Lin, S. S.; Huang, C. R.; Lee, M. C.; Dann, T. E.; Chien, F. Z. Raman Spectrum of IrO_2. *Solid State Commun* **1989**, *70* (5), 517–522. https://doi.org/10.1016/0038-1098(89)90942-3.

(174) Li, C.-Y.; Dong, J.-C.; Jin, X.; Chen, S.; Panneerselvam, R.; Rudnev, A. V.; Yang, Z.-L.; Li, J.-F.; Wandlowski, T.; Tian, Z.-Q. In Situ Monitoring of Electrooxidation Processes at Gold Single Crystal Surfaces Using Shell-Isolated Nanoparticle-Enhanced Raman Spectroscopy. *J Am Chem Soc* **2015**, *137* (24), 7648–7651. https://doi.org/10.1021/jacs.5b04670.

(175) Cihlar, J.; Navarro, L. K. T.; Cihlar, J.; Kasparek, V.; Michalicka, J.; Castkova, K.; Lazar, I.; Kastyl, J.; Celko, L.; Vesely, M.; Dzik, P. Influence of Substituted Acetic Acids on "Bridge" Synthesis of Highly Photocatalytic Active Heterophase TiO_2 in Hydrogen Production. *J Solgel Sci Technol* **2023**, *105* (2), 471–488. https://doi.org/10.1007/s10971-022-06011-8.

(176) Zeradjanin, A. R.; Narangoda, P.; Spanos, I.; Masa, J.; Schlögl, R. How to Minimise Destabilising Effect of Gas Bubbles on Water Splitting Electrocatalysts? *Curr Opin Electrochem* **2021**, *30*, 100797. https://doi.org/10.1016/j.coelec.2021.100797.

(177) Trasatti, S. Electrocatalysis: Understanding the Success of DSA®. *Electrochim Acta* **2000**, *45* (15–16), 2377–2385. https://doi.org/10.1016/S0013-4686(00)00338-8.

(178) Liu, C.; Shviro, M.; Gago, A. S.; Zaccarine, S. F.; Bender, G.; Gazdzicki, P.; Morawietz, T.; Biswas, I.; Rasinski, M.; Everwand, A.; Schierholz, R.; Pfeilsticker, J.; Müller, M.; Lopes, P. P.; Eichel, R.; Pivovar, B.; Pylypenko, S.; Friedrich, K. A.; Lehnert, W.; Carmo, M. Exploring the Interface of Skin-Layered Titanium Fibers for Electrochemical Water Splitting. *Adv Energy Mater* **2021**, *11* (8), 2002926. https://doi.org/10.1002/aenm.202002926.

(179) Quinson, J.; Kunz, S.; Arenz, M. Beyond Active Site Design: A Surfactant-Free Toolbox Approach for Optimized Supported Nanoparticle Catalysts. *ChemCatChem* **2021**, *13* (7), 1692–1705. https://doi.org/10.1002/CCTC.202001858.

(180) Oh, H.-S.; Nong, H. N.; Reier, T.; Gliech, M.; Strasser, P. Oxide-Supported Ir Nanodendrites with High Activity and Durability for the Oxygen Evolution Reaction in

Acid PEM Water Electrolyzers. *Chem Sci* **2015**, *6* (6), 3321–3328. https://doi.org/10.1039/C5SC00518C.

(181) Iwakura, C.; Tada, H.; Tamura, H. The Anodic Evolution of Oxygen on Iridium Oxide Electrode. *Denki Kagaku oyobi Kogyo Butsuri Kagaku* **1977**, *45* (4), 202–207. https://doi.org/10.5796/kogyobutsurikagaku.45.202.

(182) Parthasarathy, A.; Srinivasan, S.; Appleby, A. J.; Martin, C. R. Temperature Dependence of the Electrode Kinetics of Oxygen Reduction at the Platinum/Nafion® Interface—A Microelectrode Investigation. *J Electrochem Soc* **1992**, *139* (9), 2530–2537. https://doi.org/10.1149/1.2221258.

(183) Banwell, T. C.; Jayakumar, A. Exact Analytical Solution for Current Flow through Diode with Series Resistance. *Electron Lett* **2000**, *36* (4), 291. https://doi.org/10.1049/el:20000301.

(184) Bird, J. *Electrical and Electronic Principles and Technology*, 2nd ed.; Routledge, 2003. https://doi.org/10.4324/9780080472591.

(185) Weiß, A.; Siebel, A.; Bernt, M.; Shen, T.-H.; Tileli, V.; Gasteiger, H. A. Impact of Intermittent Operation on Lifetime and Performance of a PEM Water Electrolyzer. *J Electrochem Soc* **2019**, *166* (8), F487–F497. https://doi.org/10.1149/2.0421908jes.

APPENDIX

In this section, the manuscripts II and III corresponding to Chapters 4 and 5, respectively, are appended along with their respective supporting information. The manuscript I corresponding to Chapter 3 is not included due to its preliminary stage.

MANUSCRIPT II

Aline Bornet, Rebecca Pittkowski, Tobias M. Nielsen, Etienne Berner, Annabelle Maletzko, Johanna Schröder, Jonathan Quinson, Julia Melke, Kirsten M. Ø. Jensen, and Matthias Arenz

Influence of Temperature on the Performance of Carbon- and ATO-supported Oxygen Evolution Reaction Catalysts in a Gas Diffusion Electrode Setup

ACS Catal. **2023**, 13, 7568−7577

https://doi.org/10.1021/acscatal.3c01193

ACS Catalysis

pubs.acs.org/acscatalysis

Research Article

Influence of Temperature on the Performance of Carbon- and ATO-supported Oxygen Evolution Reaction Catalysts in a Gas Diffusion Electrode Setup

Aline Bornet, Rebecca Pittkowski, Tobias M. Nielsen, Etienne Berner, Annabelle Maletzko, Johanna Schröder, Jonathan Quinson, Julia Melke, Kirsten M. Ø. Jensen, and Matthias Arenz*

Cite This: *ACS Catal.* 2023, 13, 7568−7577

Read Online

ACCESS | Metrics & More | Article Recommendations | Supporting Information

ABSTRACT: State-of-the-art industrial electrocatalysts for the oxygen evolution reaction (OER) under acidic conditions are Ir-based. Considering the scarce supply of Ir, it is imperative to use the precious metal as efficiently as possible. In this work, we immobilized ultrasmall Ir and $Ir_{0.4}Ru_{0.6}$ nanoparticles on two different supports to maximize their dispersion. One high-surface-area carbon support serves as a reference but has limited technological relevance due to its lack of stability. The other support, antimony-doped tin oxide (ATO), has been proposed in the literature as a possible better support for OER catalysts. Temperature-dependent measurements performed in a recently developed gas diffusion electrode (GDE) setup reveal that surprisingly the catalysts immobilized on commercial ATO performed worse than their carbon-immobilized counterparts. The measurements suggest that the ATO support deteriorates particularly fast at elevated temperatures.

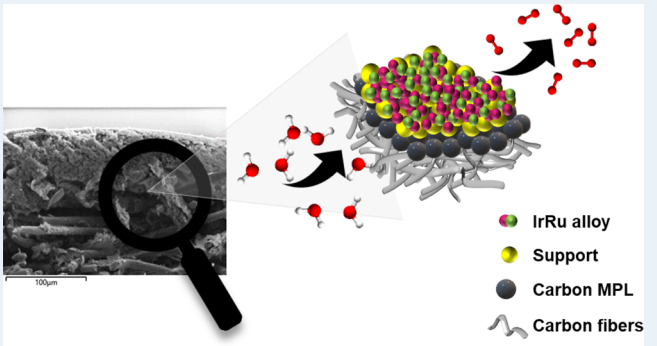

KEYWORDS: *PEM water electrolysis, oxygen evolution reaction, Ir-based nanoparticles, supported OER catalysts, GDE setup*

1. INTRODUCTION

Hydrogen is broadly used in the chemical industry, and as of today, most of it is derived from natural gas. The year 2022 has shown that the large demand for natural gas leads to critical economical dependencies. As an alternative, the production of hydrogen from electrochemical water splitting using renewable energy may be a valuable strategy for a more sustainable future.[1−3] This so-called green hydrogen can be used as a storage solution for surplus energy from renewable sources and thus can help to tackle the challenge of climate change.

Acidic proton exchange membrane water electrolyzers (PEMWEs) constitute an industrially relevant and viable technology for producing green hydrogen. Indeed, they have a compact design, can reach high current densities, and can generate high-pressurized hydrogen of high purity. In the case of energy storage, this green hydrogen can be later used in fuel cells.[1,2,4]

Catalyst development for the oxygen evolution reaction (OER) is one of the key aspects and bottlenecks to permit the PEMWE technology to be implemented at a large scale.[4,5] Despite the high price and the scarcity of Ir and Ru,[4] and although intensive efforts have been made to alleviate the need for these critical raw materials (CRMs),[6−11] Ir- and IrRu-based catalysts remain the state-of-the-art materials for the acidic OER.[12] Several approaches have been considered in order to reduce the use of CRMs in catalysts for the acidic OER. However, it is important to note that to be commercially viable, this CRM reduction needs to be calculated with respect to the converted power (hydrogen) and not only with respect to the catalyst composition. Therefore, an important strategy to maximize the dispersion (surface-to-mass ratio) of the CRMs is to tune the particle size and morphology of the Ir and/or Ru on the nanoscale. In the literature, many examples of this strategy can be found, *e.g.*, designing tailored shapes such as nanoparticles (NPs),[13−15] nanowires,[16,17] and nanodendrides[18] or hollow structures like nanoframes,[19] and nanoporous networks.[20] Another strategy to increase their mass-related activity is to introduce other non-noble elements, typically transition metals such as Co, Ni, and Cu.[21−24] Such multimetallic materials can be found in the form of core−shell structures,[24] alloys,[21,22] or composite materials.[25] Furthermore,

Received: March 15, 2023
Revised: May 9, 2023

the introduction of support materials—state-of-the-art OER catalysts are unsupported—may be a viable strategy to enhance the mass-related catalytic performance.[5] The latter strategy presents the advantage of a reduced catalyst loading thanks to a better NPs dispersion. Hence, the utilization of the catalyst is improved by increasing the amount of exposed active sites, and therefore by increasing the electrochemically active surface area (ECSA) of the catalysts.[5,26,27] In fuel cell applications, carbon black is commonly used as a support material due to its low cost, high surface area, and good conductivity. However, it is well known that carbon-based (C-based) supports are unstable under harsh OER conditions in acidic media.[20,27−29] In fact, even at oxygen reduction reaction (ORR) conditions, C-based supports are only kinetically stable.[30−33] Therefore, more recently, extensive studies have been conducted to maximize the surface area, stability, and conductivity of other support materials for OER catalysts. Among others, mesoporous conductive oxides such as antimony-doped tin oxide (ATO),[15,34] tin-doped indium oxide (ITO),[35] and fluorine-doped tin oxide (FTO)[35] were considered promising support candidates.

To address the challenge of designing a cost-effective, highly dispersed catalyst, we herein present ultrasmall Ir and Ir_xRu_y NPs deposited on a standard fuel cell carbon support (Kejten Black) as well as on commercially available ATO. The catalyst preparation was performed in two steps: first, the synthesis of surfactant-free, colloidal NPs in a low-boiling-point solvent[13,36] and second, the immobilization on the support. This flexible approach allows a versatile catalyst design by varying several parameters independent of each other, in the present case the support material independent of NP composition. That is, the same NPs are studied on different support materials.[37] The focus has been made on supported Ir and $Ir_{0.4}Ru_{0.6}$ NPs as, according to the density functional theory (DFT) calculations of Svane et al.,[38] the latter corresponds to the optimum composition for the OER. The electrocatalytic activity of the prepared OER catalysts was studied using an in-house developed gas diffusion electrode (GDE) setup. This cell has been previously used for the oxygen reduction reaction (ORR)[39−41] and recently optimized for OER studies.[42] In this screening device, more realistic and practical conditions can be reached as compared with the conventional rotating disk electrode (RDE) setup. In particular, realistic catalyst loadings are studied (up to 1 mg cm^{-2}), membranes can be introduced, and the operating temperature can be easily varied.[42,43] In the following study, the influence of the support on the overall activity was probed at a high temperature (60 °C) and its applicability in real PEMWE was discussed.

2. EXPERIMENTAL PART

Chemicals and materials are listed in the SI.

2.1. Synthesis and Deposition on a Support. Ir and $Ir_{0.4}Ru_{0.6}$ catalysts were synthesized using a slightly modified protocol from Bizzotto et al.[13,36] Ir NPs were obtained by mixing 2 mL of 20 mM $IrCl_3$ solution in ethanol (EtOH) with 7 mL of 57 mM NaOH/EtOH solution. The resulting molar ratio of NaOH and Ir is 10. This solution mixture was placed in an oil bath at 85 °C for 10 min under reflux conditions and constant stirring at 300 revolutions per minute (rpm). The color change from yellow to green and then to light brown indicates the formation of colloidal NPs. Once the reaction was completed, the solution was left to cool down under constant stirring, leading to a stable colloidal dispersion. A corresponding procedure was used to synthesize $Ir_{0.4}Ru_{0.6}$ NPs. 1 mL of 20 mM $IrCl_3$ in EtOH and 1 mL of 20 mM $RuCl_3$ in EtOH were employed, and the reaction temperature increased to 95 °C, while the reaction time stayed the same. The color transition revealing the NP formation was brown to yellowish to dark brown. The synthesis of the three other compositions (nominal composition: $Ir_{0.66}Ru_{0.33}$, $Ir_{0.33}Ru_{0.66}$, Ru) can be found in the SI.

To immobilize the NPs on the support, either carbon Ketjen Black (C) or a commercially available SbO_2-doped SnO_2 (ATO) was dispersed in EtOH (1:2, mass (support):volume (EtOH)) using a horn sonicator (4 min, pulse: 1 s on/1 s off, amplitude: 30%). The freshly prepared NPs were then poured into the beforehand-dispersed support, and the mixture was further sonicated under the same conditions for 10 more minutes.

The solvent was removed by means of a rotary evaporator (120 rpm, room temperature (RT), 5 °C cooling system) under constant sonication. The catalyst was left overnight under the hood. A second step of rotary evaporator (25 rpm, water bath at 85 °C, 5 °C cooling system, 30 mbar, 4 h) was preferably performed to completely dry the catalyst and to remove any undesired, volatile side products.

2.2. Ink Preparation. A similar procedure to the one reported by Schröder et al.[42] was used to prepare the ink. The as-synthesized catalyst was dispersed in a 3:1 volume ratio of Milli-Q water and isopropanol (IPA). 70 μL of 1 M KOH was added per 60 mL of ink. KOH was added to increase the homogeneity and to improve the stability of the ink.[44] The ink concentration was 654 μg_{metal} mL^{-1}. After 5 min of bath sonication at RT, 10 wt % of Nafion with respect to the catalyst (NPs and support) was added to the ink. Finally, the ink was sonicated for 5 more minutes at RT.

2.3. Electrode Preparation. Following the description of Yarlagadda et al.,[45] a coated carbon gas diffusion layer (GDL) was placed between a sand core filter and a glass funnel (⌀ 3.7 cm) in a vacuum setup. 4.8 mL of the 654 μg_{metal} mL^{-1} ink was diluted with 12.11 mL of Milli-Q water and 45.92 mL of IPA to reach a water/IPA volume ratio of 1:3 (metal concentration of 0.05 mg_{metal} mL^{-1}). After filtration, the catalyst layer was dried overnight in air. The obtained nominal loading was 0.292 mg_{metal} cm^{-2} (see Figure S1 and Table S1 for the loading determination of a 1 mg_{metal} cm^{-2} Ir/C sample).

Following the procedure reported by Schröder et al.,[42] a 3 mm diameter disk was punched out of the 3.7 cm catalyst film. A centered hole (⌀ 3 mm) was punched out of a coated GDL (⌀ 2 cm), where the 3 mm catalyst disk was then placed. An activated Nafion membrane was placed on top of it (see Figure S2a), and the whole system was placed between a paper sheet and an aluminum foil. It was pressed between two Teflon blocks by applying 2.5 tons of force for 10 min. To create an unbroken conductive surface, a ⌀ 2 cm noncoated GDL was placed below the Nafion-functionalized GDL-pressed system.

2.4. Electrochemical Measurements. An electrochemical cell (see Figure S2), dubbed GDE setup, in a three-electrode configuration was used to test the performance of the catalyst. The freshly pressed 3 mm functionalized GDL was employed as the working electrode and a platinum mesh as the counter electrode. All potentials were measured with respect to a reversible hydrogen electrode (RHE). The measurements were performed using a potentiostat controlled with the software EC4DAQ version 2.44. Humidified (Milli-Q water) O_2 was continuously flowing through the setup during the measurements. A flow rate between 50 and 60 mL min^{-1} was used for each measurement. 4 M $HClO_4$ was used as the electrolyte in the

https://doi.org/10.1021/acscatal.3c01193
ACS Catal. 2023, 13, 7568−7577

upper polyether ether ketone (PEEK) compartment of the setup. The electrolyte was preheated at most 7 °C above the desired temperature (30, 40, or 60 °C). The aluminum-made faradaic cage was preheated to the desired temperature using a thermocouple-controlled heating plate. Before each measurement, two cyclic voltammograms (CVs) were recorded between 1.2 and 1.6 V at 10 mV s^{-1} to ensure the correct connectivity of the cell.

Catalyst activation was performed by holding the potential at 1.6 V for 5 min.

Activity experiments were conducted using the following two current density sequences:

- For Ir catalysts: 0.85, 0.85, 2.14, 4.28, 8.56, 17.12, 25.68, 38.53, 51.37, 68.49, 85.62, 128.43, 171.23, 299.66, 428.09, 856.17, 1712.35 mA mg_{Ir}^{-1}
- For $Ir_{0.4}Ru_{0.6}$ catalysts: 0.43, 0.43, 1.07, 2.14, 4.28, 8.56, 12.84, 19.26, 25.68, 34.25, 42.81, 64.21, 85.62, 149.83, 214.04, 428.08, 856.16 mA mg_{IrRu}^{-1}

The solution resistance was determined online using an AC signal of 5 kHz with an amplitude of 1−10 mA.

For each temperature, triplicate samples were measured using a fresh electrode and new electrolyte: the first measurement followed the complete sequence, while the two others were stopped at 299.66 mA mg_{Ir}^{-1} and at 214.04 mA mg_{IrRu}^{-1} for Ir and $Ir_{0.4}Ru_{0.6}$ catalysts, respectively.

Electrochemical results have been exported and analyzed with the software EC4View. The last 100 s of each *i*R-corrected current step were averaged for activity determination.

2.5. Conductivity Measurements. A test rig was built to measure the electrical conductivity σ of the support powders by compressing them between two gold-plated copper stamps, with an area A of 38.5 mm, at different pressures with a maximum of 11.29 MPa. A multimeter was used to apply a direct current and simultaneously measure the resistance R_Ω. The thickness t of the sample was measured by a laser distance sensor and was used for the calculation of the electrical conductivity of the pellet by the following equation

$$\sigma = \frac{t}{AR_\Omega} \tag{1}$$

The measurements were repeated three times for the ATO support and two times for the C support.

2.6. Transmission Electron Microscopy (TEM). TEM micrographs of the unsupported NPs were acquired with a Jeol 2100 operated at 200 kV. TEM micrographs of the supported NPs were acquired with Tecnai Spirit operated at 80 kV. The samples were prepared by drop-casting 10 μL of the ink on a grid and dried under air at RT. The mean size particle (diameter) of 150 particles was determined using the software ImageJ.

2.7. Small-Angle X-ray Scattering (SAXS). *Ex situ* SAXS measurements were performed at the Paul Scherrer Institute (PSI), Switzerland, on the X12SA beamline, cSAXS, to assess the size change of the supported NPs before and after activation. The data were collected in a q-range of 0.0049−0.7198 $Å^{-1}$ with a beam energy of 11.2 keV. The measurements were performed on pristine and activated 3 mm catalyst-functionalized GDL. The backgrounds corresponded to the supports without any NPs deposited on a GDL. Those were pristine and activated as well (the activation step is the same as the actual samples, see Section 2.4). All samples and backgrounds were measured with a Nafion membrane and were protected in Kapton tape.

The data analysis was performed using the software XSACT 2.4. The data were analyzed in the NPs module between 0.04 and 0.35 $Å^{-1}$ for $Ir_{0.4}Ru_{0.6}$/C and Ir/ATO (both pristine and activated), between 0.045 and 0.28 $Å^{-1}$ for Ir/C (pristine and activated) and activated $Ir_{0.4}Ru_{0.6}$/ATO, and between 0.045 and 0.31 $Å^{-1}$ for pristine and $Ir_{0.4}Ru_{0.6}$/ATO. The model and the parameters for the calculation were the same for all samples, namely a spherical particle shape and a size distribution between 0.01 and 10 nm, with steps of 0.1 nm.

2.8. Energy-Dispersive X-ray Spectroscopy (EDX). EDX measurements were performed on a Zeiss GeminiSEM 450 equipped with an EDX Photodetector Ultim Max 65 from Oxford Instruments to study the elemental composition of Ir_xRu_y catalysts and the possible Sb leaching of ATO-immobilized catalysts. The data were analyzed with the AZTec 4.2 software. To obtain only the atomic (atom %) ratio between Ir and Ru, other elements present in the sample were deconvoluted. The ratio between Ir and Ru was first determined from the ink. For that, about 3 × 10 μL was drop-cast onto a graphite foil. The samples were mounted on metal stubs with conductive, adhesive Cu tape. An accelerating voltage of 10 keV, a working distance of 8.5 mm, and probe currents between 400 and 500 pA were used as measuring parameters.

The ratio between Ir and Ru was determined a second time after the catalysts have been deposited on the GDL *via* vacuum filtration (see Section 2.3). The functionalized GDL was measured in a top-view mode. Cross-section mapping was also monitored onto functionalized GDL to identify the different layers and ensure the homogeneity of the catalyst layer.

Furthermore, the activated samples were measured in a top-view mode to identify any Ru leaching after the activation step (see Section 2.4). To activate the sample, the Nafion membrane was not pressed onto the functionalized GDL but simply deposited to allow its easier removal and avoid any catalyst layer destruction.

Finally, ATO-immobilized catalysts were analyzed post-mortem to determine a possible Sb leaching. The samples were measured in a top-view mode.

2.9. Thermogravimetric Analysis (TGA). A thermogravimetric analysis (TGA) instrument (Q500 V20.13, TA Instruments) was used to determine the metal loading on the 3 mm diameter GDE sample. An Ir/C sample of 1 mg_{Ir} cm^{-2} was used as a representative measurement. The sample was heated in an O_2 atmosphere (O_2 5% in N_2) from 25 °C (RT) to 1000 °C with a temperature ramp of 10 °C min^{-1}. In the end, an isothermal step was held for 5 min. The sample was measured in the Danish Technological Institute (DTI), Denmark, *via* a send in service.

2.10. X-ray Absorption Spectroscopy (XAS). *Ex situ* X-ray absorption near-edge structure (XANES) and extended X-ray absorption fine structure (EXAFS) measurements were carried out for the C-immobilized samples at the SuperXAS beamline of the Swiss Light Source (SLS) at PSI, Switzerland (storage ring current of 400 mA), *via* a send in service. The incident beam was collimated by a mirror (Rh-coated for Ir L_{III}) and monochromatized with a liquid nitrogen-cooled channel-cut Si(111) monochromator. The measurements of the ATO-supported samples were performed at the ROCK beamline of the SOLEIL light source (storage ring current of 500 mA), France. The incident beam was collimated using a mirror with a 50 nm Ir coating and monochromatized with a Si(111) monochromator.

Energy calibrations were performed with simultaneously probed metal foils to reference the energies of the Ir L_{III}-edge

https://doi.org/10.1021/acscatal.3c01193
ACS Catal. 2023, 13, 7568−7577

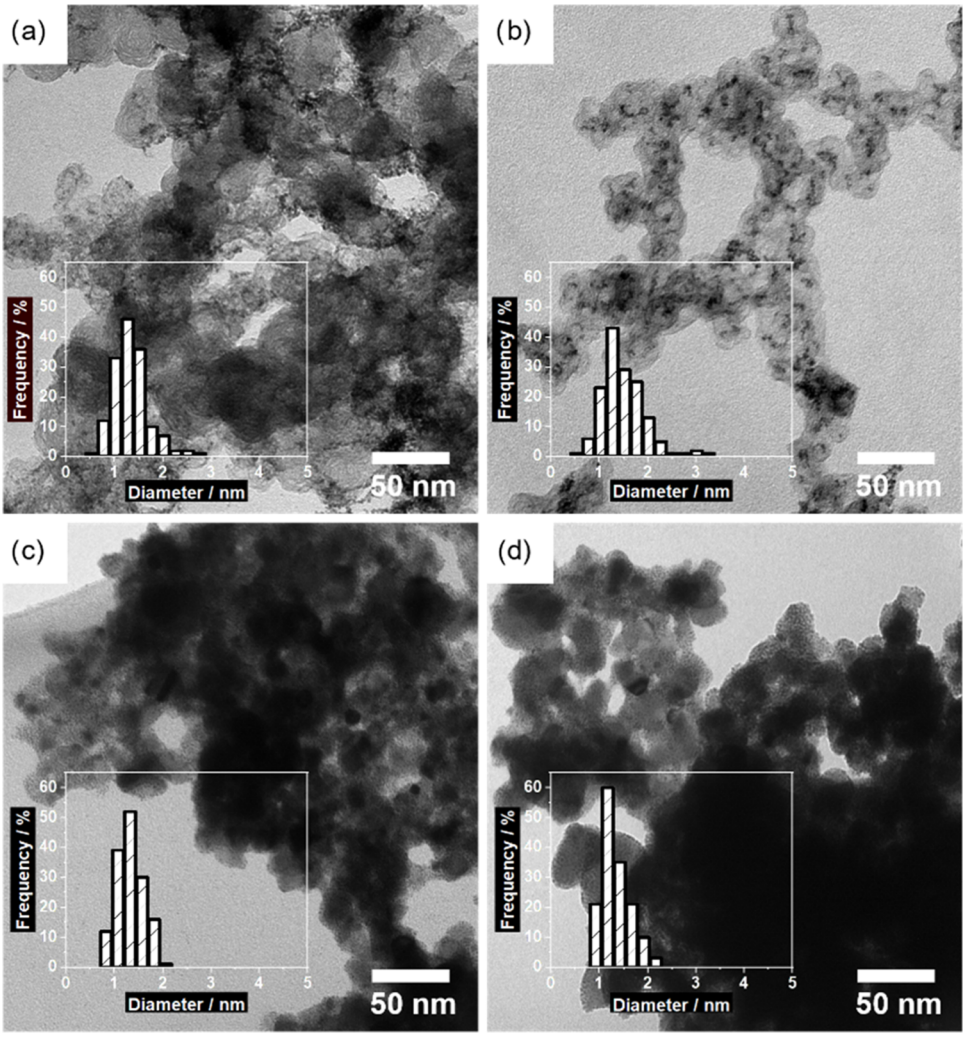

Figure 1. TEM micrographs and respective particle size distribution (insets) of Ir/C (a), $Ir_{0.4}Ru_{0.6}$/C (b), Ir/ATO (c), and $Ir_{0.4}Ru_{0.6}$/ATO (d).

and the Ru K-edge positions. X-ray absorption spectra at the Ir L_{III}-edge were collected in transmission mode, while Ru K-edge X-ray absorption spectra were measured in fluorescence mode. All spectra were collected in quick EXAFS mode (QEXAFS).[46−48] The data were processed using ProQEXAFS for calibration, interpolation, normalization, and averaging (300 s of measurement on each sample). The leached samples were protected in Kapton tape.

The averaged XAS spectra were analyzed by using the Demeter software package. The raw spectra were energy aligned to a metal reference foil, background corrected, and normalized by the edge step. After conversion of the energy units (eV) into photoelectron wave number k units ($Å^{-1}$), the resulting $\chi(k)$ functions of the XAS spectra were weighted with k^2 and Fourier transformed to obtain pseudo-radial structure functions. The fits to the EXAFS spectra were performed in Artemis of the Demeter software package based on IFFEFIT.[49] XAS spectra of the pure metal foils were used as references to estimate the amplitude reduction factors ($S0^2$). The Ir L_{III}-edge data were fitted in R-space, with a fitting weight of k^2. The k-range for the Fourier transform was from 3 to 14 $Å^{-1}$ with a fit window in an R-range of 1.1−3.0 Å. The Ru K-edge data were fitted in R-space, with a fitting weight of k^2. The k-range for the Fourier transform was from 3 to 12 $Å^{-1}$ with a fit window in an R-range of 1.0−3.0 Å.

2.11. Pair Distribution Function (PDF) Analysis. *Ex situ* synchrotron X-ray total scattering measurements were performed at the 11-ID-B beamline at the Advanced Photon Source (APS) and at the DanMAX beamline at MAXIV, with hard X-rays of 58.7 and 35.0 keV, respectively. At the APS beamline, the measurements were performed on pristine and activated 3 mm catalyst-functionalized GDLs. To isolate the scatting signal from the Ir and IrRu phases, data were collected for background subtraction. The backgrounds corresponded to the supports without any NPs deposited on a GDL. Those were pristine and activated (activation step similar to the actual samples, see Section 2.4). Scattering data from all samples and backgrounds were measured with a Nafion membrane and were protected in Kapton tape. At the DanMAX beamline, the measurements were performed in polyimide tubes filled with pristine catalyst powder or backgrounds. All diffraction patterns were collected in a wide-angle transmission geometry with 2D area detectors placed close to the sample. Fit2D,[50] pyFAI,[51] and Dioptas[52] were used to calibrate experimental parameters from a calibrant material (CeO_2 at APS, LaB_6 at DanMAX) and to azimuthally integrate the diffraction images to 1D diffraction patterns. PDFgetX3[53] and xPDFsuite[54] were used to obtain the total scattering structure function, F(Q), which was sine Fourier transformed to obtain the PDF.

https://doi.org/10.1021/acscatal.3c01193
ACS Catal. 2023, 13, 7568−7577

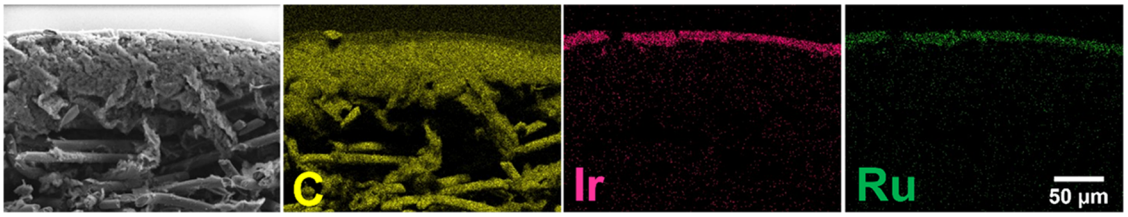

Figure 2. SEM/EDX cross-section mapping of C (yellow), Ir (pink), and Ru (green). The sample corresponds to a GDL functionalized with $Ir_{0.4}Ru_{0.6}$/C before activation.

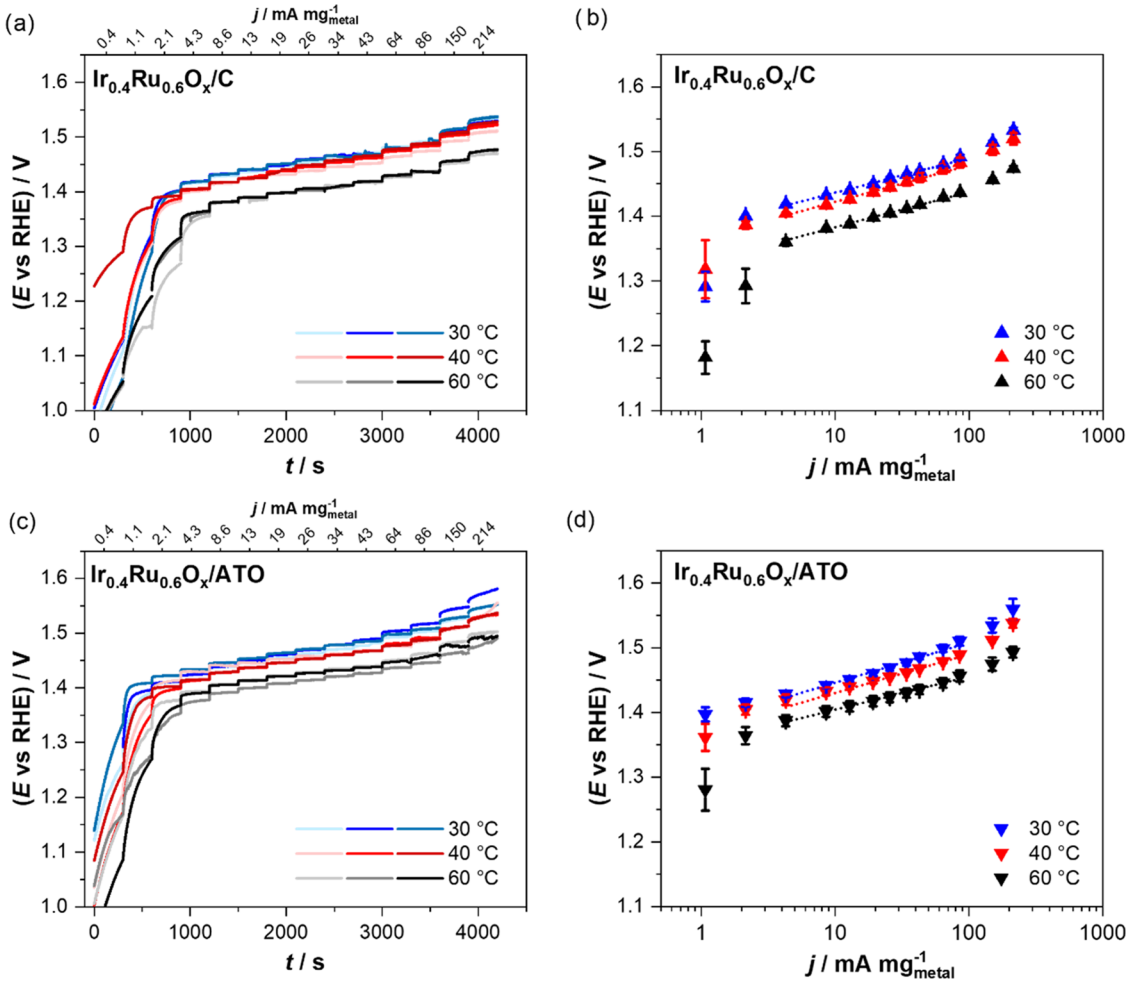

Figure 3. Electrocatalytic OER *i*R-corrected potential transients (a, c) and corresponding Tafel plots (b, d) of $Ir_{0.4}Ru_{0.6}O_x$/C (upper row) and $Ir_{0.4}Ru_{0.6}O_x$/ATO (lower row) at 30 (blue), 40 (red), and 60 °C (black). The error bars show the standard deviation of the three independent measurements. All measurements were performed in the GDE setup in an O_2 atmosphere using 4 M $HClO_4$ as an electrolyte. Nominal catalyst loading: 654 μg_{metal} cm^{-2}.

Modeling of the PDFs was carried out using PDFgui.[55] The models used were face-centered cubic Ir and NaCl ($Fm\bar{3}m$), and tetragonal IrO_2 and ATO ($P4_2/mnm$). Multiphase real-space Rietveld refinements were carried out, where scale factors, lattice constants (a, b, c), isotropic gaussian atomic displacement parameters, and spherical particle size parameters were refined. Measurement-specific resolution parameters, Q_{broad} and Q_{damp}, were obtained by the refinement of the PDF data of a calibrant material, measured in the same geometry as the samples.

3. RESULTS AND DISCUSSION

Ultrasmall, *i.e.*, *ca.* 1.5 nm in diameter, pristine Ir and Ir_xRu_y NPs were synthesized *via* a surfactant-free, colloidal route using only EtOH as a low-boiling-point solvent.[13,56,57] The NPs were immobilized in a second step on two different commercially available supports, carbon Ketjen Black and ATO, at a nominal metal loading of 50 wt %. The straightforward synthesis approach allows for synthesizing a wide range of different compositions while keeping the particle size constant (see Figure S3). It also allows immobilizing the "same" NPs onto different supports, *i.e.*, NPs from the same batch. In the used two-step synthesis strategy, the support material is expected to have a negligible influence on the properties of the immobilized NPs,[37] as the immobilization procedure does not involve any heating. This is supported by XAS data of Ir/C and Ir/ATO, in which both catalysts show overlapping spectra (Figure S4 and

https://doi.org/10.1021/acscatal.3c01193
ACS Catal. 2023, 13, 7568−7577

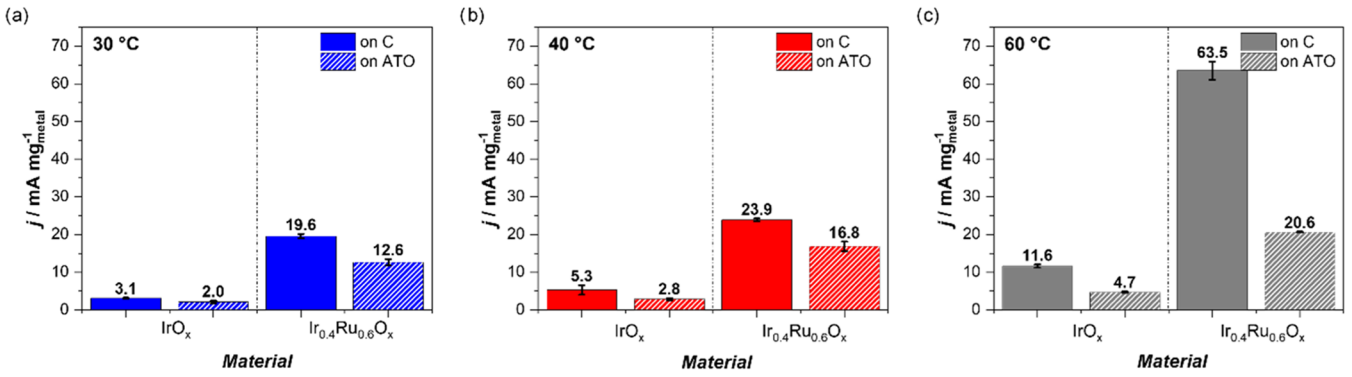

Figure 4. Comparison of the activities reached at a temperature-corrected OER overpotential η = 0.23 V for IrO_x (left-hand side of the graphs) and $Ir_{0.4}Ru_{0.6}O_x$ (right-hand side of the graphs) deposited on C (solid bars) or ATO (dashed bars) at 30 (a), 40 (b), and 60 °C (c). Values were interpolated or extrapolated based on their Tafel slopes.

Table S2). While the colloidal NPs are metallic when synthesized, they slowly oxidize when exposed to air during immobilization and subsequent storage, as evidenced by the XAS spectra (Figure S5). The degree of oxidation, therefore, depends on the duration of storage (see Figure S5). It should also be noted that upon electrochemistry measurements, the NPs can be reduced again as shown in previous work.[13] Nevertheless, the pristine samples are highly ordered and have a metallic core. PDF shows a pure fcc phase for Ir NPs, whereas $Ir_{0.4}Ru_{0.6}$ NPs can be fitted with either a pure fcc phase or a mixed fcc (as expected for Ir) and hcp phases (as expected for Ru), with similar accuracy (R_w(fcc) = 0.65, R_w(fcc + hcp) = 0.62) (Figure S6 and Table S3). However, EXAFS indicates alloying in the $Ir_{0.4}Ru_{0.6}$ NPs, *i.e.*, coordination between Ir and Ru atoms is seen (see Table S4). The morphology of the supported NPs was analyzed with a TEM, confirming spherical shape with a mean size of *ca.* 1.5 nm regardless of the composition or the support (see Figure 1 and Table S5). The micrographs reveal a slightly better dispersion of the NPs on the ATO support as compared with the C support, where small aggregates are formed.

As the active phase for the OER are oxides, the catalysts need to be activated before determining their catalytic activity.[13] Therefore, the catalyst samples were electrochemically oxidized prior to each measurement. The activation leads to a particle growth of roughly twice the initial diameter as monitored by SAXS (see Figure S7 and Table S5). Assuming fully reduced pristine NPs, the determined growth in particle size due to oxidation is slightly less than expected (see discussion in the SI). This indicates that the NPs were not completely oxidized after the activation procedure. The same phenomenon was already observed by Minguzzi et al.,[58] who highlighted the presence of both metallic and oxidic phases in Ir samples cycled up to 1.5 V *vs* RHE. To reinforce this hypothesis, PDF analysis of the total scattering of C-immobilized samples was carried out (see Figure S6) (the analysis of the ATO-immobilized was difficult due to the presence of the oxide support, see Figure S8), showing a small contribution from metallic phases, even after activation. The same is the case for the EXAFS data, which indicate metal−metal coordination of the activated samples as well (see Table S6). For the electrocatalytic measurements in the GDE setup, the catalyst was transferred onto a GDL by vacuum filtration. Figure 2 depicts a cross-sectioned SEM/EDX mapping of a representative catalyst film on a GDL. Starting from the bottom part to the top, the porous carbon fibers of the GDL, the microporous carbon layer (MPL), and the catalyst layer can be identified. The latter forms a homogeneous layer of about 12 μm thickness. No penetration of the catalyst sample into the GDL is observed, confirming a localized catalyst layer.

The OER activity of the different catalysts was determined in galvanostatic measurements at steady-state conditions. Each sample was measured at least as triplicates using a fresh sample, and independent measurements were conducted at three different temperatures, *i.e.*, 30, 40, and 60 °C. Figure 3a,c depicts the i*R*-corrected raw data with the different galvanostatic steps and the achieved reproducibility among the individual measurement for $Ir_{0.4}Ru_{0.6}O_x$/C and $Ir_{0.4}Ru_{0.6}O_x$/ATO catalysts. The measurements for the pure Ir catalysts are reported in the SI (Figure S9) and demonstrate equally good reproducibility. It is seen that at the first two galvanostatic steps, no steady-state behavior was reached. Instead, the recorded potential increased with time in this initial galvanostatic step. This observation is in agreement with incomplete oxidation after the activation procedure. Prior to the OER measurements, the samples were activated by holding the potential at 1.6 V for 5 min. Despite this relatively high activation potential, the electrocatalytic data reach steady-state behavior only at the subsequent current steps. Then, a linear Tafel behavior is observed between *ca.* 4 and 85 mA mg_{metal}^{-1} in all four cases (see Figures 3b,d and S10 and Table S7). It should be noted that taking the measurements before complete activation into account in the activity evaluation would lead to an overestimation of the OER activity as the recorded current is due to a mixture of OER and metal oxidation current. While such a behavior can be easily identified in steady-state measurements (potentiostatic or galvanostatic) applied here, it is very difficult to discern in the more commonly applied potentiodynamic cyclic or linear sweep voltammetry.

In our measurements, each catalyst demonstrates similar i*R*-corrected Tafel slopes at three different temperatures (see Table S7). At 30 °C, the Tafel slopes are in the range of 53−62 mV dec^{-1}, which lies within the data reported in the literature for Ir-based catalysts.[15,18,59,60] At higher current densities (>100 mA mg_{metal}^{-1}), deviations from the linear behavior are seen, which presumably are related to the formation of oxygen bubbles.[61]

As already shown in our previous OER GDE study,[42] and as expected from kinetics, increasing the temperature leads to an improved catalytic activity (lower OER overpotential). The catalytic activity of the four different catalysts is compared at an identical overpotential of η = 0.23 V in Figure 4a−c. This overpotential was chosen as it lies in the linear Tafel region of the individual catalysts at most temperatures. However, for IrO_x/C

https://doi.org/10.1021/acscatal.3c01193
ACS Catal. 2023, 13, 7568−7577

at 30 °C and IrO_x/ATO at 30 and 40 °C, the OER activities are obtained *via* extrapolation of the measured data. Note further that the temperature dependence of the reversible potential was corrected according to Parthasarathy et al.[62] for the conversion of one mol of water ($n = 2$). Moreover, the performance of the catalysts is also compared in Figure S11 at a fixed current density of 25.68 mA mg_{metal}^{-1}, which is close to the benchmark value of 10 mA cm_{geo}^{-2}.

From the comparison, it can be seen at first glance that Ru-containing catalyst always exhibits a higher catalytic mass activity (total metal mass) as compared with pure Ir. This agrees with an early study of Kötz et al.,[63] which suggested that combining Ru with Ir not only leads to better stability of Ru but also to an improved activity as compared with pure Ir. Note that EDX analysis of our $Ir_{0.4}Ru_{0.6}$ catalyst films indicates that during activation, part of the Ru is leached from the alloy nanoparticles (see Table S8). Despite this leaching of Ru, our data reveal that at 30 °C, the Ru-containing catalysts have a 6.3-fold higher OER activity than the pure Ir catalysts, independently of the support. The superior activity of $Ir_{0.4}Ru_{0.6}$ as compared with pure Ir is also confirmed at higher temperatures, where dependent on support and temperature, improvement factors between *ca.* 4.5- and 6-fold are observed.

As recently reported by Suermann et al.,[64] Hartig-Weiss et al.,[15] and Schröder et al.,[42] the apparent OER activation energy (E_a) can be approximated using the linearization of the Arrhenius equation (eq 2),

$$j = zFa_{app}\exp\left(\frac{-E_a}{RT}\right) \quad (2)$$

where j is the current density, z is the number of electrons exchanged, F is the Faraday constant, a_{app} is the apparent preexponential factor that includes all of the entropic terms, E_a is the apparent activation energy, R is the gas constant, and T is the temperature. eq 2 can be used when similar Tafel slopes are obtained at different temperatures. We calculated the apparent OER activation energy E_a for the four catalysts at $\eta = 0.23$ V. IrO_x/C and $Ir_{0.4}Ru_{0.6}O_x$/C exhibit an apparent E_a equal to 37 and 34 kJ mol^{-1}, respectively, which is in line with the work of Hartig-Weiss et al.[15] On the other hand, ATO-supported catalysts exhibit much lower apparent activation energy, *i.e.*, 23 and 13 kJ mol^{-1} for IrO_x and $Ir_{0.4}Ru_{0.6}O_x$, respectively. It must be emphasized that these obtained values correspond to the apparent activation energy, and therefore are artificial. A recent study by Duan et al.[65] on alkaline OER describes different factors that can lead to deviations in the activation energy. One of them is the change of active sites under operating conditions. However, our data indicate a different cause, which is support-related, for the apparent lower activation energy, *i.e.*, that ATO is not stable under operation conditions.

Comparing the support's influence on the catalytic performance of the NPs in Figure 4, it can be seen that in all investigated cases, the NPs immobilized on C were more active than the ones immobilized on ATO. As discussed above, according to the characterization, the supported NPs show a similar size distribution, crystalline structure, and elemental ratio. The TEM micrographs indicate even better particle distribution on ATO than on the carbon support. Therefore, one would assume that the activity of the NPs would be identical regardless of the support, or that the performance of the carbon-supported NPs would be inferior due to carbon corrosion. However, the opposite is observed. Major contributions to the recorded current from the carbon support oxidation seem unlikely, although it cannot be excluded that carbon corrosion takes place. However, in contrast to the typical activity determination *via* potential scans, in the quasi-steady-state measurements, it would lead to time-dependent behavior (similar to what is seen during the activation) and to a nonlinear Tafel slope.[31] Furthermore, as discussed above, the activation energy of the carbon-supported samples compares well with the literature data.[15] Therefore, the most plausible cause for this observation is a higher conductivity/stability of the carbon support (9.85 S cm^{-1}) as compared with the ATO (0.0009 S cm^{-1}) (see Table S9) (note that it has been avoided to expose the catalyst to reducing conditions during the electrochemical measurements). In particular, our data suggest that going to elevated temperature diminishes the performance of the ATO-supported samples. In the literature, there is still an ongoing debate about whether or not ATO loses its conductivity under operating conditions.[66−73] While some researchers did not observe any conductivity loss of their homemade mesoporous ATO after 15 h at 1 mA cm^{-2},[69] others detected the loss of Sb in a commercially available ATO when sweeping the potential from open-circuit potential (OCP) to 2 V *vs* RHE.[70] Determining the average Sn:Sb ratio by EDX in our pristine and postmortem samples of the catalysts supports this hypothesis (see Figures S12 and S13 and Table S10). Moreover, according to da Silva et al.,[71] the doping of their homemade SnO_2 does not significantly improve the activity of the catalyst. On the contrary, for hydrous IrO_x, the dopants accelerate the dissolution of Ir and SnO_2. The contradicting reports might be related to experimental limitations. Typically, OER studies are performed in conventional RDE measurements, where milder conditions are applied compared with MEAs or stack electrolyzers. Furthermore, only thin catalyst films are investigated that are deposited on conducting working electrode disks. The GDE setup used in this study mimics more realistic and practical conditions by using a highly acidic electrolyte, higher loading, and higher temperature.[74] Furthermore, higher current densities can be applied without massive and detrimental oxygen bubble formation. In summary, our data suggest that the observed activity trend between carbon and ATO stems from the leaching of Sb in the ATO support, which is promoted at elevated temperatures.

4. CONCLUSIONS

In the present study, we evaluated four different catalysts for the OER under acidic conditions, *i.e.*, IrO_x/C, $Ir_{0.4}Ru_{0.6}O_x$/C, IrO_x/ATO, and $Ir_{0.4}Ru_{0.6}O_x$/ATO. The catalysts were synthesized in two steps using a straightforward route that allows independent optimization of single components such as the ratio between the metals, the nature of the support material, and the metal loading. The pristine (∼1.5 nm) NPs were immobilized on carbon as well as on ATO. Activation at 1.6 V for 5 min leads to oxide formation and corresponding particle growth but is not sufficient for the complete oxidation of the catalysts, which is only reached during the activity measurements. The performance of the different catalysts was investigated using a GDE setup in a galvanostatic operation mode. $Ir_{0.4}Ru_{0.6}O_x$/C exhibits the highest activity at $\eta = 0.23$ V among the four presented catalysts. Excellent performance of 63.5 mA mg_{metal}^{-1} was achieved at 60 °C, a temperature close to realistic conditions in PEMWE. The determined performance can be seen as the intrinsic OER activity of the $Ir_{0.4}Ru_{0.6}O_x$ NPs and thus is of interest for applications. Also, the determined apparent activation energy was within promising values of 34−37 kJ

https://doi.org/10.1021/acscatal.3c01193
ACS Catal. 2023, 13, 7568−7577

mol^{-1}. The main challenge, however, remains a suitable catalyst support material. Our measurements clearly indicate that the employed commercial ATO is not a feasible support material, similar to carbon, which is not a viable option for industrial applications. In fact, ATO is inferior to carbon, despite high applied current densities and elevated temperatures. In particular, elevated temperatures lead to diminishing performance of the ATO-supported catalysts. This observation was suspected to be caused by a loss of conductivity due to Sb leaching. In consequence, further investigations need to be taken to design more suitable supports for OER catalysts. Moreover, these supports need to be tested under more realistic conditions to reveal their possible commercial applicability.

■ ASSOCIATED CONTENT

Supporting Information

The Supporting Information is available free of charge at https://pubs.acs.org/doi/10.1021/acscatal.3c01193.

Chemicals and materials, loading determination by TGA, GDE setup sketch, TEM micrographs of nonsupported particles and their size distribution, XAS of pristine Ir/C and Ir/ATO, PDF of the pristine and activated Ir/C and IrRu/C, EXAFS of Ir and IrRu samples, particle size distribution by TEM and SAXS, PDF of activated Ir/ATO, potential transients and Tafel slopes of Ir/C and Ir/ATO, comparison histograms at 25.68 mA mg_{metal}^{-1}, summary of EDX data, as well as conductivity measurements (PDF)

■ AUTHOR INFORMATION

Corresponding Author

Matthias Arenz − *Department of Chemistry, Biochemistry and Pharmaceutical Sciences, University of Bern, 3012 Bern, Switzerland;* orcid.org/0000-0001-9765-4315; Email: matthias.arenz@unibe.ch

Authors

Aline Bornet − *Department of Chemistry, Biochemistry and Pharmaceutical Sciences, University of Bern, 3012 Bern, Switzerland*

Rebecca Pittkowski − *Department of Chemistry, University of Copenhagen, 2100 Copenhagen, Denmark;* orcid.org/0000-0002-0351-4993

Tobias M. Nielsen − *Department of Chemistry, University of Copenhagen, 2100 Copenhagen, Denmark*

Etienne Berner − *Department of Chemistry, Biochemistry and Pharmaceutical Sciences, University of Bern, 3012 Bern, Switzerland;* orcid.org/0000-0002-4902-2687

Annabelle Maletzko − *Department for Applied Electrochemistry, Fraunhofer-Institute for Chemical Technology ICT, 76327 Pfinztal, Germany*

Johanna Schröder − *Department of Chemistry, Biochemistry and Pharmaceutical Sciences, University of Bern, 3012 Bern, Switzerland;* orcid.org/0000-0001-5461-4751

Jonathan Quinson − *Department of Chemistry, University of Copenhagen, 2100 Copenhagen, Denmark; Biochemical and Chemical Engineering Department, Aarhus University, 8200 Aarhus, Denmark;* orcid.org/0000-0002-9374-9330

Julia Melke − *Department for Applied Electrochemistry, Fraunhofer-Institute for Chemical Technology ICT, 76327 Pfinztal, Germany;* orcid.org/0000-0001-5574-0207

Kirsten M. Ø. Jensen − *Department of Chemistry, University of Copenhagen, 2100 Copenhagen, Denmark;* orcid.org/0000-0003-0291-217X

Complete contact information is available at: https://pubs.acs.org/10.1021/acscatal.3c01193

Notes

The authors declare no competing financial interest.

■ ACKNOWLEDGMENTS

This Project has received funding from the European Union's Horizon 2020 Research and Innovation program under grant agreement no. 861960 ("Recycalyse" project). It was also supported by the Danish National Research Foundation in the Center for High Entropy Alloy Catalysis (CHEAC) DNRF 149. The authors acknowledge access to the Microscopy Imaging Center (MIC) facilities of the University of Bern. Dr L. Theil Kuhn and S. B. Simonsen, Technical University of Denmark (DTU), are thanked for facilitating access to the Jeol 2100 TEM. A.B. and M.A. thank Dr. Andreas Menzel from the cSAXS (X12SA) beamline of the SLS at the Paul Scherrer Institute (PSI) and Dr. Jia Du from the University of Bern for their help during SAXS measurement under the beamline proposal 20201725. They further acknowledge the beamline scientist Dr. Adam H. Clark from PSI for the send in service on *ex situ* synchrotron samples. The authors acknowledge SOLEIL, France, for the provision of synchrotron radiation facilities, and they thank the beamline scientist Stephanie Belin for assistance in using beamline ROCK under the beamline proposal 20201221. Alexandra Dworzak and Prof. Dr. Mehtap Oezaslan from Technische Universität Braunschweig, Germany, are thanked for their contributions to the *ex situ* synchrotron XAS data acquisitions in SOLEIL. Acknowledgments go also to Olaf J. Borkiewicz and Tifanny Kinnibrugh for their contribution to the ex situ synchrotron PDF data acquisitions under the remote beamline proposal GUP-72059. The authors thank the beamline scientist Dr. Mads Ry Jørgensen for his help under beamline proposal 20210511. Kathrine Bjørneboe of DTI, Denmark, is acknowledged for the TGA measurements and Dr. Susan R. Cooper of DTI, Denmark, for her advice for the PDF analysis. Dr. Gustav K. H. Wiberg is thanked for his advice throughout the entire work.

■ REFERENCES

(1) Barbir, F. PEM Electrolysis for Production of Hydrogen from Renewable Energy Sources. *Sol. Energy* **2005**, *78*, 661−669.

(2) Pellow, M. A.; Emmott, C. J. M.; Barnhart, C. J.; Benson, S. M. Hydrogen or Batteries for Grid Storage? A Net Energy Analysis. *Energy Environ. Sci.* **2015**, *8*, 1938−1952.

(3) Ayers, K. E.; Capuano, C.; Anderson, E. B. Recent Advances in Cell Cost and Efficiency for PEM-Based Water Electrolysis. *ECS Trans.* **2012**, *41*, 15−22.

(4) Carmo, M.; Fritz, D. L.; Mergel, J.; Stolten, D. A Comprehensive Review on PEM Water Electrolysis. *Int. J. Hydrogen Energy* **2013**, *38*, 4901−4934.

(5) Zhang, K.; Liang, X.; Wang, L.; Sun, K.; Wang, Y.; Xie, Z.; Wu, Q.; Bai, X.; Hamdy, M. S.; Chen, H.; Zou, X. Status and Perspectives of Key Materials for PEM Electrolyzer. *Nano Res. Energy* **2022**, *1*, No. e9120032.

(6) Peng, X.; Wang, L.; Hu, L.; Li, Y.; Gao, B.; Song, H.; Huang, C.; Zhang, X.; Fu, J.; Huo, K.; Chu, P. K. In Situ Segregation of Cobalt Nanoparticles on VN Nanosheets via Nitriding of Co2V2O7 Nanosheets as Efficient Oxygen Evolution Reaction Electrocatalysts. *Nano Energy* **2017**, *34*, 1−7.

(7) Z Zhou, L.; Shinde, A.; Montoya, J. H.; Singh, A.; Gul, S.; Yano, J.; Ye, Y.; Crumlin, E. J.; Richter, M. H.; Cooper, J. K.; Stein, H. S.; Haber, J. A.; Persson, K. A.; Gregoire, J. M. Rutile Alloys in the Mn−Sb−O System Stabilize Mn^{3+} To Enable Oxygen Evolution in Strong Acid. *ACS Catal.* **2018**, *10*, 10938−10948.
(8) Huynh, M.; Ozel, T.; Liu, C.; Lau, E. C.; Nocera, D. G. Design of Template-Stabilized Active and Earth-Abundant Oxygen Evolution Catalysts in Acid. *Chem. Sci.* **2017**, *8*, 4779−4794.
(9) Han, N.; Yang, K. R.; Lu, Z.; Li, Y.; Xu, W.; Gao, T.; Cai, Z.; Zhang, Y.; Batista, V. S.; Liu, W.; Sun, X. Nitrogen-Doped Tungsten Carbide Nanoarray as an Efficient Bifunctional Electrocatalyst for Water Splitting in Acid. *Nat. Commun.* **2018**, *9*, No. 924.
(10) Lei, C.; Chen, H.; Cao, J.; Yang, J.; Qiu, M.; Xia, Y.; Yuan, C.; Yang, B.; Li, Z.; Zhang, X.; Lei, L.; Abbott, J.; Zhong, Y.; Xia, X.; Wu, G.; He, Q.; Hou, Y. Fe-N_4 Sites Embedded into Carbon Nanofiber Integrated with Electrochemically Exfoliated Graphene for Oxygen Evolution in Acidic Medium. *Adv. Energy Mater.* **2018**, *8*, No. 1801912.
(11) Moreno-Hernandez, I. A.; Macfarland, C. A.; Read, C. G.; Papadantonakis, K. M.; Brunschwig, B. S.; Lewis, N. S. Crystalline Nickel Manganese Antimonate as a Stable Water-Oxidation Catalyst in Aqueous 1.0 M H_2SO_4. *Energy Environ. Sci.* **2017**, *10*, 2103−2108.
(12) Man, I. C.; Su, H. Y.; Calle-Vallejo, F.; Hansen, H. A.; Martínez, J. I.; Inoglu, N. G.; Kitchin, J.; Jaramillo, T. F.; Nørskov, J. K.; Rossmeisl, J. Universality in Oxygen Evolution Electrocatalysis on Oxide Surfaces. *ChemCatChem* **2011**, *3*, 1159−1165.
(13) Bizzotto, F.; Quinson, J.; Zana, A.; Kirkensgaard, J. J. K.; Dworzak, A.; Oezaslan, M.; Arenz, M. Ir Nanoparticles with Ultrahigh Dispersion as Oxygen Evolution Reaction (OER) Catalysts: Synthesis and Activity Benchmarking. *Catal.: Sci. Technol.* **2019**, *9*, 6345−6356.
(14) Lee, Y.; Suntivich, J.; May, K. J.; Perry, E. E.; Shao-Horn, Y. Synthesis and Activities of Rutile IrO_2 and RuO_2 Nanoparticles for Oxygen Evolution in Acid and Alkaline Solutions. *J. Phys. Chem. Lett.* **2012**, *3*, 399−404.
(15) Hartig-Weiss, A.; Miller, M.; Beyer, H.; Schmitt, A.; Siebel, A.; Freiberg, A. T. S.; Gasteiger, H. A.; El-Sayed, H. A. Iridium Oxide Catalyst Supported on Antimony-Doped Tin Oxide for High Oxygen Evolution Reaction Activity in Acidic Media. *ACS Appl. Nano Mater.* **2020**, *3*, 2185−2196.
(16) Alia, S. M.; Shulda, S.; Ngo, C.; Pylypenko, S.; Pivovar, B. S. Iridium-Based Nanowires as Highly Active, Oxygen Evolution Reaction Electrocatalysts. *ACS Catal.* **2018**, *8*, 2111−2120.
(17) Fu, L.; Yang, F.; Cheng, G.; Luo, W. Ultrathin Ir Nanowires as High-Performance Electrocatalysts for Efficient Water Splitting in Acidic Media. *Nanoscale* **2018**, *10*, 1892−1897.
(18) Oh, H.-S.; Nong, H. N.; Reier, T.; Gliech, M.; Strasser, P. Oxide-Supported Ir Nanodendrites with High Activity and Durability for the Oxygen Evolution Reaction in Acid PEM Water Electrolyzers. *Chem. Sci.* **2015**, *6*, 3321−3328.
(19) Jin, H.; Hong, Y.; Yoon, J.; Oh, A.; Chaudhari, N. K.; Baik, H.; Joo, S. H.; Lee, K. Lanthanide Metal-Assisted Synthesis of Rhombic Dodecahedral MNi (M = Ir and Pt) Nanoframes toward Efficient Oxygen Evolution Catalysis. *Nano Energy* **2017**, *42*, 17−25.
(20) Jensen, A. W.; Sievers, G. W.; Jensen, K. D.; Quinson, J.; Arminio-Ravelo, J. A.; Brüser, V.; Arenz, M.; Escudero-Escribano, M. Self-Supported Nanostructured Iridium-Based Networks as Highly Active Electrocatalysts for Oxygen Evolution in Acidic Media. *J. Mater. Chem. A* **2020**, *8*, 1066−1071.
(21) Feng, J.; Lv, F.; Zhang, W.; Li, P.; Wang, K.; Yang, C.; Wang, B.; Yang, Y.; Zhou, J.; Lin, F.; Wang, G.-C.; Guo, S. Iridium-Based Multimetallic Porous Hollow Nanocrystals for Efficient Overall-Water-Splitting Catalysis. *Adv. Mater.* **2017**, *29*, No. 1703798.
(22) Kwon, T.; Hwang, H.; Sa, Y. J.; Park, J.; Baik, H.; Joo, S. H.; Lee, K. Cobalt Assisted Synthesis of IrCu Hollow Octahedral Nanocages as Highly Active Electrocatalysts toward Oxygen Evolution Reaction. *Adv. Funct. Mater.* **2017**, *27*, No. 1604688.
(23) Wang, C.; Sui, Y.; Xiao, G.; Yang, X.; Wei, Y.; Zou, G.; Zou, B. Synthesis of Cu−Ir Nanocages with Enhanced Electrocatalytic Activity for the Oxygen Evolution Reaction. *J. Mater. Chem. A* **2015**, *3*, 19669−19673.
(24) Nong, H. N.; Gan, L.; Willinger, E.; Teschner, D.; Strasser, P. IrOx Core-Shell Nanocatalysts for Cost- and Energy-Efficient Electrochemical Water Splitting. *Chem. Sci.* **2014**, *5*, 2955−2963.
(25) Ardizzone, S.; Bianchi, C. L.; Cappelletti, G.; Ionita, M.; Minguzzi, A.; Rondinini, S.; Vertova, A. Composite Ternary SnO_2−IrO_2−Ta_2O_5 Oxide Electrocatalysts. *J. Electroanal. Chem.* **2006**, *589*, 160−166.
(26) Shi, Z.; Wang, X.; Ge, J.; Liu, C.; Xing, W. Fundamental Understanding of the Acidic Oxygen Evolution Reaction: Mechanism Study and State-of-the-Art Catalysts. *Nanoscale* **2020**, *12*, 13249−13275.
(27) Spöri, C.; Kwan, J. T. H.; Bonakdarpour, A.; Wilkinson, D. P.; Strasser, P. The Stability Challenges of Oxygen Evolving Catalysts: Towards a Common Fundamental Understanding and Mitigation of Catalyst Degradation. *Angew. Chem., Int. Ed.* **2017**, *56*, 5994−6021.
(28) Yu, X.; Ye, S. Recent Advances in Activity and Durability Enhancement of Pt/C Catalytic Cathode in PEMFC: Part II: Degradation Mechanism and Durability Enhancement of Carbon Supported Platinum Catalyst. *J. Power Sources* **2007**, *172*, 145−154.
(29) Katsounaros, I.; Cherevko, S.; Zeradjanin, A. R.; Mayrhofer, K. J. J. Oxygen Electrochemistry as a Cornerstone for Sustainable Energy Conversion. *Angew. Chem., Int. Ed.* **2014**, *53*, 102−121.
(30) Ashton, S. J.; Arenz, M. Comparative DEMS Study on the Electrochemical Oxidation of Carbon Blacks. *J. Power Sources* **2012**, *217*, 392−399.
(31) Ashton, S. J.; Arenz, M. A DEMS Study on the Electrochemical Oxidation of a High Surface Area Carbon Black. *Electrochem. Commun.* **2011**, *13*, 1473−1475.
(32) Maass, S.; Finsterwalder, F.; Frank, G.; Hartmann, R.; Merten, C. Carbon Support Oxidation in PEM Fuel Cell Cathodes. *J. Power Sources* **2008**, *176*, 444−451.
(33) Linse, N.; Gubler, L.; Scherer, G. G.; Wokaun, A. The Effect of Platinum on Carbon Corrosion Behavior in Polymer Electrolyte Fuel Cells. *Electrochim. Acta* **2011**, *56*, 7541−7549.
(34) Puthiyapura, V. K.; Mamlouk, M.; Pasupathi, S.; Pollet, B. G.; Scott, K. Physical and Electrochemical Evaluation of ATO Supported IrO_2 Catalyst for Proton Exchange Membrane Water Electrolyser. *J. Power Sources* **2014**, *269*, 451−460.
(35) Oh, H. S.; Nong, H. N.; Strasser, P. Preparation of Mesoporous Sb-, F-, and In-Doped SnO_2 Bulk Powder with High Surface Area for Use as Catalyst Supports in Electrolytic Cells. *Adv. Funct. Mater.* **2015**, *25*, 1074−1081.
(36) Quinson, J.; Neumann, S.; Wannmacher, T.; Kacenauskaite, L.; Inaba, M.; Bucher, J.; Bizzotto, F.; Simonsen, S. B.; Theil Kuhn, L.; Bujak, D.; Zana, A.; Arenz, M.; Kunz, S. Colloids for Catalysts: A Concept for the Preparation of Superior Catalysts of Industrial Relevance. *Angew. Chem.* **2018**, *130*, 12518−12521.
(37) Quinson, J.; Kunz, S.; Arenz, M. Beyond Active Site Design: A Surfactant-Free Toolbox Approach for Optimized Supported Nanoparticle Catalysts. *ChemCatChem* **2021**, *13*, 1692−1705.
(38) Svane, K. L.; Rossmeisl, J. Theoretical Optimization of Compositions of High-Entropy Oxides for the Oxygen Evolution Reaction. *Angew. Chem., Int. Ed.* **2022**, *61*, No. e202201146.
(39) Sievers, G. W.; Jensen, A. W.; Brüser, V.; Arenz, M.; Escudero-Escribano, M. Sputtered Platinum Thin-Films for Oxygen Reduction in Gas Diffusion Electrodes: A Model System for Studies under Realistic Reaction Conditions. *Surfaces* **2019**, *2*, 336−348.
(40) Alinejad, S.; Quinson, J.; Schröder, J.; Kirkensgaard, J. J. K.; Arenz, M. Carbon-Supported Platinum Electrocatalysts Probed in a Gas Diffusion Setup with Alkaline Environment: How Particle Size and Mesoscopic Environment Influence the Degradation Mechanism. *ACS Catal.* **2020**, *10*, 13040−13049.
(41) Du, J.; Quinson, J.; Zana, A.; Arenz, M. Elucidating Pt-Based Nanocomposite Catalysts for the Oxygen Reduction Reaction in Rotating Disk Electrode and Gas Diffusion Electrode Measurements. *ACS Catal.* **2021**, *11*, 7584−7594.
(42) Schröder, J.; Mints, V. A.; Bornet, A.; Berner, E.; Fathi Tovini, M.; Quinson, J.; Wiberg, G. K. H.; Bizzotto, F.; El-Sayed, H. A.; Arenz, M. The Gas Diffusion Electrode Setup as Straightforward Testing

https://doi.org/10.1021/acscatal.3c01193
ACS Catal. 2023, 13, 7568−7577

Device for Proton Exchange Membrane Water Electrolyzer Catalysts. *JACS Au* **2021**, *1*, 247−251.
(43) Wiberg, G. K. H.; Fleige, M.; Arenz, M. Gas Diffusion Electrode Setup for Catalyst Testing in Concentrated Phosphoric Acid at Elevated Temperatures. *Rev. Sci. Instrum.* **2015**, *86*, No. 024102.
(44) Inaba, M.; Quinson, J.; Arenz, M. PH Matters: The Influence of the Catalyst Ink on the Oxygen Reduction Activity Determined in Thin Film Rotating Disk Electrode Measurements. *J. Power Sources* **2017**, *353*, 19−27.
(45) Yarlagadda, V.; McKinney, S. E.; Keary, C. L.; Thompson, L.; Zulevi, B.; Kongkanand, A. Preparation of PEMFC Electrodes from Milligram-Amounts of Catalyst Powder. *J. Electrochem. Soc.* **2017**, *164*, F845−F849.
(46) Müller, O.; Nachtegaal, M.; Just, J.; Lützenkirchen-Hecht, D.; Frahm, R. Quick-EXAFS Setup at the SuperXAS Beamline for in Situ X-Ray Absorption Spectroscopy with 10 Ms Time Resolution. *J. Synchrotron Radiat.* **2016**, *23*, 260−266.
(47) Clark, A. H.; Steiger, P.; Bornmann, B.; Hitz, S.; Frahm, R.; Ferri, D.; Nachtegaal, M. Fluorescence-Detected Quick-Scanning X-Ray Absorption Spectroscopy. *J. Synchrotron Radiat.* **2020**, *27*, 681−688.
(48) Clark, A. H.; Imbao, J.; Frahm, R.; Nachtegaal, M. ProQEXAFS: A Highly Optimized Parallelized Rapid Processing Software for QEXAFS Data. *J. Synchrotron Radiat.* **2020**, *27*, 551−557.
(49) Ravel, B.; Newville, M. ATHENA, ARTEMIS, HEPHAESTUS: Data Analysis for X-Ray Absorption Spectroscopy Using IFEFFIT. *J. Synchrotron Radiat.* **2005**, *12*, 537−541.
(50) Hammersley, A. P.; Svensson, S. O.; Hanfland, M.; Fitch, A. N.; Häusermann, D. Two-Dimensional Detector Software: From Real Detector to Idealised Image or Two-Theta Scan. *High Pressure Res.* **1996**, *14*, 235−248.
(51) Kieffer, J.; Karkoulis, D. PyFAI, a Versatile Library for Azimuthal Regrouping. *J. Phys.: Conf. Ser.* **2013**, *425*, No. 202012.
(52) Prescher, C.; Prakapenka, V. B. DIOPTAS: A Program for Reduction of Two-Dimensional X-Ray Diffraction Data and Data Exploration. *High Pressure Res.* **2015**, *35*, 223−230.
(53) Juhás, P.; Davis, T.; Farrow, C. L.; Billinge, S. J. L. PDFgetX3: A Rapid and Highly Automatable Program for Processing Powder Diffraction Data into Total Scattering Pair Distribution Functions. *J. Appl. Cryst.* **2013**, *46*, 560−566.
(54) Yang, X.; Juhas, P.; Farrow, C. L.; Billinge, S. J. L.XPDFsuite: An End-to-End Software Solution for High Throughput Pair Distribution Function Transformation, Visualization and Analysis *arXiv* 2014 DOI: 10.48550/arxiv.1402.3163.
(55) Farrow, C. L.; Juhas, P.; Liu, J. W.; Bryndin, D.; Boin, E. S.; Bloch, J.; Proffen, T.; Billinge, S. J. L. PDFfit2 and PDFgui: Computer Programs for Studying Nanostructure in Crystals. *J. Phys.: Condens. Matter* **2007**, *19*, No. 335219.
(56) Bizzotto, F.; Arenz, M.; Quinson, J. Surfactant-Free Ir Nanoparticles Synthesized in Ethanol: Catalysts for the Oxygen Evolution Reaction. *Mater. Lett.* **2022**, *308*, No. 131209.
(57) Quinson, J.; Kunz, S.; Arenz, M. Surfactant-Free Colloidal Syntheses of Precious Metal Nanoparticles for Improved Catalysts. *ACS Catal.* **2023**, *13*, 4903−4937.
(58) Minguzzi, A.; Locatelli, C.; Lugaresi, O.; Achilli, E.; Cappelletti, G.; Scavini, M.; Coduri, M.; Masala, P.; Sacchi, B.; Vertova, A.; Ghigna, P.; Rondinini, S. Easy Accommodation of Different Oxidation States in Iridium Oxide Nanoparticles with Different Hydration Degree as Water Oxidation Electrocatalysts. *ACS Catal.* **2015**, *5*, 5104−5115.
(59) Reier, T.; Oezaslan, M.; Strasser, P. Electrocatalytic Oxygen Evolution Reaction (OER) on Ru, Ir, and Pt Catalysts: A Comparative Study of Nanoparticles and Bulk Materials. *ACS Catal.* **2012**, *2*, 1765−1772.
(60) Iwakura, C.; Tada, H.; Tamura, H. The Anodic Evolution of Oxygen on Iridium Oxide Electrode. *Denki Kagaku oyobi Kogyo Butsuri Kagaku* **1977**, *45*, 202−207.
(61) El-Sayed, H. A.; Weiß, A.; Olbrich, L. F.; Putro, G. P.; Gasteiger, H. A. OER Catalyst Stability Investigation Using RDE Technique: A Stability Measure or an Artifact? *J. Electrochem. Soc.* **2019**, *166*, F458−F464.
(62) Parthasarathy, A.; Srinivasan, S.; Appleby, A. J.; Martin, C. R. Temperature Dependence of the Electrode Kinetics of Oxygen Reduction at the Platinum/Nafion Interface—A Microelectrode Investigation. *J. Electrochem. Soc.* **1992**, *139*, 2530−2537.
(63) Kötz, R.; Stucki, S. Stabilization of RuO_2 by IrO_2 for Anodic Oxygen Evolution in Acid Media. *Electrochim. Acta* **1986**, *31*, 1311−1316.
(64) Suermann, M.; Schmidt, T. J.; Büchi, F. N. Comparing the Kinetic Activation Energy of the Oxygen Evolution and Reduction Reactions. *Electrochim. Acta* **2018**, *281*, 466−471.
(65) Duan, Y.; Dubouis, N.; Huang, J.; Dalla Corte, D. A.; Pimenta, V.; Xu, Z. J.; Grimaud, A. Revealing the Impact of Electrolyte Composition for Co-Based Water Oxidation Catalysts by the Study of Reaction Kinetics Parameters. *ACS Catal.* **2020**, *10*, 4160−4170.
(66) Nong, H. N.; Oh, H.; Reier, T.; Willinger, E.; Willinger, M.; Petkov, V.; Teschner, D.; Strasser, P. Oxide-Supported $IrNiO_x$ Core−Shell Particles as Efficient, Cost-Effective, and Stable Catalysts for Electrochemical Water Splitting. *Angew. Chem.* **2015**, *127*, 3018−3022.
(67) Pérez-Viramontes, N. J.; Escalante-García, I. L.; Guzmán-Martínez, C.; Galván-Valencia, M.; Durón-Torres, S. M. Electrochemical Study of Ir−Sn−Sb−O Materials as Catalyst-Supports for the Oxygen Evolution Reaction. *J. Appl. Electrochem.* **2015**, *45*, 1165−1173.
(68) Cognard, G.; Ozouf, G.; Beauger, C.; Dubau, L.; López-Haro, M.; Chatenet, M.; Maillard, F. Insights into the Stability of Pt Nanoparticles Supported on Antimony-Doped Tin Oxide in Different Potential Ranges. *Electrochim. Acta* **2017**, *245*, 993−1004.
(69) Oh, H.-S.; Nong, H. N.; Reier, T.; Bergmann, A.; Gliech, M.; Ferreira, J.; Araújo, A.; Willinger, E.; Schlö, R.; Teschner, D.; Strasser, P. Electrochemical Catalyst−Support Effects and Their Stabilizing Role for IrO_x Nanoparticle Catalysts during the Oxygen Evolution Reaction. *J. Am. Chem. Soc.* **2016**, *138*, 12552−12563.
(70) Geiger, S.; Kasian, O.; Mingers, A. M.; Mayrhofer, K. J. J.; Cherevko, S. Stability Limits of Tin-Based Electrocatalyst Supports. *Sci. Rep.* **2017**, *7*, No. 4595.
(71) Silva, G. C.; Venturini, S. I.; Zhang, S.; Löffler, M.; Scheu, C.; Mayrhofer, K. J. J.; Ticianelli, E. A.; Cherevko, S. Oxygen Evolution Reaction on Tin Oxides Supported Iridium Catalysts: Do We Need Dopants? *ChemElectroChem* **2020**, *7*, 2330−2339.
(72) Geiger, S.; Kasian, O.; Ledendecker, M.; Pizzutilo, E.; Mingers, A. M.; Fu, W. T.; Diaz-Morales, O.; Li, Z.; Oellers, T.; Fruchter, L.; Ludwig, A.; Mayrhofer, K. J. J.; Koper, M. T. M.; Cherevko, S. The Stability Number as a Metric for Electrocatalyst Stability Benchmarking. *Nat. Catal.* **2018**, *1*, 508−515.
(73) da Silva, C. D. F.; Claudel, F.; Martin, V.; Chattot, R.; Abbou, S.; Kumar, K.; Jiménez-Morales, I.; Cavaliere, S.; Jones, D.; Rozière, J.; Solà-Hernandez, L.; Beauger, C.; Faustini, M.; Peron, J.; Gilles, B.; Encinas, T.; Piccolo, L.; de Lima, F. H. B.; Dubau, L.; Maillard, F. Oxygen Evolution Reaction Activity and Stability Benchmarks for Supported and Unsupported IrO_x Electrocatalysts. *ACS Catal.* **2021**, *11*, 4107−4116.
(74) Inaba, M.; Jensen, A. W.; Sievers, G. W.; Escudero-Escribano, M.; Zana, A.; Arenz, M. Benchmarking High Surface Area Electrocatalysts in a Gas Diffusion Electrode: Measurement of Oxygen Reduction Activities under Realistic Conditions. *Energy Environ. Sci.* **2018**, *11*, 988−994.

https://doi.org/10.1021/acscatal.3c01193
ACS Catal. 2023, 13, 7568−7577

Supporting information

Influence of temperature on the performance of carbon- and ATO-supported OER catalysts in a GDE setup

Aline Bornet[1], Rebecca Pittkowski[2], Tobias M. Nielsen[2], Etienne Berner[1], Annabelle Maletzko[3], Johanna Schröder[1], Jonathan Quinson[2,4], Julia Melke[3], Kirsten M. Ø. Jensen[2], Matthias Arenz[1,*]

[1] Department of Chemistry, Biochemistry and Pharmaceutical Sciences, University of Bern, Freiestrasse 3, 3012 Bern, Switzerland

[2] Department of Chemistry, University of Copenhagen, Universitetsparken 5, 2100 Copenhagen, Denmark

[3] Department for Applied Electrochemistry, Fraunhofer-Institute for Chemical Technology ICT, Joseph-von-Fraunhofer Strasse 7, 76327 Pfinztal, Germany

[4] Biochemical and Chemical Engineering Department, Aarhus University, Åbogade 40, 8200 Aarhus, Denmark

* Corresponding authors: matthias.arenz@unibe.ch

Chemicals and materials

Ultra-pure water (MilliQ-system, 2.7 ppb total organic carbon (TOC), 18.2 MΩ) was used to clean the GDE cell and to prepare the electrolyte and the catalyst ink.

For the catalyst synthesis, hydrated $IrCl_3$ (99.8% metals basis) and $RuCl_3$ (ReagentPlus) were purchased from Alfa Aesar and Sigma Aldrich, respectively, and stored in a glovebox. EtOH (EtOH absolute, VWR Chemicals) was used to dissolve the precursor salt, to prepare the alkaline (NaOH, Hänseler) solvent, and to disperse the support carbon Ketjen black (EC-300J, Fuel Cell Store) and ATO (NanoArc, 99.5%, Alfa Aesar). The catalyst inks were prepared using isopropanol (IPA, HPLC grade, VWR Chemicals), KOH (Hänseler) and a Nafion dispersion in H_2O (D1021, Fuel Cell Store). A horn sonicator (Q500 sonicator, QSONICA sonicators) was used to disperse the support and the catalyst. A rotary evaporator (RC 600) from knf was employed to evaporate the solvent.

The GDEs were prepared using a coated gas diffusion layer (GDL, Freudenberg H23C8, 0.230 mm thick, Fuel Cell Store) and a Nafion membrane (Nafion 117, 183 µm thick, Fuel Cell Store). H_2O_2 (30%, Hänseler) and H_2SO_4 (96%, Grogg Chemie) were used to activate the Nafion membrane (see below). The assembly of the GDE setup needed also a non-coated GDL (Freudenberg H23, 0.210 mm thick, Fuel Cell Store). The electrolyte was prepared using $HClO_4$ (ACS reagent, 70%) from Sigma Aldrich. O_2 (Alphagaz 1, 45) was purchased from Air Liquide. The electrochemical measurements were performed with a computer controlled Nordic electrochemistry potentiostat (ECi – 242).

For conductivity measurements, a Keithley 2400 multimeter and a laser distance sensor LAR-10-5V from Waycon Präzisionstechnik GmbH were used.

Cu grids (for unsupported catalyst: Quantifoil, 100 Classic Holey Carbon films; for supported catalysts: Quantifoil, 100 Lacey Carbon films) were used as sample holder for the TEM characterization. For SEM/EDX characterization, Cu tape (3M #1182 electrical tape) was used as a conductive adhesive tape. Graphite foil (0.13 mm thick, 99.8%, Alfa Aesar) was used as

sample holder for EDX characterization of the inks. Polyimide tubes (Wall thickness: 0.025 mm, outside diameter 1.05 mm, GoodFellow) were used as sample holders for total scattering experiments at DanMax beamline at MAXIV synchroton.

Nafion membrane activation

⌀ 2 cm Nafion membranes were punched out of a Nafion sheet. The ⌀ 2 cm membrane were treated at 80 °C for 30 min in 5 wt.% H_2O_2. Then, they were rinsed with excess of MilliQ water and heated in MilliQ water at 80 °C for 30 min. After rinsing them, they were treated with 8 wt.% H_2SO_4 at 80 °C for 30 min. Finally, the activated membranes were rinsed with excess of MilliQ water and stored in MilliQ water.

WE loading determination by TGA

Table S1. Summary of TGA data of Ir NPs immobilized on C-support measured in O_2-atmosphere between 25 and 1000 °C at 10 °C min^{-1}. The expected metal loading on the GDE is 1 mg_{Ir} cm^{-2}.

	m_i(Ir) / mg	Loading(Ir) / mg_{Ir} cm^{-2}	m(IrO_2) / mg	Loading(IrO_2) / mg_{IrO2} cm^{-2}
Expected values	0.071	1.000	0.082	1.166
Measured values	/	/	0.061	0.863

As the measurement was performed in an oxidative environment at elevated temperatures, a full oxidation of the Ir nanoparticles to IrO_2 is expected at the end of the experiment. The relative error to the expected loading is 26%. It must be noted that the initial mass of Ir is a nominal value (calculated from a total reduction of $IrCl_3$ during the synthesis).

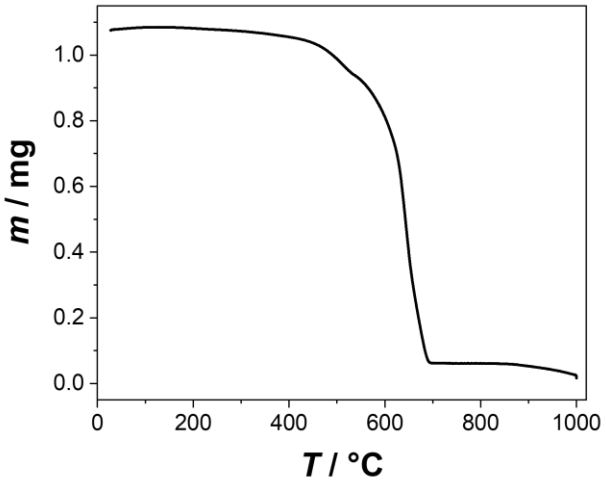

Figure S1. TGA curve of Ir NPs immobilized on C-support measured in O_2-atmosphere between 25 and 1000 °C at 10 °C min^{-1}.

GDE setup and its assembly

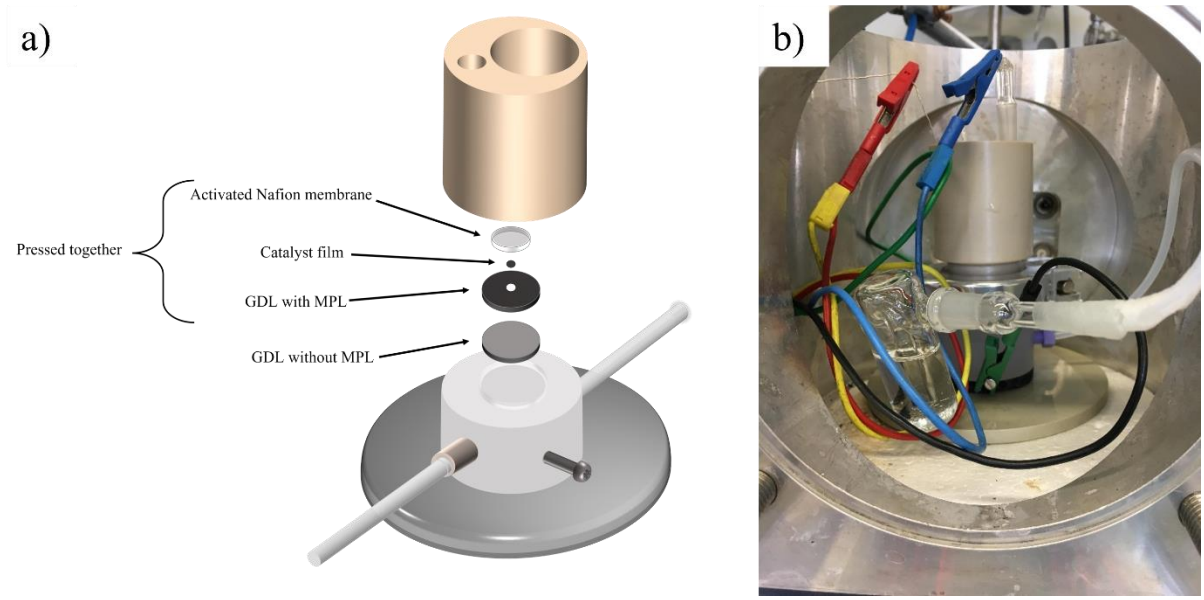

Figure S2. Sketch of the GDE setup assembly (a) (image adapted from Schröder *et al.*[1] (a) and picture of the connected GDE setup in a Faradaic cage (b).

Synthesis of different composition and TEM micrographs of the different compositions

The synthesis of the nominal composition of $Ir_{0.66}Ru_{0.33}$, $Ir_{0.33}Ru_{0.66}$ and Ru NPs follow the same approach than the one described in the experimental section **a**. Only the pipetted ratio between 20 mM $IrCl_3$ in EtOH and 20 mM $RuCl_3$ in EtOH differ and are the following:

- For $Ir_{0.66}Ru_{0.33}$ NPs: 6.67 mL of 20 mM $IrCl_3$ in EtOH and 3.33 mL 20 mM $RuCl_3$ in EtOH,
- For $Ir_{0.33}Ru_{0.66}$ NPs: 3.33 mL of 20 mM $IrCl_3$ in EtOH and 6.67 mL 20 mM $RuCl_3$ in EtOH, and
- For Ru NPs: 2 mL of 20 mM $RuCl_3$ in EtOH.

The mixtures were refluxed to 95 °C for 10 min to obtain $Ir_{0.66}Ru_{0.33}$ and $Ir_{0.33}Ru_{0.66}$, respectively 30 min to obtain pure Ru NPs.

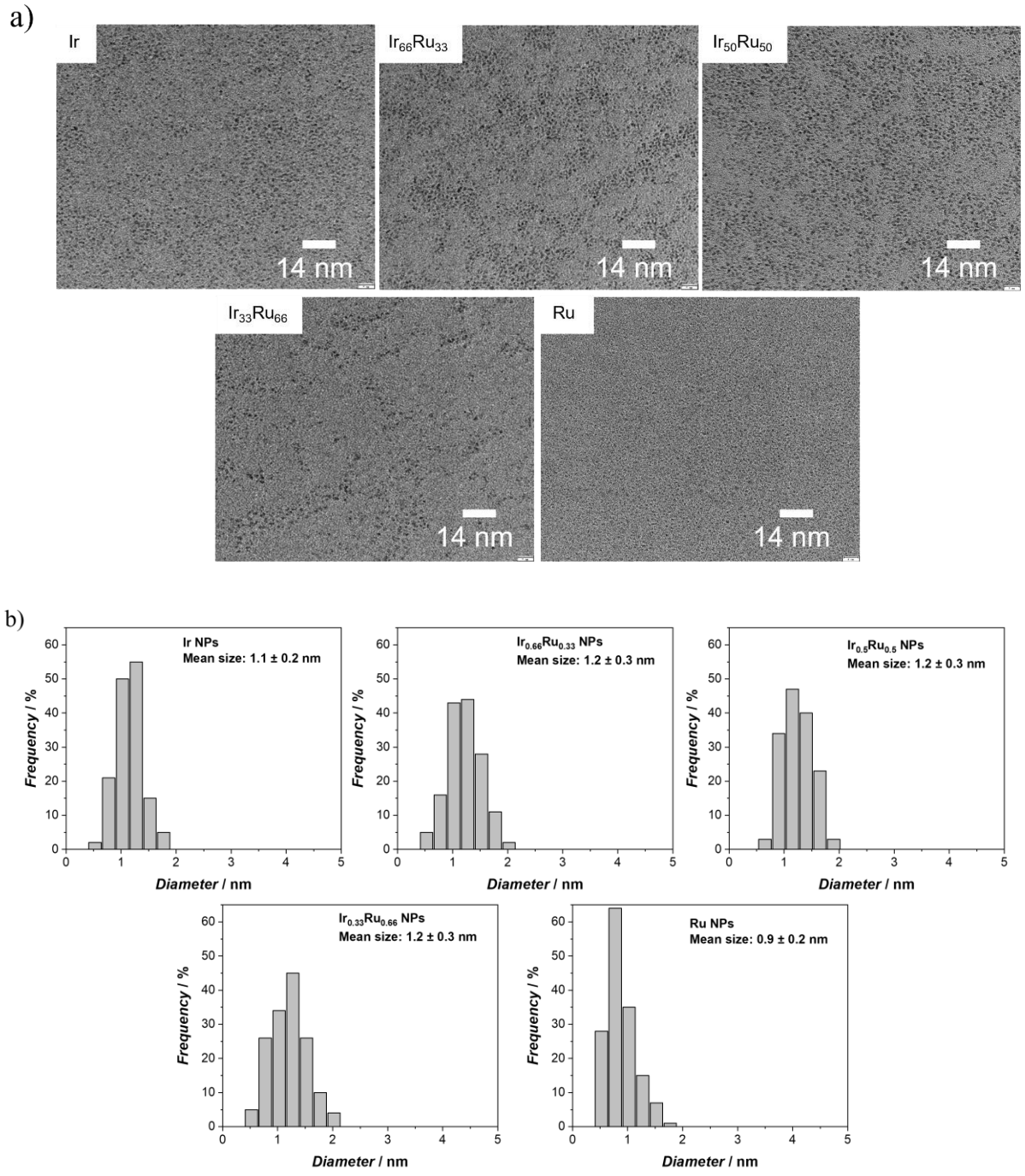

Figure S3. TEM micrographs of different nominal compositions of unsupported Ir_xRu_y NPs (a) and their respective size distribution (b).

XAS of pristine Ir/C and Ir /ATO – influence of the support on the structure of the NPs

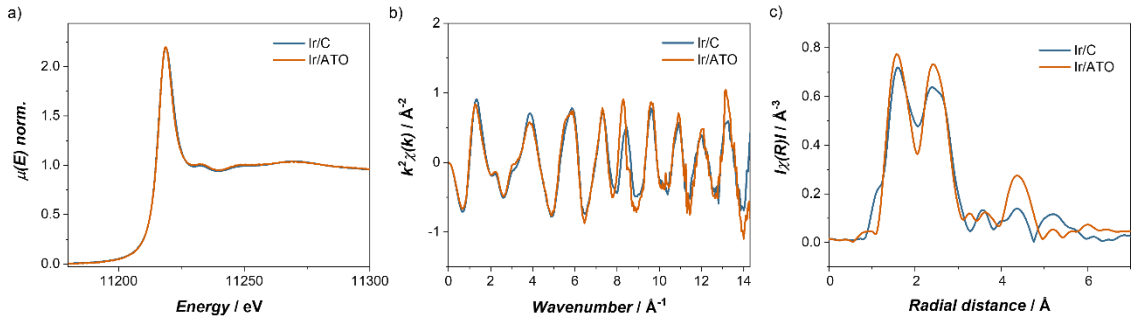

Figure S4. XANES spectra (a) and Fourier transform magnitudes of the k^2-weighted extended X-ray absorption fine structure (EXAFS) (b) and (c) data of pristine Ir/C and Ir/ATO measured at the Ir L_{III}-edge.

As both the Iridium XANES spectra and the EXAFS of the NPs supported on C and ATO agree, we find no influence of the support on the structure of the metal NPs. This is further supported in the modelling of the EXAFs data, see Table S2.

Table S2. Parameters obtained for EXAFS data fitting of pristine Ir/C and Ir/ATO on the Ir L_{III}-edge, that shows first nearest neighbour coordination shell (N), atomic bond length (R), Debye Waller factors (mean squared bond length disorder) (σ^2), absorption edge energy (E_0), and R_f-factor as a measure of fit quality.

Ir edge of pristine samples						
Sample	Bond	N	R / Å	σ^2 / Å^2	E_0 / eV	R_f
Ir/C	Ir-O_1	3.0 ± 0.4	1.99(2)	0.006(2)	11225 ± 1	0.008
	Ir-Ir_1	6.4 ± 0.6	2.70(2)	0.005(4)		
Ir/ATO	Ir-O_1	2.5 ± 0.4	1.99(2)	0.002(2)	11225 ± 3	0.019
	Ir-Ir_1	5.9 ± 2.0	2.71(1)	0.004(2)		

Aging process monitored by XAS

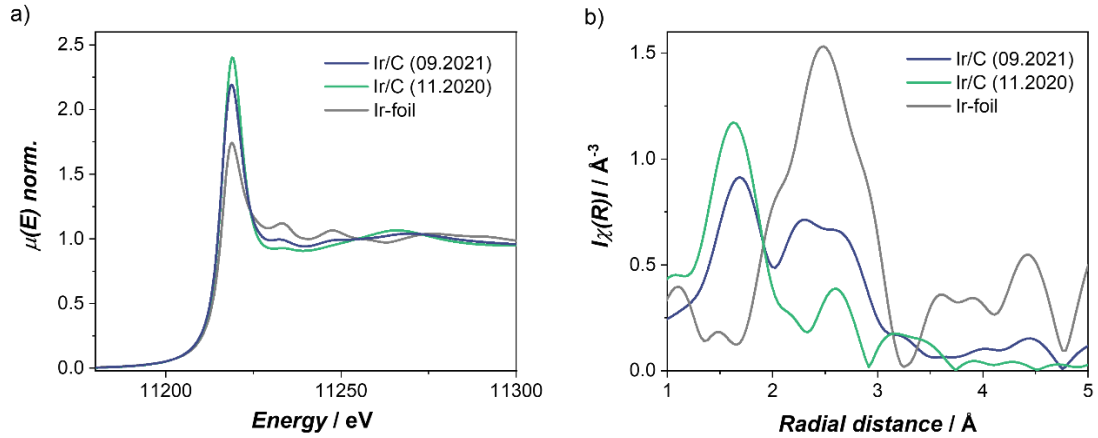

Figure S5. Effect of storage on the degree of oxidation of the catalyst (Ir/C) film stored in the air. XANES spectra (a) and Fourier transform magnitudes of the k^2-weighted extended X-ray absorption fine structure (EXAFS) data (b) of differently aged Ir/C and an Ir metal foil reference measured at the Ir L_{III}-edge. The Ir/C film corresponding to the green line was prepared 15 months prior and the one corresponding to the blue line only 5 months prior the measurements performed in February 2022.

PDF analysis of pristine and activated C-immobilized catalysts

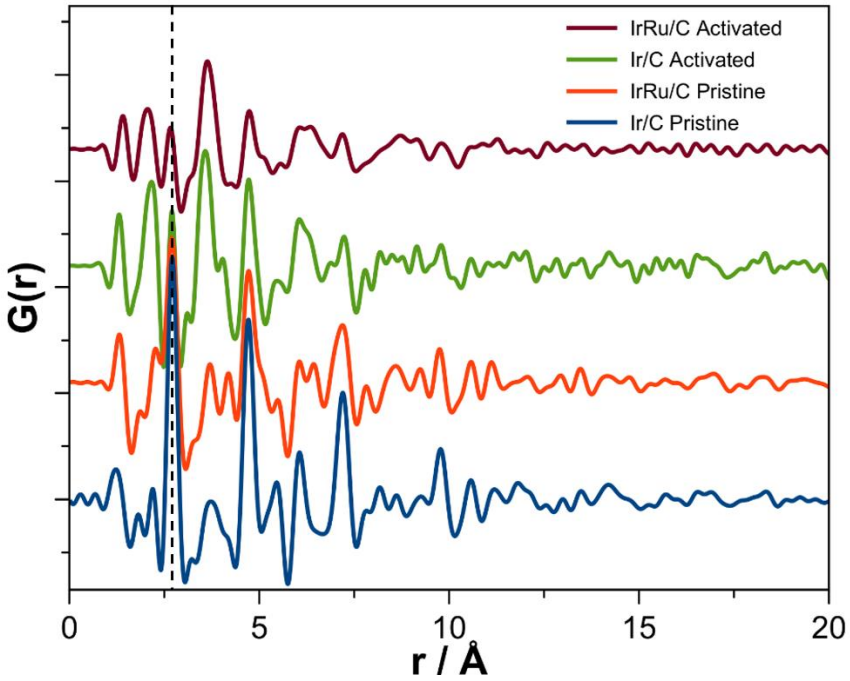

Figure S6. PDF of the total scattering experiments on C-immobilized Ir and $Ir_{0.4}Ru_{0.6}$, both pristine and activated. All data are background subtracted.

The peak at *ca.* 3.6 Å is more intense for the activated samples than for the pristine ones. This peak arises from a metal-oxygen distance in the structure, showing the presence of the oxide phase in the material. At *ca.* 2.7 Å (dotted line), the peak (metal-metal distance) of the activated samples losses its intensity, but do not vanish, thus, confirming the coexistence of both metallic and oxide species in the activated samples.

Table S3. Summarized particle sizes, unit cell parameter and atomic displacement parameter (ADP) for all pristine and activated Ir and $Ir_{0.4}Ru_{0.6}$ catalyst immobilized on carbon-support. For the pristine $Ir_{0.4}Ru_{0.6}$ sample, both a fcc Ir phase and a hcp Ru phase were included to get the best fit. The quality of the fits was determined by the R_w values and are R_w= 0.33 for Ir/C, R_w= 0.69 for IrO_2/C, R_w= 0.62 for the $Ir_{0.4}Ru_{0.6}$/C and R_w= 0.57 for $Ir_{0.4}Ru_{0.6}O_x$/C.

Ir/C pristine – Ir fit	
Particle size	15 Å
Unit cell parameter a, b, c	3.85 Å
ADP	0.00783 $Å^2$
IrO_x /C activated – Ir fit	
Particle size	14 Å
Unit cell parameter a, b, c	3.86 Å
ADP	0.002865 $Å^2$
IrO_x/C activated – IrO_2 fit	
Particle size	7 Å
Unit cell parameter a, b	4.59 Å
Unit cell parameter c	3.18 Å
ADP for Ir	0.009216 $Å^2$
ADP for O	0006872 $Å^2$
$Ir_{0.4}Ru_{0.6}$/C pristine – Ir fit	
Particle size	14 Å
Unit cell parameter a, b, c	3.84 Å
ADP	0.01276 $Å^2$
$Ir_{0.4}Ru_{0.6}$/C pristine – Ru fit	
Particle size	36 Å
Unit cell parameter a, b	2.88 Å
Unit cell parameter c	3.99 Å
ADP	0.03846 $Å^2$
$Ir_{0.4}Ru_{0.6}O_x$/C activated – Ir fit	
Particle size	13 Å
Unit cell parameter a, b, c	3.85 Å
ADP	0.002283 $Å^2$
$Ir_{0.4}Ru_{0.6}O_x$/C activated – IrO_2 fit	
Particle size	7 Å
Unit cell parameter a, b	4.63 Å
Unit cell parameter c	3.44Å
ADP for Ir	0.006167 $Å^2$
ADP for O	0.004166 $Å^2$

EXAFS of pristine $Ir_{0.4}Ru_{0.6}$/C and $Ir_{0.4}Ru_{0.6}$/ATO – alloy determination

Table S4. Parameters obtained for EXAFS data fitting of pristine $Ir_{0.4}Ru_{0.6}$/C and $Ir_{0.4}Ru_{0.6}$/ATO on the Ir L_{III}-edge and the Ru K-edge, that shows first nearest neighbour coordination shell (N), atomic bond length (R), Debye Waller factors (mean squared bond length disorder) (σ^2), absorption edge energy (E_0), and R_f-factor as a measure of fit quality.

$Ir_{0.4}Ru_{0.6}$/C pristine						
Edge	Bond	N	R / Å	σ^2 / Å^2	E_0 / eV	R_f
Ir	Ir-O_1	2.7 ± 0.8	2.00(2)	0.007(4)	11226 ± 2	0.019
	Ir-Ru_1	3.2 ± 1.3	2.69(2)	0.004(3)		
	Ir-Ir_1	2.8 ± 1.2	2.69(2)	0.003(2)		
Ru	Ru-O_1	2.6 ± 0.7	2.00(2)	0.002(1)	22119 ± 3	0.010
	Ru-Ru_1	2.2 ± 0.3	2.68(2)	0.002(3)		
	Ru-Ir_1	3.0 ± 0.5	2.69(2)	0.002(3)		
$Ir_{0.4}Ru_{0.6}$/ATO pristine						
Ir	Ir-O_1	3.1 ± 2.4	2.00(2)	0.002(3)	11225 ± 4	0.055
	Ir-Ru_1	2.4 ± 1.3	2.67(4)	0.007(5)		
	Ir-Ir_1	2.8 ± 0.5	2.67(4)	0.007(6)		
Ru	Ru-O_1	4.1 ± 1.1	2.00(1)	0.007(4)	22119 ± 4	0.002
	Ru-Ru_1	1.3 ± 0.6	2.66(1)	0.005(7)		
	Ru-Ir_1	2.9 ± 2.5	2.68(1)	0.005(7)		

Particle size determination by TEM and SAXS of the supported catalysts

Table S5. Summarized diameter obtained by averaging particles sized for 150 NPs on TEM micrographs and by analysing SAXS data of the four supported catalysts.

Sample	TEM	SAXS	
	⌀, pristine sample / nm	⌀, pristine sample / nm	⌀, activated sample / nm
Ir/C	1.3 ± 0.4	1.8 ± 0.7	2.6 ± 1.3
$Ir_{0.4}Ru_{0.6}$/C	1.5 ± 0.4	2.8 ± 1.1	2.8 ± 1.3
Ir/ATO	1.3 ± 0.3	1.8 ± 0.8	2.8 ± 0.1
$Ir_{0.4}Ru_{0.6}$/ATO	1.3 ± 0.3	1.7 ± 0.7	2.7 ± 0.2

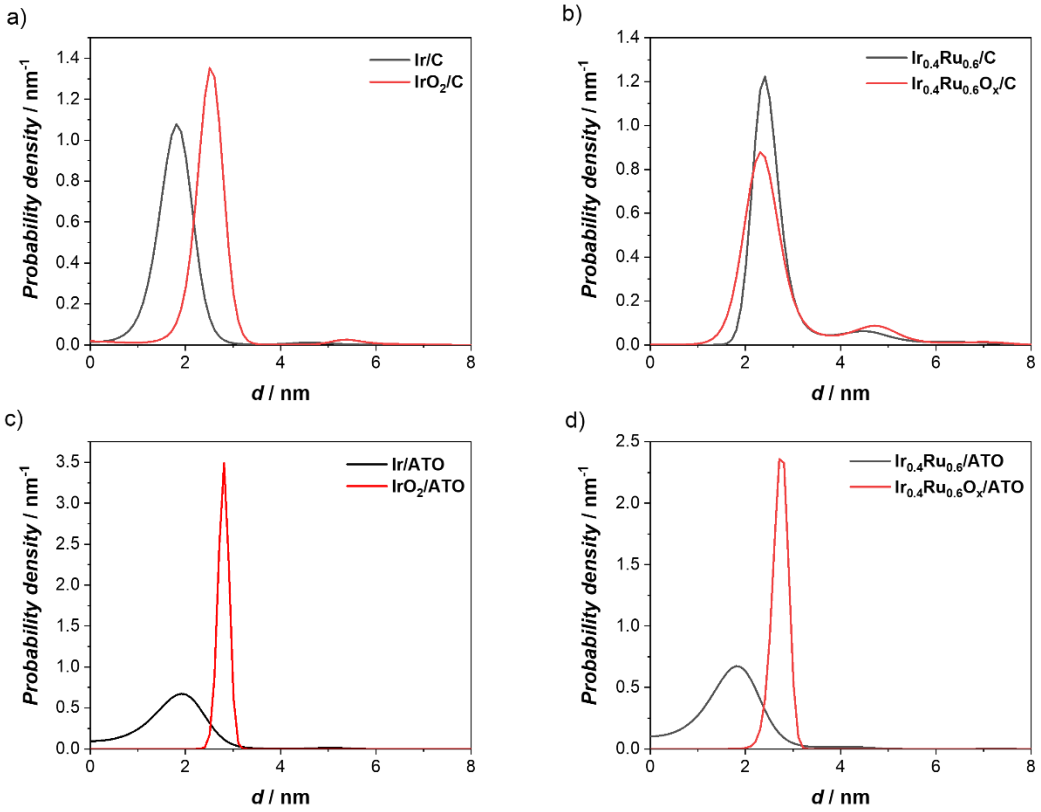

Figure S7. Particle size distribution monitored by SAXS for Ir/C (a), $Ir_{0.4}Ru_{0.6}$/C (b), Ir/ATO (c), and $Ir_{0.4}Ru_{0.6}$/ATO (d). The pristine (black) and the activated (red) samples are compared.

All samples beside $Ir_{0.4}Ru_{0.6}/C$ face a particle growth after the activation step. The reason behind the non-growth of $Ir_{0.4}Ru_{0.6}/C$ is explained by an aging process. The pristine film was prepared about a year prior the actual SAXS measurement, thus the NPs had time to oxidize in air. Therefore, both pristine and activated samples demonstrate a similar particle size.

Moreover, based on the density of Ir and IrO_2 (Ir: 22.6 g cm^{-3}, IrO_2: 2.00 g cm^{-3}) [2] and assuming fully reduced pristine species, a slightly higher than two-fold growth is expected if the entire NPs would be fully oxidized (from 1.8 to 4.0 nm). However, according to the obtained SAXS results, the particles grew only 1 nm (Table S5). This was explained by an incomplete oxidation of the NPs.

PDF analysis of activated Ir/ATO

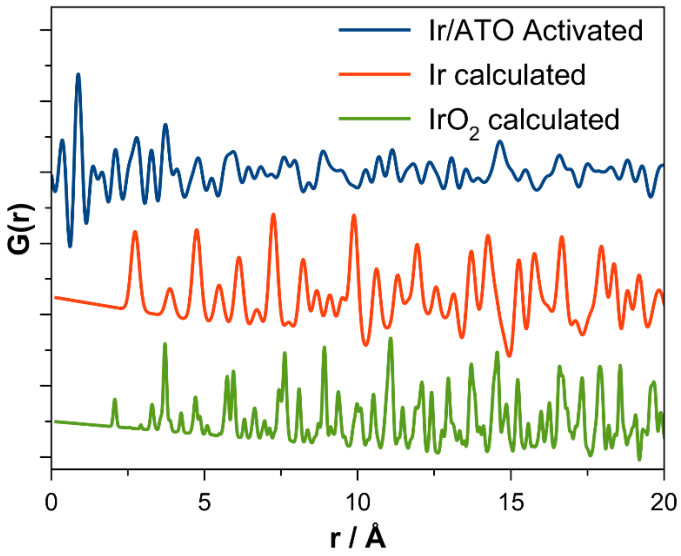

Figure S8. PDF of activated Ir/ATO. The peaks arising from either Ir or IrO_2 are difficult to distinguish due to the presence of the oxide support.

EXAFS of activated Ir/C and $Ir_{0.4}Ru_{0.6}$/C – metal-metal coordination after activation

Table S6. Parameters obtained for EXAFS data fitting of activated Ir/C and $Ir_{0.4}Ru_{0.6}$/C on the Ir L_{III}-edge and the Ru K-edge, that shows first nearest neighbour coordination shell (N), atomic bond length (R), Debye Waller factors (mean squared bond length disorder) (σ^2), absorption edge energy (E_0), and R_f-factor as a measure of fit quality.

Ir/C activated						
Edge	Bond	N	R / Å	σ^2 / Å^2	E_0 / eV	R_f
Ir	Ir-O_1	5.7 ± 0.7	2.02(1)	0.007(2)	11227 ± 2	0.016
	Ir-Ir_1	1.1 ± 0.9	2.70(1)	0.007(6)		
$Ir_{0.4}Ru_{0.6}$/C activated						
Ir	Ir-O_1	5.7 ± 0.7	2.00(1)	0.006(2)	11227 ± 2	0.016
	Ir-Ru_1	0.3 ± 0.3	2.67(6)	0.004(6)		
	Ir-Ir_1	1.1 ± 0.9	2.68(3)	0.004(6)		
Ru	Ru-O_1	3.6 ± 0.5	1.92(1)	0.003(2)	22115 ± 3	0.045
	Ru-Ru_1	1.1 ± 0.4	2.66(1)	0.002(4)		
	Ru-Ir_1	2.9 ± 0.6	2.68(4)	0.002(4)		

i*R*-corrected potentials transients of IrO_x/C, IrO_x/ATO

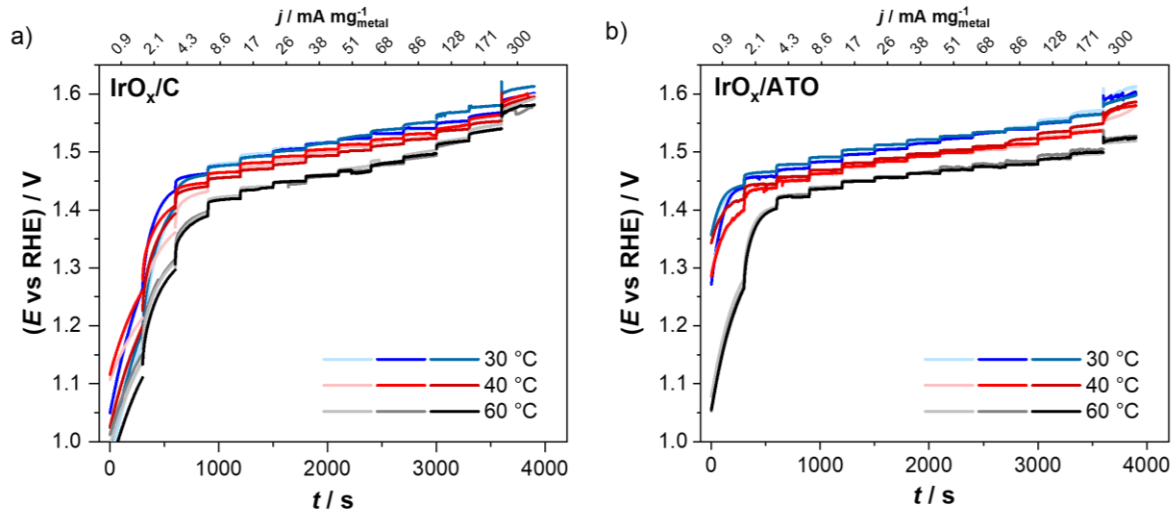

Figure S9. Electrocatalytic OER i*R*-corrected potential transients of IrO_x/C (a) and IrO_x/ATO (b) at 30 (blue), 40 (red) and 60 °C (black). All measurements were performed in the GDE setup in an O_2-atmosphere using 4 M $HClO_4$ as an electrolyte. Nominal catalyst loading: 654 μg_{metal} cm^{-2}.

Tafel plots and slopes of IrO_x/C and IrO_x/ATO

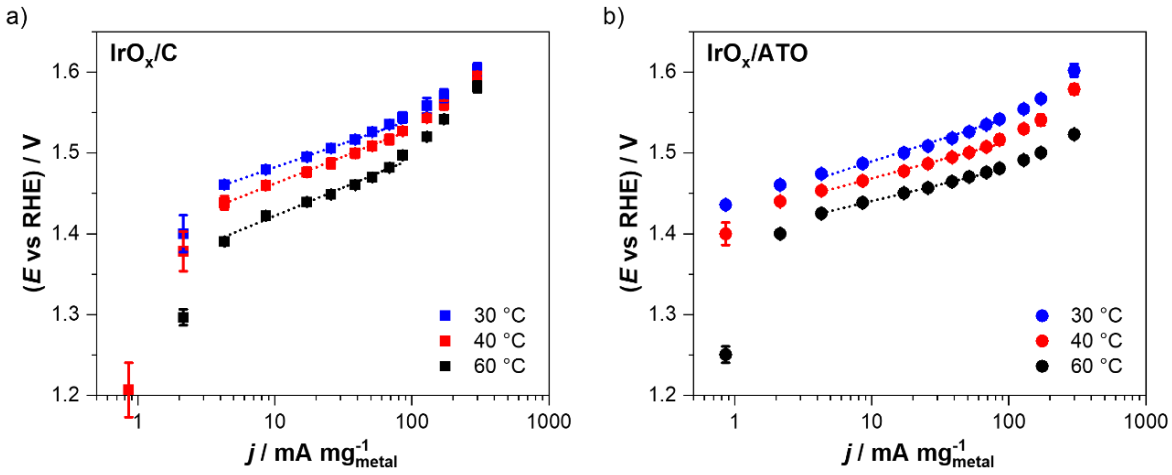

Figure S10. Tafel plots of IrO_x/C (a) and IrO_x/ATO (b) at 30 (blue), 40 (red) and 60 °C (black). The error bars show the standard deviation of the three independent measurements. All measurements were performed in the GDE setup in an O_2-atmosphere using 4 M $HClO_4$ as an electrolyte. Nominal catalyst loading: 654 μg_{metal} cm^{-2}.

Table S7. Tafel slopes of IrO_x/C, IrO_x/ATO, $Ir_{0.4}Ru_{0.6}O_x$/C and $Ir_{0.4}Ru_{0.6}O_x$/ATO at 30, 40 and 60 °C. The same mass current density range (ca. 4 and 85 mA mg_{metal}^{-1}) was chosen to determine the Tafel slopes.

Sample	Tafel slopes (mV dec^{-1}) at		
	30 °C	40 °C	60 °C
IrO_x/C	59	69	70
$Ir_{0.4}Ru_{0.6}O_x$/C	53	57	55
IrO_x/ATO	54	47	41
$Ir_{0.4}Ru_{0.6}O_x$/ATO	62	60	51

Comparison of OER activities measured at 30, 40, and 60 °C

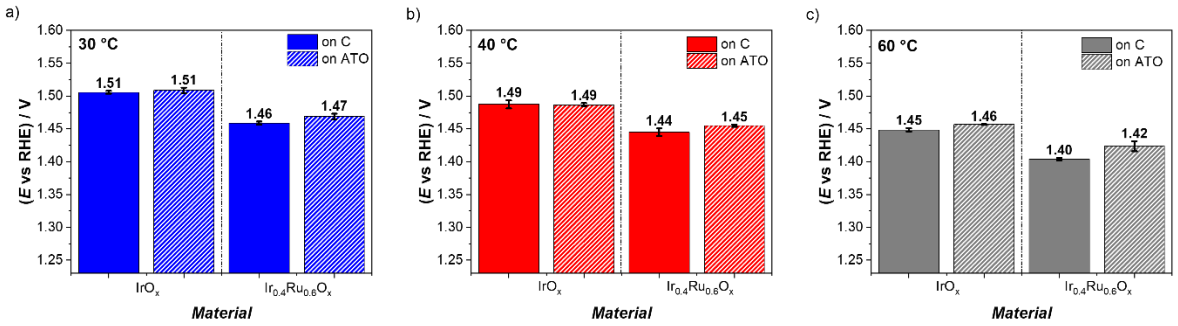

Figure S11. Comparison of the electrode potential reached at fixed a current density of 25.68 mA mg_{metal}^{-1} (which corresponds to ca. 7.5 mA cm^{-2}) for IrO_x (left hand side of the graphs) and $Ir_{0.4}Ru_{0.6}O_x$ (right hand side of the graphs) deposited on C (solid bars) or ATO (dashed bars) at 30 (a), 40 (b) and 60 °C (c).

EDX data – Ru leaching

Table S8. Summarized ratios (at.%) between Ir and Ru calculated by top-view EDX for $Ir_{0.4}Ru_{0.6}$/C and $Ir_{0.4}Ru_{0.6}$/ATO catalysts. The catalyst is in a form of an ink or a film.

Sample		Ratio / at.%	
		Ir	**Ru**
$Ir_{0.4}Ru_{0.6}$/C pristine - ink		41	59
$Ir_{0.4}Ru_{0.6}$/C pristine - film		41	59
$Ir_{0.4}Ru_{0.6}O_x$/C activated at 60 °C - film	centre	41	59
	edges	64	36
$Ir_{0.4}Ru_{0.6}$/ATO pristine - ink		41	59
$Ir_{0.4}Ru_{0.6}$/ATO pristine - film		40	60
$Ir_{0.4}Ru_{0.6}O_x$/ATO activated at 60 °C - film	centre	38	62
	edges	70	30

Activated Ru-containing samples at 60 °C were analysed to quantify any elemental leaching. It was found that Ru was partially and not homogenously leached out of the sample. The edges of the 3 mm sample showed a decrease of the Ru content, while the centre displayed an identical ratio as the pristine one.

Conductivity measurements

Table S9. Summarized ATO- and C-support individual conductivity measurements and their sample thickness. All measurements were performed with a mass of 100 mg and a pressure of 11.29 MPa.

Sample	Conductivity / S cm^{-1}	Sample thickness / mm
ATO support	$9.67008 * 10^{-4}$	1.23046
	$7.96755 * 10^{-4}$	1.16972
	$9.11954 * 10^{-4}$	1.21542
C support	9.72869	6.06978
	9.98393	5.89936

EDX data – Sb leaching

The suspected Sb leaching from the ATO support was determined *post-mortem* by EDX. It must be noted that the pristine and the *post-mortem* samples are different samples. In Fig. S11 and S12, the *post-mortem* samples measured at 30 °C and 60 °C for IrO_x/ATO and $Ir_{0.4}Ru_{0.6}O_x$/ATO are represented.

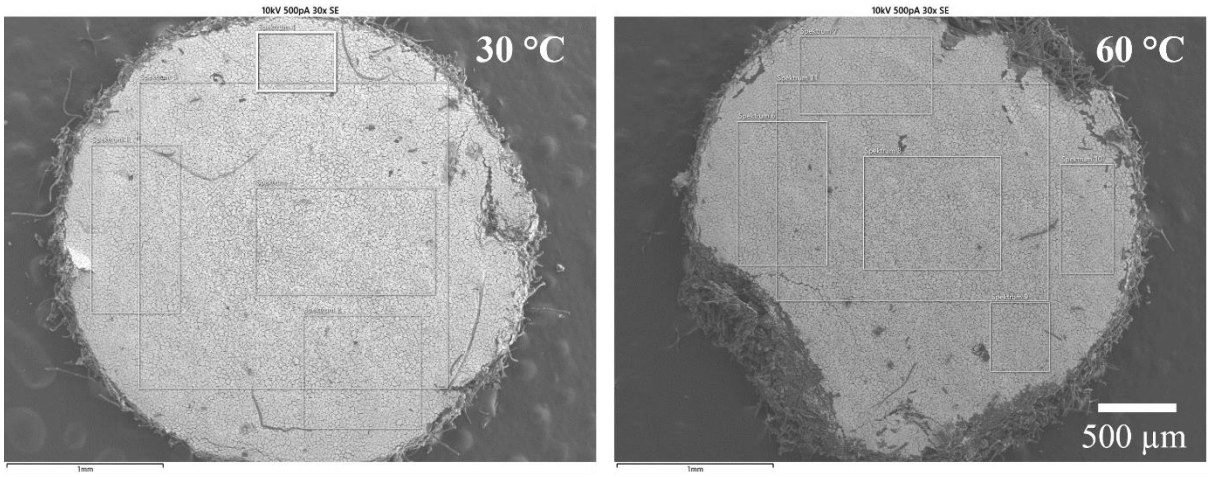

Figure S12. SEM images of the *post-mortem* IrO_x/ATO ⌀ 3 mm sample disks measured at 30 and 60 °C. The squares on the images correspond to the different areas analysed by EDX.

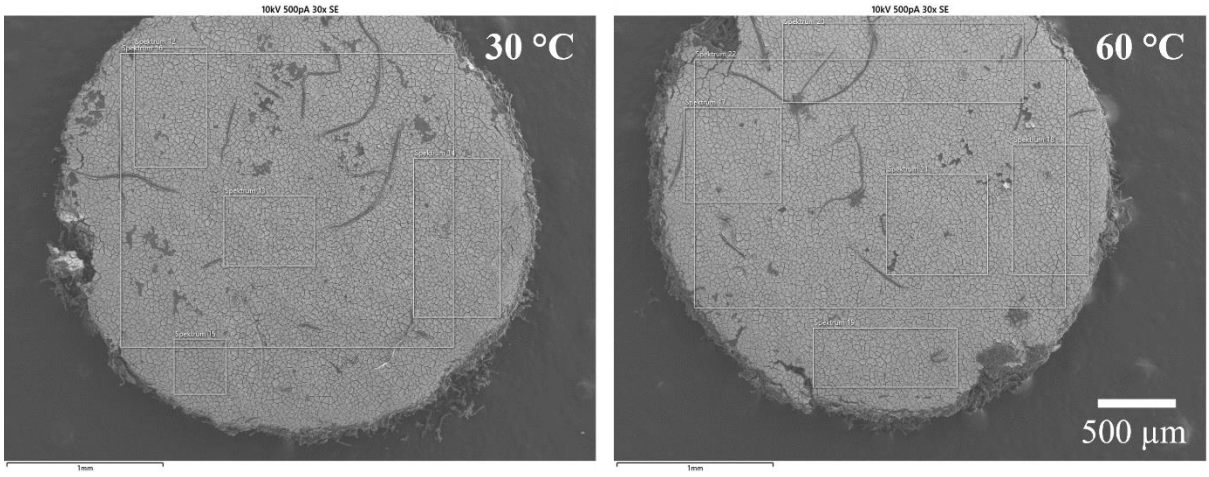

Figure S13. SEM images of the *post-mortem* $Ir_{0.4}Ru_{0.6}O_x$/ATO ⌀ 3 mm sample disks measured at 30 and 60 °C. The squares on the images correspond to the different areas analysed by EDX.

Table S10. Comparison of the ratios (wt.%) between Sn and Sb for pristine and *post-mortem* (30 and 60 °C) IrO_x/ATO and $Ir_{0.4}Ru_{0.6}O_x$/ATO catalyst films. The measurements were performed in a top-view configuration.

Sample	Area	Sn:Sb ratio (wt.%)	Average Sn:Sb ratio (wt.%)
Pristine Ir/ATO	/	/	87 : 13
Post-mortem IrO_x/ATO at 30 °C	1	90.5 : 9.5	89 : 11
	2	87.8 : 12.2	
	3	89.3 : 10.7	
	4	89.7 : 10.3	
	5	88.9 : 11.1	
Post-mortem IrOx/ATO at 60 °C	6	92.0 : 8.0	91 : 9
	7	90.2 : 9.8	
	8	90.3 : 9.7	
	9	90.4 : 9.6	
	10	91.0 : 9.0	
	11	89.6 : 10.4	
Pristine $Ir_{0.4}Ru_{0.6}$/ATO	/	/	85 : 15
Post-mortem $Ir_{0.4}Ru_{0.6}O_x$/ATO at 30 °C	12	87.4 : 12.6	87 : 13
	13	87.7 : 12.3	
	14	87.9 : 12.1	
	15	86.4 : 13.6	
	16	87.0 : 13.0	
Post-mortem $Ir_{0.4}Ru_{0.6}O_x$/ATO at 60 °C	17	87.7 : 12.3	88 : 12
	18	87.6 : 12.4	
	19	88.5 : 11.5	
	20	88.0 : 12.0	
	21	87.1 : 12.9	
	22	88.1 : 11.9	

References

(1) Schröder, J.; Mints, V. A.; Bornet, A.; Berner, E.; Fathi Tovini, M.; Quinson, J.; Wiberg, G. K. H.; Bizzotto, F.; El-Sayed, H. A.; Arenz, M. The Gas Diffusion Electrode Setup as Straightforward Testing Device for Proton Exchange Membrane Water Electrolyzer Catalysts. *JACS Au* **2021**, *1* (3), 247–251. https://doi.org/10.1021/JACSAU.1C00015.

(2) Hartig-Weiss, A.; Miller, M.; Beyer, H.; Schmitt, A.; Siebel, A.; Freiberg, A. T. S.; Gasteiger, H. A.; El-Sayed, H. A. Iridium Oxide Catalyst Supported on Antimony-Doped Tin Oxide for High Oxygen Evolution Reaction Activity in Acidic Media. *ACS Appl Nano Mater* **2020**. https://doi.org/10.1021/ACSANM.9B02230.

MANUSCRIPT III

Aline Bornet, Simon Pitscheider, Annabelle Maletzko, Nedjeljko Seselj, Erlend Bertheussen, Christoffer M. Pedersen, Gustav K. H. Wiberg, Julia Melke, Christian Kallesøe, and Matthias Arenz

Beyond RDE Characterisation - Unveiling IrRu/ATO OER Catalyst Stability with a GDE Setup

Submitted to Electrochimica Acta

Beyond RDE Characterisation – Unveiling IrRu/ATO OER Catalyst Stability with a GDE Setup

Aline Bornet[1], Simon Pitscheider[2], Annabelle Maletzko[3], Nedjeljko Seselj[4], Erlend Bertheussen[2], Christoffer M. Pedersen[2], Gustav K. H. Wiberg[1], Julia Melke[3], Christian Kallesøe[2], Matthias Arenz[1,*]

[1] Department of Chemistry, Biochemistry and Pharmaceutical Sciences, University of Bern, Freiestrasse 3, 3012 Bern, Switzerland

[2] Danish Technological Institute, Gregersensvej 1, 2630 Taastrup, Denmark

[3] Department for Applied Electrochemistry, Fraunhofer-Institute for Chemical Technology ICT, Joseph-von-Fraunhofer Strasse 7, 76327 Pfinztal, Germany

[4] Blue World Technologies, Egeskovvej 6C, 3490 Kvistgaard, Denmark

* Corresponding author: matthias.arenz@unibe.ch

Abstract

In this study, we have investigated the stability of antimony-doped tin oxide (ATO) supported IrRu nanoparticles, as catalyst for the oxygen evolution reaction (OER). Conventional stability tests using a rotating disc electrode (RDE) are demonstrated to lead to distorted results, a fact typically addressed to the massive formation of O_2 gas bubbles which block the catalytic active sites. In agreement with previous results, our investigations suggest that the observed decay in current density is not to be confused with catalyst degradation. To mitigate the limitations of the RDE approach, a gas diffusion electrode (GDE) setup was used instead for the stability measurements. Using a carbon gas diffusion layer (GDL) as substrate for the catalyst film, similar beginning-of-life (BoL) and end-of-life (EoL) activities were observed in the low current density region; however, large disparities were found at larger current densities. For meaningful degradation studies, the carbon GDL had to be replaced by a titanium-based substrate. This way a more accurate assessment of the catalyst stability is demonstrated. Although at steady-state conditions the tested IrRu/ATO catalyst exhibited a slight decrease in current densities with time, the BoL and EoL activities are nearly identical.

1. Introduction

Finding a sustainable, long-term solution for storing surplus energy is crucial to advancing renewable energy technologies and efficiently addressing the challenges imposed by the climate change. Energy storage into chemical bonds represents an attractive and promising alternative.[1] Given its high gravimetric energy density,[2] hydrogen has gained considerable attention over the recent years as an adequate energy carrier candidate.[3] Therefore, water splitting by electrical means into H_2 and O_2 is expected to play a crucial role as a long-term storage technology. One distinguishes between two main kinds of water electrolysis, *i.e.*, alkaline water electrolysis (AWE) and proton exchange membrane water electrolysis (PEMWE). AWE is a mature technology that is already commercialised on a large scale.[4] However, it still suffers from several drawbacks such as low current densities, limited H_2 purity due to gas crossover, and a slow adaptative response to variations in the load.[5,6] On the other hand, PEMWE demonstrates the capacity to mitigate the three above-mentioned AEM drawbacks by the incorporation of a thin membrane electrolyte. Unfortunately, PEMWE faces its own set of challenges that prevent its penetration into the mass market. Indeed, due to the highly corrosive PEMWE environment, expensive and rare materials are required for its implementation. For instance, bipolar flow field plates, often made from gold- or platinum-coated titanium, amount to more than 50% of the cost of the PEMWE stack components. On the other hand, electrocatalysts only contribute on average to less than 10% of the entire PEMWE cost. Although this cost contribution seems small, efforts need to be taken to reduce the use of the scarce platinum group metals (PGMs) as catalyst materials due to their limited availability.[7] The state-of-the-art oxygen evolution reaction (OER) catalyst is unsupported Ir black, with a loading of about 2 mg_{Ir} cm^{-2} in a membrane electrode assembly (MEA).[8] Iridium, one of the scarcest elements on Earth, is mined only as a byproduct of platinum. Moreover, its distribution on Earth is highly unequal, making Europe heavily dependent on other countries for its supply.[9]

Therefore, to decrease our dependence on raw material imports, the Recycalyse project within the European Horizon 2020 Research funding aimed to create a circular economy for PEMWEs. Mainly focusing on the anodic site, efforts were first taken to reduce the PGM content in the OER electrocatalyst. The optimised catalyst was subsequently tested in a real-size stack PEMWE, and the entire system was subjected to recycling. Finally, the recycled components, with focus on the PGM elements of the electrocatalyst, were reused for the synthesis of a new catalyst.[10] The anode electrocatalyst optimised within the Recycalyse project combined two strategies to reduce the PGM content: *1)* the down-scaling of active sites to increase the surface-to-mass ratio and therefore enlarge the specific surface area and *2)* the use of a support material to improve the dispersion of the nanoparticles (NPs) and thus improve the accessibility of the catalyst's active sites to the reactant.[6,8] Similar approaches have been successfully implemented for PEM fuel cell catalysts using Pt NPs immobilized onto high-surface carbon supports.[11] Although carbon supports exhibit good electric conductivity and high surface area, they are unsuitable for the highly oxidative environment of the OER.[12] Therefore, extensive studies have been performed to find an adequate substitute for carbon support.[13–19] Within the Recycalyse project, different candidates have been tested and the most suitable one in terms of conductivity and high surface area was Sb-doped SnO_2 (ATO) with a doping level of 7.5 mol%.[10]

As there was a lack of facile and straightforward stability tests at laboratory scale, the catalyst selected for integration into an MEA and the first-generation electrolyser stack was chosen primarily based on its improved activity in half-cell tests. Within the project, however, we developed a strategy for stability testing through straightforward lab-scale experiments prior to conducting MEA tests.

In the presented work, we compare two different methods to assess stability aspects of the optimised Recycalyse catalyst. First, rotating disc electrode (RDE) experiments were performed as standard tests. While RDE measurements are routinely applied in academic laboratories, they are currently criticised concerning their applicability to OER stability tests.[20–22] To circumvent the limitations of the RDE technique for stability testing, which some are going to be discussed below, a more advanced setup, namely a gas diffusion electrode (GDE) setup, was used. The use of this technique for OER studies was already demonstrated in our previous work to compare the temperature-dependent performance of Ir and IrRu NPs supported on two different supports: high surface carbon and commercially available (com.) ATO. Surprisingly, we found that the performance of catalyst immobilised onto com. ATO was inferior than that of its carbon counterpart when tested at elevated temperature (60 °C).[23] The observed performance decline was associated to leaching of Sb, in agreement with the literature.[24–27] In this current study, the catalyst support material is therefore the ATO developed within the Recycalyse project, and results obtained are shortly compared to our previous study. Most importantly, the stability tests presented here were performed by introducing a titanium-based porous transport layer (PTL) as substrate instead of the previously used carbon-based gas diffusion layer (GDL).

2. Experimental Methods

2.1. Catalyst synthesis

Support material synthesis

The ATO support material was prepared using a sol-gel synthesis. In this process, $SnCl_4$ (anhydrous, 98%, Alfa Aesar) was dissolved in absolute ethanol (99.9% synthesis grade, Chemsolute), heated to 70 °C, and stirred for 2 hours under reflux. Subsequently, the corresponding amount of $SbCl_3$ (99+%, Alfa Aesar) was added to achieve a doping level of 7 mol% Sb:Sn. The solution underwent an additional 4-hour stirring. The ATO was then precipitated using NH_4OH (25%, Carl Roth GmbH + Co. KG) until a pH of 10 was obtained. After turning off the heating and stirring, the solution was allowed to settle overnight. The resulting precipitation was washed with ethanol using a centrifuge with 3500 rpm (Hettich) until a pH of 5 was reached. The solid sample was dried at 75 °C in a drying chamber (Binder), and then mortared. In the last step, the sample was calcined (Thermconcept oven) for 4 hours at a temperature of 600 °C in an air atmosphere.

Catalyst synthesis

The catalyst materials were synthesized using a solvothermal flow reactor, allowing for precise control of the particle size distribution, while being suitable for both small and large scale production.[28,29] Before the synthesis, the desired stoichiometric amounts of Ir, Ru and Ni precursors ($IrCl_3 \cdot xH_2O$: reagent grade, Sigma Aldrich; $RuCl_3 \cdot xH_2O$: 99.9% PGM basis, Alfa Aesar; $Ni(NO_3)_2 \cdot 6H_2O$: 98%, Alfa Aesar) were premixed with the support material, synthesized using

the above-described procedure, in deionised water. The premixed support and metal precursors were pressurised to 300 bar and mixed with a preheated flow of deionised water at 450 °C and 300 bar. The flow of preheated water was adjusted to obtain a mixing temperature with the cold support/precursor streams reaching 270 °C. The mixture was then flowed through a heated reactor section, kept at 270 °C and 300 bar, before being cooled down and tapped. The tapped products were then washed by centrifugation (Thermofisher Multifuge x3) 4 times using deionised water for 10 minutes at 15300 xg. Finally, the products were dried in a ventilated oven at 75 °C until all the remaining water had evaporated.
The obtained catalyst had the following composition: $(Ir_{0.68}Ru_{0.32})_{0.96}Ni_{0.04}$/ATO with a loading of 42 wt.% (determination by energy-dispersive X-ray spectroscopy – see below). TEM micrograph of the catalyst is shown in Figure S1.

2.2. Material Characterization

Transmission electron microscopy (TEM)

A Tecnai Spirit microscope operated at 80 kV was used to acquire TEM micrographs of the catalyst. 10 µL of catalyst ink was dropcasted onto a grid (Quantifoil, 100 Lacey Carbon films) and let to dry in the air at room temperature (RT).

Energy-Dispersive X-Ray Spectroscopy (EDX)

The elemental composition of synthesised sample was analysed using scanning electron microscopy (SEM)/EDX. A field emission SEM (XB-1540 EsB, Carl Zeiss NTS GmbH) equipped with an EDX system (Oxford X-Max 50 mm^2 SDD, Oxford Instruments) and AZtec 3.3 SP1 software was used. The powder was mounted on double adhesive carbon tape and flattened to minimize the effect of the microstructure on the EDX spectra. EDX was performed on dried catalyst powder with an accelerating voltage of 20 keV, a working distance of approximately 5.5 mm, and probe current of 100 pA. EDX spectra were collected from 3 random areas at 250X magnification (455*340 μm^2) with a lifetime of 60 seconds. The Sn and Sb data were converted to SnO_2 and Sb_2O_5 assuming full oxidation, and the catalyst loading was determined by dividing their mass fractions with the mass fractions of all catalyst elements and support oxides combined.
Further EDX measurements were performed on a Zeiss GeminiSEM 450 equipped with an EDX Photodetector Ultim Max 65 from Oxford Instruments to study the possible Sn and Sb leaching of ATO support material. The data were analysed with the AZTec 6.1 software. To obtain only the weight (wt.%) ratio between Sn and Sb, other elements present in the sample were deconvoluted. The ratio between Sn and Sb was first determined from the ink. For that, about 3x10 µL was dropcasted onto a graphite foil (0.13 mm thick, 99.8%, Alfa Aesar). The sample was mounted on metal stubs with conductive, adhesive Cu tape (3M #1182 electrical tape). Post-mortem elemental analysis was directly performed on the used electrode. For each sample, EDX spectra were collected from 3 random areas. An accelerating voltage of 10 keV, a working distance of 8.5 mm, and probe current of 200 pA were used as measuring parameters. All samples were measured in a top-view mode.

Inductively coupled plasma mass spectrometry (ICP-MS)

ICP-MS measurements were performed to determine the composition of the electrolyte before and after electrochemical measurements. For that 1 mL electrolyte aliquots were taken and digested following the procedure described by Edgington et al.[30] 0.5 mL of the aliquots were digested in 0.3 mL of concentrated nitric acid (69.3%, <1ppb, BASF) at 65 °C for 3 h.

Ultrapure H_2O (18.2 MΩ cm, MilliQ, Merck) was added to produce final solutions of 5% nitric acid (v/v) in a total sample volume of 6 mL.
These solutions were analysed by ICP–MS (NexION 2000 ICP–MS, PerkinElmer) to quantify the Ir, Ru, Ni, Sn and Sb contents. Calibration solutions (Merck, ICP-Standard, 1000 mg L^{-1}) of 1, 10, 100, 1000 and 10000 ppt (ng L^{-1}) were prepared, using a matrix (50 ml HNO_3, 28.8 mL HCl and 0.464 mL H_2SO_4 in 1 L of ultrapure water) as a solvent. 20 ppb Y, Rh and W was used as internal standard during the ICP-MS analysis.

2.3. Electrochemical Testing

Ink preparation

The inks for RDE and GDE electrodes were prepared as previously reported.[23] The washed and dried catalyst was dispersed in a 3:1 volume ratio of ultrapure water and isopropanol (IPA, HPLC grade, VWR Chemicals). 70 µL of 1 M KOH (Hänseler) was added per 60 mL of ink. KOH was added to increase the homogeneity and to improve the stability of the ink.[31] The ink concentrations were 196 $\mu g_{metal}\, mL^{-1}$ and 654 $\mu g_{metal}\, mL^{-1}$ for the RDE and the GDE electrode, respectively. After 5 min of bath sonication at RT, 10 wt.% of Nafion™ dispersion in H_2O (D1021, Fuel Cell Store) with respect to the catalyst (NPs and support) was added to the ink. The final dispersion was sonicated for 5 more min at RT.
The ink recipe for the preparation of catalyst-coated membrane (CCM) slightly differs from the one described above. For the preparation of CCM, the washed and dried catalyst was dispersed in IPA and some water (to prevent ignition of the catalyst). The concentration of the ink was 12 $mg_{Ir}\, mL^{-1}$. A 10 wt.% Nafion™ dispersion (D2020, Fuel Cell Store) was added with respect to Ir content. The final dispersion was sonicated for ca. 5 min at RT.

Electrode preparation

Polished 5 mm diameter glassy carbon (GC) disc embedded in Teflon were used as working electrode for RDE measurement. A 10 µL droplet of the beforehand sonicated ink (196 $\mu g_{metal}\, mL^{-1}$) was deposited on the surface of the GC electrode. The electrode was dried overnight under air atmosphere at RT. The loading resulted in 10 $\mu g_{metal}\, cm^{-2}$. The quality of the electrode was assessed with a light microscope (VHX-6000, Keyence).
The C-based electrodes for the GDE setup were prepared similarly to the procedure described in our previous publication.[23] A microporous layer (MPL) coated carbon GDL (Freudenberg H23C8, 0.230 mm thick, Fuel Cell Store) was placed between a sand core filter and a glass funnel (1.5 or 3.7 cm diameter) in a vacuum setup. 4.8 mL (for ⌀ 3.7 cm), 1.35 mL (for ⌀ 1.5 cm), or 2.7 mL (for ⌀ 1.5 cm) of the 654 $\mu g_{metal}\, mL^{-1}$ ink was diluted with water and IPA to reach a water/IPA volume ration of 1:3. After filtration, the catalyst film was dried overnight under air atmosphere at RT. The obtained nominal loading corresponds to 0.292, 0.500 and 1.000 $mg_{metal}\, cm^{-2}$, respectively. A 3 mm diameter disc was punched out of the catalyst film as well as out of a fresh unfunctionalized MPL coated GDL (of 2 cm diameter). The 3 mm catalyst film was placed in the 3 mm hole-punched 2 cm unfunctionalized coated GDL, and a preactivated Nafion™ membrane (Nafion™ 117, 183 µm thick, Fuel Cell Store) was placed on top of it. The whole system was placed between a paper sheet and an aluminium foil, and was pressed between two Teflon blocks by applying 2.5 tons of force for 10 min. When preparing the cell, a ⌀ 2 cm noncoated GDL (Freudenberg H23, 0.230 mm thick, Fuel Cell Store) was placed below the Nafion™-functionalized GDL-pressed system to create an unbroken conductive surface.

The Ti-based electrodes for the GDE setup were prepared by the so-called CCM procedure. Non-activated ⌀ 1.3 cm Nafion™ membranes (115, 127 µm thick, Fuel Cell Store) were placed on a vacuum heating plate covered by Teflon coated fibre glass and dried for ca. 5 min at 60 °C. They were then weighted and masked with a ⌀ 4 mm holed Scotch tape. An air spray gun (Iwata Eclipse HP-BCS 0.5mm) filled with the beforehand sonicated ink was used to deposit the catalyst on the membranes to achieve a target loading of 0.500 mg_{metal} cm^{-2}. After spraying, the membranes were let to dry at 60 °C for ca. 5 min and weighted again. A previously used Ti PTL (Ti fibre felt, Fuel Cell Store) was employed as substrate. The PTL was cleaned by sonication in IPA and pressed at 7.5 t. The prepared CCMs were then hot-pressed onto ⌀ 2 cm Ti-PTLs at 130 °C with a pressure of 60 kg cm^{-2} for 2 min (custom-built hot press).

Electrochemical measurements with RDE setup

The electrochemical experiments were performed in a three-electrode glass cell setup. All the glassware were first boiled with 25 vol.% HNO_3 (60%, Grogg Chemie) and let to cool down overnight. They were then thoroughly rinsed with ultrapure water. The measurements were conducted in 0.1 M $HClO_4$ (70%, Suprapur, Merck) aqueous electrolyte at RT. A Pt mesh (annealed and thoroughly rinsed with ultrapure water) and a reversible hydrogen electrode (RHE) connected to the cell by a Luggin capillary were used as counter and reference electrode, respectively, along with the functionalised GC working electrode (see prepapration above). The measurements were performed using a Nordic Electrochemistry ApS potentiostat (ECi - 200) controlled with the software EC4™ DAQ version 4.2.142.1 and a rotator from Radiometer analytical (Model EDI 101). The electrolyte was purged with O_2 (Alphagaz 1, 45, Air Liquide) for 30 min before the working electrode was immersed in. All electrochemical results have been exported and analysed with the software EC4View (version 1.2.113.1).

During each specific electrochemical techniques, an AC signal of 5 kHz with an amplitude of 5-10 mV was superposed to the set values. This AC signal was then used to online measure the solution resistance, as this is the main contributor to the impedance values.

First, 100 cycling voltammograms (CVs) were recorded between 1.2 and 1.7 V vs RHE with a scan rate of 10 mV s^{-1} and a rotation speed of 2000 rotation per minute (rpm). Duplicate samples were measured using a fresh electrode and new electrolyte.

In a second set of experiment, using a fresh electrode and new electrolyte, the capacitance double layer region was scanned between 1.2 and 1.4 V vs RHE with scan rates of 500, 400, 300 and 200 mV s^{-1} and a rotation speed of 2000 rpm. Afterwards, 50 CVs were recorded between 1.35 and 1.625 V vs RHE with a scan rate of 2.5 mV s^{-1} and a rotation speed of 2000 rpm. Finally, the same capacitance measurements were repeated. For this second set of experiments, 100% adaptative iR compensation was applied during the CVs. The adaptive iR compensation is a software scheme that uses the online measured solution resistance as well as the current to adjust the set value. The end effect is that the voltage limits set by the technique are exceeded. However, after post-measurement iR-correction, an iR-free CV is obtained.

Capacitance double layer measurement was also performed on a bare GC electrode. Similar conditions than described above were applied.

Electrochemical measurements with GDE setup

Electrochemical experiments performed in the GDE setup had a three-electrode configuration, where a Pt mesh (annealed and thoroughly rinsed with ultrapure water) and a RHE connected to the cell by a Luggin capillary were used as counter and reference electrode, respectively. The freshly pressed ⌀ 3 mm functionalised GDL and the hot-pressed CCMs were

used as working electrodes. The upper polyether ether ketone (PEEK) compartments were first soaked into a 25 vol.% HNO_3 overnight. Then, they were thoroughly rinsed and boiled with ultrapure water. 4 M $HClO_4$ (ACS reagent, 70%, Sigma Aldrich) was used as the electrolyte in the upper PEEK compartment of the setup. The electrolyte was preheated at most 7 °C above the desired temperature (60 °C). Humidified (ultrapure H_2O) O_2 was continuously flowing through the setup during the measurements with a flow rate between 50 and 60 mL min^{-1}. The aluminium-made faradaic cage was preheated to the desired temperature using a thermocouple-controlled heating plate. To guarantee the connectivity of the entire system, two CVs were recorded between 1.2 and 1.6 V vs RHE at 10 mV s^{-1}. The solution resistance was determined online using an AC signal of 5 kHz with an amplitude of 1−10 mA. The measurements were performed using a potentiostat (ECi – 242, Nordic Electrochemistry ApS) controlled with the software EC4™ DAQ version 2.44. Electrochemical results have been exported and analysed with the software EC4™ View.

Although the catalyst is supposedly completely oxidized after its synthesis, an activation step was performed to ensure it (potentiostatic step of 5 min at 1.6 V vs RHE).

Then, the following protocol was used: *1)* activity, *2)* stability, and *3)* activity similar to 1). The activity protocol of part *1)* and *3)* consisted in stepping the current density every 5 min at different values (5, 10, 20, 45, 60, 80, 100, 150 and 200 mA mg_{metal}^{-1}). The applied current steps were normalised on ⌀ 3 mm and on the loading of the electrode. The following sequences were used:

- For 0.292 mg_{metal} cm^{-2}: 0.103, 0.103, 0.206, 0.413, 0.619, 0.929, 1.238, 1.651, 2.064, 3.096, 4.128 mA
- For 0.500 mg_{metal} cm^{-2}: 0.177, 0.177, 0.353, 0.707, 1.060, 1.590, 2.121, 2.827, 3.534, 5.301, 7.069 mA.
- For 1.000 mg_{metal} cm^{-2}: 0.353, 0.353, 0.707, 1.414, 2.121, 3.181, 4.241, 5.655, 7.069, 10.603, 14.137 mA.

For the determination of the Tafel slope, the last 100 s of each iR-corrected current step were averaged.

The stability consisted in holding the potential at 1.6 V vs RHE for 2 h. During this step, a 100% adaptative iR compensation was applied.

The same protocol was used for all electrodes (C-GDL and Ti-PTL). Current steps of the Ti-PTL were normalised on ⌀ 3 mm and based on 0.500 mg_{metal} cm^{-2} loading.

3. Results and discussion

The optimised Recycalyse catalyst, ATO supported $(Ir_{0.68}Ru_{0.32})_{0.96}Ni_{0.04}$ NPs with a metal loading of 42 wt.%, was used in this study. For simplicity, the catalyst is hereafter named IrRu/ATO.

The RDE setup and its limitations

First, the stability of the catalyst was assessed with the most commonly used electrochemistry approach, RDE measurements. In literature, three main protocols are employed to determine the stability of an OER catalyst using the RDE technique: *i)* galvanostatic, *ii)* potentiostatic, and *iii)* potential cycling tests. The latter involves a dynamic operational mode (in contrast to a steady-state mode) which is believed to best mimic fluctuations in the power output when PEMWE is directly coupled to renewable energies.[32] Therefore, in this study, 100 CVs were

recorded between 1.2 and 1.7 V vs RHE with a scan rate of 10 mV s^{-1} and a rotation speed of 2000 rpm. Figures 1a and 1b depict every 10^{th} CV (forward scans) for both, the as-recorded raw data and the data after correction for the resistance (iR post-correction). The experiment was replicated using a fresh electrode and new electrolyte to ensure reproducibility across measurements. Figure S2 demonstrates that the CVs obtained with different electrodes are similar, thus confirming good reproducibility in terms of electrode preparation and electrochemical testing.

a)

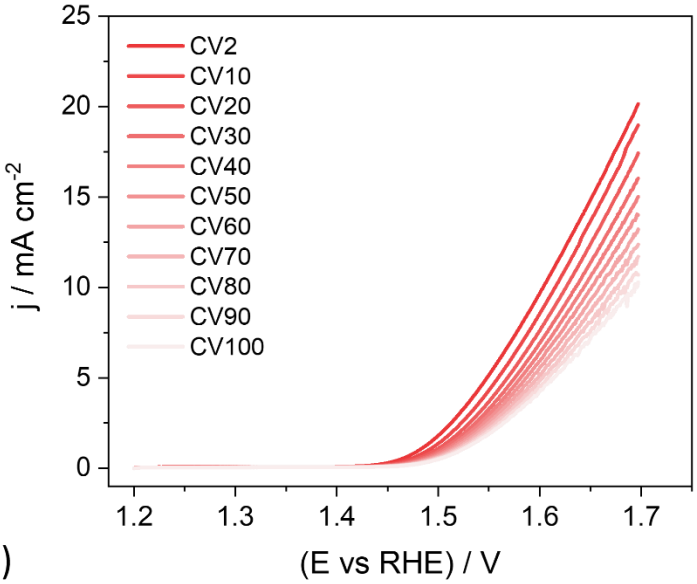
CV2
CV10
CV20
CV30
CV40
CV50
CV60
CV70
CV80
CV90
CV100
j / mA cm-2
(E vs RHE) / V

b)

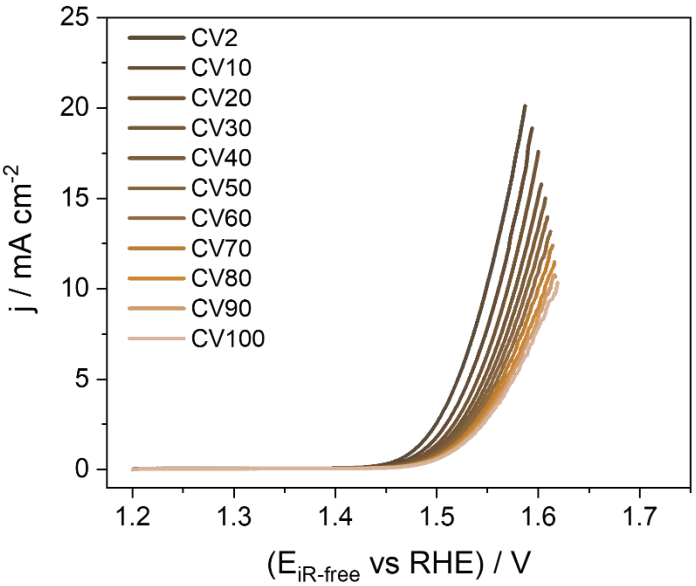
CV2
CV10
CV20
CV30
CV40
CV50
CV60
CV70
CV80
CV90
CV100
j / mA cm-2
(EiR-free vs RHE) / V

c)

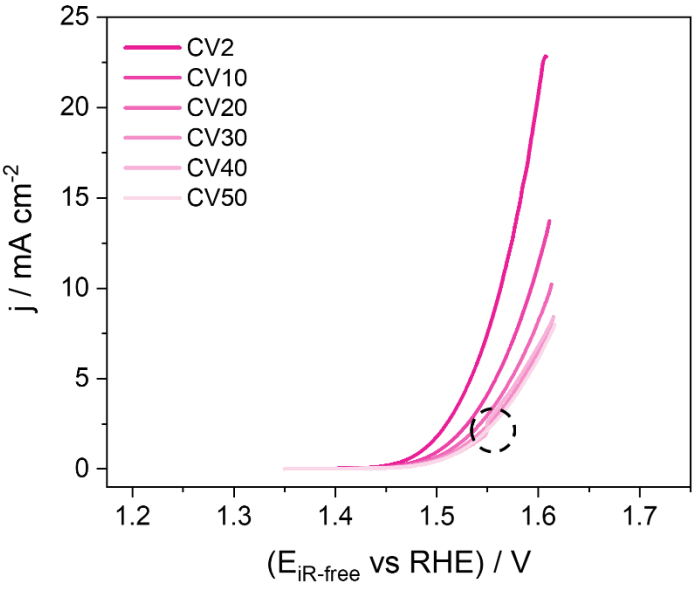
CV2
CV10
CV20
CV30
CV40
CV50
j / mA cm-2
(EiR-free vs RHE) / V

Figure 1. *OER evolution of IrRu/ATO through CVs (forward scans - every 10th cycle). The obtained data are plotted (a) as-recorded (raw data) and (b) with iR post-correction. These measurements were recorded at 10 mV s^{-1} between 1.2 and 1.7 V vs RHE. (c) Another set of CVs was recorded between 1.35 and 1.625 V vs RHE at 2.5 mV s^{-1} with a 100% adaptative iR compensation. The black circle highlights the jump in activity due to gas bubble release. All measurements were performed in O_2-saturated 0.1 M $HClO_4$ at RT with the catalyst deposited on a GC disc with a nominal loading of 10 μg_{metal} cm^{-2}.*

It is important to underscore that no iR compensation was applied during the aforementioned experiments. To ensure more reliable data and mitigate possible misinterpretations, a similar experiment was conducted using a fresh electrode while applying an adaptative iR compensation. The adaptive iR compensation is a software scheme that adds an offset to the set potential, similarly to a hardware positive feedback compensation. However, in contrast to the hardware positive feedback compensation, the solution resistance, R_{sol}, is not assumed to be constant. As the R_{sol} is measured continuously together with the current, the iR drop is calculated and used to offset the set potential. This software compensation is relative slow and should only be used for slow scan rate. Lastly, after the measurement, the measured data is iR-corrected in order to obtain the iR-free potential.

The results of these iR-compensated CVs are shown in Figure 1c. The implementation of the adaptive compensation required slight adjustments to the experimental protocol regarding the scan speed. Hence, 50 CVs between 1.35 and 1.625 V vs RHE with a scan rate of 2.5 mV s^{-1} were recorded. While a direct one-to-one comparison between the experiments is not feasible, a consistent trend emerges across all three cases: a rapid decline in OER activity upon potential cycling. Such deterioration in current density upon potential cycling is commonly associated in the literature with catalyst degradation.[33,34] However, this interpretation is questionable. From Figure S3, depicting the decay in current density over cycles as well as the apparent activity loss at 1.5 V vs RHE for both iR-corrected and iR-compensated data, it is evident that both protocols result in a similar apparent loss in activity (75-80%). This is a surprising coincidence as it would be expected that the choice between iR correction or iR compensation as well as scan speed should influence the degree of the recorded degradation. However, this is not observed in our results. In this context, it is noteworthy that the accumulation of gas bubbles on top of the catalyst film is a well-known limitation of the RDE technique for gas-evolving processes.[35] Recently, it has been proposed that micro- and nanobubbles are incorporated into the porous structure of the catalyst during the measurement. This potentially poses a major limitation that can lead to misinterpretations when OER catalyst degradation studies are based on thin-film RDE measurements.[22,36,37] Our findings support that criticism. When iR compensation is applied, a stronger activity loss is expected as the upper potential limit, that is truly reached during the potential scans, is substantially higher than in a non-compensated experiment. The obtained similar apparent activity losses are most likely influenced by the accumulation of gas bubbles. The detachment of the macroscopic gas bubbles translates into a decrease in resistance and thereby a recovery in activity. This effect is indeed observed, as demonstrated in Figure 1c by the black circle, where a jump to higher current density is observed at CV40, and in Figure S4, where the determined iR resistance of CV40 goes back to the initial value of CV2.

To remedy the issue of micro- and nanobubbles, El-Sayed et al. proposed to purge the electrolyte with Ar after completion of their galvanostatic experiment, so that electrogenerated O_2 gas bubbles would diffuse from the inside of the pores to the electrolyte.

Doing so, they observed a slight recovery of the catalyst activity, claiming that the observed abrupt potential jump during galvanostatic measurement was exclusively due to "gas bubble shielding" of the active sites.[22,36] Based on these observations, similar experiments were performed by Edgington et al., however, without observing any recovery of their OER catalyst.[30] To circumvent bubble accumulation, Wang et al. proposed to apply, on top of electrolyte convection, a reductive current/potential protocol to eliminate bubbles formed on a macro- and microscopic scale (oxygen reduction reaction).[38] Furthermore, ultrasonication was proposed to bypass the accumulation of bubbles on/into the catalyst.[39] However, in their study, Hartig-Weiss et al. used an iridium disc, which does not represent adequately the porous catalyst deposited onto a glassy carbon disc. Ultrasonication applied to eliminate gas bubbles in a thin catalyst film system - as in our case - can easily lead to mechanical detachment of the catalyst which is difficult to distinguish from degradation.

Furthermore, it is important to highlight that the formation of O_2 gas bubbles will always occur during the OER, however, the shielding of the catalyst layer with those electrogenerated gas bubbles is an unpredictable phenomenon. By inverting the routinely used RDE setup by 180°, Moreno-García et al. proposed an ingenious solution to circumvent the unpredictable bubble-shielding of catalysts. Thanks to buoyancy and convection, the macro- and potentially micro- and nanoscopic bubbles can escape the surface of the electrode and reach the surface of the electrolyte.[40,41] Unfortunately, so far commercial inverted RDE setups are missing. Moreover, as such inverted RDE still represents aqueous model system (AMS), the achievable current density is limited.

To further shed light on the potential causes contributing to the activity decay, different complementary methods were employed such as capacitance measurements, EDX analysis and ICP-MS. Unfortunately, despite these methods, it is quasi-impossible to deconvolute the intrinsic degradation of the catalyst from the external factors inherent to the system – see discussion in SI. Therefore, the decay in the upper limit potential should always be treated carefully to avoid misinterpretation about catalyst stability, when thin-film RDE approach is used.

The GDE setup to overcome RDE limitations

As recently highlighted by Cherevko et al., other techniques are required to obtain more reliable information on the catalyst stability compared to those obtained in AMS.[20,21] Therefore, in the current study, none of the aforementioned approaches proposed by El-Sayed et al., Wang et al., or Moreno-García et al. to mitigate potential gas bubble retention were applied given their AMS nature. Instead, a different approach was taken, *i.e.*, GDE measurements. GDE setups, often described as bridging tools between RDE (*i.e.*, AMS) and MEA, enable studies of individual electrode reactions under more relevant conditions, resembling those in electrolyser stacks.[42–44]

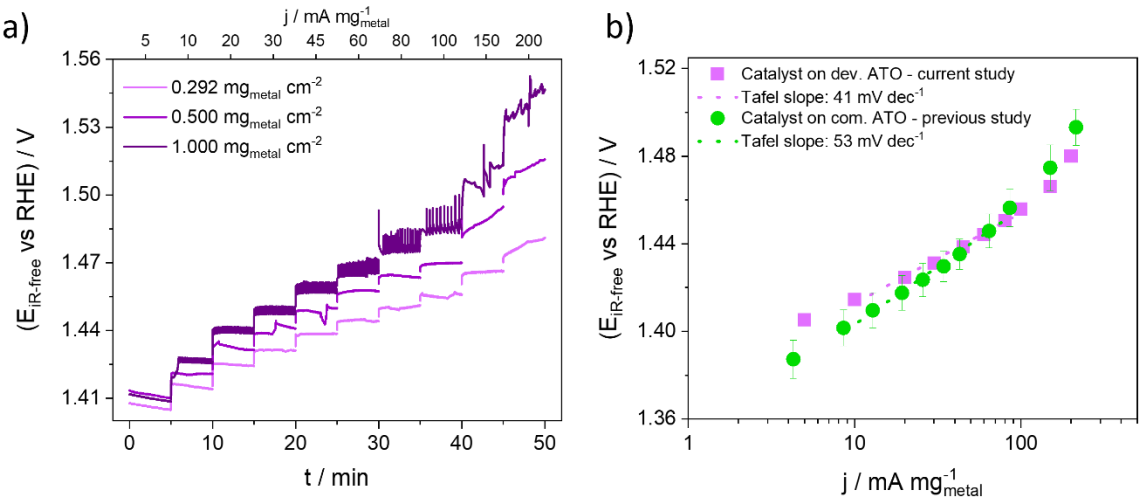

Figure 2. *(a) Loading dependence of OER iR-corrected potential transients for IrRu/ATO on a C-based substrate. The measurements were performed in the GDE setup in an O_2 atmosphere at 60 °C using 4 M $HClO_4$ as an electrolyte. (b) comparison of the Tafel slopes of the 0.292 mg_{metal} cm^{-2} IrRu/ATO of this current study and the one in our previous study (similar loading – commercial (com.) ATO) (b). The error bars for the green dots show the standard deviation of three independent measurements. Data taken from Bornet et al.*[23]

Consequently, the identical GDE setup as presented in our previous study[23] was used to investigate the Recycalyse IrRu/ATO catalyst at 60 °C. All measurements followed the following protocol: *1)* beginning-of-life (BoL) activity through galvanostatic steps, *2)* stability *via* a potentiostatic step, and *3)* end-of-life (EoL) activity identical to BoL (see Figure S7).

First, the loading dependence of the catalyst was examined. For that, the catalyst was deposited on a carbon-based GDL with three distinct metal loading, namely, 0.292, 0.500 and 1.000 mg_{metal} cm^{-2} and their BoL galvanostatic steps were compared. Figure 2a shows that the recorded potentials for all three loadings exhibit a rather stable behaviour during the 5-minute steps up to 100 mA mg_{metal}^{-1}. At higher mass current densities, deviations are observed, probably due to mass transport limitations, similar to Collantes-Jiménez et al. observations.[44] The oscillations observed in the dark violet curves (1.000 mg_{metal} cm^{-2} loading) stem from intensive bubble release. Furthermore, higher mass activity is achieved with lower loading. This is attributed to a better accessibility of the active sites and, thereby, an enhanced utilisation of the catalyst. Comparison of the Tafel slopes between IrRu/ATO (0.292 mg_{metal} cm^{-2}) of the current study (pink dots/line) and that of our previous study (green dots/line) reveals a slight improvement (41 versus 53 mV dec^{-1}, respectively) (see Figure 2b). Despite slightly different catalyst compositions ($Ir_{0.7}Ru_{0.3}$ – this work (pink) vs $Ir_{0.4}Ru_{0.6}$ – previous work (green)), we ascribe this 12 mV dec^{-1} improvement in Tafel slope to the support material. This is corroborated by a comparative study performed on both ATO supports, which reported that the developed Recycalyse support material exhibited a higher conductivity as well as a higher surface area than its commercial counterpart.[10]

Subsequently, the stability of the Recycalyse IrRu/ATO catalyst was assessed by applying a demanding potentiostatic step of 1.6 V vs RHE during 2 hours at 60 °C. Figure 3a depicts the response for the 1.000 mg_{metal} cm^{-2} loading on GDL (violet curve). Interestingly, the recorded current density initially rises to ca. 280 mA cm^{-2} within the 5 first minutes to fall drastically to ca. 65 mA cm^{-2} after the 2 hours of potentiostatic step (loss: 77%). Similar behaviour was

observed for the two lower loadings, see Figure S8. This suggests substantial degradation, either of the catalyst layer or the carbon GDL.

BoL and EoL activity measurements are compared in Figure 3b, violet lines. It is observed that despite the suggested degradation, at low mass current densities (up to 10 mA mg_{metal}^{-1}), similar BoL and EoL activities were monitored. However, as the mass current density was increased, large discrepancies between BoL and EoL occur. At EoL conditions the required electrode potential to maintain a current density of 150 mA mg_{metal}^{-1} even exceeded 2 V vs RHE, indicating a tremendous deterioration of the system. This may explain why such drastic performance loss was not observed by Schröder et al. when performing a short-term stability test with C-GDL under less severe conditions (1 h at 10 mA mg_{Ir}^{-1}).[45]

From these experiments, we can conclude several points. First, given that this catalyst sustained MEA tests and could be operated in an electrolyser stack without facing fast and drastic activity loss,[10] such a decay cannot be solely assigned to the catalyst degradation. Therefore, rather than documenting catalyst degradation, the observed behaviour is due to the degradation of the carbon-based substrate. Pictures of a burnt GDL presented in Table S4 support the hypothesis of GDL degradation rather than catalyst degradation. Second, degradation and EoL activity tests have to be employed under harsh conditions and high current densities. Activity tests applying only small geometric or mass normalised current densities, as typically employed in RDE tests, may not reflect a realistic picture of catalyst stability. Last but not least, given the tendency of carbon to oxidise under the harsh OER conditions,[46] this work, along with findings from other researchers[20,44,45,47] confirm that GDL is an unsuitable substrate for medium- to long-term stability tests. Instead, a more resistant substrate needs to be used. In this respect, PTL, typically used in electrolyser stack,[10] was selected as a suitable candidate to continue our study.

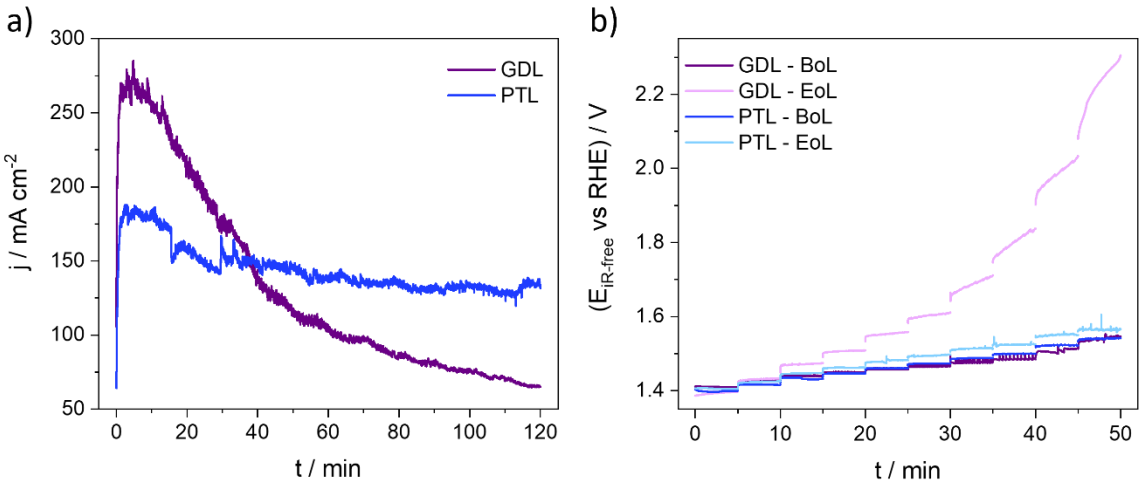

Figure 3. *(a) OER current density transients for IrRu/ATO on a C-GDL (violet curve) and on a Ti-PTL (blue curve) and (b) the iR-corrected potential transients before (dark colour) and after (light tone) the potentiostatic step at 1.6 V vs RHE. The nominal loading for the GDL-catalyst is 1 mg_{metal} cm^{-2} and the targeted one for the PTL-catalyst is 0.5 mg_{metal} cm^{-2}. The measurements were performed in the GDE setup in an O_2 atmosphere at 60 °C using 4 M $HClO_4$ as an electrolyte. The potential was held at 1.6 V vs RHE (performed with adaptative compensation) for 2 hours.*

Given that Ti-PTLs do not have an MPL on top of their fibres as GDLs do, an alternative electrode preparation method was required instead of vacuum filtration. Several different approaches exist for preparing PTL electrodes, among others, increasing the viscosity of the

catalyst ink (*e.g.*, glycerol inks) and dropcasting it directly onto a PTL that was coated beforehand with Teflon. This approach, used by Schröder et al., led to similarities in catalytic activity between the catalyst functionalised on GDL and PTL.[45] However, glycerol inks are difficult to handle, and the drop casting method may lead to discrepancies between samples. Moreover, this approach is not suitable for large-scale electrode preparation, and thus cannot be applied in MEA tests. Therefore, an alternative approach, namely CCM preparation, was adopted in this work. CCM preparation is a standard approach for the preparation of MEA electrodes and consists of spraying the catalyst (dispersed in water/IPA solvent) directly onto a membrane electrolyte (in our case a non-activated Nafion™ membrane). The CCM can also be prepared *via* a decal process.[5] For MEA tests, the CCM is subsequently sandwiched between a GDL (cathode side) and a PTL (anode side).[5] To implement the CCM into our half-cell, we coated (by spaying) the electrolyte membrane only one-sided and pressed it face-down onto the PTL.

The prepared PTL electrode was then used in our GDE setup following the same protocol as used for testing the GDL electrode (Figure S7). Comparing both substrates, the BoL galvanostatic steps of the PTL-electrode exhibit similar behaviour as compared to the GDL-electrode (Figure 3b). This observation corroborates the claim by Schröder et al., *i.e.*, that both substrates can be used for activity measurement when taking care that no carbon oxidation currents are misassigned as OER currents.[45] However, upon stability testing *via* the potentiostatic step, a drastic difference as compared to the catalyst-GDL system was observed, see Figure 3a (blue curve). Unlike the catalyst-GDL system, the catalyst-PTL system did not exhibit a severe loss of activity within the 2 hours of holding the potential at 1.6 V vs RHE. On the contrary, despite a targeted loading twice as small, its activity remained rather stable (at 5 min: ca. 180 mA cm^{-2}, at 2 h: ca. 130 mA cm^{-2}, loss: 28%). Furthermore, during EoL activity measurements *via* current steps, the observed activity of the catalyst-PTL system remained more or less identical as compared to the BoL activity (Figure 3b). Only a slight increase in the Tafel slope (17 mV dec^{-1}) was noted, similar to observations of Collantes-Jiménez et al.[44]

In literature, based on changes in the Tafel slope, sometimes a change in reaction mechanism is claimed. However, without any additional investigations, we refrain from such interpretation, considering that a degraded sample is not expected to change its electron transfer mechanism. Furthermore, one can attribute the increase in Tafel slope to a limitation of the system such as mass transport due to gas bubble formation. Gas bubble release is expected to be sensitive to the catalyst film structure which might be affected during degradation tests. In this context, it was shown that using humidified gas as a reactant can lead to higher mass transport limitations as compared to pumping deionised water through the GDE cell.[44,47] Nevertheless, as the Tafel slope was determined within the kinetic region, we believe this second interpretation does not correctly account for the deviation in Tafel slope. Finally, changes in resistance can induce changes in Tafel slopes as well. Unlike the GDL system, no “burning” of the PTL was witnessed after the completion of the protocol (see Table S4). Additionally, as no gap between the CCM and the PTL was evidenced, the observed increase in resistance between BoL and EoL steps could not refer to the degradation of PTL during this relatively short stability experiment (Figure S9). On the other hand, considering the instability of antimony in ATO,[24–27] this scenario might more adequately address the change in the Tafel slope. This was further supported by the exponential function obtained

from plotting the differences in BoL and EoL potentials versus the current densities (*i.e.*, Δ(E_{EoL}, E_{BoL}) vs j), see Figure S10. In the literature, exponential functions describing a resistance are attributed to a diode,[48] whereas a normal resistor would result in a linear behaviour (Ohm's law).[49] Given that ATO is a semiconductor, it should follow the exponential behaviour of a diode. Consequently, considering the observations from our previous work,[23] the observed rise in Tafel slope was most likely due to the degradation of ATO.

4. Conclusion

In agreement with previous research, we strongly advocate for departing from the traditional RDE measurements when investigating the catalyst stability in gas-evolving processes such as the OER. Considering the significant discrepancies between AMS data and MEA stability measurements, special care should be taken when interpreting data obtained by the RDE technique. To address the limitations posed by gas bubbles in the RDE setup, the GDE configuration is demonstrated as a suitable alternative, which offers an environment for studying catalyst behaviour under conditions closer to "real-world" scenarios. While carbon-based substrates present an economical and straightforward option for initial catalyst activity analysis, they prove inadequate for long-term stability evaluations under relevant conditions due to their susceptibility to corrosion. It is shown that materials such as titanium PTLs are superior alternatives than carbon GDLs, despite their higher cost and the need for more intricate electrode preparation. We assert that titanium-based substrates should be exclusively employed for conducting effective stability measurements. Using this technique, the developed Recycalyse IrRu/ATO catalyst exhibits limited degradation, and its performance can be further optimised in MEA measurements.

Acknowledgements

This project has received funding from the European Union's Horizon 2020 Research and Innovation program under grant agreement N. 861960 ("Recycalyse" project). The authors acknowledge access to the Microscopy Imaging Center (MIC) facilities of the University of Bern. Erik Wiseaus from the Danish Technological Institute and Beatrice Frey from the University of Bern are thanked for the EDX measurement. We thank Mike Liechti from the University of Bern for the ICP-MS measurements.

Conflicts of interest

The authors declare that the synthesis method is subjected to a patenting process (WO 2015/104025 A1)

References

(1) Gür, T. M. Review of Electrical Energy Storage Technologies, Materials and Systems: Challenges and Prospects for Large-Scale Grid Storage. *Energy Environ Sci* **2018**, *11* (10), 2696–2767. https://doi.org/10.1039/C8EE01419A.

(2) Tashie-Lewis, B. C.; Nnabuife, S. G. Hydrogen Production, Distribution, Storage and Power Conversion in a Hydrogen Economy-A Technology Review. *Chemical Engineering Journal Advances* **2021**, *8*, 100172. https://doi.org/10.1016/j.ceja.2021.100172.

(3) Abe, J. O.; Popoola, A. P. I.; Ajenifuja, E.; Popoola, O. M. Hydrogen Energy, Economy and Storage: Review and Recommendation. *Int J Hydrogen Energy* **2019**, *44* (29), 15072–15086. https://doi.org/10.1016/j.ijhydene.2019.04.068.

(4) Carmo, M.; Stolten, D. Energy Storage Using Hydrogen Produced From Excess Renewable Electricity. In *Science and Engineering of Hydrogen-Based Energy Technologies*; Elsevier, 2019; pp 165–199. https://doi.org/10.1016/B978-0-12-814251-6.00004-6.

(5) Carmo, M.; Fritz, D. L.; Mergel, J.; Stolten, D. A Comprehensive Review on PEM Water Electrolysis. *Int J Hydrogen Energy* **2013**, *38* (12), 4901–4934. https://doi.org/10.1016/j.ijhydene.2013.01.151.

(6) Yoon, H.; Ju, B.; Kim, D. Perspectives on the Development of Highly Active, Stable, and Cost-effective OER Electrocatalysts in Acid. *Battery Energy* **2023**, *2* (5). https://doi.org/10.1002/bte2.20230017.

(7) IRENA. *GREEN HYDROGEN COST REDUCTION SCALING UP ELECTROLYSERS TO MEET THE 1.5˚C CLIMATE GOAL*; Abu Dhabi., 2020. https://www.irena.org/publications/2020/Dec/Green-hydrogen-cost-reduction (accessed 2024-02-26).

(8) Zhang, K.; Liang, X.; Wang, L.; Sun, K.; Wang, Y.; Xie, Z.; Wu, Q.; Bai, X.; Hamdy, M. S.; Chen, H.; Zou, X. Status and Perspectives of Key Materials for PEM Electrolyzer. *Nano Research Energy* **2022**, *1* (3), e9120032. https://doi.org/10.26599/NRE.2022.9120032.

(9) Minke, C.; Suermann, M.; Bensmann, B.; Hanke-Rauschenbach, R. Is Iridium Demand a Potential Bottleneck in the Realization of Large-Scale PEM Water Electrolysis? *Int J Hydrogen Energy* **2021**, *46* (46), 23581–23590. https://doi.org/10.1016/j.ijhydene.2021.04.174.

(10) Melke, J.; Maletzko, A.; Gomez Villa, E. D.; Bornet, A.; Wiberg, G. K. H.; Arenz, M.; Sandig-Predzymirska, L.; Thiere, A.; Charitos, A.; Stelter, M.; Wang, Z.; Pitscheider, S.; Bertheussen, E.; Pedersen, C. M.; Finsdóttir, S.; Kokborg, M. S.; Berman, D. G.; Dalvang, S.; Müller, S. S.; Seidel, F.; Seselj, N.; Höglinger, M.; Kartusch, S.; Eder, J.; Macherhammer, M.; Trattner, A.; Kallesøe, C. Recycalyse – New Sustainable and Recyclable Catalytic Materials for Proton Exchange Membrane Electrolysers. *Chemie Ingenieur Technik* **2024**, *96* (1–2), 126–142. https://doi.org/10.1002/cite.202300143.

(11) Wilson, M. S.; Gottesfeld, S. High Performance Catalyzed Membranes of Ultra-low Pt Loadings for Polymer Electrolyte Fuel Cells. *J Electrochem Soc* **1992**, *139* (2), L28–L30. https://doi.org/10.1149/1.2069277.

(12) Maass, S.; Finsterwalder, F.; Frank, G.; Hartmann, R.; Merten, C. Carbon Support Oxidation in PEM Fuel Cell Cathodes. *J Power Sources* **2008**, *176* (2), 444–451. https://doi.org/10.1016/J.JPOWSOUR.2007.08.053.

(13) Oh, H.; Nong, H. N.; Strasser, P. Preparation of Mesoporous Sb-, F-, and In-Doped SnO_2 Bulk Powder with High Surface Area for Use as Catalyst Supports in Electrolytic Cells. *Adv Funct Mater* **2015**, *25* (7), 1074–1081. https://doi.org/10.1002/adfm.201401919.

(14) Duan, X.; Liu, H.; Zhang, W.; Ma, Q.; Xu, Q.; Khotseng, L.; Su, H. Boosting the Efficiency of IrO_x Nanoparticles with Micron-Flower $Nb_4 N_5$ Support for Oxygen Evolution Reaction in Polymer Electrolyte Membrane Water Electrolyzer. *Electrochim Acta* **2023**, *470*, 143271. https://doi.org/10.1016/j.electacta.2023.143271.

(15) Pham, C. Van; Bühler, M.; Knöppel, J.; Bierling, M.; Seeberger, D.; Escalera-López, D.; Mayrhofer, K. J. J.; Cherevko, S.; Thiele, S. IrO_2 Coated TiO_2 Core-Shell Microparticles Advance Performance of Low Loading Proton Exchange Membrane Water Electrolyzers. *Appl Catal B* **2020**, *269*, 118762. https://doi.org/10.1016/j.apcatb.2020.118762.

(16) Nikiforov, A. V.; Tomás García, A. L.; Petrushina, I. M.; Christensen, E.; Bjerrum, N. J. Preparation and Study of IrO_2/SiC–Si Supported Anode Catalyst for High Temperature PEM Steam Electrolysers. *Int J Hydrogen Energy* **2011**, *36* (10), 5797–5805. https://doi.org/10.1016/j.ijhydene.2011.02.050.

(17) Hao, C.; Lv, H.; Zhao, Q.; Li, B.; Zhang, C.; Mi, C.; Song, Y.; Ma, J. Investigation of V-Doped TiO2 as an Anodic Catalyst Support for SPE Water Electrolysis. *Int J Hydrogen Energy* **2017**, *42* (15), 9384–9395. https://doi.org/10.1016/j.ijhydene.2017.02.131.

(18) Li, H.; Pan, Y.; Wu, L.; He, R.; Qin, Z.; Luo, S.; Yang, L.; Zeng, J. Highly Active and Stable IrO_2 and IrO_2–Ta_2O_5 Catalysts for Oxygen Evolution Reaction. *Int J Hydrogen Energy* **2023**, *48* (67), 26021–26031. https://doi.org/10.1016/j.ijhydene.2023.03.360.

(19) Han, B.; Risch, M.; Belden, S.; Lee, S.; Bayer, D.; Mutoro, E.; Shao-Horn, Y. Screening Oxide Support Materials for OER Catalysts in Acid. *J Electrochem Soc* **2018**, *165* (10), F813–F820. https://doi.org/10.1149/2.0921810jes.

(20) Ehelebe, K.; Escalera-López, D.; Cherevko, S. Limitations of Aqueous Model Systems in the Stability Assessment of Electrocatalysts for Oxygen Reactions in Fuel Cell and Electrolyzers. *Curr Opin Electrochem* **2021**, *29*, 100832. https://doi.org/10.1016/j.coelec.2021.100832.

(21) Cherevko, S.; Katsounaros, I. And yet It Rotates! *Nat Catal* **2024**, *7* (1), 10–11. https://doi.org/10.1038/s41929-023-01100-5.

(22) Tovini, M. F.; Hartig-Weiß, A.; Gasteiger, H. A.; El-Sayed, H. A. The Discrepancy in Oxygen Evolution Reaction Catalyst Lifetime Explained: RDE vs MEA - Dynamicity within the Catalyst Layer Matters. *J Electrochem Soc* **2021**, *168* (1), 014512. https://doi.org/10.1149/1945-7111/ABDCC9.

(23) Bornet, A.; Pittkowski, R.; Nielsen, T. M.; Berner, E.; Maletzko, A.; Schröder, J.; Quinson, J.; Melke, J.; Jensen, K. M. Ø.; Arenz, M. Influence of Temperature on the Performance of Carbon- and ATO-Supported Oxygen Evolution Reaction Catalysts in a Gas Diffusion Electrode Setup. *ACS Catal* **2023**, *13* (11), 7568–7577. https://doi.org/10.1021/acscatal.3c01193.

(24) Abbou, S.; Martin, V.; Claudel, F.; Sola, L.; Beauger, C.; Dubau, L.; Maillard, F. Manipulating the Corrosion Resistance of SnO_2 Aerogels through Doping for Efficient and Durable Oxygen Evolution Reaction Electrocatalysis in Acidic Media. **2024**. https://doi.org/10.1021/acscatal.0c01084.

(25) da Silva, G. C.; Venturini, S. I.; Zhang, S.; Löffler, M.; Scheu, C.; Mayrhofer, K. J. J.; Ticianelli, E. A.; Cherevko, S. Oxygen Evolution Reaction on Tin Oxides Supported Iridium Catalysts: Do We Need Dopants? *ChemElectroChem* **2020**, *7* (10), 2330–2339. https://doi.org/10.1002/CELC.202000391.

(26) Ferreira da Silva, C. D.; Claudel, F.; Martin, V.; Chattot, R.; Abbou, S.; Kumar, K.; Jiménez-Morales, I.; Cavaliere, S.; Jones, D.; Rozière, J.; Solà-Hernandez, L.; Beauger, C.; Faustini, M.; Peron, J.; Gilles, B.; Encinas, T.; Piccolo, L.; Barros de Lima, F. H.; Dubau, L.; Maillard, F. Oxygen Evolution Reaction Activity and Stability Benchmarks for Supported and Unsupported IrO_x Electrocatalysts. *ACS Catal* **2021**, *11* (7), 4107–4116. https://doi.org/10.1021/acscatal.0c04613.

(27) Geiger, S.; Kasian, O.; Mingers, A. M.; Mayrhofer, K. J. J.; Cherevko, S. Stability Limits of Tin-Based Electrocatalyst Supports. *Scientific Reports 2017 7:1* **2017**, *7* (1), 1–7. https://doi.org/10.1038/s41598-017-04079-9.

(28) Silva, H.; Hernandez-Fernandez, P.; Baden, A. K.; Hellstern, H. L.; Kovyakh, A.; Wisaeus, E.; Smitshuysen, T.; Chorkendorff, I.; Christensen, L. H.; Chakraborty, D.; Kallesøe, C. Supercritical Flow Synthesis of PtPdFe Alloyed Nanoparticles with Enhanced Low-Temperature Activity and Thermal Stability for Propene Oxidation under Lean Exhaust Gas Conditions. *Catal Sci Technol* **2019**, *9* (23), 6691–6699. https://doi.org/10.1039/C9CY00634F.

(29) Kallesøe, C.; Clausen, H. F.; Christensen, L. H. METHOD OF PREPARING A CATALYST STRUCTURE, Patent WO 2015/104025 A1. July 26, 2015.

(30) Edgington, J.; Deberghes, A.; C. Seitz, L. Glassy Carbon Substrate Oxidation Effects on Electrode Stability for Oxygen Evolution Reaction Catalysis Stability Benchmarking. *ACS Appl Energy Mater* **2022**, *5* (10), 12206–12218. https://doi.org/10.1021/acsaem.2c01690.

(31) Inaba, M.; Quinson, J.; Arenz, M. PH Matters: The Influence of the Catalyst Ink on the Oxygen Reduction Activity Determined in Thin Film Rotating Disk Electrode Measurements. *J Power Sources* **2017**, *353*, 19–27. https://doi.org/10.1016/J.JPOWSOUR.2017.03.140.

(32) Weiß, A.; Siebel, A.; Bernt, M.; Shen, T.-H.; Tileli, V.; Gasteiger, H. A. Impact of Intermittent Operation on Lifetime and Performance of a PEM Water Electrolyzer. *J Electrochem Soc* **2019**, *166* (8), F487–F497. https://doi.org/10.1149/2.0421908jes.

(33) Oh, H.-S.; Nong, H. N.; Reier, T.; Bergmann, A.; Gliech, M.; Ferreira de Araújo, J.; Willinger, E.; Schlögl, R.; Teschner, D.; Strasser, P. Electrochemical Catalyst–Support Effects and Their Stabilizing Role for IrO_x Nanoparticle Catalysts during the Oxygen

Evolution Reaction. *J Am Chem Soc* **2016**, *138* (38), 12552–12563. https://doi.org/10.1021/jacs.6b07199.

(34) Oakton, E.; Lebedev, D.; Povia, M.; Abbott, D. F.; Fabbri, E.; Fedorov, A.; Nachtegaal, M.; Copéret, C.; Schmidt, T. J. IrO_2-TiO_2 : A High-Surface-Area, Active, and Stable Electrocatalyst for the Oxygen Evolution Reaction. *ACS Catal* **2017**, *7* (4), 2346–2352. https://doi.org/10.1021/acscatal.6b03246.

(35) Fabbri, E.; Habereder, A.; Waltar, K.; Kötz, R.; Schmidt, T. J. Developments and Perspectives of Oxide-Based Catalysts for the Oxygen Evolution Reaction. *Catal. Sci. Technol.* **2014**, *4* (11), 3800–3821. https://doi.org/10.1039/C4CY00669K.

(36) El-Sayed, H. A.; Weiß, A.; Olbrich, L. F.; Putro, G. P.; Gasteiger, H. A. OER Catalyst Stability Investigation Using RDE Technique: A Stability Measure or an Artifact? *J Electrochem Soc* **2019**, *166* (8), F458–F464. https://doi.org/10.1149/2.0301908jes.

(37) Hartig-Weiss, A.; Tovini, M. F.; Gasteiger, H. A.; El-Sayed, H. A. OER Catalyst Durability Tests Using the Rotating Disk Electrode Technique: The Reason Why This Leads to Erroneous Conclusions. *ACS Appl Energy Mater* **2020**, *3* (11), 10323–10327. https://doi.org/10.1021/ACSAEM.0C01944/ASSET/IMAGES/LARGE/AE0C01944_0002.JPEG.

(38) Wang, R.; Jiang, W.; Xia, D.; Liu, T.; Gan, L. Improving the Wettability of Thin-Film Rotating Disk Electrodes for Reliable Activity Evaluation of Oxygen Electrocatalysts by Triggering Oxygen Reduction at the Catalyst-Electrolyte-Bubble Triple Phase Boundaries. *J Electrochem Soc* **2018**, *165* (7), F436–F440. https://doi.org/10.1149/2.0371807jes.

(39) Hartig-Weiss, A.; Tovini, M. F.; Gasteiger, H. A.; El-Sayed, H. A. OER Catalyst Durability Tests Using the Rotating Disk Electrode Technique: The Reason Why This Leads to Erroneous Conclusions. *ACS Appl Energy Mater* **2020**, *3* (11), 10323–10327. https://doi.org/10.1021/acsaem.0c01944.

(40) Moreno-García, P.; Kovács, N.; Grozovski, V.; Gálvez-Vázquez, M. de J.; Vesztergom, S.; Broekmann, P. Toward CO_2 Electroreduction under Controlled Mass Flow Conditions: A Combined Inverted RDE and Gas Chromatography Approach. *Anal Chem* **2020**, *92* (6), 4301–4308. https://doi.org/10.1021/acs.analchem.9b04999.

(41) Moreno-García, P.; Grozovski, V.; Vázquez, M. de J. G.; Mysuru, N.; Kiran, K.; Kovács, N.; Hou, Y.; Vesztergom, S.; Broekmann, P. Inverted RDE (IRDE) as Novel Test Bed for Studies on Additive-Assisted Metal Deposition under Gas-Evolution Conditions. *J Electrochem Soc* **2020**, *167* (4), 042503. https://doi.org/10.1149/1945-7111/ab7984.

(42) Ehelebe, K.; Schmitt, N.; Sievers, G.; Jensen, A. W.; Hrnjić, A.; Collantes Jiménez, P.; Kaiser, P.; Geuß, M.; Ku, Y.-P.; Jovanovič, P.; Mayrhofer, K. J. J.; Etzold, B.; Hodnik, N.; Escudero-Escribano, M.; Arenz, M.; Cherevko, S. Benchmarking Fuel Cell Electrocatalysts Using Gas Diffusion Electrodes: Inter-Lab Comparison and Best

Practices. *ACS Energy Lett* **2022**, *7* (2), 816–826. https://doi.org/10.1021/acsenergylett.1c02659.

(43) Wiberg, G. K. H.; Nösberger, S.; Arenz, M. Evolution of a GDE Setup: Beyond Ambient Conditions. *Curr Opin Electrochem* **2022**, *36*, 101129. https://doi.org/10.1016/j.coelec.2022.101129.

(44) Collantes Jiménez, P.; Wiberg, G. K. H.; Sievers, G. W.; Brüser, V.; Arenz, M. Bridging the Gap between Basic Research and Application: A Half-Cell Setup for High Current Density Measurements of Ir-Based Oxygen Evolution Reaction Catalysts on Porous Transport Electrodes. *J Mater Chem A Mater* **2023**, *11* (37), 20129–20138. https://doi.org/10.1039/D3TA04136K.

(45) Schröder, J.; Mints, V. A.; Bornet, A.; Berner, E.; Fathi Tovini, M.; Quinson, J.; Wiberg, G. K. H.; Bizzotto, F.; El-Sayed, H. A.; Arenz, M. The Gas Diffusion Electrode Setup as Straightforward Testing Device for Proton Exchange Membrane Water Electrolyzer Catalysts. *JACS Au* **2021**, *1* (3), 247–251. https://doi.org/10.1021/jacsau.1c00015.

(46) Eastwood, B. J.; Christensen, P. A.; Armstrong, R. D.; Bates, N. R. Electrochemical Oxidation of a Carbon Black Loaded Polymer Electrode in Aqueous Electrolytes. *Journal of Solid State Electrochemistry* **1999**, *3* (4), 179–186. https://doi.org/10.1007/s100080050145.

(47) Geuß, M.; Milosevic, M.; Bierling, M.; Löttert, L.; Abbas, D.; Escalera-López, D.; Lloret, V.; Ehelebe, K.; Mayrhofer, K. J. J.; Thiele, S.; Cherevko, S. Investigation of Iridium-Based OER Catalyst Layers in a GDE Half-Cell Setup: Opportunities and Challenges. *J Electrochem Soc* **2023**, *170* (11), 114510. https://doi.org/10.1149/1945-7111/ad07ac.

(48) Banwell, T. C.; Jayakumar, A. Exact Analytical Solution for Current Flow through Diode with Series Resistance. *Electron Lett* **2000**, *36* (4), 291. https://doi.org/10.1049/el:20000301.

(49) Bird, J. *Electrical and Electronic Principles and Technology*, 2nd ed.; Routledge, 2003. https://doi.org/10.4324/9780080472591.

Supporting information

Beyond RDE Characterisation – Unveiling IrRu/ATO OER Catalyst Stability with a GDE Setup

Aline Bornet[1], Simon Pitscheider[2], Annabelle Maletzko[3], Nedjeljko Seselj[4], Erlend Bertheussen[2], Christoffer M. Pedersen[2], Gustav K. H. Wiberg[1], Julia Melke[3], Christian Kallesøe[2], Matthias Arenz[1, *]

[1] Department of Chemistry, Biochemistry and Pharmaceutical Sciences, University of Bern, Freiestrasse 3, 3012 Bern, Switzerland

[2] Danish Technological Institute, Gregersensvej 1, 2630 Taastrup, Denmark

[3] Department for Applied Electrochemistry, Fraunhofer-Institute for Chemical Technology ICT, Joseph-von-Fraunhofer Strasse 7, 76327 Pfinztal, Germany

[4] Blue World Technologies, Egeskovvej 6C, 3490 Kvistgaard, Denmark

* Corresponding author: matthias.arenz@unibe.ch

TEM micrographs of support and catalyst

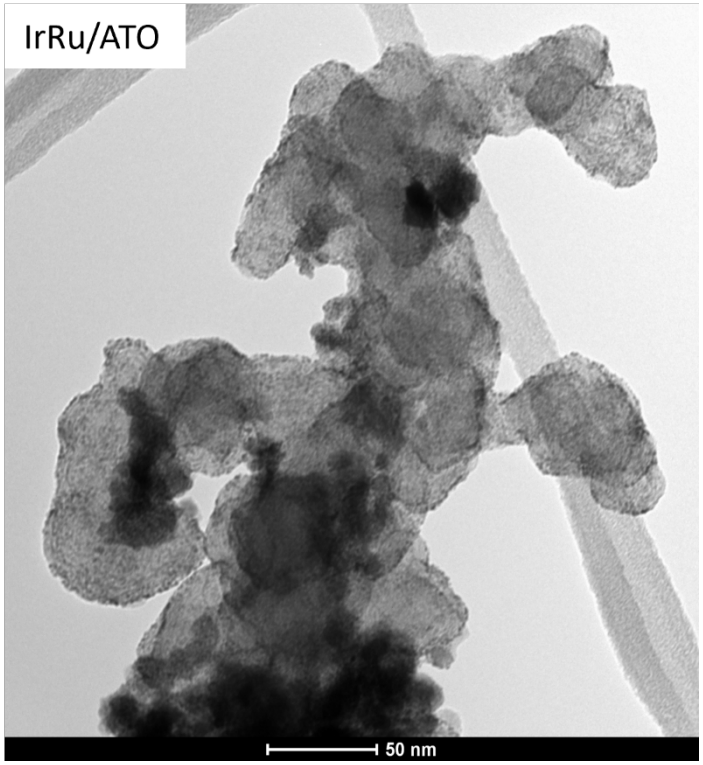

Figure S1. *TEM micrograph of the catalyst, $(Ir_{0.68}Ru_{0.32})_{0.96}Ni_{0.04}$/ATO.*

Reproducibility between electrodes

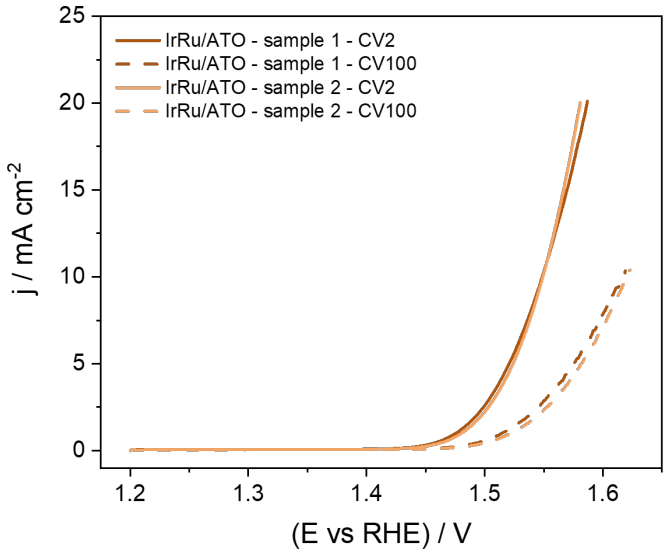

Figure S2. *OER evolution of IrRu/ATO by means of iR post-corrected CVs (forward scans – 2nd and 100th CVs). These measurements were recorded at 10 mV s^{-1} between 1.2 and 1.7 V vs RHE, using fresh electrode and new electrolyte. The measurements were performed in O_2-saturated 0.1 M $HClO_4$ at RT with the catalyst deposited on a GC disc with a nominal loading of 10 μg_{metal} cm^{-2}.*

Activity loss

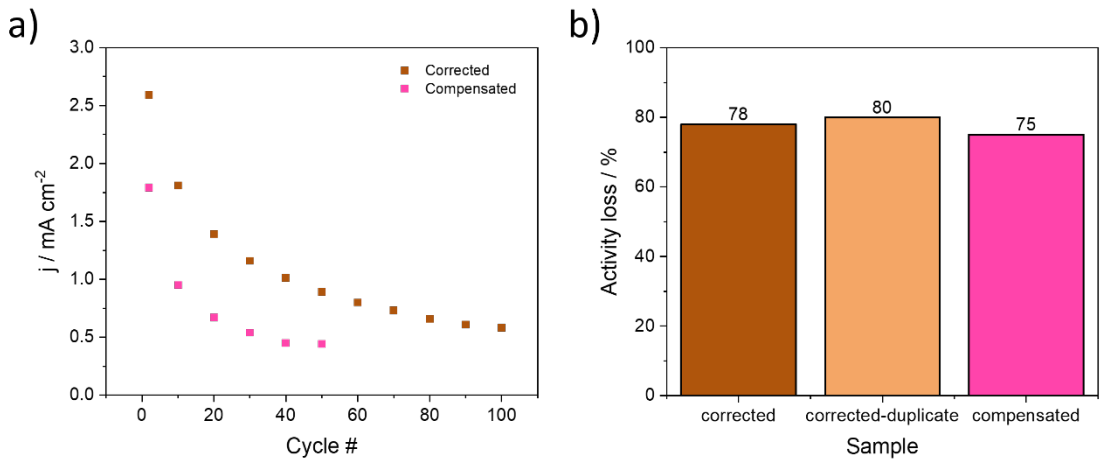

Figure S3. *(a) Decay in the OER current density extracted from Figure 1b and 1c at 1.5 V vs RHE against every 10th cycle. (b) Activity loss in % at 1.5 V vs RHE.*

The activity loss was calculated with the following formula:

$$Activity\ loss\ (\%) = \frac{CV_{last} - CV_2}{CV_2}$$

Recorded resistance of the compensated experiment

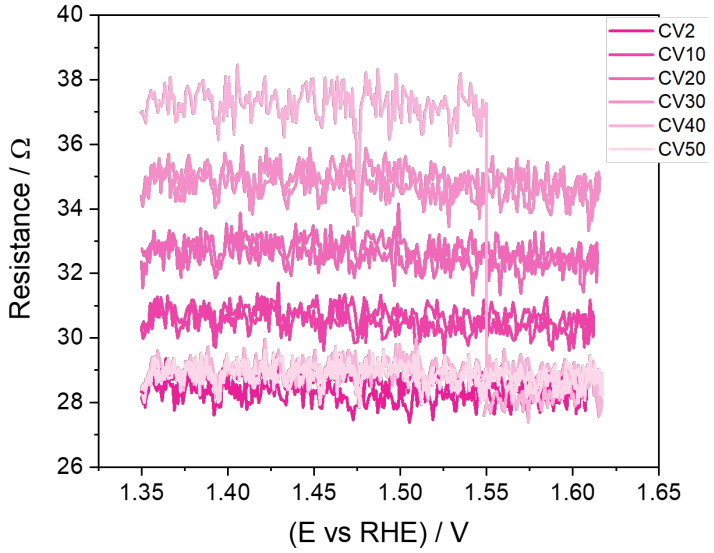

Figure S4. *Recorded resistance during the compensated experiment with IrRu/ATO*

Discussion based on the complementary methods used to understand the activity decay:

Capacitance measurements of the double-layer region (where no O_2 evolves) were conducted prior to and after the recording of the iR compensated CV series. As shown in Table S1, the capacitance of the bare GC is negligible as compared to the one of the electrodes covered with catalysts. The observed decrease in capacitance accounts for approximately 32%, substantially lower than the observed loss in apparent activity based on the CVs. This confirms that the observed decay in OER activity during the CVs cannot be solely attributed to the detachment and/or dissolution of the catalyst.

Table S1. *Summary of the obtained value for the capacitance double layer determination. For the actual sample, measurements were performed before and after the compensated 50 CVs. The loss was calculated similarly to the activity loss.*

Sample	*Capacitance in F m^{-2}*	*Standard deviation in F m^{-2}*	*Loss in %*
GC bare	0.79	0.02	
IrRu/ATO before	66.12	1.61	32.3
IrRu/ATO after	44.73	2.67	

It is worth pointing out that the determination of surface area and especially electrochemical surface area (ECSA) for non-metallic catalysts, like in our study, should be treated cautiously and is challenging.[1] Furthermore, the capacitance reflects the changes in the catalyst surface only if no other electrochemical process occurs in the investigated potential range. Unfortunately, this condition was not met since there is basically no inert backing electrode material at relevant OER potentials. Indeed, the widely used GC baking electrode suffers from passivation when exposed to the highly oxidative conditions of the OER.[2–6] This poses problems when dealing with porous NP-based catalysts that do not entirely cover the substrate material. Therefore, assumptions on catalyst stability only based on capacitance measurements should be taken with caution, too. Nevertheless, qualitative loss of catalyst can undoubtedly be pronounced based on the digital microscope images, see Figure S5.

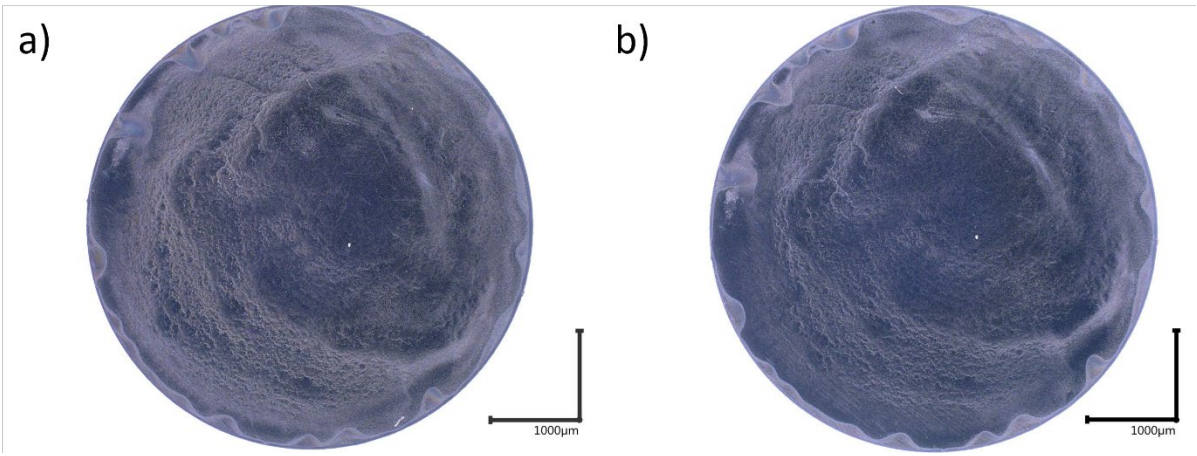

Figure S5. *Photographs of the electrode (a) before and (b) after the compensated CVs.*

EDX analysis was also performed to assess the degradation of the catalyst and especially the possible leaching of elements in the support. For that, the ratio between Sn and Sb was determined on the catalyst ink and the post-mortem electrode, see Table S2. It was found that the average between Sn and Sb goes from 93.7:6.3 wt.%, respectively, to 93.1:6.9 wt.%, resulting in an Sb increment of 0.6%, suggesting that Sn is being dissolved. Interestingly, some post-mortem SEM/EDX images of IrRu/ATO display islands with higher Ir wt.% and lower Sn wt.%. A representative example is depicted in Figure S6. One could hypothesise this phenomenon by the dissolution of Sn favouring the Ir dissolution and its subsequent redeposition onto larger particles during the experiment, similar to Ostwald ripening. However, attention needs to be paid that an error of 2% is often expected for EDX measurements. Therefore, as the difference between the ink and the post-mortem electrode is below 1%, these results must be taken with precaution.

Table S2. *Summary of the obtained ratios between Sn and Sb on IrRu/ATO (compensated experiment). The data were collected on 3 different spots and in total 8 different spectra were recorded for each sample.*

Sample	Area	Sn:Sb ratio (wt.%)	Average Sn:Sb ratio (wt.%)
$IrRu/ATO_{ICT}$ ink	149	93.4 : 6.6	93.7 : 6.3
	150	93.8 : 6.2	
	151	92.8 : 7.2	
	163	93.4 : 6.6	
	164	92.2 : 7.8	
	165	95.3 : 4.7	
	157	95.4 : 4.6	
	159	93.5 : 6.5	
$IrRu/ATO_{ICT}$ electrode postmortem	70	94.1 : 5.9	93.1 : 6.9
	71	94.9 : 5.1	
	88	92.3 : 7.7	
	92	93.9 : 6.1	
	94	93.7 : 6.3	
	101	91.4 : 8.6	
	102	92.2 : 7.8	
	108	92.6 : 7.4	

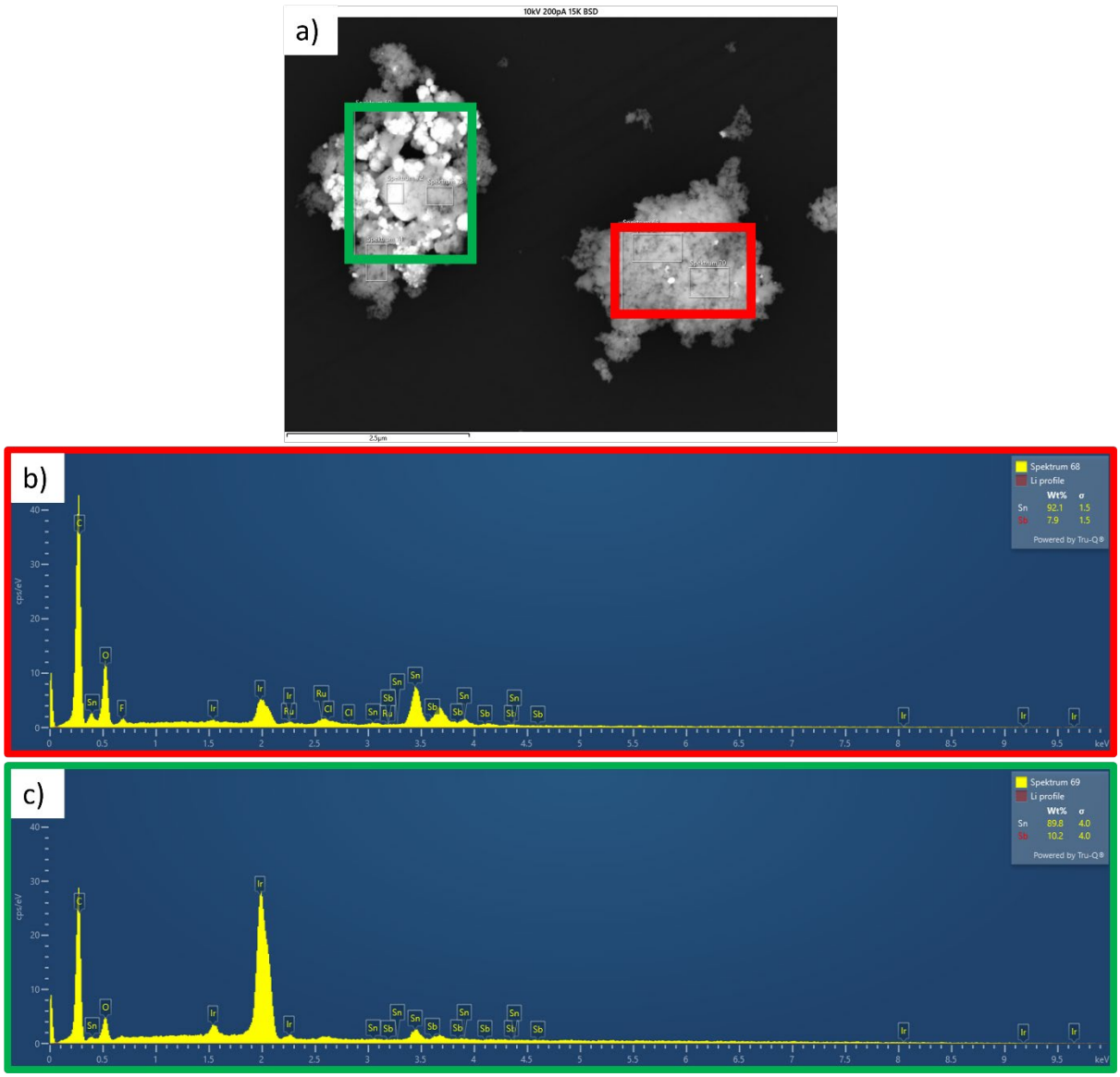

Figure S6. *(a) SEM/EDX image of postmortem IrRu/ATO and (b)-(c) the corresponding spectra.*

ICP-MS has a low detection limit of 1 ppt, thus allowing more accurate detection of leached elements. Therefore, analysis of electrolyte aliquots before inserting the electrode and after the completion of the experiment was conducted. It was found that Sn was leached by 4 ppt, while only trace amounts (*i.e.*, below the detection limit) of Sb were detected, see Table S3. This confirms the observations made by EDX, where a lower Sn-content was observed. As these amounts are minimal (in the range of ng L^{-1}), conclusions on the stability of support should be considered with hindsight. Nevertheless, our results follow the claim of other researchers that ATO is not stable when tested in an aqueous model system (AMS).[7–10]

Table S3. *Obtained ICP-MS concentration (conc.) for IrRu/ATO (compensated experiment).*

	Sn conc. in ng L^{-1}	Sb conc. in ng L^{-1}
1 mL aliquot – before	6.7	Below detection limit
1 mL aliquot – after	10.9	Below detection limit
Difference	4.2	/

Protocol:

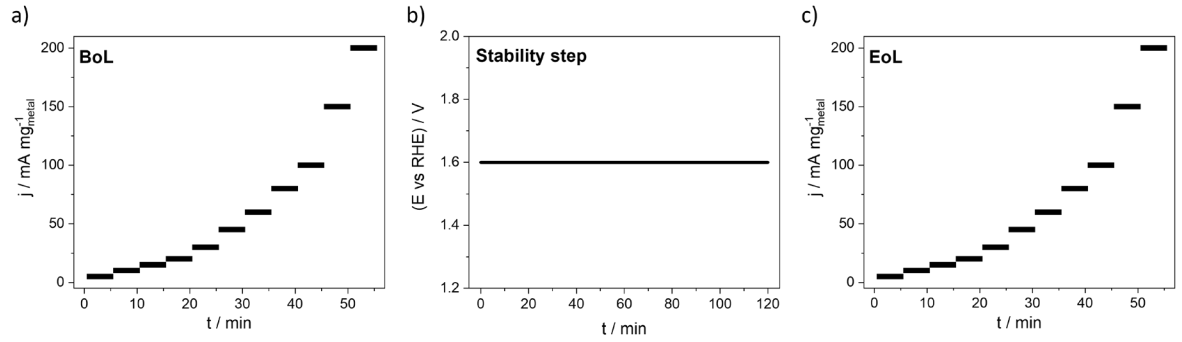

Figure S7. *Protocol used to assess the stability of the catalyst, with (a) BoL activity performed through constant current steps, (b) stability through a constant potential at 1.6 V vs RHE with an adaptative compensation, and (c) EoL activity through constant current steps.*

Electrode after experiment:

Table S4. *Photographs of the electrode after completion of the GDE experiments.*

	C-based GDL	Ti-based PTL
Front side		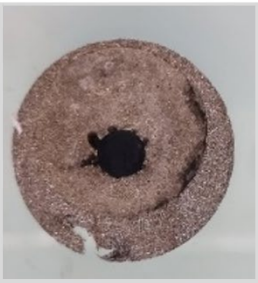
Back side	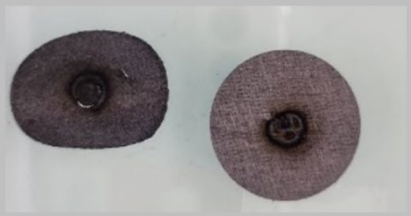	

Stability step – Loading dependence:

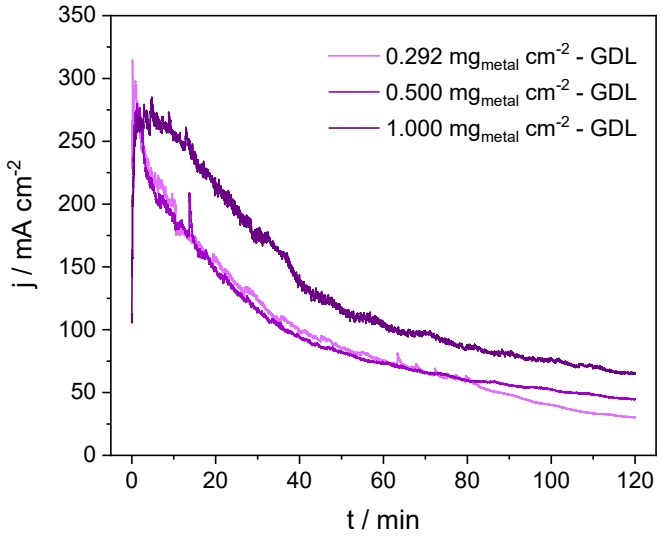

Figure S8. *Loading dependence of the OER current density transients for IrRu/ATO on a C-GDL. The nominal loadings are 0.292, 0.500 and 1.000 mg$_{metal}$ cm^{-2}. The measurements were performed in the GDE setup in an O_2 atmosphere at 60 °C using 4 M $HClO_4$ as an electrolyte. The potential was held at 1.6 V vs RHE (performed with adaptative compensation).*

Resistance comparison of the BoL and EoL steps for the PTL electrode:

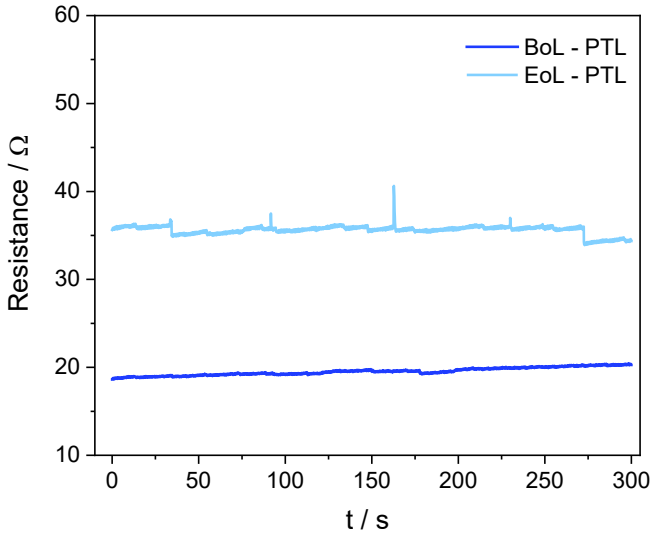

Figure S9. *Resistance comparison of the BoL and EoL last step for the catalyst-PTL system.*

Difference in BoL and EoL potentials versus the current densities:

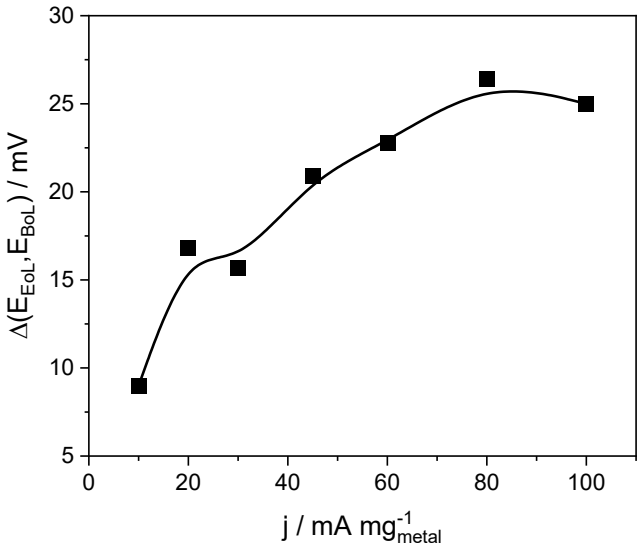

Figure S10. *BoL and EoL potentials versus the current densities for the catalyst-PTL system.*

References

(1) Wei, C.; Rao, R. R.; Peng, J.; Huang, B.; Stephens, I. E. L.; Risch, M.; Xu, Z. J.; Shao-Horn, Y. Recommended Practices and Benchmark Activity for Hydrogen and Oxygen Electrocatalysis in Water Splitting and Fuel Cells. *Advanced Materials* **2019**, *31* (31), 1806296. https://doi.org/10.1002/adma.201806296.

(2) Yi, Y.; Weinberg, G.; Prenzel, M.; Greiner, M.; Heumann, S.; Becker, S.; Schlögl, R. Electrochemical Corrosion of a Glassy Carbon Electrode. **2017**. https://doi.org/10.1016/j.cattod.2017.07.013.

(3) Edgington, J.; Deberghes, A.; C. Seitz, L. Glassy Carbon Substrate Oxidation Effects on Electrode Stability for Oxygen Evolution Reaction Catalysis Stability Benchmarking. *ACS Appl Energy Mater* **2022**, *5* (10), 12206–12218. https://doi.org/10.1021/acsaem.2c01690.

(4) Zlatar, M.; Escalera-López, D.; Rodríguez, M. G.; Hrbek, T.; Götz, C.; Mary Joy, R.; Savan, A.; Tran, H. P.; Nong, H. N.; Pobedinskas, P.; Briega-Martos, V.; Hutzler, A.; Böhm, T.; Haenen, K.; Ludwig, A.; Khalakhan, I.; Strasser, P.; Cherevko, S. Standardizing OER Electrocatalyst Benchmarking in Aqueous Electrolytes: Comprehensive Guidelines for Accelerated Stress Tests and Backing Electrodes. *ACS Catal* **2023**, *13* (23), 15375–15392. https://doi.org/10.1021/acscatal.3c03880.

(5) Ehelebe, K.; Escalera-López, D.; Cherevko, S. Limitations of Aqueous Model Systems in the Stability Assessment of Electrocatalysts for Oxygen Reactions in Fuel Cell and Electrolyzers. *Curr Opin Electrochem* **2021**, *29*, 100832. https://doi.org/10.1016/j.coelec.2021.100832.

(6) Geiger, S.; Kasian, O.; Mingers, A. M.; Nicley, S. S.; Haenen, K.; Mayrhofer, K. J. J.; Cherevko, S. Catalyst Stability Benchmarking for the Oxygen Evolution Reaction: The Importance of Backing Electrode Material and Dissolution in Accelerated Aging Studies. *ChemSusChem* **2017**, *10* (21), 4140–4143. https://doi.org/10.1002/cssc.201701523.

(7) Geiger, S.; Kasian, O.; Mingers, A. M.; Mayrhofer, K. J. J.; Cherevko, S. Stability Limits of Tin-Based Electrocatalyst Supports. *Scientific Reports 2017 7:1* **2017**, *7* (1), 1–7. https://doi.org/10.1038/s41598-017-04079-9.

(8) da Silva, G. C.; Venturini, S. I.; Zhang, S.; Löffler, M.; Scheu, C.; Mayrhofer, K. J. J.; Ticianelli, E. A.; Cherevko, S. Oxygen Evolution Reaction on Tin Oxides Supported Iridium Catalysts: Do We Need Dopants? *ChemElectroChem* **2020**, *7* (10), 2330–2339. https://doi.org/10.1002/CELC.202000391.

(9) Abbou, S.; Martin, V.; Claudel, F.; Sola, L.; Beauger, C.; Dubau, L.; Maillard, F. Manipulating the Corrosion Resistance of SnO_2 Aerogels through Doping for Efficient and Durable Oxygen Evolution Reaction Electrocatalysis in Acidic Media. **2024**. https://doi.org/10.1021/acscatal.0c01084.

(10) Ferreira da Silva, C. D.; Claudel, F.; Martin, V.; Chattot, R.; Abbou, S.; Kumar, K.; Jiménez-Morales, I.; Cavaliere, S.; Jones, D.; Rozière, J.; Solà-Hernandez, L.; Beauger, C.; Faustini, M.; Peron, J.; Gilles, B.; Encinas, T.; Piccolo, L.; Barros de Lima, F. H.; Dubau, L.; Maillard, F. Oxygen Evolution Reaction Activity and Stability Benchmarks for Supported and Unsupported IrO_x Electrocatalysts. *ACS Catal* **2021**, *11* (7), 4107–4116. https://doi.org/10.1021/acscatal.0c04613.

DECLARATION OF CONSENT

Declaration of consent

on the basis of Article 18 of the PromR Phil.-nat. 19

Name/First Name: Aline Bornet

Registration Number: 12-928-487

Study program: Chemistry and Moleculare Sciences

Bachelor ☐ Master ☐ Dissertation ☑

Title of the thesis: Electrocatalyst Advancements for Acidic Oxygen Evolution Reaction: From Synthesis to Reliable Performance Evaluation

Supervisor: Prof. Dr. Matthias Arenz

I declare herewith that this thesis is my own work and that I have not used any sources other than those stated. I have indicated the adoption of quotations as well as thoughts taken from other authors as such in the thesis. I am aware that the Senate pursuant to Article 36 paragraph 1 litera r of the University Act of September 5th, 1996 and Article 69 of the University Statute of June 7th, 2011 is authorized to revoke the doctoral degree awarded on the basis of this thesis.
For the purposes of evaluation and verification of compliance with the declaration of originality and the regulations governing plagiarism, I hereby grant the University of Bern the right to process my personal data and to perform the acts of use this requires, in particular, to reproduce the written thesis and to store it permanently in a database, and to use said database, or to make said database available, to enable comparison with theses submitted by others.

Bern, May 6th 2024

Place/Date

Signature